Quantum teleportation-based protocols with hybrid entanglement of light

Tom Darras

SORBONNE UNIVERSITÉ
CRÉATEURS DE FUTURS DEPUIS 1257

Laboratoire Kastler Brossel
Physique quantique et applications

THÈSE DE DOCTORAT DE SORBONNE UNIVERSITÉ

Spécialité : Physique Quantique

École doctorale n°564: Physique en Île-de-France

réalisée

au Laboratoire Kastler Brossel

sous la direction de Julien Laurat

présentée par

Tom Darras

pour obtenir le grade de :

DOCTEUR DE SORBONNE UNIVERSITÉ

Sujet de la thèse :

Quantum teleportation-based protocols with hybrid entanglement of light

soutenue le 30 Juin 2021

devant le jury composé de :

M.	Ulrik Lund ANDERSEN	Rapporteur
M.	Olivier PFISTER	Rapporteur
Mme	Virginia D'AURIA	Examinatrice
Mme	Eleni DIAMANTI	Examinatrice
M.	Rinaldo TROTTA	Examinateur
M.	Philip WALTHER	Examinateur
M.	Julien LAURAT	Directeur de thèse

Remerciements

Paris, le 22 septembre 2021

Quand j'ai commencé ma thèse il y a quatre ans, je n'avais pas conscience du courage et de la résilience dont j'allais avoir besoin pour mener à bien mes travaux, mais surtout, de la quantité de personnes que je rencontrerais et qui me soutiendraient tout au long de ce projet. Dans la frénésie du quotidien, on a souvent tendance à croire, à tort, que nous sommes seuls face à la difficulté. Mais certains moments de grâce nous rappellent toute la chance qui nous est donnée et tous les privilèges dont nous avons bénéficié. Cette thèse n'aurait jamais été si fructueuse sans les conditions d'étude et d'épanouissement personnel exceptionnelles dont j'ai pu profiter, et je remercie l'ensemble des personnes qui y ont contribué.

Je tiens d'abord à remercier ma famille, qui s'est toujours efforcée de rester unie malgré les difficultés, et qui a toujours mis à disposition les moyens matériels pour me permettre d'effectuer mes études dans les meilleures conditions. En particulier, merci à mes parents qui m'ont inculqué depuis le plus jeune âge le goût du travail et de l'effort. Merci à mes soeurs pour leur affection sans faille.

J'ai eu le privilège de bénéficier, au Laboratoire Kastler Brossel, d'un environnement de recherche d'exception. Merci à mon superviseur Julien Laurat qui m'a accueilli dans son équipe et qui m'a fourni les meilleures conditions de travail que je puisse imaginer, d'abord en mettant à ma disposition l'ensemble des ressources matérielles nécessaires à la réussite de mon projet, et ensuite en apportant un encadrement subtilement équilibré entre pédagogie sur les questions techniques et scientifiques, et autonomie sur la gestion de mon travail. Merci au directeur Antoine Heidmann et au personnel du service administratif qui ont su être à mon écoute dans les moments difficiles. Merci à l'ensemble des chercheurs du laboratoire avec qui j'ai pu échanger et apprendre sur la recherche de haut vol dans des domaines passionnants et variés. Merci au personnel des services techniques, notamment de l'atelier de mécanique, qui m'ont aidé pendant ma thèse.

Merci à Adrien Cavaillès et Giovanni Guccione avec qui j'ai partagé mes deux premières années de thèse et qui m'ont formé sur l'expérience avec une grande bienveillance (et qui m'ont surtout laissé mettre ma musique de dégénéré pendant nos longues heures d'alignement). Merci à mes prédécesseurs Olivier Morin, Kun Huang et Hanna Le Jeannic qui ont su répondre à mes nombreuses questions sur les étapes antérieures de la manip. Merci à mes collègues de l'équipe, dont la plupart sont maintenant des amis : Félix Hoffet,

Jérémy Berroir, Adrien Bouscal, Jérémy Raskop, Thomas Nieddu, Tridib Ray et Alban Urvoy. Merci aux amis doctorants du LKB, notamment l'équipe du "Friday Bar", pour tous les moments de convivialité que nous avons partagé. Merci à mes successeurs sur le projet, en particulier Beate Asenbeck pour son énergie positive qui m'a permis de finaliser le projet dans une ambiance chaleureuse. Je leur souhaite le plus de succès dans les épreuves à venir.

J'aimerais également remercier les professeurs et encadrants dont la passion pour la physique fondamentale a contribué à orienter mon projet de carrière dans la recherche. Mon professeur de physique quantique à l'ESPCI, Nicolas Bergeal, mes superviseurs Daiki Hatanaka et Tim Byrnes qui m'ont encadré pendant mes projets de recherche respectivement à NTT BRL et à la NYU à Shanghai. Merci à Arthur Goetschy qui m'a aidé à m'orienter vers l'information quantique et qui m'avait conseillé de rejoindre le groupe de Julien pour ma thèse.

Je remercie les membres de mon jury de thèse : mes deux rapporteurs Ulrik Lund Andersen et Olivier Pfister, les examinateurs Viriginia D'Auria, Rinaldo Trotta et Philip Walther, et la présidente du jury Eleni Diamanti qui ont pris les temps d'étudier mes travaux malgré leurs nombreuses solliciations.

Enfin, merci à mes amis qui subliment ma vie déjà privilégiée en la rendant exceptionnelle. Merci à la bande "Bretzels & Techno" pour tous ces moments partagés ensemble. Une pensée particulière à mes frères (et soeur) Alexandre Kehren, Edouard Quérel, Rémi Laumont et Violette Jaecki qui m'accompagnent depuis désormais plus de dix ans. Merci à mes compagnons de voyage Mathieu Durand, Quentin Nozet et Alain Quentel. Merci à tous les autres que je ne mentionne pas mais qui me sont tout autant chers.

Introduction

Hybrid quantum information processing

In analogy to what has happened for classical signals with the digital and analog paradigms, quantum information has developed along two traditionally separated lines. One approach, referred to as the *discrete-variable* one, relies on quantum systems, such as single photons, living in a Hilbert space of finite dimension [1]. The resulting state, called a *qubit*, can be written as a superposition of two quantum states:

$$|\psi\rangle = c_0 |0\rangle + c_1 |1\rangle . \tag{1}$$

An alternative approach, referred to as the *continuous-variable* one, is based on wave-like states belonging to an infinite dimensional Hilbert space [2]. Following this strategy, a continuous-variable qubit can be defined as a superposition of classical coherent states in the form of *Schrödinger cat states*:

$$|\psi\rangle = c_\alpha |\alpha\rangle + c_{-\alpha} |-\alpha\rangle . \tag{2}$$

In recent years, few groups, including the Quantum Networks Team at LKB, have tackled the effort to combine these two traditionally-separated approaches, integrating continuous- and discrete-variable tools and concepts in optical hybrid realizations [3]. These protocols can overcome some limitations of the schemes taken individually or provide novel capabilities. In that prospect the team has recently demonstrated a so-called *hybrid entanglement of light* between particle-like and wave-like qubits to bridge the two approaches of quantum information processing [4, 5].

Since then our team aims at exploring the uniqueness and benefits of hybrid entanglement light and at harnessing this yet unexplored photonic resource to realize first advanced protocols. This resource opens up the promise of heterogeneous quantum protocols and networks where the two encodings can be combined or interconverted in the form best suited for a particular process. In this framework, the goal of this thesis is to implement for the first time *quantum teleportation-based protocols with hybrid entanglement of light* for the transmission of quantum information between discrete- and continuous- variable states, and the interconnection of remote quantum nodes of different natures in heterogeneous quantum networks.

Context and outline

I joined the group of Prof. Julien Laurat as an intern in April 2017 and started my PhD in October 2017. Four PhD students had preceded my arrival: Olivier Morin, Kun Huang, Hanna le Jeannic, and Adrien Cavaillès. Each generation of PhD student had an overlap of at least one year with the previous and the next ones as to enable an efficient transfer of knowledge. Olivier Morin started his PhD in 2011 and installed during his thesis two optical parametric oscillators (OPOs) for the generation of discrete-variable and continuous-variable quantum states [6]. The conjoint work of Olivier, Kun and Hanna led to the first realization of hybrid entanglement of light in 2014 [4]. During their thesis Kun and Hanna developed the use of superconducting nanowire single-photon detectors (SNSPDs) on our experiment [7], following a collaboration with NIST and JPL. They extended the quantum engineering to more exotic non-Gaussian states [8, 9] and developed for that purpose micro-controller-based digital locking techniques [10]. Adrien started his PhD in 2015 and worked with Hanna for the first half of his thesis. Together they implemented quantum information protocols where hybrid entanglement was for the first time used as a resource in itself: the remote state preparation of continuous-variable qubits [11] and a non-locality steering test [12]. Upon my arrival, the group had developed a strong expertise in the engineering of hybrid non-Gaussian resources [13]. The experiment, which involved at that time two OPOs and two SNSPDs, was fully operational at the beginning of my PhD.

The start of my project in 2017 coincided with the arrival of Giovanni Guccione who pursued a Marie Curie post-doc fellowship in our group. The goal of our team at that time was to extend the range of protocols in which hybrid entanglement could be employed, and in particular, we targeted quantum teleportation protocols, the implementation of which required a significant progress in experimental resources. This experimental effort included the installation of a cryocooler that our group acquired in 2017 to increase our single-photon detection capability. During the first two years of my PhD I worked with Adrien and Giovanni. It enabled an efficient transfer of experimental skills. Together, we designed and implemented an entanglement-swapping protocol with hybrid entanglement of light [14]. This scheme, based on a time-multiplexed use of the two OPOs and SNSPDs, enabled the demonstration of the protocol with minimum resources. Still it required a significant improvement of the setup with the addition of a 15-m long free-space delay line and a reorganization of the light paths. The experiment, which was employing all the resources available in our lab at that time, has been an excellent training for me. After these two years I could be entirely autonomous in the lab.

After this project, Adrien and Giovanni concurrently left the group in February and May 2019 and I had to lead the experiment on my own. In parallel, Julien followed a sabbatical research program in the group of Jeff Kimble at Caltech from August 2019 to December 2019. I took that opportunity to finish the installation of a cryocooler on which I was working on in parallel to the swapping experiment. In the summer of 2019 we had an operational cooling system with which we could double the number of single-photon detector available for our experiment. The installation of the cryocooler was directly

followed by the building of a spectral filtering system inclusive of a home-made 400 μm long bulk micro-cavity, and a coincidence detection system.

After the increase in single-photon detection capability, an increment in the number of single-photon sources was required in order to perform experiments involving simultaneously - at least - three independent quantum states. To that end I built a second triply-resonant type-II OPO for our experiment. This was an important challenge as the design we developed, based on the tilting of the crystal in the cavity, had never been attempted before, and it was not trivial at all that the three optical parametric oscillators could then be employed simultaneously on our experiment. Though interrupted for several weeks by the simultaneous failure of both our laser and cryocooler which I had to repair myself, the first development of this source from January to March 2020 gave very promising results where we could achieve the concurrent operation of our three OPOs in parallel. This was opening the way to the implementation of even more ambitious protocols.

Unfortunately, in March 2020, our experimental research activity had to stop because of the first lockdown in France which lasted three months. I took the opportunity, during that time, to study theoretically the next protocol we were targeting: the quantum teleportation from a discrete-variable to a continuous-variable qubit via hybrid entanglement. This protocol could not be achieved in our previous scheme involving a delay line, and we were very enthusiastic to implement it with our novel resources. In parallel, I worked on a collaboration with the group of Radim Filip who developed a new benchmark for single-photon sources that we adapted to the heralded single photons generated from our OPOs [15]. These theoretical works on hybrid teleportation have been very fruitful for us as we developed an efficient procedure for the generation of discrete-variable qubits that we would certainly have missed otherwise. After these three months I was totally ready to go back in the lab and finish the last developments that were required to perform the protocol. The activity in the lab was only partially recovered for the next months, but the team adapted the schedule so that I could work on the project as much as possible. I am very grateful to them. By the beginning of July 2020 the experiment, which had misaligned during the confinement, was back on the state where we left it in March 2020. To compensate for that delay my thesis contract had been extended for nine months.

Yet, even with all the experimental resources at hand, operating a complex quantum optics experiment, especially since we had almost doubled the experimental setup, was very challenging to perform on one own. Very luckily our team was joined by Beate Asenbeck who started her PhD in October 2020. Together we finished the calibration of the experiment and, by January 2021, we succeeded in demonstrating the hybrid quantum teleportation from discrete- to continuous-variable qubits. This setup was involving all the resources initially available on the experiment supplemented by the ones I had built, almost from the ground up, during the last two years of my PhD.

For clarity the manuscript is organized in a chronological fashion:

- **Chapter 1** introduces the conceptual ideas required for the understanding of the thesis. We first motivate the development of quantum technologies in order to supplement current, classically-limited, devices. Following the superposition principle, we present how quantum information can be encoded in either discrete- or continuous-variable quantum states and define the mathematical tools required for their description. We introduce in the same manner quantum entanglement, which is at the heart of our work, and is essential for the development of quantum-enhanced tasks. We finally proceed to the theoretical presentation of the quantum teleportation and entanglement swapping protocols in the framework of heterogeneous quantum networks addressed in this thesis.

- **Chapter 2** focuses on the basic experimental tools we employ in our lab for the engineering of non-Gaussian quantum states. We first describe the optical parametric oscillators which show a very large escape efficiency thanks to a semi-monolithic design. They enable the production of either single-mode or two-mode squeezing for the generation of high purity continuous- and discrete-variable states. We present the superconducting nanowire single-photon detectors that are used in our work for the heralding of events with their initial operating cryogenic system. These detectors show record system detection efficiencies with minimum dark counts.

- **Chapter 3** presents the basic protocols realized with our optical parametric oscillators and superconducting nanowire single-photon detectors for the generation of discrete- and continuous-variable quantum states. These two schemes are combined in a setup where hybrid entanglement between discrete- and continuous-variable qubits is created by mixing the two heralding modes in an indistinguishable fashion. We also present in this chapter the benchmark we developed in collaboration with the group of Radim Filip, called Fock-state bunching capability, which studies the ability of experimentally generated single photons to follow extreme multi-photon interference. This chapter concludes the introduction of the experimental tools and protocols we employ in our lab for quantum state engineering.

- In **Chapter 4** we theoretically introduce the hybrid technique we developed for the implementation of a Bell-state measurement, which is central to the success of the teleportation protocols we will perform in this work. This Bell-state measurement combines experimental techniques from both the discrete- and continuous-variable paradigms, namely photon counting on a single-photon detector and quadrature conditioning on homodyne detection. After discussing the interest of this technique for hybrid quantum teleportation, we study theoretically, taking into account experimental imperfections, the performance of the Bell-state measurement for both quantum teleportation and entanglement swapping. We finally describe the implementation of this new technique with our experimental resources.

- **Chapter 5** presents the first protocol we demonstrated in this work, namely entanglement swapping with hybrid entanglement of light. After motivating the interest of this scheme in the framework of heterogeneous quantum networks, we present the experimental setup based on the time-multiplexed use of two OPOs and two SNSPDs. By consecutively using the same OPOs, we first create single-photon entanglement and store one of its mode in a free-space delay line. This mode is brought to interfere, after an appropriate delay, with the DV mode of a hybrid entangled state. Upon success of the Bell-state measurement, a new hybrid entangled state is created between two modes which never interacted. All the involved states are characterized by two-mode quantum state tomography to assess the amount of entanglement. We then study theoretically the performances of the swapping protocol for the propagation of hybrid entanglement in heterogeneous quantum networks. In the end we present the limitations of the setup involving two OPOs and two SNSPDs only.

- In **Chapter 6**, following the analysis of the entanglement swapping scheme, we describe the two major assets that have been added to the experiment during this thesis, i.e. a type-II OPO based single-photon source and a cryocooler for the operation of four SNSPDs. We present the challenging task of operating two triply resonant simultaneously on a single experiment and describe the protocol we will employ for the generation of high purity discrete-variable qubits using this new OPO. We introduce the design and assembly of the cryocooler and study its performances for the operation of four independent SNSPDs. We finally present an improved method for the detection of coincidences between different detectors.

- **Chapter 7** concludes our work with the demonstration of quantum teleportation from a discrete-variable qubit to a continuous-variable qubit. We first create the discrete-variable input from the OPO we built, then herald independently hybrid entanglement, and conclude the protocol by the application of the hybrid Bell-state measurement. Both the input and output states are characterized by single-mode quantum state tomography and the success of the protocol is assessed by the measure of a fidelity of teleportation above the classical bound. We study the interest of our post-selection-free experiment in the context of heterogeneous quantum networks and propose some extension of the scheme to other quantum encodings.

List of publications

- *Engineering optical hybrid entanglement between discrete- and continuous-variable states.*
  Kun Huang, Hanna Le Jeannic, Olivier Morin, Tom Darras, Giovanni Guccione, Adrien Cavaillès, and Julien Laurat
  New Journal of Physics, **21**, 083033 (2019) doi:10.1088/1367-2630/ab34e7.

- *Connecting heterogeneous quantum networks by hybrid entanglement swapping.*
  Giovanni Guccione*, Tom Darras*, Hanna Le Jeannic, Varun B. Verma, Sae Woo Nam, Adrien Cavaillès, and Julien Laurat
  Science Advances, **6**, eaba4508 (2020) doi:10.1126/sciadv.aba4508.

- *Experimental Fock-state bunching capability of non-ideal single-photon states.*
  Petr Zapletal, Tom Darras, Hanna Le Jeannic, Adrien Cavaillès, Giovanni Guccione, Julien Laurat, and Radim Filip
  Optica, **8**, 743 (2021) doi:10.1364/OPTICA.419230.

- *A quantum bit encoding converter.*
  Tom Darras, Beate Asenbeck, Giovanni Guccione, Adrien Cavaillès, Hanna Le Jeannic, and Julien Laurat
  To be submitted.

- *A hybrid Bell-state measurement combining photon counting and homodyne conditioning.*
  Tom Darras, Beate Asenbeck, Giovanni Guccione, Adrien Cavaillès, Hanna Le Jeannic, and Julien Laurat
  In preparation.

Contents

Chapter 1

Teleportation-based protocols in heterogeneous quantum networks

This chapter presents the conceptual ideas central to this thesis. We first introduce the field of quantum information processing in which the development of quantum technologies is nowadays surpassing classically-limited tasks. Then, we present the two paradigms for the encoding of quantum information using discrete- or continuous-variable states. After recalling the properties of entanglement and its use in quantum networks, we will describe the protocols of quantum teleportation and entanglement swapping, which are key building blocks of quantum repeaters and long distance communication in heterogeneous quantum networks.

1 Quantum information science and technology

Quantum information processing is, by definition, the use of the laws of quantum mechanics - such as superposition and entanglement - to process information in a more efficient way than what is possible with devices governed by classical physics [16]. This field of research historically emerged a few decades ago to overcome the growing limitations of classical processors, and is now developing a second generation of quantum-enhanced technologies, with applications in communication, computing and sensing.

1.1 The limits of classical information processing

The development of classical information processors is nowadays facing several obstacles requiring the emergence of novel technologies. First, the reduction of the size of the classical processors leads to the requirement of taking into account quantum effects that start becoming significant at the scales involved. Second, classical computation seems to be unable to solve efficiently certain classes of problems that could be useful for the development of science and technology. Finally, classical processors fail at simulating even simple quantum systems, such as molecules, since the number of operations required scales exponentially with the number of particles involved.

1.1.1 Reducing the size of the processors

Moore's law [17] describes the empirical regularity of the number of transistors in integrated circuits to double approximately every two years. Following this trend, the reduction of the size of the processors, from about 10 μm in 1971 to sub-nanometer scale expected around 2025, leads to the emergence of new physical quantum phenomena which need to be taken into account for the design and operation of new generations of processors. As envisioned by Richard Feynman at the American Physical Society meeting in 1959 [18]: "*When we get to the very, very small world we have a lot of new things that would happen that represent completely new opportunities for design. Atoms on a small scale behave like nothing on a large scale, for they satisfy the laws of quantum mechanics. So, as we go down and fiddle around with the atoms down there, we are working with different laws, and we can expect to do different things*". The classical processors will thus naturally be limited as they approach the quantum world, and new technologies, ideally based on these quantum phenomena, should be employed in replacement. It turns out that quantum processors offer much more than smaller and faster processors.

1.1.2 Computational complexity classes

In computer science, problems or tasks are sorted into *complexity classes*, which are collections of computational problems that share some common features with respect to the computational resources needed - such as time or memory - to solve those problems [19]. The two most important classes are called **P** and **NP**, where **P** is the class of computational problems that can be solved quickly on a classical computer while **NP** is the class of problems that have solutions that can be quickly checked on a classical computer. Even though if it not clear whether these two classes are different or not, there are some tasks, such as finding the prime factors of an integer, that appear to belong, for now, in the class **NP** but not **P**.

Quantum complexity classes can be defined similarly. The **BQP** class is defined as the class of all computational problems which can be solved efficiently on a quantum computer. It has been proved that **BQP** contains **P** [20], i.e. all quantum computers can solve all the problems that classical computer can solve. Quantum computer can thus, on first sight, solve **NP** problems more efficiently than classical computers. An emblematic example is the Shor's algorithm which enables the factorization of prime numbers in a polynomial number of operations [21].

1.1.3 The failure to simulate quantum systems

The computational power required to even describe a quantum system scales exponentially with the number of its constituents. For instance, the description of a simple quantum state composed of N spin-1/2 particles requires the evaluation of 2^NHilbert space coefficients, which is in practice impossible to achieve with a classical computer if N is larger than 50 [22]. This makes very unpractical the simulation of basic elements, such as molecules or condensed matter systems. The strategy proposed by Feynman already

in 1982 [23] is to employ for the simulation alternative quantum systems in which the interactions can be engineered to the task at hand. The description of quantum systems thus requires by itself the development of quantum information processing for the design and engineering of such quantum simulators.

1.2 Towards quantum-enhanced applications with quantum technologies

Following the first quantum revolution, which enabled the development of lasers and transistors in the second part of the 20^{th} century, a *second quantum revolution* is now actively employing quantum mechanics to develop new technologies by engineering quantum states for novel purposes [24]. Quantum technology delivers useful devices and processes based on quantum principles such as quantization, uncertainty principle, tunneling, decoherence, quantum superposition and entanglement, the latter two being the ones of interest for this thesis and will be presented in details in the following sections. As presented in Figure 1.1, the field of quantum technology is usually divided in four domains [25]. First, *quantum communication* where individual or entangled photons are employed to transmit data in a conceptually, completely secure, way; second, *quantum computation* where quantum effects can be harnessed to speed up some calculations and optimization tasks; third, *quantum simulation* where well-engineered quantum systems are used to reproduce the behaviour of others; and fourth, *quantum sensing and metrology* where the high sensitivity of quantum states is exploited to enhance the measurement of physical quantities.

1.2.1 Quantum communication

Quantum communication [26] is based on the propagation of quantum states of light, such as single photons, quantum superpositions of states or entangled states. Many applications ranging from ultra-secure quantum cryptography [27, 28], the interfacing of remote quantum systems [29, 30, 31], or even the transfer of quantum states between two physical systems of different natures [32, 33, 34, 35], are now surpassing proof-of-principle experiments in academic labs to give rise to the development of real-life applications and commercial solutions [36].

1.2.2 Quantum computation

Quantum computing consists in the processing of information in a massively parallel way using superposed or entangled states within quantum processors running quantum algorithms. These processors are implemented nowadays using a range of competitive physical systems, and so far, many elementary instances of quantum algorithms have been demonstrated [37, 38, 39, 40]. Yet, the development of a fully featured universal quantum computer, where the control and error-correction of about 100 logical qubits is required, imposes a major scalability challenge comprising the integration of a large number of qubits and error correction codes [41]. The efforts that are nowadays growing from academic labs, start-ups [40, 42] and large companies [38, 39] with a variety of physical systems, are a clear

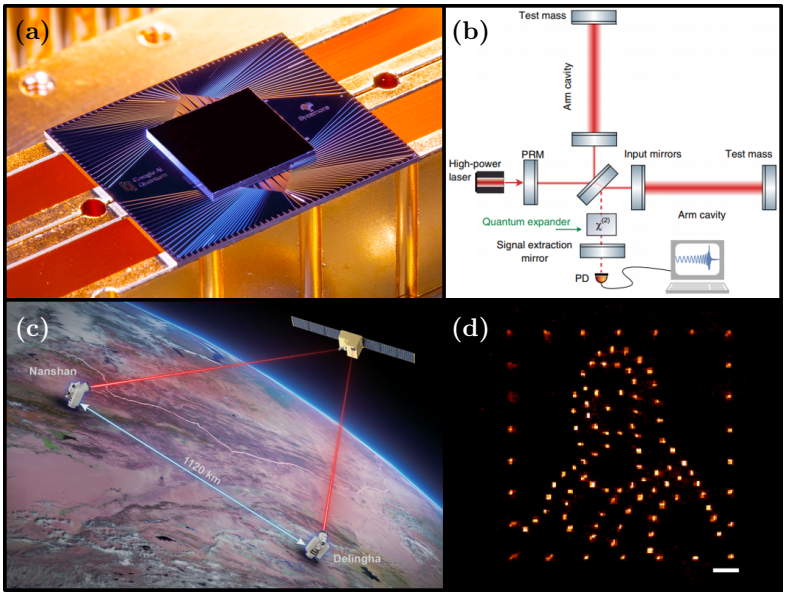

Figure 1.1: **Quantum technologies of the second revolution**. (a) From [39]. Photograph of the Sycamore superconducting quantum processor from Google AI composed of an array of 54 qubits. (b) From [43]. The sensitivity of gravitational wave detectors can be enhanced by employing quantum squeezed light. (c) From [28]. Illustration of the Micius satellite enabling entanglement-based secure cryptography over 1200 km. (d) From [44]. Engineered two-dimensional array of single Rydberg atoms for quantum simulation.

sign that large scale quantum computation is considered as a challenging but potentially rewarding goal.

1.2.3 Quantum simulation

As introduced earlier, quantum simulation consists in the use of an experimental system following the rules of quantum physics, called quantum simulator, to imitate an interacting system with many degrees of freedom. Such systems can be observed in many branches of science, including condensed-matter theory, quantum statistical mechanics, high-energy physics, cosmology, atomic physics or quantum chemistry [22]. Interestingly, a quantum simulator might be less challenging to build as compared to a quantum computer, as the more modest tasks to-be-simulated do not necessary need a knowledge of the complete many-body wavefunction, but rather specific physical quantities where error correction may therefore not be needed. There are nowadays many physical platforms which enable the broad engineering of the parameters of the simulated model, as well as the control of the preparation, manipulation and detection of the states of the system. Among them are Rydberg atoms [44], ultracold quantum gases [45], trapped ions [46] or photonic platforms [47].

1.2.4 Quantum sensing and metrology

By definition, a sensor is composed of a probe interacting with an appropriate system, the properties of which are of interest, and that changes the state of the probe. The measurements of the probe then reveal the characteristics of the desired system. In quantum-enhanced sensors [48, 49], the probe is generally prepared in a particular non-classical state, which can be a superposition of states, a quantum state with reduced noise, or an entangled state. The best classical sensors are limited by a precision that depends to the square root of the number of particles in the probe - known as the *Standard Quantum Limit* - while the best quantum sensors can in principle attain a precision that scales linearly with the number of particles in a suitable entangled state, known as the *Heisenberg limit*. Sensors of this quantum type can be implemented either in the optical domain, with, for instance, applications in the detection of gravitational waves [43, 50]; with atomic systems for clocks [51] or gravimeters [52]; and finally using spin-based [53, 54, 55] or optomechanical systems [56] for the precise detection of electric fields and other physical quantities.

The development of quantum technologies along these four directions has now passed the efforts in basic science only. Novel, quantum-enhanced tasks, are in intense development phase, with many actors in academia, start-ups and large companies. The interest and applications of these new technologies seems to go much beyond the interest of sole fundamental science, with many competing research programs emerging nationwide and even at continental scales.

2 Quantum states and encodings

Following the introduction of quantum information processing and quantum technologies, we now turn to the key elements of these research fields, i.e. quantum states and encodings. After introducing the properties of quantum superposition, we describe the two separate encodings of quantum information that have historically emerged, based either on discrete- or continuous- quantum variables. Finally we present the theoretical tools used in this thesis for the description of the quantum states.

2.1 Quantum superposition

The quantum superposition principle plays a central role in quantum information, and is at the heart of most of the *Gekanden experiments* and the "paradoxes" of quantum mechanics. To present its essence, let us go back to the *double-slit experiment* [57], considered at the "heart of quantum mechanics" [58], and elected by the readers of *Physics World* as the most beautiful experiment in physics to date [59]. The experiment is composed of a source, a double-slit and an observation screen. An interference fringe is visible on the screen, even when the particle are transmitted one by one, as long as it is not possible to infer through which of the two slits the particle passes. Thus, quantum mechanically,

the state of the system can only be described as a *coherent superposition* for the two possible configurations with either one of the two slits opened. It is important to note that "*the absence of any such information is the essential criterion for quantum interference to appear*" [60, 61].

Beyond its fundamental significance, the superposition principle can be used to encode information in superpositions of discrete or continuous quantum states. In the following we describe these two approaches of quantum information.

2.2 The discrete-variable approach

In classical information processing, the information is encoded digitally in the form of elementary system called *bits* which carry two possible values "0" or "1". Quantum information can be encoded, thanks to the superposition principle, as a coherent superposition of two orthogonal quantum states $|0\rangle$ and $|1\rangle$ in the form of a *qubit*:

$$|\psi\rangle = c_0 |0\rangle + c_1 e^{i\theta} |1\rangle . \tag{1.1}$$

The encoded information is given by the real amplitudes c_0 and c_1, following the relation $|c_0|^2 + |c_1|^2 = 1$, and θ, which is the relative phase between the two quantum states. As the computational basis $\{|0\rangle, |1\rangle\}$ is composed of a finite number of elements, i.e. the quantum state $|\psi\rangle$ belongs to a Hilbert space of finite dimensions, we say that the basis is *discrete*.

Discrete-variable basis can be generated from any two orthogonal eigenstates of observables of a single quantum system. In practice, it can be emulated by the presence or the absence of a photon - that we call *Fock basis* -, the polarization of a photon, the spin of an electron, or the current in a superconducting loop [3].

It is often useful to represent the quantum state on the surface of a sphere, called *Bloch sphere* [19]. As shown in Figure 1.2, this sphere has a unit radius, which corresponds to all the possible pure states. Opposite points represent a pair of mutual orthogonal states. The north and south poles of the sphere represent the states $|0\rangle$ and $|1\rangle$ respectively. In the general case, the qubit can be written using the spherical coordinates (ϕ, θ):

$$|\psi\rangle = \cos\left(\frac{\phi}{2}\right) |0\rangle + \sin\left(\frac{\phi}{2}\right) e^{i\theta} |1\rangle . \tag{1.2}$$

Any unitary evolution of the state $\hat{U}$ will then correspond to a rotation of the qubit on the Bloch sphere.

The superposition principle thus enables to encode information on superposition of eigenstates of discrete observables. A second quantum encoding can be defined equivalently from observables which have a continuous of spectrum eigenvalues.

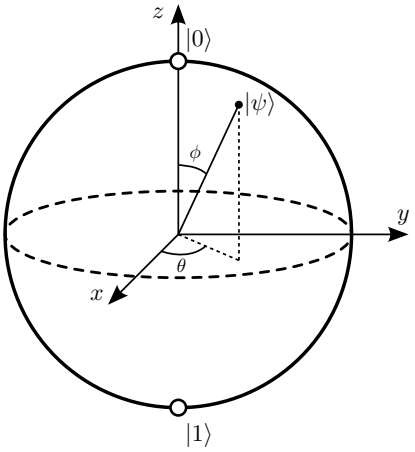

Figure 1.2: **Bloch sphere representation of a qubit**. The state of a two-level quantum state can be represented as a point in a sphere. It is characterized by its two spherical coordinates (ϕ, θ). The surface of the sphere with unit radius represents all possible pure states whereas the points inside the sphere correspond to mixed states.

2.3 The continuous-variable approach

2.3.1 Ideal continuous-variable states

An alternative representation of the discrete-variable approach is the encoding of a state on the eigenvectors $|x\rangle$ of a continuous operator $\hat{x}$ in the form of a *qumode*:

$$|\psi\rangle = \int_{-\infty}^{+\infty} \psi(x) |x\rangle \, dx, \tag{1.3}$$

where the information is encoded in the complex wavefunction, or probability amplitude density, $\psi(x)$.

The operator $\hat{x}$, and its conjugate $\hat{p}$ can, for instance, be represented by the spin variable of an atomic ensemble, the position and momentum of a mechanical oscillator, or in the optical domain as the amplitude and phase quadratures of the field [3] defined as:

$$\begin{aligned} \hat{x} =& \sigma_0(\hat{a} + \hat{a^\dagger}), \\ \hat{p} =& -i\sigma_0(\hat{a} - \hat{a^\dagger}), \end{aligned} \tag{1.4}$$

with σ_0^2 is the *variance of the vacuum state*, i.e $\langle 0| \hat{x}^2 |0\rangle = \sigma_0^2$. $\hat{a}$ and $\hat{a}^\dagger$ are the *annihilation* and *creation operator* respectively, defined as the subtraction or the addition of a photon in the number state - or *Fock state* - $|n\rangle$:

$$\begin{aligned} \hat{a} |n\rangle =& \sqrt{n} |n-1\rangle, \\ \hat{a}^\dagger |n\rangle =& \sqrt{n+1} |n+1\rangle, \end{aligned} \tag{1.5}$$

such that we recover the number operator $\hat{n} = \hat{a}^\dagger \hat{a}$ with $\hat{n} |n\rangle = n |n\rangle$.
The quadrature operators follow the commutation relation:

$$\left[\hat{x}, \hat{p}\right] = 2i\sigma_0^2, \tag{1.6}$$

and, as conjugate observables, they follow the Heisenberg uncertainty relation:

$$\Delta x \Delta p \geq \sigma_0^2. \tag{1.7}$$

Therefore, the quantum fluctuations of the field induce a fundamental noise, even for vacuum.
Finally, we can define from $\hat{x}$ and $\hat{p}$ the *the field quadrature operator at phase* θ as:

$$\hat{q}_\theta = \hat{x}\cos\theta + \hat{p}\sin\theta, \tag{1.8}$$

with the quadrature operator eigenvalues given by:

$$\hat{q}_\theta \left|q,\theta\right\rangle = q \left|q,\theta\right\rangle. \tag{1.9}$$

Finally, a quantum state can be fully described by its projection along the orthogonal quadratures, for example $|x\rangle$ and $|p\rangle$, to recover the wave-functions in phase space:

$$\begin{aligned} \psi(x) &= \langle x|\psi\rangle, \\ \psi(p) &= \langle p|\psi\rangle. \end{aligned} \tag{1.10}$$

These wavefunctions are related by the probabilities of measuring a corresponding quadratures, called the *marginal distributions* $P(q_\theta)$ and defined as:

$$P(q_\theta) = |\psi(q_\theta)|^2. \tag{1.11}$$

2.3.2 The Schrödinger cat states

Similarly to a discrete-variable qubit which is encoded as a superposition of two orthogonal quantum states, a continuous-variable qubit can be defined as a superposition of two orthogonal macroscopic "classical" states, such as *coherent states*. Such superpositions, which represent an extension to the quantum states into the macroscopic world are often called *Schrödinger cat states* as a reference to the Schrödinger's gekanden experiment [62]. They are expressed in the form:

$$|cat_\theta\rangle = \frac{1}{N_\theta}\Big[\,|\alpha\rangle + e^{i\theta}\,|-\alpha\rangle\,\Big], \tag{1.12}$$

where $N_\theta = \sqrt{2(1+\cos(\theta)e^{-2|\alpha|^2})}$ is a normalization factor, and $|\alpha\rangle$ is a coherent state of amplitude $|\alpha|$, with mean photon number $|\alpha|^2$. The coherent state is defined as the eigenvector of the annihilation operator:

$$\hat{a}\,|\alpha\rangle = \alpha\,|\alpha\rangle, \tag{1.13}$$

which can equivalently be seen as the action of the displacement operator $\hat{D}(\alpha) = e^{\alpha\hat{a}^\dagger - \alpha^*\hat{a}}$ on the vacuum state, $\hat{D}(\alpha)\,|0\rangle = |\alpha\rangle$, leading to the expansion in the Fock basis

$$|\alpha\rangle = e^{-|\alpha|/2}\sum_{n=0}^{+\infty}\frac{\alpha^n}{\sqrt{n!}}\,|n\rangle. \tag{1.14}$$

We can note that the definition of the cat state does not exactly follow the description of Schrödinger who considered the entanglement of the macroscopic object to a quantum system. For that reason, we prefer to use the name *coherent-state superposition* (CSS).

Two specific cases correspond to the terms of the superposition either in phase or out of phase. In the first case, the state is a superposition of even photon numbers only, and is called an *even cat*. In the second case the superposition is composed of odd Fock states only, and the state is called *odd cat*:

$$\begin{aligned} |cat+\rangle &= \frac{1}{N_+}(|\alpha\rangle + |-\alpha\rangle) = \frac{2}{N_+}e^{-|\alpha|/2}\sum_{n=0}^{+\infty}\frac{\alpha^{2n}}{\sqrt{2n!}}|2n\rangle\,, \\ |cat-\rangle &= \frac{1}{N_-}(|\alpha\rangle - |-\alpha\rangle) = \frac{2}{N_-}e^{-|\alpha|/2}\sum_{n=0}^{+\infty}\frac{\alpha^{2n+1}}{\sqrt{(2n+1)!}}|2n+1\rangle\,. \end{aligned} \tag{1.15}$$

When the overlap between the two orthogonal coherent states $|\langle-\alpha|\alpha\rangle|^2 = e^{-4|\alpha|^2}$ is negligible (in practice, for $|\alpha| = 1$ and $|\alpha| = 1.5$ it amounts to 1.8% and 0.01% respectively), we can define, from these two cat states, a coherent-state superposition basis $\{|cat+\rangle\,, |cat-\rangle\}$ where any continuous-variable qubit can be written as:

$$|\psi\rangle = c_0\,|cat+\rangle + c_1 e^{i\theta}\,|cat-\rangle\,. \tag{1.16}$$

It is important to note that this basis does not constitute an exact continuous-variable approach, as the basis is still composed of a finite number of elements and the state still presents a qubit structure. Yet such a type of states are proven to enable an exponential speed up of computations in the framework of coherent state quantum computing (CSQC) [63, 64]. Thus this "CV-like" basis offers in itself many applications that differ from the discrete-variable approach, as exemplified by CV quantum computing [65], and CV quantum sensing based on cat states [66].

After having introduced the quantum states and the two paradigms for encoding quantum information, we now turn to the presentation of the mathematical tools that we will employ in this thesis to represent and characterize these states.

2.4 State representation

If the state vector representation can be efficiently employed for the description of *pure* quantum states, this description does not take into account the lack of knowledge that an observer, such as an experimentalist, has on the quantum system. Instead, the system shall be described as a *statistical mixture* of quantum states, which cannot be depicted accurately with a wavefunction and thus a state vector. Here we will describe two state representations which can completely describe a mixed quantum system: the *density matrix* and the *Wigner function*. Even though these representations are typically respectively employed for the DV and CV formalisms, there is conceptually no limitation for employing a specific representation for a given state, so that in this thesis the two representations will be used equivalently.

2.4.1 The density matrix

Though the state of a quantum system is always perfectly defined by a state vector, the lack of knowledge of the observer is modeled by writing the system as a statistical mixture of states [67]. Namely, in practice, an observer measures a number of pure quantum states $|\psi_k\rangle$ each with a probability p_k. The density matrix of the statistical mixture is then defined as the sum of the density matrices of the pure states $|\psi_k\rangle\langle\psi_k|$ weighted by their probability p_k:

$$\hat{\rho} = \sum_k p_k |\psi_k\rangle\langle\psi_k| . \tag{1.17}$$

Typically in this work, we will represent the density matrix in the Fock basis $\{|n\rangle\}_n$:

$$\hat{\rho} = \sum_{n,m} c_{n,m} |n\rangle\langle m| . \tag{1.18}$$

By definition, the diagonal terms $|n\rangle\langle n|$ are called the *populations* while the anti-diagonal terms $|n\rangle\langle m|$ are called the *coherences*, characteristic of the quantum interference between the different quantum states.

The mathematical properties of the density matrix are presented in **Appendix A**.

2.4.2 The Wigner function

As we have seen earlier, a quantum state can be described by its projections on quadrature observables, from which the phase-space wave-functions can be returned. The corresponding marginal distributions can be recovered and represent the probability distributions of measuring a given quadrature result. The Wigner function $W(x,p)$ [68] is a phase-space representation that can be seen as a root function from which all the marginal distributions can be extracted:

$$P(q_\theta) = \int W(q_\theta, p_\theta) dp_\theta, \tag{1.19}$$

with p_θ the conjugate quadrature defined as $\hat{p}_\theta = -\hat{x}\sin\theta + \hat{p}\cos\theta$.

The Wigner function represents a visual description of the quantum state where imperfections such as losses or phase noise can directly be seen in phase space. Contrary to a classical phase-space representation, it can exhibit negativities, which are strong signatures of the non-classicality of the state and define a class of *non-Gaussian* quantum states [69]. This feature is purely quantum, so that the Wigner function is typically seen as a *quasi-distribution*.

It is important to note that the density matrix and the Wigner function descriptions are fully equivalent and correspond each to a complete characterization of the quantum state, i.e. for a given mixed state, there exists a unique density matrix and Wigner function associated, and conversely. The Wigner function can thus be calculated from a density matrix $\hat{\rho}$ by:

$$W_{\hat{\rho}}(x,p) = \frac{1}{2\pi\sigma_0^2} \int e^{ipy/\sigma_0^2} \langle x-y|\,\hat{\rho}\,|x+y\rangle\, dy. \tag{1.20}$$

Details on properties of the Wigner function and its calculations are given in the **Appendix B**.

2.4.3 An example: the loss of a photon

To illustrate the importance of the density and Wigner representations, let us have a look at a basic situation in a quantum optics experiment. Let us imagine that an experimentalist generates a pure single photon described by a density matrix $|1\rangle\langle 1|$. Then, for practical reasons, this photon is lost in the environment with a probability of 50%. This loss of photon is not inherent to the quantum state itself, which can still be described by a state vector $|1\rangle$. But from his imperfect experiment, what is the state that the experimentalist will measure ?

Following the density matrix representation, the state generated will be expressed in the Fock basis as:

$$0.5\,|0\rangle\langle 0| + 0.5\,|1\rangle\langle 1| = \frac{1}{2}\begin{pmatrix} 1 & 0 \\ 0 & 1 \end{pmatrix} \tag{1.21}$$

that is an even statistical mixture of vacuum and single-photon. We note that the coherence terms are null. The corresponding density matrix and Wigner function are shown in Figure 1.3 (a).

Now let us calculate the density matrix obtained starting from a pure quantum state written in the state vector representation as $|\psi\rangle = \frac{1}{\sqrt{2}}(|0\rangle + e^{i\theta}|1\rangle)$:

$$|\psi\rangle\langle\psi| = 0.5\,|0\rangle\langle 0| + 0.5\,|1\rangle\langle 1| + 0.5e^{-i\theta}\,|0\rangle\langle 1| + 0.5e^{i\theta}\,|1\rangle\langle 0| = \frac{1}{2}\begin{pmatrix} 1 & e^{-i\theta} \\ e^{i\theta} & 1 \end{pmatrix}. \tag{1.22}$$

We see here the emergence of coherence terms. The density matrix, and so the quantum state, is thus fundamentally different to the state presented earlier. The density matrix and Wigner function are given in Figure 1.3 (b). The coherences are here characteristic of the quantum interference, and thus reveal the phase between the states $|0\rangle$ and $|1\rangle$, which is seen directly in the rotational symmetry breaking in the Wigner representation.

From this comparison two conclusions arise. First there exist quantum states, which are mere statistical mixtures, that cannot be described using the state-vector representation. So that the relevant description of the experiments, in particular the inclusion of losses, must be performed using the density matrix or the Wigner function formalism. Second, generating a pure qubit, such as $\frac{1}{\sqrt{2}}(|0\rangle + |1\rangle)$, experimentally requires subtle protocols to create the coherences and encode information in its phase.

In this section we have presented the quantum states built from the superposition principle, which defines two possible encodings of quantum information called discrete- and continuous-variable. These quantum states can be described using the density matrix and the Wigner functions formalisms, which are two equivalent state representations. In the following we will introduce the fundamental concepts based on another fundamental quantum feature: entanglement.

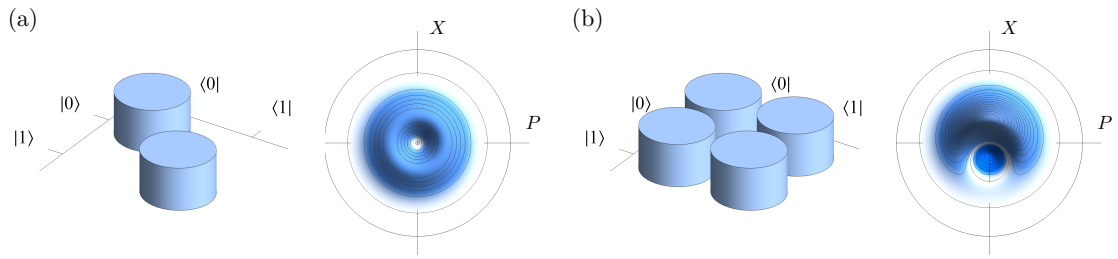

Figure 1.3: **State representations of a mixed state**. (a) Density matrix and Wigner function of a fully mixed state $|0\rangle\langle 0| + |1\rangle\langle 1|$. (b) In comparison we present the density matrix and Wigner functions of a pure evenly weighted qubit $|\psi\rangle = |0\rangle + |1\rangle$. We observe the apparition of coherences in the density matrix characteristic of the quantum interference and a rotational symmetry breaking in phase space given by the qubit phase.

3 Entanglement

Entanglement is a purely quantum phenomenon occurring when, in a group of particles, the quantum state of each particle of the group cannot be described independently of the state of the others, no matter how distant the particles can be. In such an entangled system, there exist correlations between physical observables of the distinct particles, resulting in non-local actions, and the need to interpret the global system as an entity in itself. Such a fascinating property, which is one of the main features of quantum mechanics, is at the heart of our work. After recalling the historical considerations on entanglement and non-locality, we will present how entanglement is experimentally characterized and how it can be used as a resource in itself for quantum communication.

3.1 Historical approach: the non-locality of quantum mechanics

The surprising behaviour of entangled states has for the first time been underlined by Albert Einstein, Boris Poldolsky and Nathan Rosen (EPR) in a thought experiment in 1935 [70] with the intent to refute the Copenhagen interpretation of quantum physics and prove that "*the description of reality as given by a wavefunction is not complete*". The EPR paradox was based on the idea that, when two entangled particles are sufficiently separated, for the measurement of the first particle to be in accordance with the result of the measurement of the second, either there would be an instantaneous influence between the particle, a "*spooky action at a distance*", that would rule out *local realism*, or there would exist *local hidden variables* that would determine the result of the measurement prior the first measurement, i.e. when the entangled state is created, and thus prove that the quantum theory is incomplete.

It is only only three decades later, in 1964, that John Stewart Bell discovered theoretically that the principle of local reality was inconsistent with the predictions of quantum

theory. He developed, to that end, an upper limit on the correlations obtainable by system following local realism, called *Bell's inequality*, and showed that certain entangled states, which could be experimentally generated, could present a violation of local realism [71]. From that point, the first violations of Bell's inequalities have been observed experimentally by Freedman and colleagues [72], with the first demonstration ruling out the locality loophole by Aspect and collaborators [73] and more recently several loophole-free experiments [74, 75, 76]. All the experimental results are in agreement with the non-local description of quantum mechanics.

3.2 Two-party entanglement

Entanglement is mathematically defined in opposition to a certain class of quantum states called *separable* states, i.e., the state of a global system $\{A, B\}$ is written as the tensor product of its constituents A and B:

$$\hat{\rho}_{AB} = \sum_k p_k \hat{\rho}_{A_k} \otimes \hat{\rho}_{B_k}. \tag{1.23}$$

So, by definition, a *non-separable* or *entangled* state cannot be written as a product state, hinting at the fact that the two modes cannot be considered independently.

For example, given two two-dimensional Hilbert spaces A and B, a quantum state written as follows

$$\frac{1}{\sqrt{2}}(|0\rangle_A |1\rangle_B + |1\rangle_A |0\rangle_B), \tag{1.24}$$

is an entangled state. Interestingly, neither of the two particles carry a definite value. But what is known is that as soon as one of the two modes is measured - the result of which being completely random - the other one will immediatly be found in the corresponding state. Quantum mechanically, this is a two-mode quantum superposition state which can be observed experimentally if and only if there is not way to distinguish the two outcomes $|0\rangle_A |1\rangle_B$ or $|1\rangle_A |0\rangle_B$. Thus indistinguishability is a crucial condition for the production and observation of entangled states.

Any two mode entangled state can be written as a superposition of the four states forming a basis of two-mode entangled state, called *Bell states* defined as:

$$\begin{aligned}
\left|\Psi^+\right\rangle_{AB} &= \frac{1}{\sqrt{2}}(\,|0\rangle_A |1\rangle_B + |1\rangle_A |0\rangle_B\,),\\
|\Psi^-\rangle_{AB} &= \frac{1}{\sqrt{2}}(\,|0\rangle_A |1\rangle_B - |1\rangle_A |0\rangle_B\,),\\
\left|\Phi^+\right\rangle_{AB} &= \frac{1}{\sqrt{2}}(\,|0\rangle_A |0\rangle_B + |1\rangle_A |1\rangle_B\,),\\
|\Phi^-\rangle_{AB} &= \frac{1}{\sqrt{2}}(\,|0\rangle_A |0\rangle_B - |1\rangle_A |1\rangle_B\,).
\end{aligned} \tag{1.25}$$

The notion of entanglement can be extended to more parties, in more exotic structures such as *graph states* or *cluster states* [77, 78, 79, 80], but these considerations go out of the scope of this thesis that focuses on two-party entanglement.

3.3 Entanglement characterization: the negativity of entanglement

Several mathematical tools can be employed to characterize entangled states [81]. A first strategy can consist in defining a functional, called an *entanglement witness* that distinguishes a specific entangled state from separable ones. Another technique consist in defining an *entanglement measure*, which is a entanglement monotone capable of quantifying the amount of entanglement in the system. Since entanglement is a property which depends on the nature of the states and the basis in which it is described, many tools and quantifiers can be used to describe the entanglement [82].

In our work we will employ the *negativity of entanglement* [83], which is an entanglement monotome specifically well suited for our study, i.e. applicable to mixed states for both the discrete- and the continuous-variable approaches. The only disadvantages of this quantifier is that it requires the full knowledge of the multi-partite density matrix, which can sometimes be rather challenging to recover experimentally. This figure of merit is used to characterize the quality of the protocols where the generation of entanglement is the goal. It is defined as:

$$\mathcal{N}(\hat{\rho}_{AB}) = \left(||\hat{\rho}_{AB}^{T_A}||_1 - 1\right)/2, \tag{1.26}$$

where $\hat{\rho}_{AB}^{T_A}$ stands for the partial transpose of the two-mode density matrix $\hat{\rho}_{AB}$ and $||X||_1$ is the trace norm defined as:

$$||X||_1 = \mathrm{Tr}(\sqrt{X^\dagger X}). \tag{1.27}$$

A more useful expression is given by considering the eigenvalues λ_i of the partial transpose $\hat{\rho}_{AB}^{T_A}$:

$$\mathcal{N}(\hat{\rho}_{AB}) = \frac{1}{2}\sum_i |\lambda_i| - \lambda_i. \tag{1.28}$$

In the ideal case, the negativity of entanglement is upper-bounded to 0.5.
In experiments where the amount of entanglement is small, we might also employ the *logarithmic negativity of entanglement* defined as:

$$E_{\mathcal{N}}(\hat{\rho}_{AB}) = \log_2(||\hat{\rho}_{AB}^{T_A}||_1) = \log_2(2\mathcal{N}(\hat{\rho}_{AB}) + 1). \tag{1.29}$$

3.4 Entanglement as a resource for quantum technologies

In addition to its fundamental significance, entanglement has, in itself, become a fundamental resource for the development of quantum technologies. In quantum sensing, entanglement is a necessary condition for surpassing the Standard Quantum Limit [84] and thus beating the precision of classically-limited devices. Entanglement is a key resource for the establishment of *one-way* or *measurement-based quantum computing* with cluster states [85, 86, 87]. In quantum communications, entanglement is central to the implementation of cryptographic tasks such as *entanglement-based quantum key distribution* [28]. Very interestingly, untrusted sources or detection apparatus can be tested by implementing some Bell tests [88, 89, 90], thus providing unconditionally secure - although experimentally very challenging - device-independent protocols. Finally entanglement is

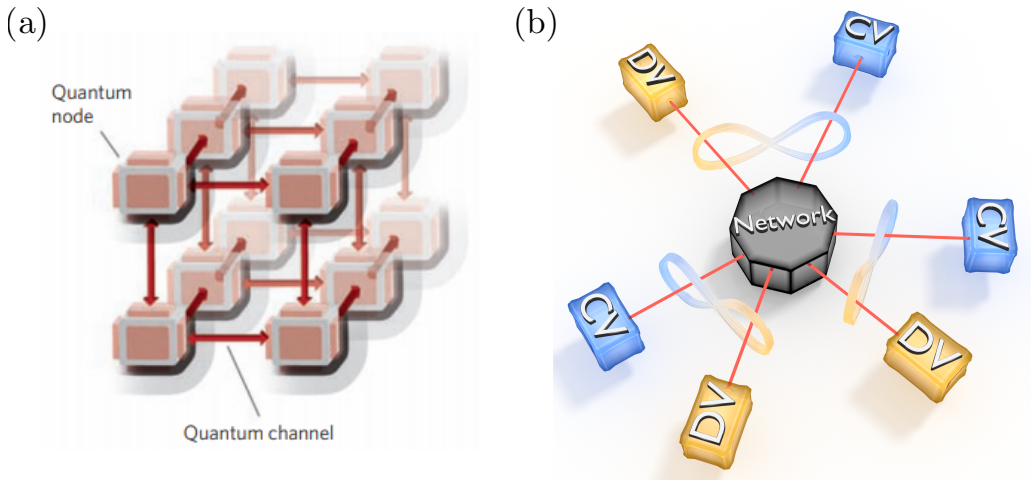

Figure 1.4: **Heterogeneous quantum networks**. (a) A quantum network as pictured by Kimble in [91], composed of quantum nodes where quantum states are stored and processed, and quantum links for the distribution of information. (b) A quantum network is composed of a heterogeneous structure with discrete-variable (DV) and continuous-variable (CV) quantum nodes.

fundamental for the establishment of long-distance communication in quantum networks, as introduced in the following sections.

4 Heterogeneous quantum networks

Envisaged in 2008 by Kimble [91], a quantum network, or quantum internet [92], is an architecture which enables the connection of remote quantum processors to provide new opportunities in quantum communication [93], quantum computation [94] and metrology [95, 96]. The development of such networks requires the implementation of quantum repeaters allowing the end to end generation of entanglement and transmission of qubits with quantum teleportation protocols. In this section we will present the basic components of quantum networks and describe its central element, namely, the teleportation-based quantum repeaters.

4.1 The architecture

As sketched in Figure 1.4 (a), quantum networks are composed of two key elements: the *quantum nodes* - where quantum information is processed and stored - and the *quantum channels* - which connect remote quantum nodes via quantum correlations in the form of entanglement. We will present these two ingredients in detail and show how prospective networks relying on different physical platforms and encodings will necessarily comprise a heterogeneous structure.

4.1.1 The quantum nodes

The quantum nodes, or end nodes, of a quantum network are composed of quantum processors which can perform specific quantum enhanced tasks, ranging from the preparation and measurement of single qubits to large-scale quantum computing. Matter-based qubits are particularly well-suited for that task as they allow, first, a robust storage of information during the time needed for the establishment of entanglement between the nodes, and second, the high-fidelity processing of quantum information. In these platforms, the main scientific challenge is the ability to coherently control the light-matter interaction at the single-photon level to convert quantum states from one matter system to light, and conversely. Different physical matter platforms can be addressed to perform photon-mediated entanglement generation - ideally at telecom wavelength. Among them are atomic systems [97, 98], trapped ions [99], vacancy centers [35] or semiconductor quantum dots [100]. In particular, our team at LKB is pushing experimental efforts towards quantum optical interconnects allowing the reversible mapping of quantum states between light and matter, either using elongated atomic clouds in free space [101], or at the vicinity of nano-waveguides, such as nanofibers [102] or slow-mode photonic crystals [103].

4.1.2 The quantum channels

The quantum channel enables the physical connection between remote nodes for the transmission of information. Light being an ideal carrier of information, photonic channels establish quantum links between distant repeater stations or end nodes. These channels can be performed either in free space (with satellites [28]), or using fiber-based links [104]. Yet, the quantum channels are inherently inducing noise, which modifies the properties of the quantum state along its propagation. In this thesis we will focus mostly on two sources of noise described in [19], which are the *amplitude damping*, an effect due to the loss of energy from a quantum system, and which we will represent by *transmission losses*, and *phase damping*, describing the loss of quantum information without loss of energy, and that we will call *phase noise*.

The **transmission losses** can be modeled employing the *beamsplitter operator* [105]. The beamsplitter operator represents the coupling of two optical modes A and B following:

$$\hat{B}(\theta) = e^{\theta(\hat{a}^\dagger \hat{b} - \hat{a}\hat{b}^\dagger)}, \tag{1.30}$$

with the reflection and transmission coefficients defined as:

$$r = \sin\theta, \qquad t = \cos\theta. \tag{1.31}$$

The application of the beamsplitter operation can directly be performed by considering the evolution of the creation operators of each mode:

$$\begin{aligned} \hat{a}^\dagger &\rightarrow t\hat{a}^\dagger + r\hat{b}^\dagger, \\ \hat{b}^\dagger &\rightarrow t\hat{b}^\dagger - r\hat{a}^\dagger. \end{aligned} \tag{1.32}$$

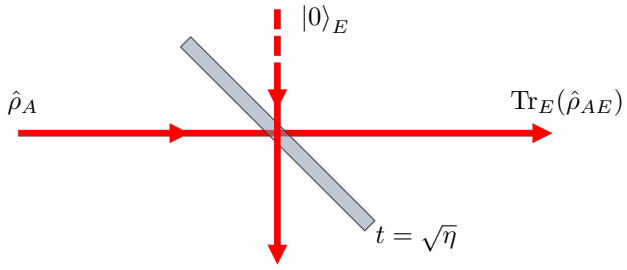

Figure 1.5: **Model for transmissions losses**. The quantum state $\hat{\rho}_A$ is coupled to vacuum in an environmental mode, $|0\rangle_E$, with a beamsplitter of transmission $t = \sqrt{\eta}$.

The transmission losses can then be modeled by considering the coupling of a mode A where a quantum state propagates $\hat{\rho}_A$ with an environmental mode E. A beamsplitter of transmission $t = \sqrt{\eta}$, where η is the efficiency of the channel, couples the state to vacuum in mode E:

$$\hat{\rho}_A \otimes |0\rangle\langle 0|_E \xrightarrow{\hat{B}(\eta)} \hat{B}(\eta)(\hat{\rho}_A \otimes |0\rangle\langle 0|_E)\hat{B}^\dagger(\eta) \tag{1.33}$$

and the lossy state is obtained by tracing out the reflected environmental mode:

$$\hat{\rho}_A \to \mathrm{Tr}_E(\hat{\rho}_{AE}). \tag{1.34}$$

In the specific example of a single photon $|1\rangle_A$ propagating in the channel, we have:

$$|1\rangle_A |0\rangle_E \to \sqrt{\eta}\,|1\rangle_A |0\rangle_E + \sqrt{1-\eta}\,|0\rangle_A |1\rangle_E\,, \tag{1.35}$$

which gives by tracing out mode E:

$$|1\rangle\langle 1|_A \to \eta\,|1\rangle\langle 1|_A + (1-\eta)\,|0\rangle\langle 0|_A\,. \tag{1.36}$$

As we have seen earlier, we obtain, from the application of losses, a statistical mixture of states, without any coherence.

The **phase noise** is modeled by considering the state as a mixture of states with phases distributed as a Gaussian centered around a phase θ with a standard deviation of δ_θ. This mirrors the observed deviation of phases during the data acquisition:

$$\hat{\rho}_\theta \to \frac{1}{\sqrt{2\pi\delta_\theta}} \int_{-\infty}^{+\infty} \hat{\rho}_{\theta'} e^{-\frac{(\theta-\theta')^2}{2\delta_\theta^2}}\, d\theta'. \tag{1.37}$$

The phase noise affects only the coherences of the quantum state involved, and leaves unchanged the populations of the density matrix.

Noise in quantum channels alter the quality of the protocols and limits the range at which they can be extended, so that a great attention has to be put to reduce them as much as possible. In some cases, the decrease of fidelity can be compensated by the use of

photon heralding. Yet, the inherent losses inevitably reduce the communication rates over the network. The reduction of losses and the increase of rates can be performed by considering more resilient and suited-to-the-task information encodings [106] and employing a multiplexing of the channels [107].

4.1.3 A heterogeneous structure

Given the parallel development of different physical platforms based on the two quantum encodings, it is fair to assume that future quantum networks will be composed of interconnects between discrete- and continuous-variable nodes in an heterogeneous structure allowing full functionality (cf Figure 1.4 (b)). All the more since each quantum encoding is well suited only for specific tasks. For instance the discrete-variable encoding is well suited for the high-fidelity generation and processing of quantum states [1], but the protocols that are implemented are mostly probabilistic [108], which makes them hard to extend to large scales. On the other hand, continuous-variable systems enable the implementation of deterministic protocols [2, 109]. However, continuous-variable states are known to be much more challenging to transmit in quantum channels as they are more sensitive to channel noise [110, 9]. Overall, a judicious use of the physical platforms, of the encodings and protocols, should be performed to the task at hand, with the integration of hybrid interconnects, that would allow the parallel involvement of all the actors of the heterogeneous quantum networks in the most efficient manner [111].

We have thus presented the quantum network architecture comprising a heterogenous struture composed of discrete- and continuous-variable nodes. In the following we will address the quantum repeaters, which are another central element of quantum networks and would enable long-distance quantum communication.

4.2 Quantum repeaters

Contrary to classical networks, quantum networks are fundamentally limited by the no-cloning theorem that forbids the copy of any quantum state, and so its amplification for long-distance quantum communication. A quantum approach has thus to be developed to overcome the transmission losses encountered during propagation in the channels. To that end, quantum repeaters [112, 113, 114] can be implemented by performing - at an intermediate station between two end nodes - quantum teleportation between two entangled states. These repeaters can be assisted by quantum memories for synchronization and active protocols, such as entanglement purification, for error protection.

4.2.1 The no-cloning theorem

In their paper of 1982 [115], William Kent Wooters and Wojciech Hubert Zurek observed that the linearity of quantum mechanics forbids the copy of any unknown quantum state. This observation, today called *no-cloning theorem* is a purely quantum mechanical behaviour that has many consequences in quantum computing, where the application of

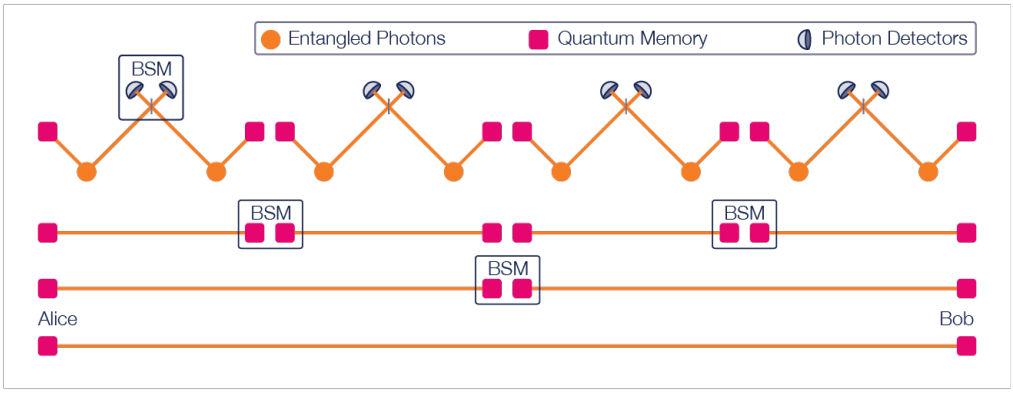

Figure 1.6: **Quantum repeater for long-distance quantum communication**. From [116]. Two parties, Alice and Bob, are too remote for the direct establishment of entanglement. The long distance is divided into several shorter links in which entanglement can be distributed. The connection of the links is performed by entanglement swapping heralded by a Bell-state measurement at the intermediate stations. For scalability, quantum memories are employed to synchronize the incoming photons prior the Bell-state measurement. The operation is employed in cascade to longer links to finally entangle the two end nodes.

repetition error-correcting codes cannot be performed, and in quantum communication with the unavailability to create network amplifiers. Although only based on the linearity of quantum mechanics, the no-cloning theorem is of fundamental importance as it prevents superluminal communication and is a necessary condition for the Heisenberg uncertainty relation [16].

4.2.2 Quantum teleportation and entanglement swapping

Fortunately, the connection of nodes that would be too distant for direct entanglement propagation can be performed by using *quantum teleportation* protocols in a quantum repeater architecture as presented in Figure 1.6. Consider first two end nodes that would be too distant to enable the transmission of a qubit. The quantum repeater would act as an intermediate station, considering that the distance between each end node and the repeater is small enough to allow direct entanglement propagation. In the procedure, entanglement is first generated between the repeater and each end node. Then teleportation is performed at the level of the repeater to entangle the two end nodes together. This procedure is called *entanglement swapping* and is essential for the creation of entanglement over large distance. Entanglement can then be propagated over larger distance by consecutive entanglement swapping between several quantum segments located accordingly between the two end nodes. Finally, once entanglement between the parties is created, quantum teleportation can be employed to transfer any qubit between the two connected nodes.

After introducing several other considerations about quantum repeaters, we will present in details, in the two next sections, the protocols of quantum teleportation and entangle-

ment swapping, which are key features of quantum networks and that have been experimentally implemented in a hybrid framework during this thesis. For now, let us continue our description of the quantum repeaters.

4.2.3 Quantum memories

When looking at the quantum-repeater architecture, one of the key challenges is two ensure that the two intermediate entangled states are generated simultaneously for the swapping to occur. If this simultaneity can be performed efficiently when entanglement is deterministically generated, synchronization tools are required when entanglement is probabilistically create in heralded fashion. To that end, local *quantum memories* [117] must be employed at the intermediate repeater node to store the first arrived entangled mode and wait for the second entangled state to be created.

Not only quantum memories are fundamental synchronization tools required for the implementation of world first's quantum repeaters, but they are also at the center of many classes of protocols for quantum memory networks, such as secure assisted quantum computation [118], quantum secret sharing [119] and metrology devices synchronization [95].

4.2.4 Entanglement purification

If entanglement swapping enables the connection of quantum nodes that would be too distant for direct propagation, entanglement will inherently be altered by the noise of the channels and the imperfections of the different operations. Thus, active protocols, such as *entanglement purification* (also called *entanglement distillation*) [120] has to be performed at the level of the end nodes to improve the quality of the entanglement connecting the two systems. In the original proposal from Bennett and colleagues [121], highly entangled states can be obtained out of a larger number of less entangled states (provided that the quality of the initial pairs is sufficiently high), by performing local operations and classical communication. Finally, by repeating the same procedure, always starting from the state produced in the former purification step, it is possible to distil states of arbitrarily high entanglement quality. The higher the quality desired, the more original of the less entangled pairs are needed. Entanglement purification has been demonstrated for the first time in 2001 [120] and has since been applied to various systems [122, 123], and has proven to be an essential protocol for the development of fully operational quantum networks.

Elementary instances of quantum repeaters [124, 125, 126] and quantum networks [127] have recently been experimentally reported. However, they do not yet incorporate all their key ingredients in a single architecture, and a lot of experimental effort still has to be put to develop fully fledged quantum internet with long-distance quantum communication.

Having introduced the quantum networks and repeaters architectures, we now turn to the presentation of the protocols at their heart: quantum teleportation and entanglement swapping.

5 The teleportation of an unknown quantum state in a heterogeneous quantum network

Quantum teleportation is, by definition, the transfer through a classical channel of an unknown quantum state between two nodes sharing entanglement. After the generation and distribution of entanglement between the two parties, an external system in an arbitrary unknown quantum state - the one to be teleported - is measured jointly with one mode of the entangled state. The result of this joint measurement, called *Bell-state measurement*, is transferred throught a classical channel to the other half of the entangled state who can, by applying a unitary transformation conditioned upon the measurement outcome, recover the initial quantum state.

Quantum teleportation is one of the most important protocols of quantum information processing, and is a crucial requirement for the development of many quantum technologies. As we have seen earlier, quantum teleportation of states is an essential tool for quantum communication as it enables the creation of quantum repeaters [112] fundamental for long distance quantum communication, and the implementation of scalable quantum networks [92]. In the field of quantum computation, quantum teleportation enables the reliable implementation of universal quantum computing [128] and measurement-based quantum computing with cluster states [87, 85, 129].

In the following we will detail the properties of quantum teleportation, from the basic principles of entanglement generation, Bell-state measurement and state recovery, to its applications in heterogeneous quantum networks.

5.1 Principle

The scheme for quantum teleportation was originally proposed by Bennett and collaborators in 1993 [131] and is sketched in Figure 1.7. It is valid both for discrete- and continuous-variable quantum states, so that in the following we will label the logical states $|\mathbf{0}\rangle$ and $|\mathbf{1}\rangle$, where $\{|\mathbf{0}\rangle, |\mathbf{1}\rangle\}$ is the encoding basis which can stand for DV encoded states (for example the Fock basis $\{|0\rangle, |1\rangle\}$) or for CV encoded qubits (for example the CSS basis $\{|cat+\rangle, |cat-\rangle\}$). The two parties, generally called *Alice* and *Bob*, share an entangled state $|\Psi\rangle_{AB}$. This state can be written:

$$|\Psi\rangle_{AB} = \frac{1}{\sqrt{2}}\Big(|\mathbf{0}\rangle_A |\mathbf{1}\rangle_B + |\mathbf{1}\rangle_A |\mathbf{0}\rangle_B \Big). \tag{1.38}$$

An unknown quantum state $|\psi_{in}\rangle_C$ is sent to Alice who wishes to tranfer it to Bob. The unknown state is a qubit of the form

$$|\psi_{in}\rangle_C = c_0 |\mathbf{0}\rangle_C + e^{i\theta} c_1 |\mathbf{1}\rangle_C . \tag{1.39}$$

If Alice does not use entanglement, any measurement performed by her will destroy the quantum state at hand without revealing to Bob all the information necessary for him to reconstruct the state. However when using entanglement an important property is that as soon as a measurement is performed on one of the modes, it projects the other one on a

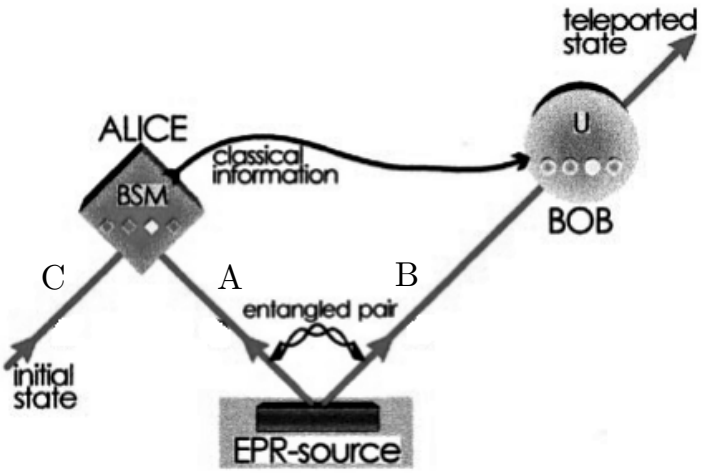

Figure 1.7: **Principle of quantum teleportation**. From [130] . Alice and Bob share an EPR entangled state labeled A-B. An unknown quantum state in mode C is given to Alice who performs a joint Bell-state measurement (BSM). The result of the Bell-state measurement is transmitted to Bob via a classical channel who recover a replica of the original state by applying the unitary operation (U) corresponding to the result of the Bell-state measurement.

correlated state. Instead Alice performs a joint Bell-state measurement between her mode and the unknown state, even though her mode is not entangled with the unknown state which is given to her.
Indeed the three-mode entangled state,

$$|\Psi\rangle_{ABC} = \frac{1}{\sqrt{2}}(c_0 |\mathbf{0}\rangle_C + e^{i\theta} c_1 |\mathbf{1}\rangle_C) \otimes (|\mathbf{0}\rangle_A |\mathbf{1}\rangle_B + |\mathbf{1}\rangle_A |\mathbf{0}\rangle_B), \tag{1.40}$$

can always be expressed as a superposition of the four maximally entangled Bell states which form an orthogonal basis:

$$\begin{aligned} |\Psi\rangle_{ABC} = \frac{1}{2}\Big[& \left|\Psi^+\right\rangle_{CA} \otimes (c_0 |\mathbf{0}\rangle_B + c_1 e^{i\theta} |\mathbf{1}\rangle_B) \\ & + \left|\Psi^-\right\rangle_{CA} \otimes (c_0 |\mathbf{0}\rangle_B - c_1 e^{i\theta} |\mathbf{1}\rangle_B) \\ & + \left|\Phi^+\right\rangle_{CA} \otimes (c_1 e^{i\theta} |\mathbf{0}\rangle_B + c_0 |\mathbf{1}\rangle_B) \\ & + \left|\Phi^-\right\rangle_{CA} \otimes (-c_1 e^{i\theta} |\mathbf{0}\rangle_B + c_0 |\mathbf{1}\rangle_B)\Big]. \end{aligned} \tag{1.41}$$

Alice now performs a Bell-state measurement between modes A and C, namely, she projects her two-mode state onto one of the four Bell states. As a result, Bob's mode will be found in a state directly related to the initial state. For instance, if the result of Alice's Bell-state measurement is $\left|\Psi^+\right\rangle_{AC}$, then Bob's state is in the input qubit state $|\psi_{in}\rangle_B$. More

precisely, any Bell-state measurement result on Alice mode project Bob's state onto a given unitary evolution of the unknown input qubit:

$$\begin{aligned}|\Psi\rangle_{ABC} = \frac{1}{2}\Big[&\left|\Psi^+\right\rangle_{CA} \otimes |\psi_{in}\rangle_B + \left|\Psi^-\right\rangle_{CA} \otimes \hat{\sigma}_Z |\psi_{in}\rangle_B \\ &+ \left|\Phi^+\right\rangle_{CA} \otimes \hat{\sigma}_X |\psi_{in}\rangle_B + \left|\Phi^-\right\rangle_{CA} \otimes e^{-i\pi/2}\hat{\sigma}_Y |\psi_{in}\rangle_B \Big],\end{aligned} \tag{1.42}$$

with $\hat{\sigma}_X$, $\hat{\sigma}_Y$, and $\hat{\sigma}_Z$ the *Pauli operators* defined as:

$$\hat{\sigma}_X = \begin{pmatrix} 0 & 1 \\ 1 & 0 \end{pmatrix}, \qquad \hat{\sigma}_Y = \begin{pmatrix} 0 & -i \\ i & 0 \end{pmatrix}, \qquad \hat{\sigma}_Z = \begin{pmatrix} 1 & 0 \\ 0 & -1 \end{pmatrix}. \tag{1.43}$$

Thus, Alice has to inform Bob on her measurement result via a classical channel, so that he can perform the appropriate unitary evolution $\hat{U}$ on his mode to recover the initial unknown state $|\psi_{in}\rangle_B$.

5.2 Comments and definitions

Following the description of the quantum teleportation protocol, three conclusions arise:

- The unknown input state remains unknown during the entire teleportation procedure to Alice, Bob, or any other party. The unknown state could thus be completely undefined or part of an entangled state where it has no well-defined properties of his own. In addition if Alice gained any information through her measurement, Bob would not recover a perfect replica of the initial state.

- The input state does not remain in its initial state after the Bell-state measurement is performed. The input state is destroyed at Alice's side during the teleportation. This ensures that the no-cloning theorem is not violated.

- Superluminal communication is prevented by the need to transfer classically the results of the Bell-state measurement. Quantum teleportation is therefore restricted by the speed of light. Only the quantum information contained in the particle, and not the particle itself is teleported.

Finally, several definitions have to be addressed depending on the implementation of the protocol:

- If Alice is able to distinguish the four Bell-states, the Bell-state measurement is *complete* and the teleportation protocol is *deterministic*. If some of the Bell-states cannot be distinguished, some of the events have to be discarded and the protocol is *probabilistic*.

- If the unitary evolution $\hat{U}$, corresponding to feed-forward, is performed by Bob in real-time we say that the protocol is *active*, whereas if the operation is applied a posteriori or not at all the protocol is *passive*. In that case, the Bell-state measurement consists in a filtering, or conditioning, of the successful events.

It is important to note that, in practice, the implementations of the Bell-state measurement and of the feed-forward depend on the nature of the quantum state involved and the choice of quantum encoding. In particular in this thesis we have developed a new hybrid Bell-state measurement technique, presented in **Chapter 4**, that is best suited for the resources at hand. In our experimental implementations of the hybrid quantum teleportation-based protocols, we will focus on probabilistic and passive protocols.

5.3 Quantum teleportation in heterogeneous quantum networks

As we have seen earlier, quantum networks are very prone to be composed of both DV and CV nodes. If quantum teleportation has been established historically for the two paradigms [130, 132], quantum states based on different physical systems should be able to be transferred from one encoding to the other, and conversely, as to allow full functionality. Thus, hybrid quantum teleportation between discrete- and continuous-variable nodes would not only enable the transfer of a quantum state between two remote quantum processors but also its conversion from one encoding to the other. Such an operation would represent a quantum equivalent of the digital-to-analog and analog-to-digital converter that are commonly employed in classical information processing to enable full transport, storage and processing of information in the most efficient manner.

For quantum teleportation to occur between two different encodings, it must rely on an entangled state that is itself correlating quantum states that belong to different paradigms. In that prospect *hybrid entanglement*, the creation of which will be presented in **Chapter 3**, has been recently developed in several groups [4, 5], including initially in our team at LKB, to link discrete- and continuous-variable qubits. For instance, a hybrid entangled state between a DV Fock basis $\{|0\rangle, |1\rangle\}$ and a CV coherent state superposition basis $\{|cat+\rangle, |cat-\rangle\}$, of the form:

$$|\Psi\rangle_{AB} = \frac{1}{\sqrt{2}}(|0\rangle_A |cat-\rangle_B + |1\rangle_A |cat+\rangle_B) \tag{1.44}$$

is an essential resource. It can be employed for two operations:

- The conversion of quantum information from a DV qubit in the Fock basis $\{|0\rangle, |1\rangle\}$ to a CV qubit encoded in the CSS basis $\{|cat+\rangle, |cat-\rangle\}$:

$$\mathrm{DV} \otimes \mathrm{DV}\infty\mathrm{CV} \rightarrow \mathrm{CV}, \tag{1.45}$$

  which will be experimentally demonstrated for the first time in this thesis in **Chapter 7**.

- The conversion from a CV qubit in the CSS basis to a DV qubit in the Fock basis.

$$\mathrm{CV} \otimes \mathrm{CV} \infty \mathrm{DV} \rightarrow \mathrm{DV}, \tag{1.46}$$

  which has been partially demonstrated in related works [133].

5.4 Threshold for successful quantum teleportation, figures of merit

In a quantum teleportation protocol, it is important to ensure that no better replica of the input state could be obtained by Bob by any other protocol, including the use of classical correlations. Traditionally, the fidelity between the input and the teleported state, which we will call *teleportation fidelity* $\mathcal{F}$, is a figure of merit for the success of the protocol that quantifies the degree of resemblance of the teleported state with the unknown input state. It is defined using the density matrix formalism as:

$$\mathcal{F} = \left[\mathrm{Tr}\left(\sqrt{\sqrt{\hat{\rho}_{in}} \hat{\rho}_{out}(\hat{\rho}_{in}) \sqrt{\hat{\rho}_{in}}} \right) \right]^2, \tag{1.47}$$

with $\hat{\rho}_{out}(\hat{\rho}_{in})$ the teleported state corresponding to the input state $\hat{\rho}_{in}$. In practice the fidelity is measured for an ensemble of input qubits, such as a mutually unbiaised basis of the Bloch sphere, that accurately describes all possible input states.

The success of the teleportation is then assessed by comparing the measured fidelity for each qubit with a *fidelity bound* or *fidelity threshold*. If the fidelity surpasses the bound for all qubits, then it is proven that no better copy could be obtained by the other party. The usual threshold that is considered corresponds to a classical teleportation where Alice measures the unknown state and $|\psi_{in}\rangle$ and transfer the result to Bob via the classical channel who then creates the output state accordingly without the use of entanglement.

The fidelity bound for quantum teleportation depends on the system at hand and the choice of encoding [134]. We simply note that the classical bound both the DV and CV basis with which we work in this thesis is $\mathcal{F}_{classical} = 2/3$, which corresponds to the maximum information retrievable from a single measurement of the input qubit [135]. This is the figure of merit we will use to assess the success of the teleportation protocol in **Chapter 7**.

A second important figure of merit to consider is the *efficiency* of the teleportation ε which characterizes the probability of success of the protocol. Indeed, even if the teleportation occurs above the fidelity bound, if the efficiency is too small no event will be measured and the protocol will not be implementable. The efficiency depends on the implementation of the Bell-state measurement. In the case of deterministic, active, teleportation all the events are recovered and the efficiency is $\varepsilon = 1$. For probabilistic protocols, the efficiency will drop from its ideal value. As we will see in **Chapter 4**, in our implementation of the Bell-state measurement, there is a compromise to ensure between fidelity and efficiency of teleportation, as a decrease of rate leads to a better filtering of the events, and so a better teleportation fidelity, and conversely.

In this section we have thus presented the quantum teleportation protocol in the context of heterogeneous quantum networks. We have introduced its basic principles, giving the relevant definitions necessary for the description of its implementation, and the figures of merit required for its characterization. Hybrid quantum teleportation can be performed to transfer and convert quantum information between different encodings. By employing the hybrid entanglement of light which will be introduced in **Chapter 3**, with a hybrid Bell-state measurement of **Chapter 4**, we will perform this hybrid protocol for the conversion of DV qubits to CV qubits in **Chapter 7**.

Following the theoretical introduction of quantum teleportation we finally proceed to the presentation of its extension to the teleportation of entanglement in a protocol called entanglement swapping.

6 The teleportation of entanglement: entanglement swapping

As we have introduced earlier, the unknown quantum state subject to teleportation does need to have properties of his own, and could thus be part of an entangled state. The generalization of quantum teleportation to an input state that is one mode of an entangled state is called *entanglement swapping*, and is a protocol allowing the creation of entanglement between two modes that have never interacted. Entanglement swapping makes use of a projective Bell-state measurement between two modes of two independent entangled states to collapse the remaining modes into an entangled state. In the following we will introduce the principle of entanglement swapping and present its applications in the context of heterogeneous quantum networks.

6.1 Principle

The entanglement swapping protocol [137], represented in Figure 1.8 relies on two entangled states that can be written under the form:

$$\begin{aligned} |\Psi\rangle_{AB} =& \frac{1}{\sqrt{2}}(|\mathbf{0}\rangle_A |\mathbf{1}\rangle_B + |\mathbf{1}\rangle_A |\mathbf{0}\rangle_B), \\ |\Psi\rangle_{CD} =& \frac{1}{\sqrt{2}}(|\mathbf{0}\rangle_C |\mathbf{1}\rangle_D + |\mathbf{1}\rangle_C |\mathbf{0}\rangle_D). \end{aligned} \tag{1.48}$$

Similarly to teleportation, the four mode state

$$|\Psi\rangle_{ABCD} = |\Psi\rangle_{AB} \otimes |\Psi\rangle_{CD}\,, \tag{1.49}$$

can be factorized as:

$$\begin{aligned} |\Psi\rangle_{ABCD} = \frac{1}{2}\Big[&\left|\Psi^+\right\rangle_{CA} \otimes \left|\Psi^+\right\rangle_{DB} - |\Psi^-\rangle_{CA} \otimes |\Psi^-\rangle_{DB} \\ &+ \left|\Phi^+\right\rangle_{CA} \otimes \left|\Phi^+\right\rangle_{DB} - |\Phi^-\rangle_{CA} \otimes |\Phi^-\rangle_{DB} \Big]. \end{aligned} \tag{1.50}$$

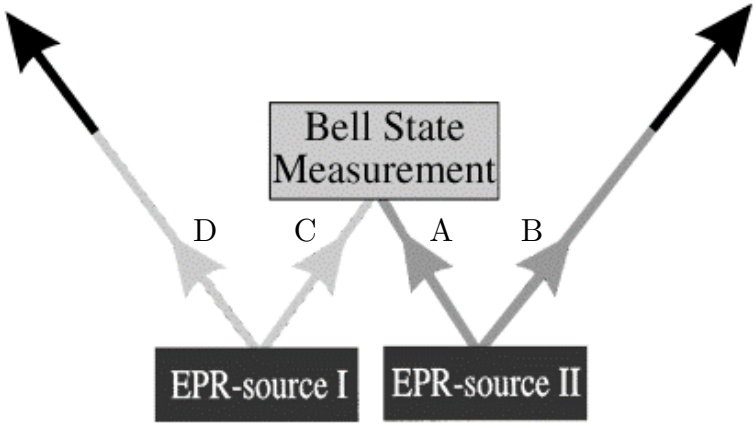

Figure 1.8: **Principle of entanglement swapping**. From [136] .Starting from two independent entangled states A-B and C-D, the success of the Bell-state measurement creates entanglement between modes B and D which have never interacted.

The application of the Bell-state measurement on modes A and C projects the modes D and B into one of the four maximally-entangled Bell states. In all cases, entanglement between modes A-B and C-D are swapped, and the states A-C and B-D each become entangled, even though they were initially uncorrelated. Entanglement swapping can be seen equivalently as the teleportation of the state of A to the mode D or the state of C onto the mode B.

The same considerations as for the teleportation protocol on the implementation of the Bell-state measurement and the recovery of the swapped state have to be applied. The success of the swapping will in this work be assessed by the measurement of the negativity of entanglement which is a natural figure of merit for proving the creation of entanglement between the two ouput modes.

6.2 Entanglement swapping in heterogeneous quantum networks.

One of the main application of entanglement swapping is the ability to distribute entangled state between nodes of a quantum network that would be too distant for direct propagation. This protocol is a key requirement for the development of long-distance quantum communication based on quantum repeaters [92]. Again, if the quantum network is composed of a heterogeneous structure with DV and CV nodes, entanglement swapping using hybrid entanglement would enable the connection of nodes based on different encodings and physical platforms. Many protocols could thus be envisioned in that framework:

- The connection of a CV platform-only to a DV node via hybrid entanglement:

$$\mathrm{CV}\infty\mathrm{CV} \otimes \mathrm{CV}\infty\mathrm{DV} \rightarrow \mathrm{CV}\infty\mathrm{DV}, \tag{1.51}$$

- The connection of a DV platform-only to a CV node via hybrid entanglement:

$$\mathrm{DV}\infty\mathrm{DV} \otimes \mathrm{DV}\infty\mathrm{CV} \rightarrow \mathrm{DV}\infty\mathrm{CV}, \tag{1.52}$$

  which will be experimentally demonstrated for the first time in **Chapter 5**.

- The interconversion of hybrid links in single-encoding platforms:

$$\begin{aligned} &\mathrm{DV}\infty\mathrm{CV} \otimes \mathrm{CV}\infty\mathrm{DV} \rightarrow \mathrm{DV}\infty\mathrm{DV}, \\ &\mathrm{CV}\infty\mathrm{DV} \otimes \mathrm{DV}\infty\mathrm{CV} \rightarrow \mathrm{CV}\infty\mathrm{CV}, \end{aligned} \tag{1.53}$$

  which could be performed with our current ressources but goes out of the scope of this thesis.

We have presented the principle of entanglement swapping, which is an extension of quantum teleportation to an entangled state. Entanglement swapping is an essential protocol for the distribution of entanglement and the interconnection of different remote platforms. It will be experimentally implemented in **Chapter 5** between a DV-DV entangled state and a hybrid entangled state, by employing the same hybrid Bell-state measurement technique introduced in **Chapter 4**. To conclude this first chapter we finally present the different classes of quantum information processing protocols.

7 Stages of functionality and applications of quantum information processing protocols

In the development of a quantum internet, the quantum information processing protocols, such as quantum teleportation and entanglement swapping, are divided in different classes depending on the level of complexity required to enable novel applications [92, 138] - which is not necessary related to the complexity of the experiments. In experimental implementations several considerations have to be taken into account to estimate to what extend the protocol represents either real-world quantum advantages or only a proof-of-principle experiment. To that end we will describe three classes of schemes with increasing scopes, namely *post-selected*, *heralded* and *deterministic* protocols.

7.1 Post-selection in quantum information processing protocols

Post-selection corresponds to the selection of some subsets of an ensemble of identical systems depending on the result of a measurement. From a practical point of view this corresponds to the only consideration of the events of interest, while discarding the other events as if they had never occurred. For instance in a two-party scenario where a qubit is sent through a quantum channel this could amount to ignoring the non-detected events corresponding to a loss of the state in the environment. Such scenarios are the easiest to implement in practice as they neglect some sources of noise of the quantum channels, and the selection operation can be performed by processing recorded data. Post-selection

can be tolerated in some prepare-and-measure schemes [92] such as BB84 QKD [27]. Yet, more complex protocols require the transmission of unknown quantum states where no post-selection on detection events can be allowed. Indeed, as the state is unknown, and the senders blind, it is not possible to infer when the events occur or which events can be ignored. Thus, post-selection fails for many quantum information processing protocols and post-selected experimental implementations can hardly be extended further [138].

7.2 Heralded protocols

A step towards the deterministic implementation of protocols is to make use of *heralding*, which consists in signaling the success of the protocol with an event independent of the delivered states. The protocol can be considered as deterministic in the time period when the heralding occurs. The traveling modes are thus subjected to all the sources of noise and imperfections of the quantum channels that are not neglected anymore in the process. Heralded schemes can thus describe protocols involving unknown quantum states and entanglement distribution over large distance. The heralding can also be employed to improve the fidelity of some protocols at the expense of success rate. The heralding then corresponds to a filtering of the events of interest in time. The inconvenience of heralded scheme is that the heralded signals come in a probabilistic and stochastic fashion. This induces an exponential decrease of the probability of success of the protocols as the number of heralding increases [139]. Quantum memories can be employed to synchronize the stochastic events, with an improvement of the rate that decrease polynomially with the number of heralding [125].

In this work we will focus on heralded teleportation and entanglement swapping protocols.

7.3 Deterministic protocols

The deterministic distribution of entanglement and quantum states remains a long-standing goal for the development of quantum networks. In practice, a protocol is defined as deterministic when its succeeds with unity probability. In that case, the deterministic protocol not only represents a tangible real-world protocol where all experimental imperfections are included, but it also offers a practical operation contrary heralded scheme which success probability become quickly negligible. Experimentally, deterministic protocols can be performed from on-demand sources [140] or from heralded ones if the generation rates overcome the loss rate of the states [141].

8 Conclusion

In this chapter we have introduced conceptually all the quantum principles and architectures that are necessary for the understanding of this thesis. We have first motivated the development of quantum technologies, and presented the quantum states at its basis, with the two possible encodings of information. We have detailed the theoretical

tools for the characterization of quantum states and entanglement. Finally we have presented quantum teleportation and entanglement swapping protocols in the framework of long-distance communication in heterogeneous quantum networks. Before presenting the implementation of these hybrid protocols, i.e entanglement swapping in **Chapter 5** and hybrid quantum teleportation in **Chapter 7**, we need first to describe the experimental tools for the engineering of discrete-, continuous-, and hybrid entangled states. This description is given in the next two chapters.

Chapter 2

Experimental tools for non-Gaussian quantum state engineering

In this chapter we present the experimental tools used for the engineering of non-Gaussian quantum states of light. We will describe first the semi-monolithic optical parametric oscillators from which the discrete- and continuous-variable quantum states are created. We will then introduce, with their operating cryogenic system, the single-photon detectors that are used for the heralding of the states. These experimental tools are the basic elements required for the quantum engineering presented in **Chapter 3**, and the teleportation protocols implemented in **Chapter 5** and **Chapter 7**.

1 Generating squeezed light with semi-monolithic linear cavity-based optical parametric oscillators

In this section we present how single-mode and two-mode squeezed light can be generated by combining a second-order non-linear crystal with an optical cavity. We will describe the theoretical performances of such devices, called *optical parametric oscillators*, and show how large amount of squeezing can be obtained in a semi-monolithic cavity design with high escape efficiency.

1.1 Cavity-enhanced parametric down-conversion

1.1.1 Squeezing from spontaneous parametric down conversion

The generation of squeezed light requires the use of a non-linear medium. Indeed, when an electromagnetic field E propagates in a dielectric medium, it induces a redistribution of charges leading to a macroscopic density of polarization:

$$P = \epsilon_0 \chi^{(1)} E + \epsilon_0 \chi^{(2)} E^2 + \epsilon_0 \chi^{(3)} E^3 + ..., \tag{2.1}$$

where ϵ_0 is the electric permitivity of free space and $\chi^{(i)}$ is the non-linear electric susceptibility of order i.

The first order $\epsilon_0\chi^{(1)}E$ represents the *linear* response of the medium, which describes classical effects such as refraction or absorption. Yet, since the response is linear, all the quadratures of the field evolve symmetrically, so that no quadrature squeezing can be obtained. The higher order terms, which are observed under the action of a sufficiently intense external field, act asymmetrically on the different quadrature components and can couple different fields. They can thus yield the generation of squeezed or correlated non-classical states. Yet, the second order non-linear interaction $\chi^{(2)}$ is typically much stronger than the higher order non-linear processes typically observed in fibers or hot vapors, and can thus yield higher level of squeezing. Spontaneous parametric down-conversion (SPDC) is a $\chi^{(2)}$ - or three-wave - non-linear process that has a long standing record as a generator of squeezed light [142].

Spontaneous parametric down-conversion [143] consists in the conversion of a *pump* photon of frequency ω_0 into two photons called *signal* and *idler* at frequencies ω_1 and ω_2. The process is governed by the conservation of energy under the form:

$$\omega_0 = \omega_1 + \omega_2. \tag{2.2}$$

In addition, the phase accumulated by the fields at ω_0 has to be the same as the one accumulated by the fields at ω_1 and ω_2, otherwise the resulting amplitudes can interfere destructively. This is referred to as the *phase-matching condition*:

$$\vec{k_0} = \vec{k_1} + \vec{k_2}, \tag{2.3}$$

where $\vec{k_i}$ is the wave vector of the field i.
The phase-matching condition is written in the case of co-linear fields as:

$$n(\omega_0)\omega_0 = n(\omega_1)\omega_1 + n(\omega_2)\omega_2. \tag{2.4}$$

In general, because of the dispersion of the material, $n(\omega_0) \neq n(\omega_{1,2})$, so that without any particular precaution, the converted fields have negligible amplitude. The usual way to ensure phase-matching is to use a birefringent medium. In the case of a uniaxial crystal the refractive indices n_o and n_e along the *ordinary* and *extraordinary* axis can be engineered to fulfill the condition. We will focus on two possible configurations:

- **Type-I phase-matching:** $n_o(\omega_0)\omega_0 = n_e(\omega_1)\omega_1 + n_e(\omega_2)\omega_2$.
  The pump coincides with the ordinary axis while the signal and idler are degenerate in polarization along the extraordinary axis.

- **Type-II phase-matching:** $n_e(\omega_0)\omega_0 = n_{e/o}(\omega_1)\omega_1 + n_{o/e}(\omega_2)\omega_2$.
  The pump coincides with the extraordinary axis while the signal and idler are non-degenerate in polarization.

In any case, the Hamiltonian that corresponds to the coupling of the pump with signal and idler modes is written:

$$\mathcal{H} = i\frac{\hbar g}{2}\hat{a}_i^\dagger \hat{a}_s^\dagger \hat{a}_p + h.c, \tag{2.5}$$

where $\hat{a}_i$, $\hat{a}_s$ and $\hat{a}_p$ are the annihilation operators of the idler, signal and pump modes respectively and g is a coupling constant characteristic of the material.

The input pump field being in our case a bright coherent state $|\alpha_p\rangle$, we can replace $\hat{a}_p^\dagger \approx \alpha_p$ which simplifies the hamiltonian using the notation $\kappa_p = \alpha_p g$:

$$\mathcal{H} \approx i\frac{\hbar \kappa_p}{2}(\hat{a}_i^\dagger \hat{a}_s^\dagger - \hat{a}_i \hat{a}_s). \tag{2.6}$$

For the type-I phase-matching, when signal and idler are degenerate in frequency, i.e $\hat{a}_s = \hat{a}_i \equiv \hat{a}$, it corresponds to the single-mode *squeezing operator* [144] with a *squeezing parameter*, r:

$$\hat{S}_I(r) = e^{\frac{r}{2}(\hat{a}^2 - (\hat{a}^\dagger)^2)} = e^{-i\frac{\mathcal{H}}{\hbar}t}, \qquad \text{with} \quad r = \kappa_p t, \tag{2.7}$$

and t the interaction time.

From this Hamiltonian, we can observe the evolution of the quadrature operators $\hat{x} = \sigma_0(\hat{a}^\dagger + \hat{a})$ and $\hat{p} = i\sigma_0(\hat{a}^\dagger - \hat{a})$, considering in the Heisenberg representation for the signal and idler modes:

$$i\hbar\frac{d\hat{a}}{dt} = \left[\mathcal{H}, \hat{a}\right] \tag{2.8}$$

that yields

$$\frac{d\hat{a}}{dt} = -\kappa_p \hat{a}^\dagger(t), \tag{2.9}$$

and can be integrated in

$$\hat{a}(t) = \hat{a}(0)\cosh(\kappa_p t) - \hat{a}^\dagger(0)\sinh(\kappa_p t). \tag{2.10}$$

As a result the quadratures $\hat{x}$ and $\hat{p}$ evolve as

$$\begin{aligned} \hat{x}(t) &= e^{-r}\hat{x}(0), \\ \hat{p}(t) &= e^{r}\hat{p}(0), \end{aligned} \tag{2.11}$$

which corresponds to position squeezing and momentum anti-squeezing. If the initial state is vacuum, the evolution will result in a squeezed vacuum state.

In the case of non-degenerate signal and idler, the interaction Hamiltonian corresponds to a two-mode squeezing operator:

$$\hat{S}_{II}(r) = e^{r(\hat{a}_i \hat{a}_s - \hat{a}_i^\dagger \hat{a}_s^\dagger)}. \tag{2.12}$$

It is interesting to look at the polarization modes rotated by 45° and defined by:

$$\begin{aligned} \hat{a}_1 &= i(\hat{a}_s - \hat{a}_i)/\sqrt{2}, \\ \hat{a}_2 &= (\hat{a}_s + \hat{a}_i)/\sqrt{2}. \end{aligned} \tag{2.13}$$

Injected into the operator $\hat{S}_{II}(r)$, it leads to

$$\hat{S}_{II}(r) = e^{r(\frac{1}{2}(\hat{a}_2+i\hat{a}_1)(\hat{a}_2-i\hat{a}_1)-h.c)} = e^{r(\frac{1}{2}(\hat{a}_2^2+\hat{a}_1^2)-h.c)} \tag{2.14}$$

and thereby

$$\hat{S}_{II}(r) = S_1(r)S_2(r). \tag{2.15}$$

A two-mode squeezed vacuum state is equal, up to a basis change, to two independent single-mode squeezers.

Thus, spontaneous parametric down-conversion corresponds to the application of single or two-mode squeezing depending on the phase-matching type. In the case of type-I phase-matching, the signal and idler photons are degenerate in both frequency and polarization, leading to the application of a single-mode squeezing operator. In the case of type-II phase-matching the signal and idler photons are degenerate in frequency but not in polarization. This corresponds to the application of a two-mode squeezing operator.

1.1.2 Adding an optical cavity

The $\chi^{(2)}$ nonlinearity is in general very weak and different considerations have to be taken into account in order to reach efficient squeezing. A first technique to address the small $\chi^{(2)}$ non linearity is to use an increased pump amplitude concentrated in ultra-short pump pulses in a single-pass configuration. However the pulse shape may lead to a difficult definition of the temporal-mode shape of the generated states and so the value of squeezing that can be reached [145, 146, 147, 148]. Another solution is to insert the non-linear medium into a cavity. Combining a non-linear crystal with an optical cavity in such a way defines an *optical parametric oscillator*.
In this cavity configuration, having the signal and idler co-resonant with the pump field thereby enhances the effective non-linearity. For SPDC, the cavity induces a new dynamics and also defines the spatio-temporal properties of the down-converted beams.

We can efficiently simulate the dynamics of the OPO by considering a round trip of the signal and idler modes inside the cavity [149, 150]. The non-linear coupling inside the non-linear crystal of length l is called g. The pump field is considered as a coherent state of amplitude α_p^{in} entering the input mirror. The input mirror has an intensity reflection of R for the pump and is highly-reflective (HR) for the signal and idler. The output coupler is highly reflective for the pump. The cavity is supposed to be resonant for the two signal and idler fields, so that they accumulate a phase-shift of an integer of 2π after one round-trip. The cavity is characterized by two fundamental parameters:

- **The intensity transmission of the output coupler T.**
  In our case the reflection being small, we can write $\sqrt{R} = \sqrt{1-T} \approx 1 - T/2$.
- **The intra-cavity losses L.**
  It can be modeled by a beamsplitter of intensity reflection L which couples the intra-cavity modes $\hat{a}_{s,i}$ to environmental modes $\hat{a}_{s,i}^L$.

Considering one round trip yields two coupled equations for the signal and idler fields:

$$\hat{a}_{s,i}(t+\tau) = \sqrt{(1-L)(1-T)}\Big[\hat{a}_{s,i}(t) + \alpha_p g_{crystal}\hat{a}^{\dagger}_{i,s}(t)\Big] + \sqrt{L}\hat{a}^{L}_{s,i} + \sqrt{T}\hat{a}^{in}_{s,i}(t), \quad (2.16)$$

with $g_{crystal}$ the non-linear gain through the crystal given by $g_{crystal} = 2lg$ (note that the beams passes two times inside the crystal in one round trip).
With low intra-cavity losses and high transmission of the output coupler, we can simplify this expression. With $\sqrt{(1-L)(1-T)} \approx 1-(L+T)/2$, it becomes:

$$\hat{a}_{s,i}(t+\tau) = (1-\frac{L+T}{2})\Big[\hat{a}_{s,i}(t) + \alpha_p g_{crystal}\hat{a}^{\dagger}_{i,s}(t)\Big] + \sqrt{L}\hat{a}^{L}_{s,i} + \sqrt{T}\hat{a}^{in}_{s,i}(t). \quad (2.17)$$

Keeping only the first order terms, it leads to:

$$\tau\frac{d\hat{a}_{s,i}}{dt} = -\frac{L+T}{2}\hat{a}_{s,i}(t) + \alpha_p g_{crystal}\hat{a}^{\dagger}_{i,s}(t) + \sqrt{L}\hat{a}^{L}_{s,i} + \sqrt{T}\hat{a}^{in}_{s,i}(t). \quad (2.18)$$

From our modeling, several figures of merit characteristic of the dynamics of the of the optical parametric oscillator can be obtained.

1.2 Figures of merit

1.2.1 Oscillation threshold

As compared to the single-pass configuration, the cavity induces a critical condition known as the oscillation threshold. With our model with a bright, non-resonant, pump beam, the equations present a threshold where the losses of the cavity are compensated by the gain. It thus defines the pump threshold as:

$$|\alpha_{p,th}|^2 = \frac{(T+L)^2}{4g^2_{crystal}}. \quad (2.19)$$

The oscillation threshold scales quadratically with both the intracavity losses and the transmission of the output coupler. The threshold gives the pump power that corresponds to the maximum obtainable *squeezing factor*: $s_{max} = e^{-2r_{max}}$. In our case, to create high-purity quantum states, we will always remain as far as possible below the threshold to limit the generation of multi-photon events.

1.2.2 Escape efficiency

The escape efficiency η_{OPO} of an OPO is defined as the ratio between the decay rate of the down-converted fields through the output coupler over the total decay rate of the cavity at the fundamental frequency. It represents the probability for a down-converted photon to escape the cavity by the output mirror. It can be expressed as:

$$\eta_{OPO} = \frac{T}{T+L}. \quad (2.20)$$

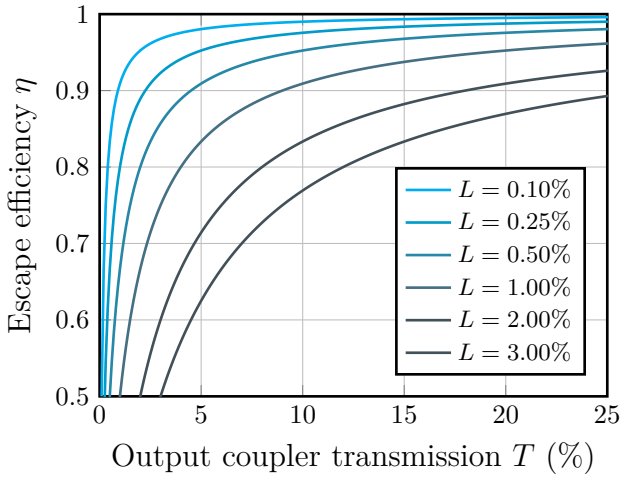

Figure 2.1: **Escape efficiency of an optical parametric oscillator.** Theoretical escape efficiency as a function of the transmission of the output mirror T, for different intra-cavity losses L. The escape efficiency is maximized when the intra-cavity losses are small as compared to the transmission of the output coupler.

The escape efficiency is limited mostly by the intracavity losses inside the cavity. We plot in Figure 2.1 the escape efficiency for different output coupler transmission and intra-cavity losses. We see that escape efficiency grows with the output coupler transmission and that intra-cavity losses, even at a very low level, have a drastic impact on the escape efficiency. A general rule of thumb is thus to say that the escape efficiency is high when the losses are much smaller than the transmission of the output coupler.

The escape efficiency is directly related to the maximum squeezing amount that can be obtained at the oscillation threshold:

$$s_{max} = 1 - \eta_{OPO}. \tag{2.21}$$

The escape efficiency is thus a key characteristic of the quality of an OPO [6]. An OPO with a large escape efficiency is an OPO that can generate a very large squeezing close to oscillation threshold, or equivalently a single-photon with high purity if operated far below threshold.

1.2.3 Bandwidth

The bandwidth of the quantum states generated by an OPO are directly given by the bandwidth of the cavity. The bandwidth γ_{OPO} is inversely proportional to the length of the cavity l_{cav} and scales linearly with the transmission of the output coupler when considering an input mirror with negligible transmission:

$$\gamma_{OPO} = \frac{c}{2\pi}\frac{T}{l_{cav}}. \tag{2.22}$$

As we will see later, the bandwidth of the OPO is related to the *temporal mode* of the generated state. It represents the probability of measuring the heralded quantum state in a given time window. It is important to note that the larger the bandwidth the shorter will be the states. As we will see in **Chapters 5** and **7**, when detecting coincidences between different states in a fixed time window, the shorter the temporal mode the harder the detection will be.

1.3 OPO design and experimental specifications in our lab

When designing an OPO-based squeezing source, it is important to optimize the three figures of merit presented before. First, one would target a close-to-unity escape efficiency to improve as much as possible the purity of the generated states. This is achieved by targeting intra-cavity losses L small relative to the transmission of the output coupler. Second, one would target a pump threshold of a few tens of milliwatts as to maintain a decent production rate and minimum multi-photon production with a pump power far below threshold at the milliwatt level. One strategy to increase these two parameters is to increase the transmission of the output coupler T. The problem is that as T increases the bandwidth of the generated photons increase, so that we are rapidly limited by the bandwidth of the detection. Having T fixed to its maximum value by the detection, the only way of increasing the escape efficiency is to reduce the intra-cavity losses as much as possible.

The design of the OPO should thus be a good trade-off between a high escape efficiency, a not too large bandwidth, and a reasonable threshold. It is important to note that in the OPO design, the higher the purity of the generated states, the larger their bandwidth, and so the shorter their temporal mode. As we will see later, it is thus harder with our sources to perform temporal interferences between high-purity quantum states. This reveals an intrinsic trade-off between purity of the states and indistinguishability.

We present now the design of the type-I and type-II optical parametric oscillators that were present at the start of the thesis, and that were involved in all the protocols performed in this work. In **Chapter 6** we will present in details the third OPO that have been built on top to increase our experimental capability. The OPOs are pumped by a frequency-doubled continuous-wave Nd:YAG laser (Innolight GmbH) at 532 nm, which leads to the generation of signal and idler fields at 1064 nm (IR). The cavity are in a plano-concave configuration, with a curvature of the output mirror of 38 mm.

We first discuss the spectral properties of the optical parametric oscillators. It is important to note that requiring all the quantum states to be indistinguishable, their spectro-temporal properties need to be matched, so that the bandwidth of all the OPOs should be the same. The detection bandwidth of the homodyne detector being limited to 60 MHz, we target an OPO bandwidth around 50 MHz. To that end we choose a transmission of the output coupler of $T = 10\%$ for the infrared beam. The cavities have a length of 38 mm, which gives a free-spectral range (FSR) of 4.3 GHz.

In order to minimize the intra-cavity losses, we use a for these OPOs a *semi-monolithic* configuration in which the input mirror is directly coated on the surface of the non-

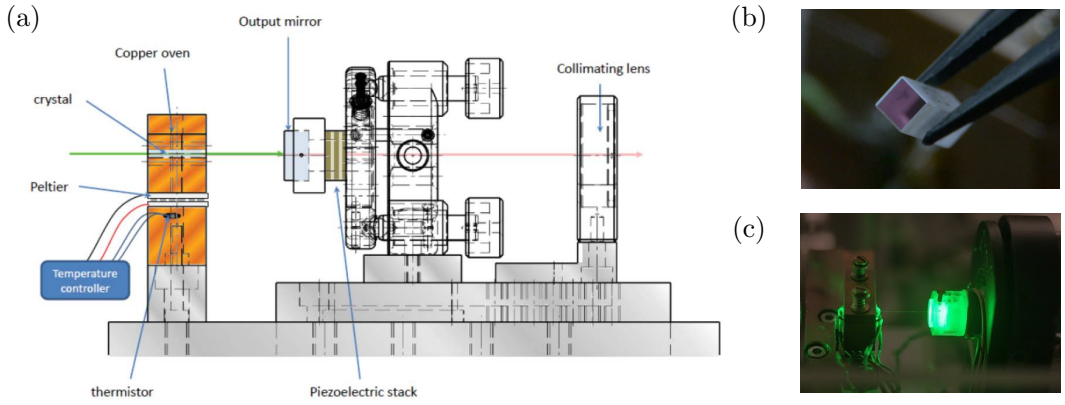

Figure 2.2: **Design of the optical parametric oscillator.** (a) Schematic of the design of a semi-monolithic optical parametric oscillator. The pump at 532 nm is injected from the left. The non-linear crystal is placed inside a home-made copper oven and controlled by a Peltier module. The input mirror is directly coated on the surface of the crystal (R=95% for the pump, HR for the IR). The output mirror is mounted on a piezo-electric transducer fixed in on a high-stability mirror mount. The concave output mirror (HR for the pump, $T = 10\%$ for the IR) has a radius of curvature of 38 mm. A collimating lens is used to collimate the down-converted beams at 1064 nm. All the elements are fixed on a home-made Invar ultra-stable mount. (b) Picture of the KTP crystal of the type-II OPO. (c) Picture of the type-II OPO locked on the resonance of the pump.

linear crystal. This cavity design enables to reduce the number of interfaces inside the cavity and thus the losses that can result from scattering or absorption. The input mirror has a reflection coefficient $R = 95\%$ for the pump and is highly reflective (HR) for the infrared. Conversely the output mirror is highly reflective for the pump and has the output transmission T given above for the IR.

For the type-II OPO we use a type-II KTP crytal of dimensions 3x3x10 mm^3 and for the type-I OPO we use a type-I ppKTP crystal of dimensions 1x2x10 mm^3. The crystals are provided by the company **Raicol** and the coating is performed by the company **Layertec GmbH**.

The OPOs aiming at being resonant for both the pump and the down-converted fields, meaning that the OPO-II is *triply resonant* while the type-I OPO is *doubly resonant*. The resonance of the pump is adjusted by mounting the output mirror on a piezo-electric transducer (PZT) to adjust the length of the cavity accordingly. The non-linear crystal is placed in a copper oven controlled by a Peltier module and the temperature of the crystal is adjusted to ensure the resonance of the down-converted fields. Finally, for the type-II OPO, the resonance of the second, orthogonally polarized, down-converted field is adjusted by tuning the laser frequency.

The characterization of the intracavity losses is done by performing squeezing measurements with the type-I OPO. The corresponding measurements [6] are given in Figure

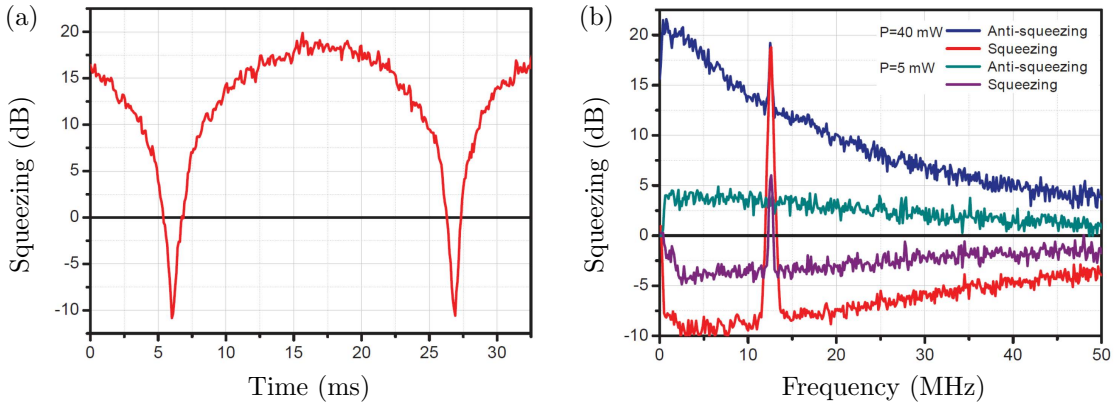

Figure 2.3: **Squeezing measurement with the type-I OPO.** From [6]. (a) Squeezing measured by homodyne detection at a sideband frequency of 5 MHz, while sweeping the phase of the local oscillator in time. At a pump power of 40 mW (80% of the threshold) we reach 10.5 dB of quadrature squeezing and 19 dB of quadrature anti-squeezing. (b) Quadrature squeezing and anti-squeezing measured between 0 and 50 MHz for a pump power of 5 mW and 40 mW, corresponding respectively to 3 dB and 10.5 dB of measured squeezing. The peak at 12 MHz originates from the internal modulation of the laser.

2.3. At a sideband frequency of 5 MHz, we observe a quadrature squeezing of 10.5 dB and an anti-squeezing of 19 dB, that gives considering our model with losses a very large escape efficiency $\eta = 92\%$. Such semi-monolithic OPOs designs can thus yield very low intracavity losses, down to 0.5%.

We have presented the two initial sources of squeezed states at our disposal for the experiments. The type-I OPO, doubly resonant, allows the generation of a single-mode squeezed vacuum state, while the type-II OPO, triply resonant, allows the generation of a two-mode squeezed vacuum state, or equivalently two independent single-mode squeezed vacuum states. The semi-monolithic cavity design, where the intra-cavity losses are small as compared to the transmission of the output coupler, enables the generation of high purity quantum states. Yet at that point all the quantum states created are *Gaussian*, i.e their Wigner function is always positive. Although those states are fundamentally quantum, they can be simulated efficiently using classical systems [151]. We thus need to create *non-Gaussian* states exhibiting negativities of their Wigner function [152]. These states can be created from Gaussian state using non-linearities, which can be implemented experimentally with a probabilistic *photon-subtraction*. In the next section we will present the single-photon detector-based measurement apparatus we employ in our group to perform this photon subtraction.

2 Heralding quantum states with superconducting nanowire single photon detectors

Photon subtraction is a key requirement for the creation of non-Gaussian quantum states. This operation is performed using single-photon detectors [153], i.e. measurement systems sensitive to individual quantized packets of energy. Since the energy of a single-photon is very small (typically 10^{-19} J in the near-infrared), the devices that are used for their detection are extremely sensitive. Different technologies, such as single-photon avalanche photodiodes (SPADs) can be used to detect single photons, yet their *quantum efficiency* (QE), i.e. the probability to detect a single photon arriving on the detector, has historically remained low at our working frequency of 1064 nm. Very recently a lot of progress has been obtained in the field with the development of *superconducting nanowire single-photon detectors* (SNSPDs) [154]. These detectors promise record quantum efficiencies above 90% [155]. Our team took part in the effort by collaborating with the group of V. Verma and S. W. Nam for the National Institute of Technology (NIST) and F. Marsili and M. D. Shaw from the Jet Propulsion Laboratory (JPL). SNSPDs are now extensively used in the field of quantum information processing, including in quantum key distribution and optical quantum communications [156].

We will now introduce the working principle of these single-photon detectors and present the first cooling system that was used at the start of this thesis work to operate them.

2.1 SNSPDs: structure and performance

2.2 Working principle

The SNSPDs are composed of a thin and narrow superconducting wire patterned in a compact meander geometry. The thickness of the wire is typically of a few nanometers, while its width is below the micrometer. The length of the nanowire is itself of a few hundreds micrometers. The meander forms the light sensitive area as shown in Figure 2.4. When the meander is in its superconducting state, the application of a current above its *switching current* yields a phase transition towards the normal resistive state. This property can be exploited to make the meander sensitive down to the detection of a single photon. At a fixed temperature below the critical temperature, the detector is placed in a constrained superconducting state by applying a *bias current* right below its switching current. When a single photon hits the meander, its energy is sufficient to create a local hotspot, i.e. the material of the wire locally phase-transits to the resistive state, yielding a local increase of the current density. Thanks to the confined and small geometry of the wire, the increase of current density propagates in the full meander, that fully transitions to the resistive state. This creates a macroscopic resistance along the full wire of a few kΩ, and consequently a measurable voltage.

After the absorption of the photon and the switching into the resistive state, the detector then cools down back to its superconducting state. During that period the detector

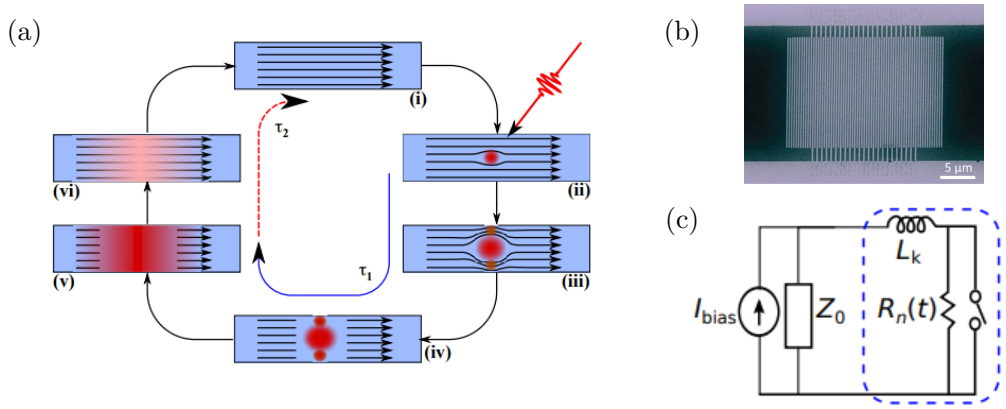

Figure 2.4: **Working principle of SNSPDs.** From [157]. (a) Schematic of the detection cycle (i) The SNSPD is maintained well below the critical temperature and is DC current biased below the critical current. (ii) A local resistive hotspot is created by the absorption of a photon. (iii) The current is forced to flow around the hotspot. Because of the narrow geometry, the current density around the hotspot exceeds the superconducting critical current density. (iv) This leads to the formation of a resistive barrier across the width of the nanowire. (v) The resistive region grows along the axis of the nanowire until the current flow is blocked and the bias curent is shunted. (vi) It allows the resitive region to cool down back to its superconducting state, with the bias current going back to its initial value. (b) SEM photograph of the sensitive meander of a WSi SNSPD. (c) Equivalent electric circuit of the SNSPD. L_k is the inductance of the superconducting nanowire and $R_n(t)$ the hotspot resistance. The aboprtion of a photon corresponds to the opening of the switch.

cannot measure another incoming photon, which defines the detector *dead time* that depends on the wire geometry, the material employed, and the working temperature. The voltage pulse originating from the absorption of the photon can thus be directly used -after proper amplification - as a triggering signal for the experiment.

2.3 Our single-photon detectors

The SNSPDs that have been employed to implement the teleportation protocols are made by the NIST and optimized for our detection wavelength at 1064 nm [7]. My predecessors at LKB have worked on the characterization on the quantum efficiency of the detectors and helped designing each time the next generation of detectors. Several materials have been used, starting from Niobium Nitride (NbN) before turning to amorphous materials: Tungsten Silicide (WSi) and Molybdenum silicide (MoSi). Details on the NIST design is given in Figure 2.5 for a WSi detector. The width of the nanowire is equal to 140 nm and the pitch is equal to 245 nm. The thickness of the wire is about 4 nm. The sensitive area is mounted on a copper base on which a zirconia sleeve enables the direct plugging of an optical fiber to the device. The active 16 μm x 16 μm area, larger than the

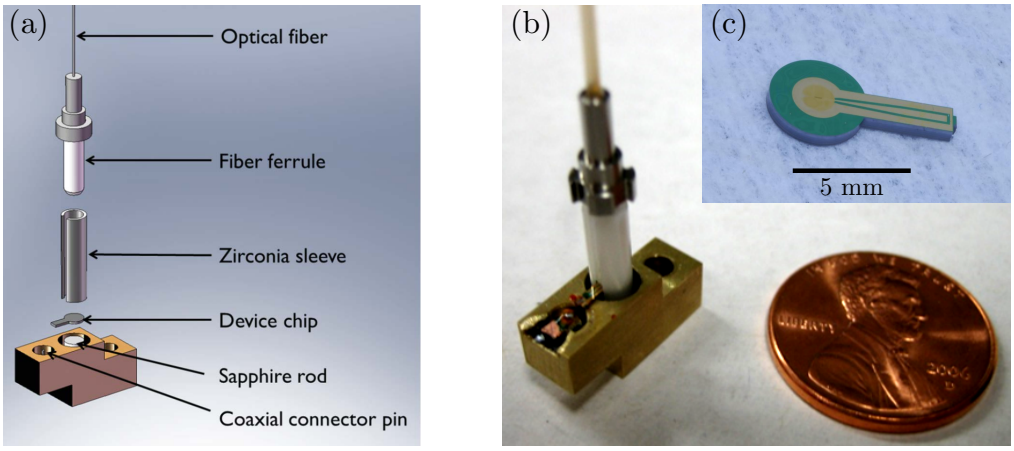

Figure 2.5: **NIST superconducting nanowire single-photon detectors.** (a) Detector assembly of the SNSPD. The device chip is mounted on a copper base and a Zirconia sleeve is used to enable the direct plugging of a single-mode optical fiber to the device. (b) Picture of a SNSPD connected to an optical fiber. (c) Picture of the device chip. The superconducting meander is located at the center of the circular part.

10 μm mode field diameter of a standard single-mode fiber, ensures a high coupling from the fiber to the detector and allows for slight misalignment.

The precise measurement of the *system detection efficiency* (SDE), i.e. the probability that an input photon will lead to a measurable pulse, which comprises all the losses in the coupling system as well as the QE of the detector, has been extensively described in previous works [134, 7, 158] and will not be detailed here. For our work, we will only consider the lastest generation of SNSPDs made of MoSi. The response of the best detector is shown in Figure 2.6, where the system detection efficiency is given as a function of the bias current. As the current increases, the detectors become more sensitive, until the efficiency reaches a *plateau*. This plateau can only be attained if the SNSPDs are well designed and the switching current is high enough. Indeed, if the bias current reaches the switching current, the SNSPD is no more sensitive. In practice it is important to be able to go as far as possible in this plateau where the voltage pulse originating from the detector are the best defined and have the most consistent rising edge. Yet, as the current increases, the detectors also become too sensitive so that they can announce false events that do not correspond to the detection of the photon, that are called *dark counts*. There is thus a trade-off between dark count and quantum efficiency, but still if the plateau is large enough it is possible to work in a regime with maximum SQE and minimum dark count.

As can be seen in Figure 2.6, our detectors can reach quantum efficiencies up to 93% $\pm$ 3%, while presenting a dark count rate at the few counts per second. In our operational regime where quantum states are typically detected at a few hundred kilohertz rate, this yields a negligible (0.01%) impact of the dark count on the overall detection.

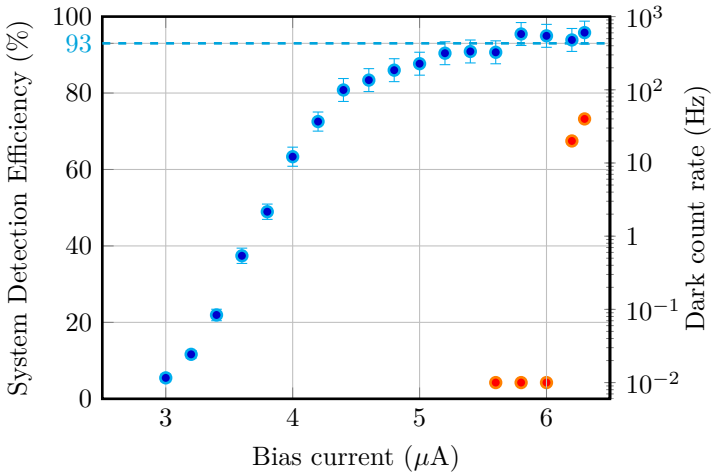

Figure 2.6: **Characterization of the MoSi SNSPDs.** (Blue) System Detection Efficiency (SDE) of the SNSPD as a function of the bias current. The SDE increases until it reaches a plateau around 93%±3%. (Orange) Dark count rate of the SNSPD as a function of the bias current. The dark count rate remains below the Hertz level almost until the end of the SDE plateau.

Such a low dark count level originates from the working temperature of the SNSPD in the superconducting state, that prevents the detection of thermal photons as compared to other room temperature technologies. In addition to exhibiting record quantum efficiency and low dark count rate, the SNSPDs present a dead time of tens of nanoseconds, with jitters - the random delay between the arrival of the photon and the creation of the pulse - of tens of picoseconds. This technology has thus become very attractive for quantum information processing, and many companies are now providing very efficient commercial detectors.

2.4 The dipstick: technique and limitations

The single-photon detectors being superconducting, they require a cryogenic environment to be operated, typically at a working temperature below 2 K. In this section we describe the first system that was used to cool down up to two SNSPDs to a temperature of 1.7 K. This setup was used in the entanglement swapping protocol presented in **Chapter 5**. In **Chapter 6** we will describe in details a second cooling system based on a two-stage cryocooler that was fully installed during this thesis and enables to cool down up to four SNSPDs to a temperature of 1.3 K. The latest system will be employed for the hybrid teleportation protocol presented in **Chapter 7**.

The first cooling method consists in direct dipping into liquid helium. The system, adapted from a commercial system made by **Scontel**, is shown in Figure 2.7. It consists in placing the detectors at the bottom of a cane - or *dipstick* - surrounded by a double-wall isolated enclosure. The double wall is directly dipped in a 60l Dewar of liquid helium.

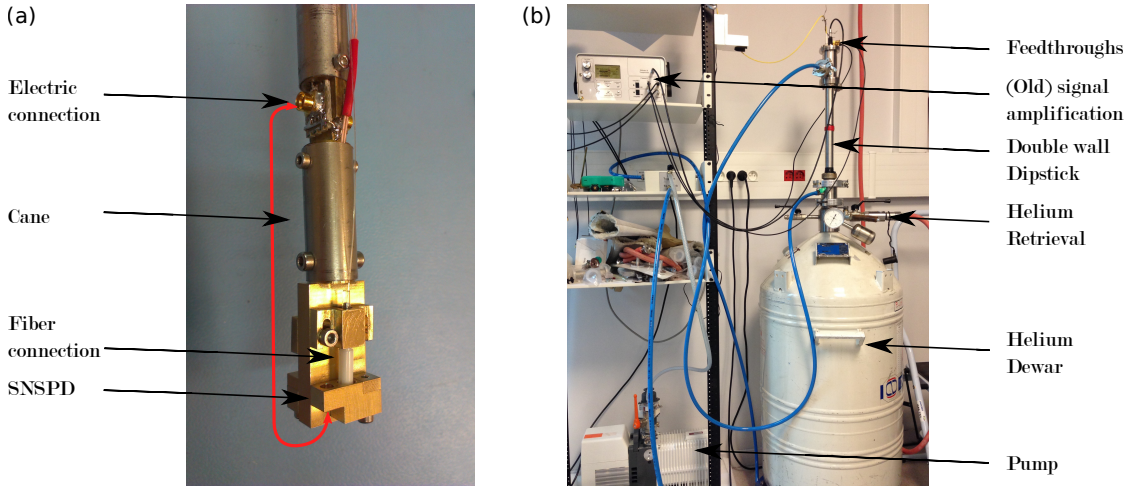

Figure 2.7: **Mounting and cooling of the dipstick.** (a) Up to two SNSPDs can be mounted at the bottom of the cane. The SNSPD is plugged to a 1.5 m long single-mode optical fiber connected to the top of the cane. The SNSPD is connected to the electrical cable using an SMP-SMP coaxial cable indicated by the red line. The fiber and the coaxial cables are circled around the cane up to the top so efficient thermalization. The cane is covered by the double wall before immersion into the liquid Helium (b). The cane is enclosed in a double-wall dipstick and inserted into a 60l liquid helium Dewar. The pump reduces the pressure inside the double-wall and enables temperature cooling down to 1.7 K. The electric signals from the detectors are connected from the top of the stick to the amplification circuit. The evaporated helium is retrieved in the university circuit and recycled by recompression.

A thin capillary present at the bottom of the enclosure allows the inflow of helium from the Dewar to submerge the detectors. The inside of the disptick is pumped by a rotary vane pump (**Adixen Pascal SD series**), resulting in a drop of temperature by adiabatic relaxation of the gaseous helium in the dipstick. This setup can reach a working temperature of 1.7 K, which is below the critical temperature of the detectors. The disptick is 1.2 m long, with an external diameter of about 5 cm. The electrical and optical connection to the detectors at the bottom of the stick to the feedthrough is performed using SMA cables and single-mode optical fibers (**Oz Optics SMJ-32.5F-1064/125-0.25-1.1-AR2**). The SNSPDs mounts are mechanically attached to a copper base at the bottom of the stick and fixed with a screw.

The dipstick is a rather efficient cooling method that offers a stable temperature at 1.7 K, and low noise on the SNSPD output electric signals. It has been used in our lab for about 5 years and has led to the implementation of first protocols with SNSPDs [4, 11, 12], including the entanglement swapping protocol presented in **Chapter 5**. Yet the cooling technique has some inconvenience. First, the dimensions of the double-wall allow only two independent SNSPDs, limiting thereby the range of protocols that can be

performed. Second, the rotary vane pump is rated at 15 hours of autonomy, which limits the duration of the data acquisition, and the helium Dewar has to be refilled typically every two weeks, that yields one working day per week where the dipstick has to be slowly removed or redipped, and that reduces the time that can be more efficiently used for the experiment. Lastly, the fact that the SNSPDs are not protected at the bottom of the disptick where they are immersed in the helium can lead to some damage on the fragile electric micro-bondings of the detectors. This deterioration can originate from the cleanness of the liquid helium but more importantly vacuum seal imperfections lead to the formation of ice directly on the detectors when they are removed from the helium. After repeated usage of the detectors, we observed scratches on the anti-reflection coating of the single-mode fiber connectors and sometimes even breaking of the electric bondings of the detectors.

As we will see in **Chapter 6**, the installation of the cryocooler alleviate all of these limitations. First up to four SNSPDs can be cooled at 1.3 K for up to 7 days in a row. The system has its own compressor so that helium renewal does not have to be performed, and the system can be operated without maintenance. Finally the cryocooler system offers a much safer environment for the SNSPDs that are cooled in a sampling region separated to the helium.

2.5 Spectral filtering and signal amplification

In addition to the cryogenic apparatus, two additional operations have to be implemented to obtain a fully functional system that can be employed in our experiments. First, the single photons to-be-detected need to be properly filtered to create the desired states on the experiment. Second, the signals from the SNSPDs need to be amplified without excess noise so that they can herald the correct events.

2.5.1 Pre-detection filtering

Before being detected by the SNSPDs, the single photon generated by the OPOs have to be spectrally filtered. Indeed, the SPDC process in the OPO is governed by the energy conservation $\omega_0 = \omega_1 + \omega_2$ which allows the generation of many energy correlated beams at frequency $\omega_1 = \omega_0/2+\omega$ and $\omega_2 = \omega_0/2-\omega$, with ω a multiple of the OPO free spectral range (FSR). In our study, where we limit ourselves to the frequency degenerate case, i.e. $\omega = 0$, narrow-band filtering has to be performed on the heralding photons.

Our procedure for spectral filtering is presented in Figure 2.8. The OPO generates frequency modes separated by its free-spectral range FSR_{OPO} of about 4.3 GHz, and a width given by the OPO bandwidth $\gamma_{OPO} = 60$ MHz. The first stage of the filtering is performed by a commercial interferential filter (IF) (**Barr associates**) centered at 1064 nm with a bandwidth of 125 GHz (i.e. 0.5 nm). This filter has a transmission of 80% at 1064 nm. As can be seen, the IF is not narrow enough and still transmits about 60 FSRs of the OPO. The filtering is improved by using a second filtering stage based on a home-made Fabry-Pérot micro-cavity (μcavity). The μcavity is designed so that the free spectral range is a least two times the one of the IF, i.e. $\mathrm{FSR}_{\mu cavity} \geq 250$ GHz. Such a large FSR

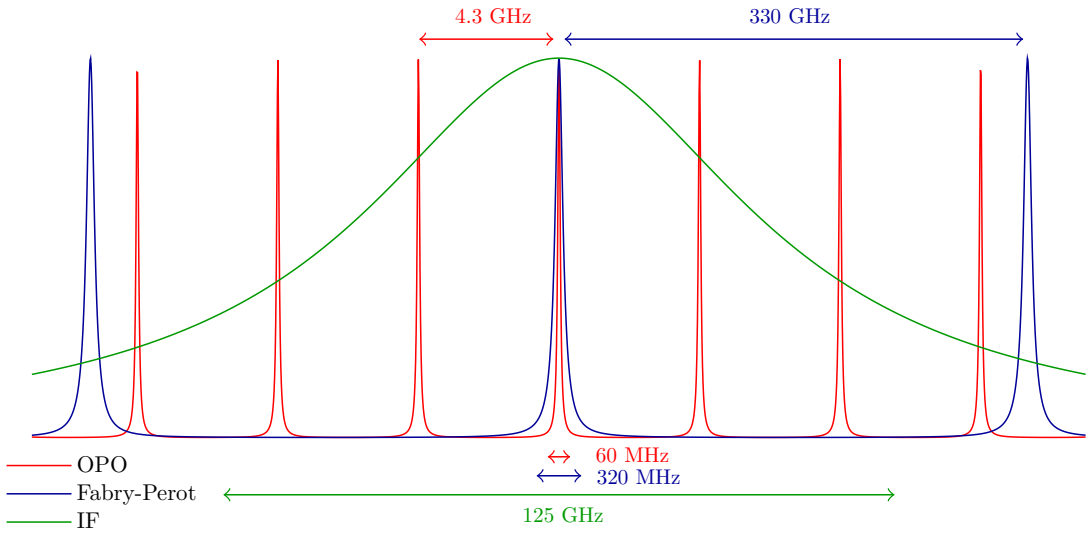

Figure 2.8: **Spectral filtering.** (Not to scale) The down-converted beams are emitted from the OPO in several FSR separated by 4.3 GHz. The non frequency-degenerate photons are first filtered using an interferential filter (IF) with a bandwidth of 0.5 nm. The second-stage of the filtering is performed by a home-made micro-cavity with a bandwidth four times larger than the OPO bandwidth and a FSR of 330 GHz.

imposes a cavity length below 0.5 mm, which gives the cavity its name. Then we want a μcavity bandwidth about four times larger than the OPO bandwidth to ensure that the degenerate modes are transmitted correctly. This imposes a constraint on the total mirror transmission $T_{\mu cav}$, considering $\text{FSR}_{OPO} \gg \gamma_{\mu cav} \geq 4\gamma_{OPO}$ with $\gamma_{\mu cav} = \text{FSR}_{\mu cav}.T_{\mu cav}/\pi$ gives $10\% \gg T_{\mu cav} \geq 0.6\%$. We thus choose for each mirror a transmission $T_{\mu cav}/2 = 0.3\%$, ensuring at the same time maximum rejection of the other frequency modes. The mirrors are provided by the company **ATFilms**.

The home-made μcavity is built in a monolithic configuration. The building of such cavities is rather challenging considering the small cavity size and that the cavity alignment cannot be settled once the cavity is closed. For a cavity length of 0.45 mm, we measure an FSR of 330 GHz and a bandwidth of 320 MHz. The transmission of the cavity is about 60%. We note that for each independent SNSPD that is used, a dedicated filtering system as to be installed. During this work we built a third micro-cavity presented in **Appendix C**.

2.5.2 Post-detection signal processing

The voltage pulse emitted by the SNSPDs cannot be directly used to trigger the experiment and need to be amplified. In our case we amplify the pulse at room temperature following a circuit design from NIST [7]. A radio-frequency bias-tee (**Minicircuits ZFBT-4R2GW+**) enables the application to the SNSPD of a bias current produced

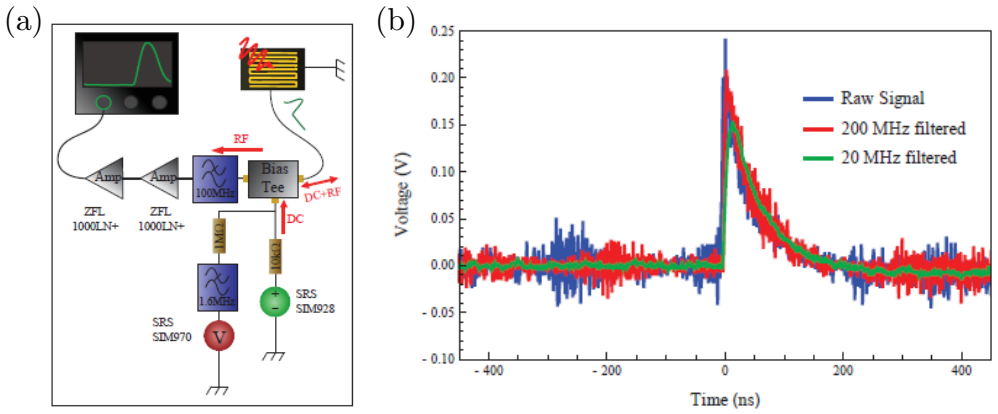

Figure 2.9: **SNSPD signal amplification.** (a) Scheme of the electrical circuit used to recover the pulse. A small DC current is sent via a stable voltage source to the detector. The current sent do the detector is measured by a voltmeter that enables to check that the detector stays in its superconducting state, i.e. that it does not become resistant under the application of the DC current. The voltage pulse resulting on the absorption of a photon is a high frequency signal. This signal (in green) is recovered thanks to a bias tee. The signal is frequency-filtered using a 100 MHz low pass filter, and then amplified using two amplifiers of 24 dB gain each. (b) Voltage pulse of the SNSPD amplification for different numerical low pass filter bandwidths. It shows a rising time, or jitter, of a few tens of picosecond with a dead time of about 200 ns. In practice we employ a low-pass filter up to 20 MHz to smoothen the triggering.

by isolated voltage sources (**Standford Research Systems SIM 928** - 1 mV on the voltage source corresponds to 0.1 μA in current). The output signals are first filtered at 100 MHz (**Minicircuits BLP-100+**) and amplified with a series of two 24 dB amplifiers (**Minicircuits ZFL-1000 LN+**). A digital voltmeter (**Standford Research Systems SIM 970**) is used to monitor the state of the SNSPDs. The amplified pulses are sent to the measurement system through 10-m long BNC cables. The BNCs capture ambient noise that is filtered before detection with a 20 MHz low-pass filter, either internally (**Teledyne Lecroy Waverunner 6Zi**) or analogically (**Crystek Corp. CLPFL-0021-BNC**). The electronic circuit and traces of voltages pulses are shown in Figure2.9.

2.6 Towards photon-number resolving detectors ?

In our operational regime, the superconducting nanowire single-photon detectors have only two possible outcomes. Either no photon is detected, corresponding to the output *off* and the projection on vacuum state $\hat{\Pi}_{off} = |0\rangle\langle 0|$. The second outcome, called *on* corresponds to the detection of anything-but-vacuum, i.e. the detection of at least one photon. The corresponding projector is thus the projection on all other Fock state $\hat{\Pi}_{on} = \mathbb{1} - \hat{\Pi}_{off} = \sum_{n=1}^{\infty} |n\rangle\langle n|$.

In practice, the detector have a limited system detection efficiency, or equivalently

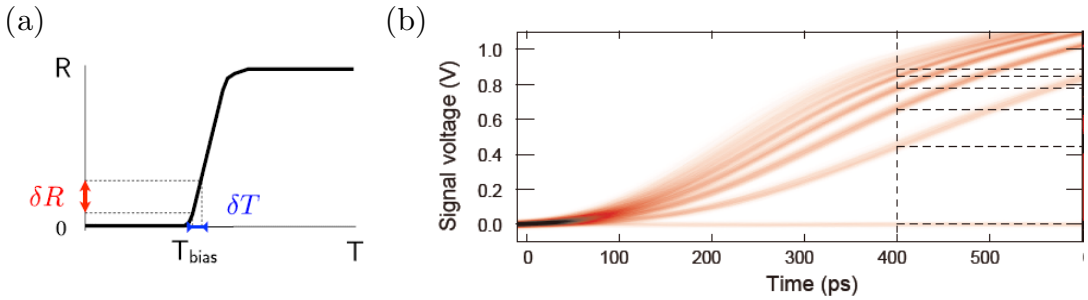

Figure 2.10: **Photon-number resolving detection.** (a) From [165]. Working principle of a superconducting transition edge sensor. The system is temperature biased at the edge of the superconducting-to-normal transition at about $T_{bias} \sim 100$ mK. Any photon absorption leads to an increase of the temperature by δT which corresponds to a measure resistance δR. The resistance measured then depends on the number of photon absorbed. The maximum photon number is limited by the saturation of the edge. (b) From [166]. Overlay of oscilloscope traces measured by a DC-biased single nanostrip detector. When the wavepacket is shorter than the hotspot relaxation time, several photon absorption lead to an increased resistance at short scale, that can be precisely measured to distinguish the photon number.

the detected photons are subject to transmission losses before the SNSPD. Taking into account the limited efficiency of the heralding path η_{herald} leads to a refinement of the model to:

$$\hat{\prod}_{off} = \sum_{n=0}^{\infty} (1 - \eta_{herald})^n \left|n\right\rangle \left\langle n\right| . \tag{2.23}$$

The probability of receiving an answer *on* for an input Fock state $|n\rangle$ is thereby $1 - (1 - \eta_{herald})^n$.
The SNSPDs are thus fundamentally unable to distinguish between single or multi-photon components, with the contributions from the different components evolving non-linearly depending on the state. As we will see later, this becomes a very limiting factor in the teleportation protocols implemented, where multi-photon events contaminate the teleportation with unwanted contributions.

To circumvent these limitations, a new generation of single-photon detectors are developed. These detectors are able to distinguish the different photon components and are thus called *photon-number resolving detectors* (PNRD). They can, in principle, perform the projection on any chosen Fock state $|n\rangle \langle n|$.

Several technique are used to implement these detectors. A first strategy consists in multiplexing single-photon detectors either spatially [159, 160, 161] or temporally [162, 163]. These methods can achieve compact photon-number resolving performance yet they are theoretically limited by the system detection efficiency of the independent detectors, and unrealistic system detection efficiencies close to 100% are required to perform efficient photon-number projection [164].

Other types of single-photon detectors, such as *superconducting transition edge sensors* (TESs) can naturally discriminate the photon number of the detected Fock state [167, 165]. Their operating principle is rather different to the one of the SNSPDs. A TES can be considered as a photon absorber than is maintained by a negative electro-thermal feedback [168] within its superconducting-to-normal transitions. When an incident photon is absorbed, it produces a photo-electron that heats up the TES and gives rise to an increased of the resistance of the TES, as can be seen in Figure 2.10 (a) . The more photon absorbed the larger the temperature rise and thus the measured resistance. The detector saturates upon reaching the top of the steep transition slope. Such devices are thus able to distinguish between zero-to-five photon Fock states with a quantum efficiency above 90%, which makes them as ideal candidates for PNRD. Yet the technology is currently limited by its time performance. As compared to SNSPDs, the TESs have a temporal resolution at most 100 times larger (about 10-100 ns) with a cooling decay tail of several microseconds. Such detectors could in theory be compatible with our experimental setup, but their require on top a much more stringent cryogenic environment at about 100 mK to operate and superconducting quantum interference device (SQUID) [169] for the read-out. For that reason, only a very limited number of groups can afford such detectors.

Finally photon-number resolution can be performed on a single SNSPD under specific conditions. The methods consists in biasing the detector in its superconducting state and looking directly at the hotspot when multiple photons are injected within its relaxation time - typically of 100 ps - [170, 166]. At this scale, when several photons are detected, several hotspots are simultaneously created along the nanostrip and the resistance of the nanostrip depends on the number of incident photons. After several hundreds of picosecond cooling of the subtrate dominates and the detector recovers its superconducting state. Traces of such detectors are shown in Figure 2.10 (b). The SNSPD can in that sense be seen in itself as a highly multiplexed single-photon detector. Even though this techniques looks appealing, it requires the detected photons to be contained in ultra-short wavepackets (of a few tens of picoseconds) and an ultra low-noise readout circuit that enables to distinguish the meagre resistance variations. Such a technique is at the moment not compatible with our experiment where the photon wave-packets are several nanoseconds long.

3 Conclusion

We have here introduced the main two experimental resources for non-Gaussian quantum state engineering. First semi-monolithic optical parametric oscillators enable the generation of high squeezing owing to their very large escape efficiency. Second, superconducting nanowire single photon detectors can be employed to perform probabilistic photon subtraction to produce non-Gaussian states. These detectors, placed in a cryogenic environment at 1.7 K, show record system detection efficiencies with minimum dark count rate. In the next chapter we will study how the combination of these experimental tools can lead to the generation of discrete- and continuous-variable quantum states, respectively single photon Fock states and optical Schrödinger cat states, and the creation of optical hybrid entanglement, which is the non-Gaussian resource at the heart of this thesis.

Chapter 3

Quantum state engineering: from single-mode quantum states to optical hybrid entanglement

With the experimental resources for optical quantum state engineering in hand, we present the methods for the generation of discrete-variable (DV) and continuous-variable (CV) non-Gaussian quantum states. These states are generated by combining either the type-II or the type-I optical parametric oscillators (OPOs) with a heralding on a superconducting nanowire single-photon detector (SNSPD). We detail the experimental setup implemented in free-space with minimum losses. Each time, we introduce the theoretical and experimental tools required for the understanding of the process. In addition we test the ability of our heralded single photons to follow extreme multi-photon interference, with a benchmark called Fock-state bunching capability that we developed in collaboration with the group of Radim Filip at Olomouc University, the results of which have been published in *Optica* [15]. In the last section we present the generation and engineering of hybrid entanglement between DV and CV optical qubits. The detailed theoretical analysis we developed during this thesis has been published in *New Journal of Physics* [13].

1 DV: Experimental Fock-state generation

In this section we present the protocol for the generation of optical Fock states from a type-II phase-matched OPO. We show how we can reach high purity of the created states thanks to the high escape efficiency of the OPO.

1.1 Fock-state decomposition of two-mode squeezed vacuum

The two-mode squeezed vacuum state at the output of the type-II OPO can be written in the Fock basis as:

$$|\psi\rangle_{AB} = (1-\lambda^2)^{1/2} \sum_{n=0}^{\infty} \lambda^n |n\rangle_A |n\rangle_B \,, \tag{3.1}$$

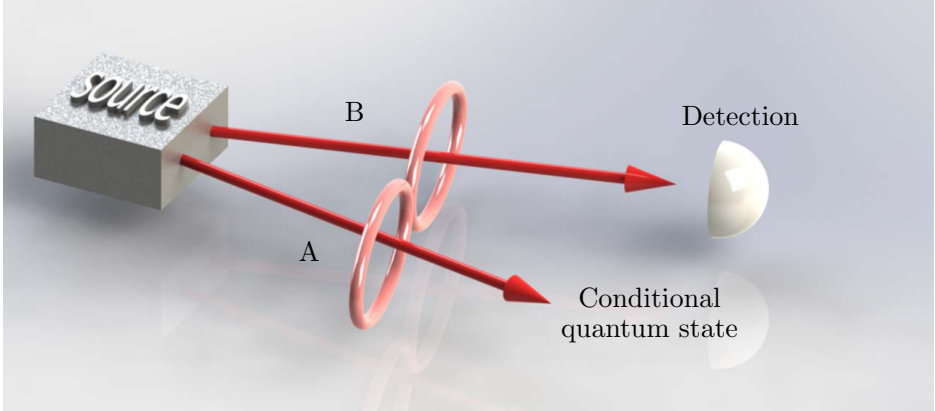

Figure 3.1: **Conditional state preparation technique.** A measurement performed on one mode B of an entangled state heralds the preparation of a conditioned state in mode A.

with $\lambda = \tanh(r)$, and r corresponds to the squeezing parameter.

This expression represents the creation of the signal and idler photons from SPDC in the two non-degenerate polarization modes A and B respectively. The two polarization modes are separated into two spatial modes using a polarizing beamsplitter (PBS) and the mode B is sent to the photon detection. Since the states are photon-number correlated, the detection of $|n\rangle\langle n|$ in mode B will *herald* the presence of the state $|n\rangle$ in the twin mode A. As schematized in Figure 3.1, the generation of the desired state in mode A is thus *conditioned* on the correct detection in mode B. The mode B will thus be called *conditioning mode* in the following.

In practice, however, the conditioning path is subject to transmission losses, and the detection on the SNSPD does not resolve the photon number. The strategy has thus to be adapted to create the desired Fock states with maximum purity.

The purity to the single-photon target state $|1\rangle$ can be optimized by reducing the pump of the OPO. Indeed, the probability of creating n pairs scales with the pump intensity to the nth power:

$$|\psi\rangle_{AB} \propto |0\rangle_A |0\rangle_B + \lambda |1\rangle_A |1\rangle_B + \lambda^2 |2\rangle_A |2\rangle_B + ... + \lambda^n |n\rangle_A |n\rangle_B , \tag{3.2}$$

It is thus important to lower the pump power as much as possible to lower the probability of generating multi-photon events. Still, a consequence of lowering λ is a reduction of the generation rate, which scales linearly with the pump power. We thus have to find a compromise between state purity and heralding rate. It is notable yet to see that a pumping power tending to zero does not necessary lead to a high purity state. Indeed as the pumping power is reduced, other effects such as back-scattering and dark counts, that are typically negligible, start to contribute significantly to the quality of the generated state.

Although this method is quite efficient for the generation of small Fock states, the

requirements for the state generation become more stringent as the target Fock size increases. Our lab has implemented a protocol for the generation of a two-photon Fock state [8]. In that case the detection of the state $|n\rangle$ in the heralding mode was mimicked by splitting the heralding path in n branches at the end of which a detector is placed. This setting drastically reduces the generation rate, and as the SNSPDs are not photon-number resolving, the pump power as to be reduced even more to obtain a reasonable state purity. Also the effect of loss on the heralding path becomes very limiting since attenuated higher photon number component can be detected, leading to the measurement of false events. It thus seems that extending this scheme to higher Fock states is still challenging currently.

1.2 State heralding and temporal mode

Since the SPDC process is by essence stochastic, the detection of an event in the conditioning mode will lead to the concurrent creation of a state in the signal mode at a specific time and with a specific probability distribution. Indeed, due to the finite bandwidth of the OPO cavity, the signal and idler photons can emerge from the source at slightly different times. The lifetime of the down-converted photon in the cavity is directly related to the OPO bandwidth γ_{OPO}. Assuming the SPDC has happened at time $t = 0$, the probability for each down-converted photon to remain inside the cavity after time t is given by [171]:

$$p(t) = 2\pi\gamma_{OPO}e^{-2\pi\gamma_{OPO}t}. \tag{3.3}$$

Conversely, the probability of detecting a signal or idler photon at $t_{s,i}$ given that SPDC occurred earlier at $t \leq t_{s,i}$ is given by $p(t_{s,i} - t)$.

Fixing the detection of the conditioning event at $t_i = 0$, the probability of detection a photon in the signal mode, $p'(t_s)$, at t_s is obtained by integrating all the events occurring before $t_{s,i}$, i.e

$$p'(t_s) = \int_{-\infty}^{min(t_i,t_s)} p(t_i - t)p(t_s - t)dt = \int_{-\infty}^{min(0,t_s)} p(-t)p(t_s - t)dt, \tag{3.4}$$

with the integration ending at $min(t_i, t_s)$ to ensure that SPDC has occurred before both the signal or idler photons.
Replacing $p(t)$ by its expression, we finally get:

$$p'(t_s) = \pi\gamma_{OPO}\left[e^{4\pi\gamma_{OPO}t}\right]_{-\infty}^{min(0,t_s)} e^{-2\pi\gamma_{OPO}t_s} = \pi\gamma_{OPO}e^{-2\pi\gamma_{OPO}|t_s|}. \tag{3.5}$$

Thus the detection of a idler photon in a time interval much smaller than the cavity lifetime - this is true because the lifetime of the micro-cavity *and* the jitter of the SNSPD are small relative to the OPO cavity lifetime - heralds the presence of a signal photon with the probability $p'(t)$.

In practice yet, we typically do not work by considering probabilities of presence, but by considering *temporal modes*, which are sets of orthogonal temporal wavepackets that can be used to represent the field. In the Heisenberg representation, taking into account

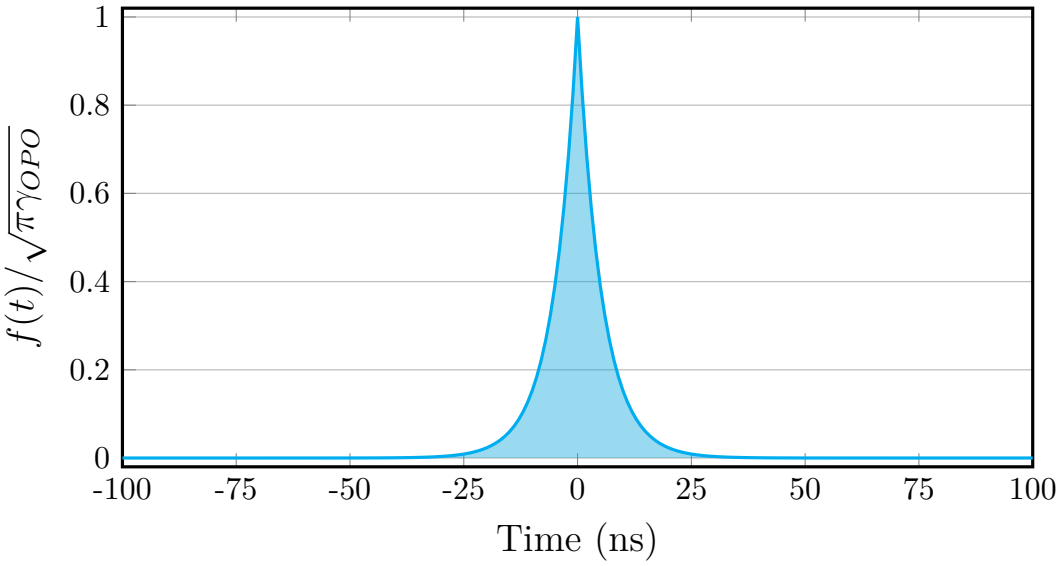

Figure 3.2: **Theoretical temporal mode.** Temporal mode extracted from Eq.(3.7) with $\gamma_{OPO} = 60$ MHz. The temporal mode has a width at half maximum of about 20 ns around the heralding event located at $t = 0$.

the temporal modes $f(t)$ weight the different elements of a set creation operators $\hat{a}^\dagger(t)$ applied at different times:

$$\hat{a}_f^\dagger = \int_{-\infty}^{+\infty} f(t)\hat{a}^\dagger(t)dt. \tag{3.6}$$

The temporal mode function $f(t)$ is directly linked to the probability of measuring a signal photon $p'(t)$ under the relation $|f(t)|^2 = p'(t)$, which gives:

$$f(t) = \sqrt{\pi\gamma_{OPO}}e^{-\pi\gamma_{OPO}|t|}. \tag{3.7}$$

Similarly, the characterization of the quantum states need to take into account the temporal mode structure. In particular in the case of a continuous measurement of the field quadrature $\hat{q}_\theta(t) = \hat{x}(t)\cos\theta + \hat{p}(t)\sin\theta$, this corresponds to the application of the temporal mode directly on the quadratures, to obtain for each heralding event the *quadrature value*:

$$\hat{q}_{\theta,f} = \int_{-\infty}^{+\infty} f(t)\hat{q}_\theta(t)dt. \tag{3.8}$$

Thus the temporal mode amounts to a specific definition of the wavepacket in time. It can be seen in different ways. It either amounts to considering the application of the creation operator in a specific time window, or the application of the measurement in the relevant mode. Note that each time, from a time-varying continuous quantity we obtain, from the application of the temporal mode, a value independent of time.

In practice, the expression of the temporal mode given in Eq. (3.7) is not exactly suited to our experimental states since it neglects the effect of the finite detection bandwidth and

the jitter of the SNSPDs. Hopefully, and as we will see later, its is possible to measure experimentally the temporal mode shape of the states and thus estimate experimental imperfections. We measure in practice an overlap between experimental and theoretical temporal mode above 99% [172]. It is important for the state reconstruction to consider the correct experimental temporal mode since a mode mismatch is directly equivalent to detection losses. The temporal mode of the generated states does not only depend on the parameters of the sources but also on their design. We note that in [173], single photons with exponentially rising temporal modes can be obtained from a singly-resonant asymmetric OPO.

1.3 Experimental setup for heralded single photon generation

Having understood the principle of conditional preparation in the relevant temporal mode, we present the experimental setup for the creation of high purity single-photon Fock states. It is shown in Figure 3.3.

Laser and pumping. In the whole thesis we work with a dual-output continuous-wave Nd:YAG laser (**Innolight GmbH Diabolo**). The system outputs about 300 mW of infrared at 1064 nm. It is frequency doubled to produce about 600 mW of green at 532 nm. The green light is used as a pump for the different optical parametric oscillators. This beam is modulated at 12 MHz. The infrared beam is used as a *seed beam*. It is first filtered with a mode-cleaning ring cavity, locked on resonance via tilt locking [174], and then sent on the experiment for different purposes. It is passed through the OPO cavities to enable the setting of the different resonances and acts as a phase reference. The seed beam also serves as an alignment beam and is used to lock the different cavities or optical paths before the measurement. The seed beam at 1064 nm is finally employed as a local oscillator (LO) for the different homodyne detections.

Type-II OPO. The triply-resonant OPO is composed of type-II KTP crystal in a semi-monolithic configuration as presented earlier. We pump the OPO with 1 mW of green at 532 nm, which is far below the oscillation threshold estimated at 80 mW. The triple resonance is adjusted to have the pump and the two down-converted fields in orthogonal polarizations resonant in the cavity. The resonance of the pump is ensured by adjusting the length of the cavity by moving the output mirror mounted on a piezo-electric actuator (PZT). The OPO is locked on resonance of the pump with the *Pound-Drever-Hall* (PDH) technique: the reflection of the pump beam on the input mirror is measured on a photodiode (**Thorlabs PDA8A2**) and mixed (**Minicircuits ZLW-6+**) with the laser reference signal at 12 MHz. The demodulated RF signal is used as an error signal for a home-made *Proportional Integral Derivative* (PID) control.

Digital lockings. Apart from the mode cleaner and the OPO pump resonance which are locked using analog systems, the various lockings on the experiment are performed digitally using micro-controller units (MCUs) [10]. We employ two different MCUs: the ADUC7020 from **Analog Devices** and the Arduino Due board from **Arduino**. They

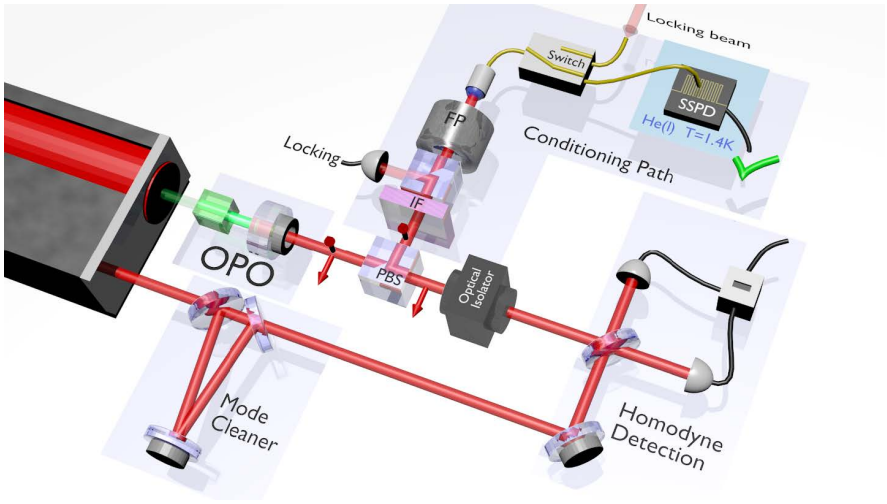

Figure 3.3: **Experimental setup for the generation of single-photon Fock states.** The type-II semi-monolithic OPO is pumped by a frequency-doubled beam at 532 nm originating from a Nd:YAG laser. The signal and idler photons at 1064 nm are separated on a polarizing beamsplitter (PBS). The idler photons are spectrally filtered with first an interferential filter (IF) and then a home-made Fabry-Pérot (FP) cavity, before being sent to a SNSPD placed in a cryogenic environment. The signal beam is sent to a high-efficiency homodyne detection for state characterization by single-mode quantum state tomography. A mode-cleaned seed beam at 1064 nm is used to adjust the triple resonance of the OPO, to lock the cavities, and as a local oscillator for the homodyne detection. The locking of the cavities is performed in a sampling-and-hold fashion. First the seed beams are sent in a 50 ms period to lock the cavities with the path to the SNSPD closed, then the locks are maintained for 50 ms with the seed beams blocked and the path to the SNSPD opened.

provide 12-bit of resolution analog-to-digital (ADC) and digital-to-analog (DAC) converters. Such a resolution is sufficient to lock interference fringes and medium finesse (up to 200) cavities. They are easy to program and cost efficient. In particular the seed that is passed through the OPO cavity is locked in phase with the pump beam. This is done by probing the parametric amplification of the seed by the pump and digitally locking on resonance by adjusting the phase of the seed with a piezo-electric transducer along its optical path before the OPO.

Conditioning path. The signal and idler modes from the type-II OPO are separated using a polarizing beamsplitter. The idler mode is sent to an SNSPD for heralding. The heralding photons are filtered with first a commercial interferential filter and then a home-made Fabry-Pérot micro-cavity as presented earlier. The micro-cavity, which has a finesse of about 1000, is locked digitally on resonance by adapting the algorithm of the MCU. Indeed with a finesse of 1000, the number of sample of the peak is about $4096/1000 \sim 4$ which does not offer a proper resolution. This resolution can be increased by coupling

two MCUs to increase the resolution from 12 to 24 bits. Another technique we employed consists in splitting the digital locking in two segments. First a coarse sweep is applied to locate the resonance of the cavity with low resolution, then the sweep is centered around the peak position and the sweep amplitude is reduced is order to increase the locking resolution. Using that technique, we can lock the micro-cavity on resonance with a phase noise of about 3% [10].

Measurement sequence. Because their power is too important and would saturate the SNSPD, the seed beam paths cannot be opened when the non-Gaussian states are heralded. We therefore have to perform the measurement in sequence. First, a *sampling* sequence is performed to reset the locks with the paths to the SNSPDs closed, followed by a *holding* sequence where the seed beams are blocked and the paths to the SNSPDs are opened. During the holding sequence, the locks are maintained at their position of the previous sampling sequence. It is thus important to have the experiment stable for at least the duration of the holding sequence otherwise the phase definition can be blurred. Yet having the holding sequence too short increases drastically the overall experimental duration. The compromise reached is to cycle 50 ms of sampling time and 50 ms of measurements.

The shutting of the corresponding beam is performed using mechanical shutter heads (**SRS 475** and **SRS 470**). They are triggered by a delay generator (**SRS DG645**) to open or close depending on the sequence. They have a rising time of 5 ms. They are installed on home-made heavy mount to decouple the mechanical vibrations to the experimental table.

After presenting of the experimental setup for the production of heralded single photons we detail the data acquisition enabling to recover, from homodyne detection measurements, the complete density matrix of the state by quantum state tomography.

1.4 Measurement, data acquisition and analysis

Homodyne detection. The characterization of the quantum states is performed using a home-made balanced homodyne detection setup represented in Figure 3.4. It consists in mixing the signal mode $\hat{a}_s$ to-be-measured with a bright coherent state $\hat{a}_{LO} \approx |\alpha_{LO}|e^{i\theta_{LO}}$, called *local oscillator*, on a 50:50 beamsplitter and then sent on two photodiodes labeled 1 and 2. The state after mixing is given by:

$$\begin{aligned} \hat{a}_1 &= \frac{1}{\sqrt{2}}(\hat{a}_{LO} + \hat{a}_s), \\ \hat{a}_2 &= \frac{1}{\sqrt{2}}(\hat{a}_{LO} - \hat{a}_s). \end{aligned} \tag{3.9}$$

The photocurrents $\hat{i}_{1,2}$ measured on the photodiodes are proportional to the number operator, i.e. $\hat{i}_{1,2} \propto \hat{n}_{1,2}$ (in the ideal case, one photon gives one electron), with:

$$\hat{n}_{1,2} = \left[\hat{a}_{LO}^\dagger \hat{a}_{LO} + \hat{a}_s^\dagger \hat{a}_s \pm \hat{a}_{LO}^\dagger \hat{a}_s \pm \hat{a}_s^\dagger \hat{a}_{LO}\right]/2, \tag{3.10}$$

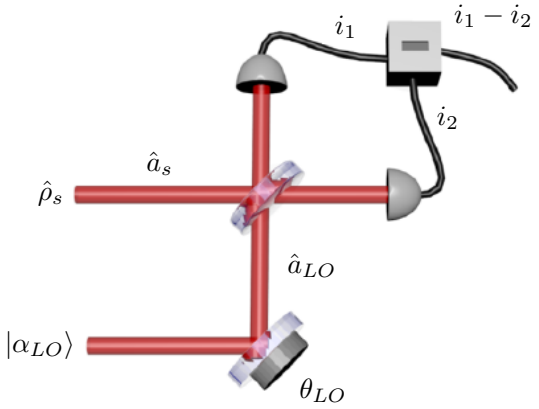

Figure 3.4: **Homodyne detection.** An incident signal quantum state $\hat{\rho}_s$ is mixed on a 50:50 beamsplitter with a bright coherent-state local oscillator $|\alpha_{LO}\rangle$. The output modes are sent to two photodiodes that provide a photocurrent proportional to the field's photon number. The subtraction of the two photocurrents gives the measurement of one quadrature of the state $\hat{\rho}_s$ at the phase of the local oscillator θ_{LO}.

so that the subtraction the photocurrents yields:

$$\hat{i}_1 - \hat{i}_2 \propto \hat{a}_{LO}^\dagger \hat{a}_s \pm \hat{a}_s^\dagger \hat{a}_{LO} \approx |\alpha_{LO}| e^{-i\theta_{LO}} \hat{a}_s + |\alpha_{LO}| e^{i\theta_{LO}} \hat{a}_s^\dagger. \tag{3.11}$$

The measured photocurrent thus gives:

$$\hat{i}_1 - \hat{i}_2 \propto |\alpha_{LO}| \hat{q}_{\theta_{LO}}, \tag{3.12}$$

which is directly the measurement of the quadrature of the signal mode $\hat{q}$ along the phase of the local oscillator θ_{LO}.
Homodyne detection is thus a phase-sensitive measurement technique. Changing the phase at which the incident field is measured is directly done by sweeping the local oscillator path with a piezo-electric actuator.

Our home-made homodyne detection is composed of two InGaAs photodiodes from **Fermionics** that can reach quantum efficiencies above 97% at 1064 nm. The subtraction of photocurrent is performed in a trans-impedance scheme with a home-made circuit [149]. The bandwidth of the detector is about 60 MHz. For the local oscillator, we use 6 mW of the seed beam at 1064 nm. This local oscillator power gives a shot noise 21 dB above the electronic noise at the central frequency of 5 MHz, which corresponds to 4% of equivalent loss [175]. Because of the linear cavity design of the OPO, an optical isolator (**Qioptiq LINOS FR-1060-5SC**) has to be inserted between the OPO and the homodyne detection to prevent the backreflections on the photodiodes or the surface of the optics to be reflected in the conditioning path. This ultimately leads to transmission losses. Overall, taking into account all sources of noise amounts to a homodyne detection efficiency of 85%. In practice, it is possible to take into account the detection losses in the measurement to correct from

them. This is valid as long as homodyne detection is used to characterize a state that would be available for subsequent operations or protocols, and not if it used to perform non-local operations.

Data acquisition. The quadratures from the homodyne detections are recorded on a high definition oscilloscope (**Lecroy Waverunner 6Zi**). The device possesses a sample rate of 20 GS/s, which enables the resolution of the traces at the nanosecond scale. From each heralding event corresponding to the detection of a single photon on a SNSPD, a voltage pulse is used to trigger the recording of the homodyne traces. The sample-and-hold cycle is included in the trigger setting to discard the events that occur outside of the measurement sequence. Given the width of the temporal mode, the traces can be neglected outside a window of about 50 ns around the event of interest. Depending on the delay between the heralding and the arrival of the signal photon to the homodyne detection, the recording window can range between 200 ns and 900 ns prior the trigger pulse. The heralding rate is measured by counting the number of clicks detected in the 50 ms holding sequence. Typically for a pump power of 1 mW, we observe a heralding rate of about 250 kHz. 50 000 heralding events are accumulated for the state characterization for a single-mode quantum state. The total data acquisition for a single-photon Fock state is thereby of a few minutes.

Temporal-mode measurement. As we have seen earlier it is important to measure the temporal mode of the state to-be-characterized prior to processing the quadrature measurements. Our technique for the measurement of the temporal mode consists in looking at the variance of the measured quadrature $\langle \hat{q}_\theta^2 \rangle$. Indeed the variance of a single photon is three times larger than the one of vacuum $\langle \hat{q}_\theta^2 \rangle_{|1\rangle} = 3\langle \hat{q}_\theta^2 \rangle_{|0\rangle} = 3\sigma_0^2$, where σ_0^2 is defined as the *variance of vacuum*. So that the detection of a higher variance of the quadratures in time gives a good estimate of the distance to the temporal mode of the state. Such a technique can be used to find the center of the temporal mode. We show in Figure 3.5 the experimental measurement of $\langle \hat{q}_\theta^2(t) \rangle$. The peak increases when the single photon is measured. Such a technique is used to calibrate the delays between the different heralding events and the recorded homodyne signals.

Data processing. From the estimation of the temporal mode presented before, we can associate to each heralding event and homodyne trace the quadrature value $\hat{q}_{\theta,f}$ following Eq.(3.8). Yet there is a final step to take into account. Indeed the quadratures measured on the homodyne detection are amplified by the local oscillator. From one measurement to the other, the amplitude of the local oscillator $|\alpha_{LO}|$ and so of the measured quadrature values $\hat{q}_{\theta,f}$ can vary. It is thus important to normalize the quadrature results to the local oscillator power. This is done by measuring the variance of the vacuum state prior the measurement of the single photon, and normalizing the quadrature values by the variance of vacuum. In practice this is done by recording 40 000 quadratures for vacuum - i.e. shutting off the path to the homodyne detection - to calculate the variance of the vacuum state $\langle \hat{q}_\theta^2 \rangle_{|0\rangle}$.

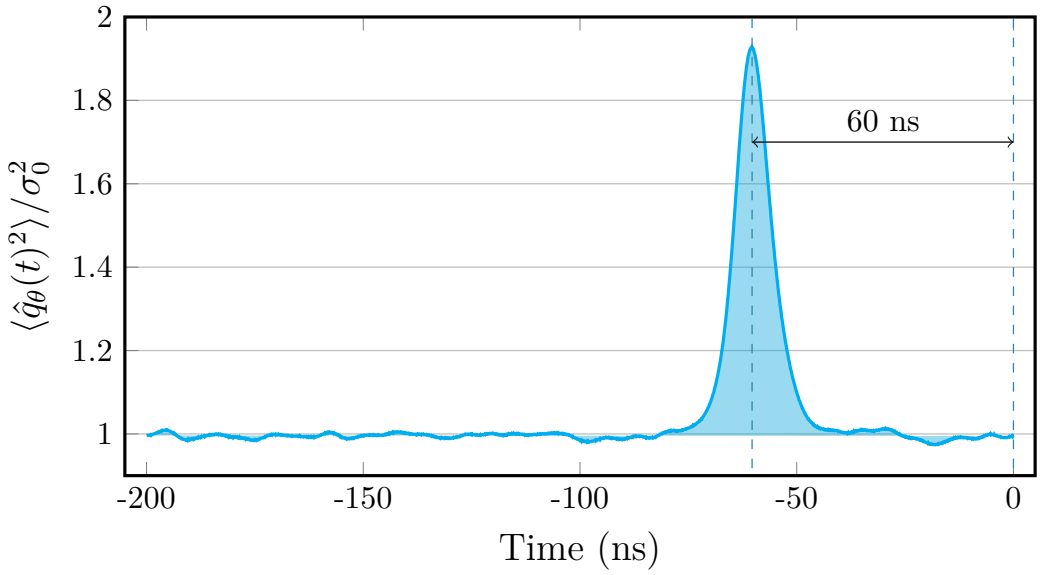

Figure 3.5: **Example of experimental temporal mode.** Variance of the homodyne signals normalized to vacuum as a function of time. The detection event occurs on the SNSPD at $t = 0$. The variance increases after a delay of 60 ns inside the 200 ns homodyne trace, with a typical width of about 40 ns. This allows to center the position of the temporal mode for the data pre-processing. This is to be compared to the theoretical temporal mode given in Figure 3.2.

The overall quadrature data processing does then correspond to the association of a quadrature value $q_f^{(n)}$ to each heralding event n, noting that $\hat{q}_{\theta,f} |q, \theta\rangle = q_f |q, \theta\rangle$:

$$q_f^{(n)} = \frac{1}{\sqrt{\langle \hat{q}_\theta^2 \rangle_{|0\rangle}}} \int_{-\infty}^{+\infty} f(t) q^{(n)}(t) dt \tag{3.13}$$

where $q^{(n)}(t)$ is the time-varying raw homodyne data - or trace - corresponding to the heralding event n, $f(t)$ the temporal mode of the measured state, and $\langle \hat{q}_\theta^2 \rangle_{|0\rangle}$ the variance of vacuum.

As we will detail in the next section, we can, on top of this, associate to each heralding event n the corresponding phase of local oscillator $\theta_{LO}^{(n)}$ at which the state is measured. This is not relevant for Fock states which are phase-invariant but it will be important for qubits or squeezed states. The final pre-processed data set in thus represented by a table $\{n, q_f^{(n)}, \theta_{LO}^{(n)}\}$

State reconstruction. The final state of the data processing is the state reconstruction by *Maximum-Likelihood* optimization [176]. It provides from the data $\{n, q_f^{(n)}, \theta_{LO}^{(n)}\}$ the density matrix of the state measured by the homodyne detection in the temporal mode

considered. Maximum Likelihood has become a standard procedure for the reconstruction of quantum states from tomographic measurements since it offers the advantage of outputting a physical state as a result with high accuracy and of correcting for losses.

From a set of data $\{n, q_f^{(n)}, \theta_{LO}^{(n)}\}$ of N quadrature measurements, the algorithm computes the *likelihood function* $\mathcal{L}(\hat{\rho})$ defined as:

$$\mathcal{L}(\hat{\rho}) = \prod_{n=1}^{N} \mathrm{Tr}\Big(\hat{\rho} \left|q_f^{(n)}, \theta_{LO}^{(n)}\right\rangle \left\langle q_f^{(n)}, \theta_{LO}^{(n)}\right| \Big). \tag{3.14}$$

This function represents the product of probabilities of observing each positive operator-valued measure (POVM) $\left|q_f^{(n)}, \theta_{LO}^{(n)}\right\rangle \left\langle q_f^{(n)}, \theta_{LO}^{(n)}\right|$ when starting from a state $\hat{\rho}$.
The Maximum-Likelihood procedure consists in exploring different quantum states $\hat{\rho}_i$ in a Hilbert space of dimensions d starting from the state $\hat{\rho}_0 = \frac{1}{d}\mathbb{1}$, and finding the state $\hat{\rho}_{ML}$ that maximizes $\mathcal{L}$. For each iteration, the new normalized density matrix is computed recursively following the expression:

$$\hat{\rho}_{n+1} \propto \hat{R}(\hat{\rho}_n)\hat{\rho}_n\hat{R}(\hat{\rho}_n), \tag{3.15}$$

with the projectors $\hat{R}(\hat{\rho}_n)$ defined as:

$$\hat{R}(\hat{\rho}_n) = \sum_{n=1}^{N} \frac{\left|q_f^{(n)}, \theta_{LO}^{(n)}\right\rangle \left\langle q_f^{(n)}, \theta_{LO}^{(n)}\right|}{\mathrm{Tr}\Big(\hat{\rho} \left|q_f^{(n)}, \theta_{LO}^{(n)}\right\rangle \left\langle q_f^{(n)}, \theta_{LO}^{(n)}\right| \Big)}. \tag{3.16}$$

Under the assumption that the algorithm converges in a reasonable amount of time, it leads to the state $\rho_{\hat{ML}}$ such that:

$$\hat{\rho}_{ML} \propto \hat{R}(\hat{\rho}_{ML})\hat{\rho}_{ML}\hat{R}(\hat{\rho}_{ML}), \tag{3.17}$$

or equivalently

$$\hat{R}(\hat{\rho}_{ML}) \to \mathbb{1}. \tag{3.18}$$

In practice, we define an error threshold from which the algorithm has converged. The dimension of the Hilbert space d is set to be larger than the expected state dimension. In practice for the reconstruction of a single photon, a Hilbert space of dimensions 1+4 is considered (where 1 stands for vacuum and 4 for the following photon numbers), and the number to iterations set for convergence for single-mode reconstruction is about 150. The procedure for correction of the losses amounts to modify the projectors $\left|q_f^{(n)}, \theta_{LO}^{(n)}\right\rangle \left\langle q_f^{(n)}, \theta_{LO}^{(n)}\right|$, effectively changing the measurement into lossy quadrature operators [149].

With now in hand all the experimental and analytical tools for the measurement of heralded single photons, we can transition to the presentation of the experimental results.

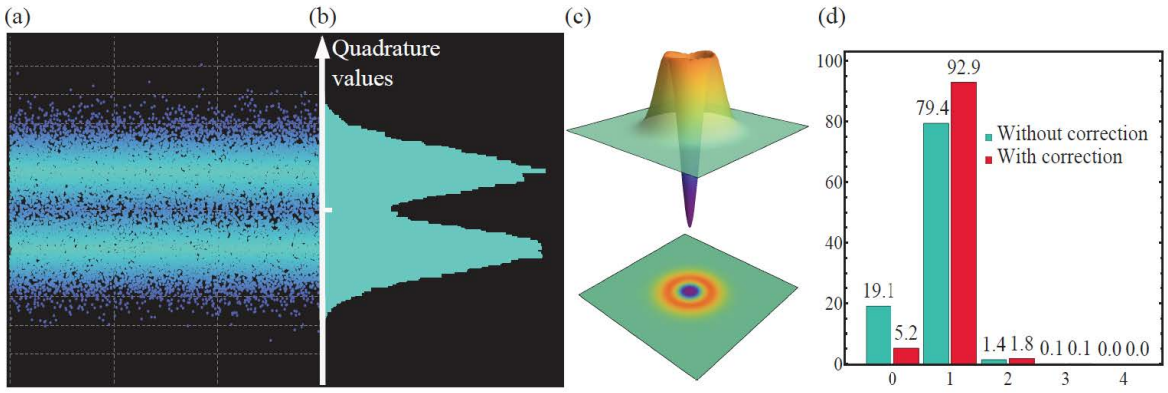

Figure 3.6: **Experimental heralded single-photon states.** From [7]. (a) Pre-processed experimental quadrature values results obtained by applying the temporal to the homodyne traces. Each point represents to a quadrature result of a corresponding heralding event for a given local oscillator phase. (b) The histogram of the quadrature values gives the marginal distribution of the experimental state, averaged over all phases. (c) Wigner function of the heralded single-photon reconstructed by single-mode quantum state tomography, corrected for 15% detection losses. (d) Photon-number distribution of the experimental heralded single-photon, without correction for detection losses (green) and correcting for 15% detection losses (red). The state at the output of the OPO presents a single-photon component of 93% with a vacuum admixture of 5%.

1.5 Experimental results

The quantum state is then reconstructed from 50 000 quadratures measurements, in a Hilbert space of dimension 1+4. We show in Figure 3.6 the best heralded single photon results [7]. The state is produced at a rate of 250 kHz. Without correction, the state exhibits a single-photon component of 80% with a vacuum component of 20%. Correcting from 15% detection losses, we are able to produce a state with a heralding efficiency of 93% with a vacuum component of 5%. This state shows a second order auto-correlation at time zero $g^2(0)$ of 0.04 (with a two-photon component 1.4%) and a spectral brightness of 6.10^3 photons/s.mW.MHz. With such a high state purity and spectral brightness, our heralded single-photon source ranges among the best sources published in literature [7, 158].

We have thus introduced the experimental procedure for the generation of the discrete-variable states that we will employ in this thesis. The heralded single photons produced from our type-II optical parametric oscillator show a high heralding efficiency, large heralding rates, and low multi-photon contributions, which makes them suitable for the implementation of more sophisticated schemes such as the ones we will present in **Chapters 5** and **7**. Before moving on to the presentation of the scheme for the preparation of continuous-variable states, let us examine at a novel benchmark that was recently developed for the characterization of single photon sources during this thesis: the Fock-state bunching capability.

2 Experimental Fock-state bunching capability

Another salient characteristic of the single photon Fock-states that is essential for quantum information processing is their ability to interfere in linear optics networks. This multi-photon interference effect is now being studied in a variety of works by considering different benchmarks based on fidelity [177] or specific photon correlation measures [178]. However these studies generally lack of evaluating the impact of the photon statistics, i.e the effect of vacuum and multi-photon components on the multi-photon interference. In addition, experimentally generated single photons will present fluctuations in their photon statistics, so that the joint and collective statistical influence of these parameters can only be taken into account by applying the benchmark on a variety of experimentally generated states. Our team, in collaboration with the group of Radim Filip at Olomouc University, developed a new benchmark called *Fock-state bunching capability*. This benchmark that considers the extreme bunching events of n single-photons into the Fock-state $|n\rangle$ relies on negativities of a Wigner function computationally determined in a clear operational procedure, and offers a very large sensitivity to the non-classicality of the generated higher Fock states. In particular this benchmark can be, in some cases, more reliable than the second-order autocorrelation function at zero delay $g^2(0)$ that only considers the multi-photon suppresion and does not take into account the vacuum admixture [179]. This work has been recently published in *Optica* [15].

2.1 Principle of the quantifier

The principle of the quantifier [180] is shown in Figure 3.7. To collectively test the ability of the generated single photons to undergo multi-photon interference, we computationally determine the Wigner function of the higher Fock state, which can, in principle, appear from multiple copies of the single-photon state. The area in phase space, where the Wigner function of the ideal Fock state $|n\rangle$ is negative, is composed of $n/2$ or $(n-1)/2$ concentric annuli if n is an even number or an odd number, respectively. By definition, *a single-photon state has the capability of the Fock state $|n\rangle$ if the Wigner function of the state, which can be generated from n independent copies of the single-photon state, has the same number of negative annuli as the ideal Fock state $|n\rangle$*. The negative annuli in the Wigner function witness the non-classical nature of the multi-photon interference in phase space. The Fock-state capability, which is determined computationally, collectively tests the copies of a single photon state, even though any multi-copy procedure is not implemented in the laboratory. In the ideal case n copies of a pure single-photon should lead to the Fock-state bunching capability n. However, in practice, vacuum admixture and multi-photon components degrade the quality of the interference and thus the higher Fock-state number that can be reached.

2.2 Experimental test and results

To test this new benchmark we use the type-II OPO presented in the previous section, with which a heralding efficiency up to $P_1 = 91\%$ can be reached. Also, by changing the

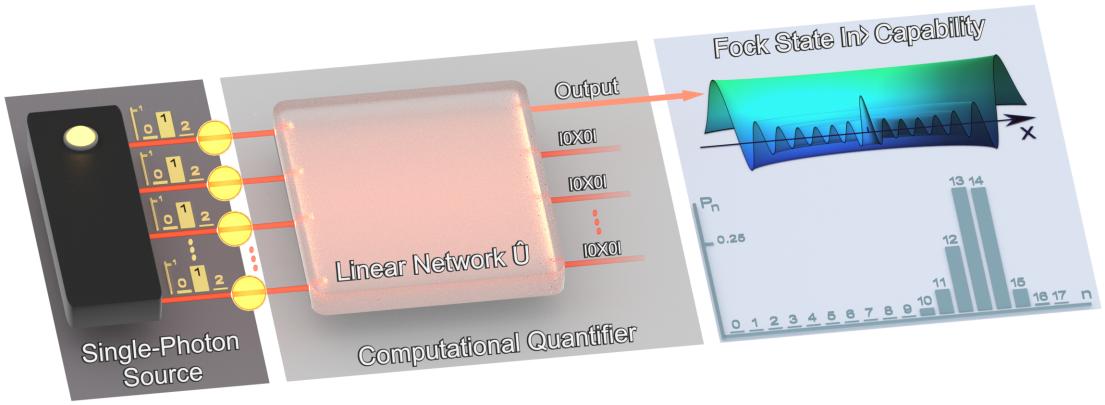

Figure 3.7: **Fock-state bunching capability of non-ideal single-photon states.** A single-photon source provides photons with different vacuum admixture and residual multi-photon components, as depicted by the photon-number distributions (left). These states are used as inputs of a balanced linear optics network $\hat{U}$. In an extreme case, all photons can bunch into just one output mode whereas all other modes are in the vacuum state. This stage is done computationally and provides the expected photon number distribution P_n for the output mode (right). The negativities of the associated Wigner function are used to determine the Fock-state bunching capability. In contrast to other measures, this collective benchmark depends not only on the vacuum admixture and multiple-photon statistics of the imperfect input photons but also on the small discrepancies between them.

pump power the multi-photon component can be increased at will. Losses can also be added to decrease the effective heralding efficiency. Overall, these features enable us to explore seven different combinations of state imperfections. The corresponding quantifier results are given in Figure 3.8.

First, single-photon states with a low purity due to a vacuum component close to 50% (brown bars) have only the trivial capability of the Fock state $|1\rangle$, despite their very low $g^2(0)$ of 0.07. This shows that the broadly used autocorrelation function does not fully characterize the ability to bunch into higher Fock states exhibiting non-classical signatures. In particular this example demonstrates that the capability is more sensitive to vacuum mixture, as a state obtained from two copies of these single photons would have a positive Wigner function. Due to their trivial capability, such states are not a useful resource for the preparation of large Fock states that could be used, e.g. for quantum metrology [181, 182, 183] or error correction [184, 185, 186].

The necessary condition for a non-trivial capability $n > 1$ is to reach a single-photon component $P_1 > 2/3$ [180]. Above this threshold, the capability moderately grows with

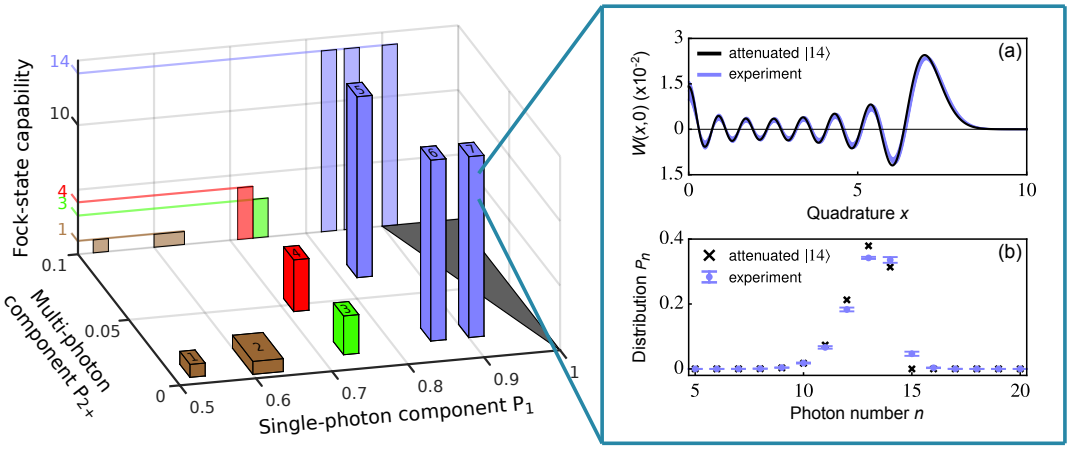

Figure 3.8: **Quantifier results.** (Left) The capability is given as a function of the single-photon component P_1 and of the multi-photon probability P_{2+} for the different sets experimentally generated. These parameters are averaged over photon-number statistics from a given data set obtained by successive measurements under the same experimental conditions. Colors denote the Fock-state capability. The gray-shaded area excludes the unphysical probabilities $P_1 + P_{2+} > 1$. The standard deviation of the probabilities are given by the thicknesses of the color bars. (Right) Quantifier output. (a) Cut through the output Wigner function $W(x, 0)$ of the computational quantifier whose inputs are fourteen experimentally obtained photon-number statistics. The thickness of the line provides the $3\,\sigma$ interval for the values of the output Wigner function. The fit given in black corresponds to the attenuated Fock state $|14\rangle$ (black line) with an attenuation parameter $\eta = 0.9205$. (b) Associated photon-number distribution (blue points) compared to photon-number distribution of the attenuated Fock state $|14\rangle$ (black crosses). The output Wigner function and the corresponding photon-number distribution are averaged over thirty random choices of photon-number statistics from the data set 7 with $P_1 = 0.91$ and $P_{2+} = 0.02$ (data set 7).

P_1. As can be seen in the Figure 3.8, the state corresponding to the green bar (set 3) has a multi-photon component $P_{2+} = 0.02$ and the capability of the Fock state $|3\rangle$. The state associated to the red bar (set 4) has the capability of the Fock state $|4\rangle$ despite having a similar single-photon component as the previous state but a larger, still low, probability $P_{2+} = 0.05$. For a given P_1, an increase in P_{2+} may thereby lead to a larger capability. Actually, this increase in P_{2+} comes in that case with a decrease in the vacuum component, indicating that the bunching is less affected by multi-photon contributions than vacuum admixture. We have shown in additional simulations that at fixed vacuum the capability decreases with the multi-photon component.

Finally, for $P_1 > 0.8$, the capability is expected to rapidly increase and to diverge at $P_1^{\infty} = 0.885$, where an arbitrary capability can be reached [180]. The experimental results agree well with this prediction and highlight the non-linearity of the quantifier.

The verification of this trend is an important benchmark for the development of single-photon sources. The data sets indicated with blue bars have at least the capability 14. For the set 7, note that its $g^2(0) = 0.05$ does not significantly differ from that of the states with the trivial Fock-state capability. The capability 14 is also achieved for lower single-photon fidelities P_1 and higher multi-photon contributions P_{2+}, even for a state with four times larger $g^2(0) = 0.2$. However, these states might have a lower capability than the set 7 due to the saturation to 14 for computational power reasons. The quantifier is presently computationally limited by the Fock-state capability 14, which is already a very large number in this operational context. All data sets for which this capability 14 is obtained may also have the capability of a higher Fock state.

In the end we show the output of the computational quantifier with fourteen input states randomly chosen from the data set 7, i.e. the set with the highest heralding efficiency and lowest multi-photon component. Figure 3.8 (a) first provides the cut through the Wigner function. The output Wigner function is fitted by the one of a lossy Fock state $|14\rangle$, with a fitted attenuation parameter $\eta = 0.92$. The fit shows that the oscillations of the output Wigner function in phase space coincide with the ones of the attenuated Fock state $|14\rangle$. The photon number statistics of the output state and attenuated Fock state are compared in Figure 3.8 (b). The good cut-off of the multi-photon contributions with more than fourteen photons in the statistics of the output state is another feature that further demonstrates the high quality of the initial single-photon states. Such result was made possible only by considering single-photon states with limited multi-photon contributions and very low vacuum admixture, as provided by the OPO-based source used in this thesis.

2.3 Discussion and outlook

In our experimental implementation, the estimation of the photon-number distribution was performed by using homodyne detections. Other detectors, such as photon-number resolving superconducting detectors [187, 188] should enable a direct measurement of the Fock state capability. The quantifier not depending on the nature of the source, it could be applied to other platforms such as microwave photons [189], phonons in trapped ions [190] and optomechanical [191] experiments, and collective excitations in atomic ensembles [102]. The benchmark can finally be modified to investigate the capability of other resources states such as Schrödinger cat states [192].

We have thus presented the Fock-state bunching capability benchmark which studies the ability of experimental single photons to follow multi-photon interference. We supplemented our theoretical definition with experimental data obtained from a tunable OPO-based single photon source and addressed different bunching regimes. With at hand the experimental and theoretical tools for the generation and characterization of discrete-variable quantum states, we now turn to the description of the experimental generation of optical continuous-variable quantum states.

3 CV: Experimental optical Schrödinger cat state generation

The protocol for the generation of CV states is very similar to the one of the DV state generation, except that we start now from a type-I OPO. Still several adaptations need to be made since the generated states are no more phase invariant. The scheme for the generation of optical Schrödinger cat states of small amplitude - often called *kittens* - has been historically performed in [193] and [194]. In this section we present the principle for the generation of the CV non-Gaussian states, the experimental setup for their production, and the corresponding results.

3.1 Single-mode squeezed vacuum Fock-state decomposition

The procedure for the generation of even or odd kitten states can be understood by looking at the Fock-state decomposition of the single-mode squeezed vacuum state at the output of the type-I OPO. It is indeed written as:

$$\hat{S}(r)\left|0\right\rangle_A = (1-\lambda^2)^{1/4}\sum_{n=0}^{\infty}\binom{2n}{n}^{1/2}\left(\frac{\lambda}{2}\right)^n\left|2n\right\rangle_A, \tag{3.19}$$

where λ is related to the squeezing parameter by $\lambda = \tanh(r)$.

We note here that, since the SPDC now produces photons in the same mode A, the parity of the state emitted from the type-I OPO, $\hat{S}(r)\left|0\right\rangle_A$, is *even*. In the same way, if a photon subtraction is applied on the state, it will change the parity of the state, to give $\hat{a}\hat{S}(r)\left|0\right\rangle_A$ with an *odd* parity. It might then be possible to find an operating regime where the squeezed-vacuum and photon-subtracted squeezed-vacuum have a high fidelity with a cat state of same parity. This scheme has been proposed historically by Dakna and collaborators [195] who noticed that for low squeezing and small cat sizes, the following property is valid without normalization:

$$\begin{aligned}\hat{S}(r)\left|0\right\rangle &\approx \left|cat+\right\rangle\\ \hat{a}\hat{S}(r)\left|0\right\rangle &\approx \left|cat-\right\rangle.\end{aligned} \tag{3.20}$$

$\left|cat+\right\rangle$ and $\left|cat-\right\rangle$ denote *coherent-state superpositions* (CSS) respectively in phase and in opposite phases, i.e.:

$$\left|cat\pm\right\rangle \propto \left|\alpha\right\rangle \pm \left|-\alpha\right\rangle \tag{3.21}$$

where $\left|\alpha\right\rangle$ is a coherent state of size $\left|\alpha\right|^2$.

We show in Figure 3.9 the theoretical fidelity between squeezed-vacuum or photon-subtracted squeezed vacuum state and the cat of corresponding parity, for different values of squeezing. As we can see the fidelity to cat states is clearly above 95% for both states up to a cat size $\left|\alpha\right|^2 = 1$ for a squeezing of 3 dB. Such small cat are typically referred to as *kitten* states. As the squeezing increases the size of the cat that can be reached with high fidelity increases. Yet in practice, the states with higher squeezing are much more

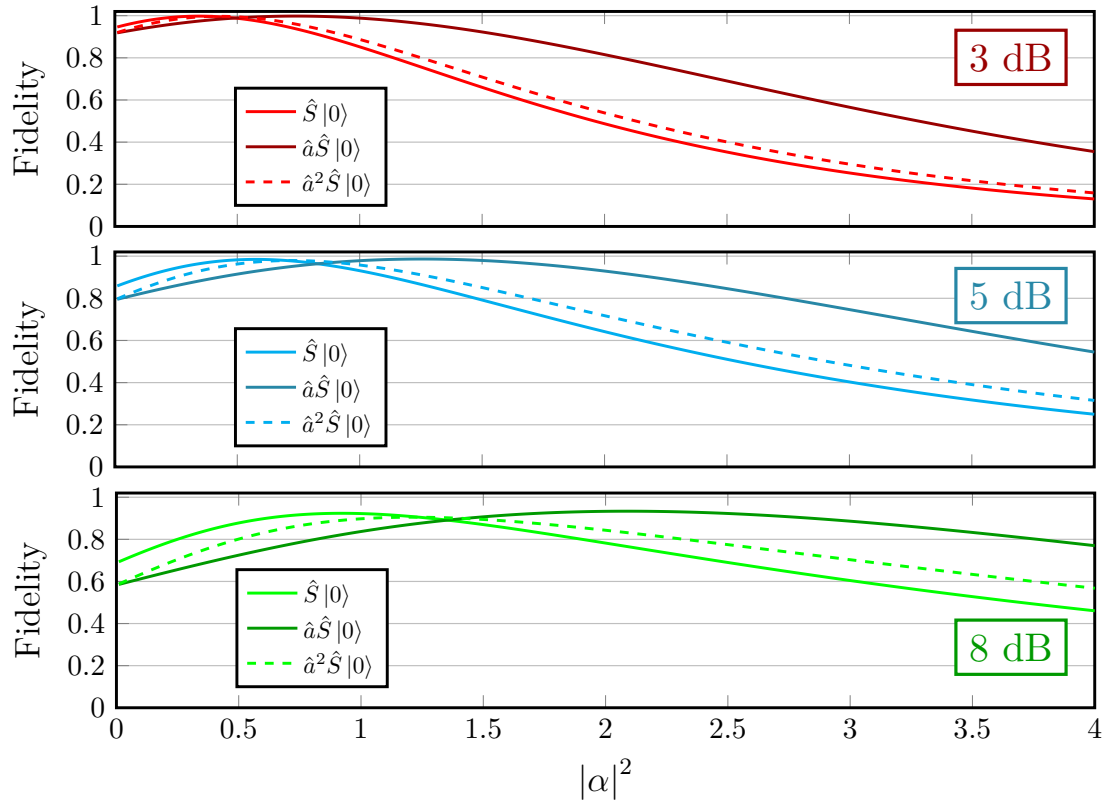

Figure 3.9: **Fidelity of squeezed vacuum and photon-subtracted squeezed vacuum states with their corresponding target cat state at fixed squeezing.** As the squeezing increases, the produced states maximize their fidelity with larger cat states. The difference of size between the even and odd cat states maximizing the fidelity increases as the squeezing increases. (Dashed lines) The fidelity to the even cat state can be increased at fixed squeezing by applying double photon subtraction.

difficult to produce because of an increased sensitivity to phase noise. We observe that the difference between even and odd cat sizes maximizing the fidelity to the target state increases as the squeezing is increased. This can be a limiting factor when projecting a CV state in the $\{|cat+\rangle, |cat-\rangle\}$ basis where the different components will not be evenly projected. We note that the fidelity to the even cat state can be increased by applying a double subtraction to $\hat{S}(r)|0\rangle$ to recover $\hat{a}^2\hat{S}(r)|0\rangle$ with the same parity. Still such a procedure is more difficult to implement experimentally.

3.2 Experimental setup

The experimental setup relies this time on a type-I OPO. The scheme is similar to the one for the heralding of a single photon with the type-II OPO. The photon-subtraction is mimicked by tapping off a small part of the beam that is sent to a single-photon detector.

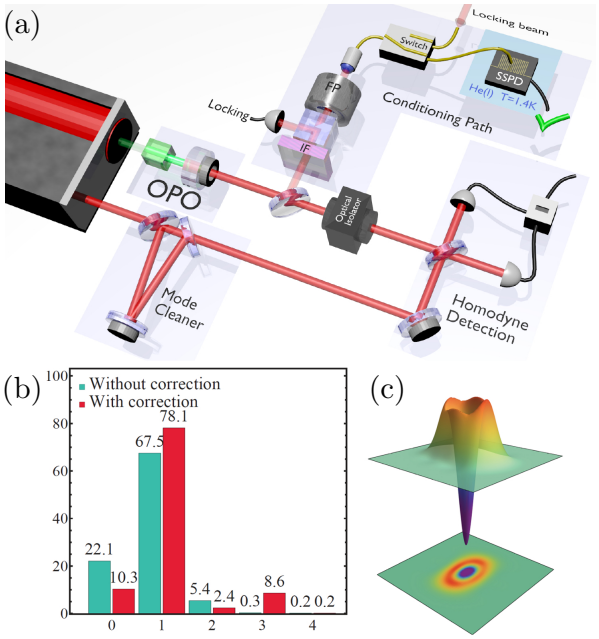

Figure 3.10: **Experimental generation of optical Schrödinger kitten states.** From [6]. (a) Experimental setup for the generation of odd cat state. The type-I OPO is pumped by 5 mW of pump at 532 nm to produce 3 dB of squeezing. The single-photon subtraction is performed by tapping 3% of the beam and conditioning on a click on the SNSPD. (b) Photon-number distribution of the odd cat state, without correction (green) and with correction for 15% detection losses (red). We obtain about 10% of vacuum component after correction, and significant population of the odd number states $|1\rangle$ and $|3\rangle$. (c) Wigner function of the state reconstructed by single-mode quantum state tomography with 15% correction. The state presents strong non-classical features indicated by the negativity of the Wigner function.

The experimental setup is shown in Figure 3.10.

Type-I OPO and photon subtraction. The OPO is composed of a type-I PPKTP crystal. The double resonance is adjusted by tuning the temperature of the non-linear crystal. The type-I OPO is pumped with 5 mW at 532 nm. It corresponds to about 3 dB of squeezing at the output of the OPO. A small part of the light is tapped by placing a beamsplitter of reflectivity R in the path of the down-converted photons. The reflected light is sent to the SNSPD for the heralding of the subtraction after the same filtering as for the heralded single photon. It is important to ensure that the tapping ratio remains small so that only a single photon - and not multiple photons - is subtracted, yet the reflectivity should be large enough in order to obtain a workable heralding rate. In practice we use a tapping ratio of $R = 3\%$, corresponding to a heralding rate of about 100 kHz. The rate can be increased by increasing the tapping ratio at the expense of state purity.

Phase calibration and data acquisition. Contrary to Fock state, the optical kitten states are phase sensitive. It is thus important to know precisely at which phase each quadrature is measured in order to perform the state tomography. To infer the relative phase between the signal and the local oscillator, we employ the seed beam to measure an interference fringe between the signal and the local oscillator. In practice the relative phase is swept by placing a mirror on the local oscillator path on a PZT-mount and applying a voltage ramp $V(t)$ synchronized with the sample and hold sequence. During the sampling sequence of 50 ms, the interference fringe between the seed and the local oscillator is recorded on a 350-MHz digital oscilloscope (**Lecroy WaveSurfer 434**). The trace will be used for the data processing to associate at each voltage $V(t)$ the corresponding phase $\theta_{LO}(V)$. During the hold sequence the seed beam is blocked, no visible fringe can be seen and the homodyne detection measures the quantum states with the PZT still swept. This enables to explore all the possible phases while accumulating the data for the state reconstruction. To determine which homodyne trace on the high definition oscilloscope (**Lecroy WaveRunner 6Zi**) corresponds to which phase, the voltage applied to the piezo is also recorded on the high definition oscilloscope. The phase of each quadrature is then recovered for each heralding event by looking at the voltage value applied at that time that corresponds to a specific phase $\theta_{LO}(V)$. In practice, we sweep the PZT with a frequency of 30 Hz.

3.3 Results

The experimental data is then pre-processed using the same procedure as for the heralded single photon. By applying the correct temporal mode we obtain the pre-processed data set $\{n, q_f^{(n)}, \theta_{LO}^{(n)}\}$. Maximum likelihood is finally applied to reconstruct the state in a Hilbert space of dimensions 1+4 (the size of the Hilbert space needs to be adapted if the cat size increases). The experimental results after single-mode quantum state tomography are shown in Figure 3.10 [6]. They are corrected from 15% detection losses. We achieve a fidelity of 87% with a Schrödinger cat state of size $|\alpha|^2 = 0.9$ at a rate of 100 kHz.

4 Hybrid entanglement as a key resource for heterogeneous quantum networks

With our knowledge on single-mode quantum state engineering we can now turn to the creation of hybrid entanglement between discrete- and continuous-variable optical qubits. This hybrid state, that has been engineered in our lab at LKB for several years [4, 13], has now become a resource in itself for the implementation of hybrid quantum information processing protocols. It has first been involved to perform the remote state preparation of CV qubits with high fidelity [11], or in a Einstein-Podolsky-Rosen steering test [12], to prove that our state can be employed in semi-device-independent security protocols. We will first present the framework of heterogeneous quantum networks in which the hybrid entanglement has been proposed for the first time, before detailing its experimental implementation and engineering.

Figure 3.11: **A heterogeneous quantum network.** The connection of DV (yellow) and CV (blue) quantum nodes is made possible by optical hybrid entanglement.

4.1 The hybrid strategy

Future quantum networks will necessarily be composed of different physical platforms and different types of encoding. Indeed, a given user might prefer to use DV or CV states depending on the task at hand and the physical system involved that can couple preferentially to one encoding or the other. For example, DV systems can efficiently be stored in state-of-the-art quantum memories [101], but the implemented DV protocols remains so far probabilistic [130], so that their extension to large scale is very demanding. On the other hand, CV systems enable the implementation of deterministic protocols [132] and efficient quantum computation [129], but the propagation of CV states in quantum channels is less efficient than for DV states [9]. As represented in Figure 3.11, the quantum networks must thus uphold a heterogeneous structure to enable full functionality. Yet users depending on different encodings should be able to communicate inside this heterogeneous networks. It is thus fundamental to link the two different types of quantum states - and communities - via quantum links in the form of *hybrid entanglement*.

The hybrid strategy initially refers to the combination of the experimental tools belonging to the two paradigms [3]. Historically, the detection of DV optical quantum states was performed with DV tools such as single-photon detectors, and the homodyne detection was used mostly for the detection of CV states. Combining the different tools has enabled the implementation of enhanced protocols, such as the trustworthy witnessing

of single-photon entanglement [196], or the high fidelity teleportation of DV states using a hybrid technique [197]. Photon subtraction can be employed in a hybrid framework for the distillation of Gaussian entanglement [198, 199, 200]. Several improved protocols involving hybrid entangled states are being developed in parallel [201, 202, 203]. It is notable to see that the schemes for the heralded creation of DV and CV non-Gaussian states are already hybrid protocols combining DV photon counting and high efficiency CV homodyne detection.

In the most general context, a pure two-mode hybrid entangled state is written under the form:

$$|\Psi\rangle_{AB} = \sum_n |\psi_n\rangle_{DV} |\psi_n\rangle_{CV}, \tag{3.22}$$

where $\{|\psi_n\rangle_{DV}\}_n$ represents a complete orthonormal basis of the DV mode and $\{|\psi_n\rangle_{CV}\}_n$ is an ensemble of infinite-dimensional qumodes. The choice of encoding in the DV or CV mode depends on the physical system at hand and the desired application. The DV mode can for example be encoded in the Fock basis $\{|0\rangle, |1\rangle\}$, or in dual-rail time bin qubits $\{|s\rangle, |l\rangle\}$ or in the polarization basis $\{|H\rangle, |V\rangle\}$. The CV encoding can be performed in the coherent state basis $\{|cat+\rangle, |cat-\rangle\}$.

The hybrid entangled state that will be at the heart of this thesis is of the form:

$$|\Psi\rangle_{AB} = \frac{1}{\sqrt{2}}(|0\rangle_A |cat-\rangle_B + e^{i\theta_{hybrid}} |1\rangle_A |cat+\rangle_B), \tag{3.23}$$

i.e. the DV mode will be encoded in the Fock basis $\{|0\rangle, |1\rangle\}$ and the CV mode in the basis $\{|cat+\rangle, |cat-\rangle\}$. As we will see later in **Chapter 5** and **7**, such entangled states can enable the connection of disparate node based on different encoding, and the conversion of quantum information from one encoding to the other.

4.2 Experimental implementation

In this section we will present the generation and engineering of the optical hybrid entangled initially published in [4]. The experimental setup is shown in Figure 3.12. The idea to create the entanglement between the DV and CV modes is to combine the two setups presented in the previous sections and to mix the two heralding paths in an *indistinguishable* fashion. The non-local click then corresponds to two indistinguishable outcomes. Either the single photon was originating from the type-II OPO and in that case squeezed vacuum was present at the output of the OPO I, or the single photon was originating from the subtraction, and in that case the state at the output of OPO I is a photon-subtracted squeezed vacuum state, while the state at the output of the type-II OPO is vacuum. A detection event therefore heralds the state:

$$|\Psi\rangle_{AB} \propto |0\rangle_A \hat{a}\hat{S} |0\rangle_B + e^{i\theta_{hybrid}} |1\rangle_A \hat{S} |0\rangle_B, \tag{3.24}$$

with θ_{hybrid} the relative phase between the two heralding paths.

As we have seen earlier, for a squeezing of 3 dB, the state at the output of the type-I OPO has a large fidelity with a cat state of amplitude $|\alpha|^2 = 0.9$, so that the hybrid state

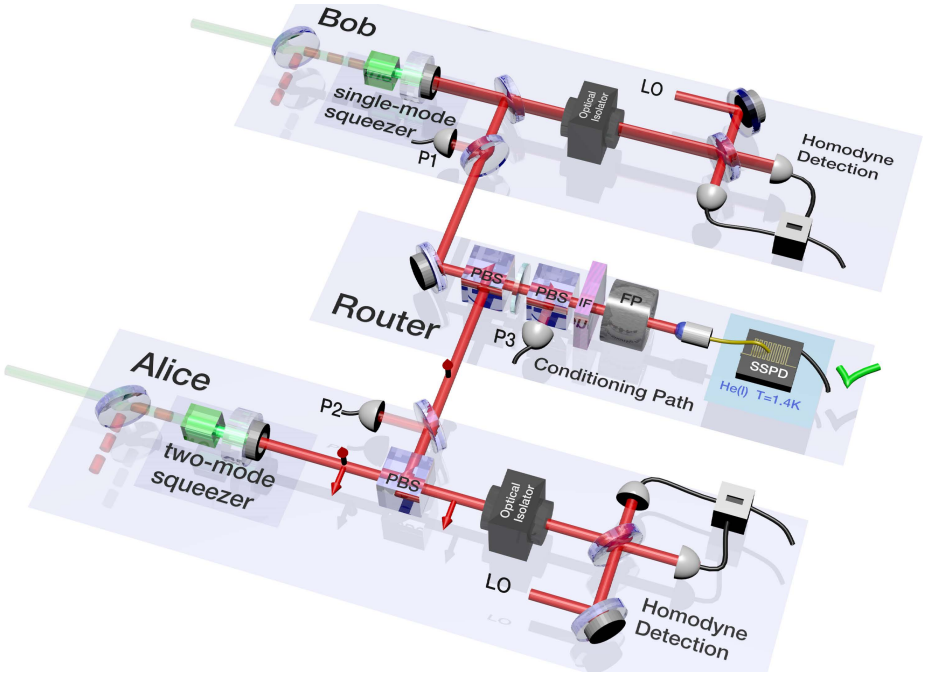

Figure 3.12: **Experimental generation of hybrid entanglement of light.** The type-I and type-II OPOs are pumped far below threshold. The type-I OPO emits 3 dB of squeezed vacuum while the type-II OPO emits orthogonally-polarized photon pairs. The idler mode from OPO II is mixed with the tapped mode corresponding to 3% of the mode from OPO I. The projected mode is spectrally filtered by an interferential filter (IF) and a home-made Fabry-Pérot cavity (FP) before being sent to an SNSPD placed in a cryogenic environment. The two heralding modes are indistinguishable through fine tuning of both OPO bandwidths and the balancing of their respective heralding rates. The photodiode $P1$ and $P2$ are used to lock the seed of each OPO in phase with their respective pump. The creation of the same state at every heralding click is ensured by phase locking between the two conditioning paths at $P3$. Each mode of the heralded state is measured by a high-efficiency homodyne detection, and the state is fully characterized by two-mode quantum state tomography.

has a high fidelity with the target state:

$$|\Psi\rangle_{AB} = \frac{1}{\sqrt{2}}(|0\rangle_A |cat-\rangle_B + e^{i\theta_{hybrid}} |1\rangle_A |cat+\rangle_B), \tag{3.25}$$

which is equivalent up to a basis change to the state:

$$|\Psi\rangle_{AB} = \frac{1}{\sqrt{2}}(|+\rangle_A |\alpha\rangle_B + e^{i\theta_{hybrid}} |-\rangle_A |-\alpha\rangle_B), \tag{3.26}$$

with $|\pm\rangle = (|0\rangle \pm + |1\rangle)\sqrt{2}$.

Non-local conditioning. The key element for the success of the generation of the hybrid entangled state is to maximize the indistinguishability between the idler of the OPO II and the tapped beam of OPO I. This is ensured by matching spectrally the bandwidth of the two OPOs and applying the same spectral filtering of the projected conditioning paths. The conditioning paths are projected by first having the two optical beams co-propagate in the same spatial mode on a PBS before projecting their polarizations on a second PBS with a half-waveplate of adjustable angle. The indistinguishability is maximized by rotating the half-waveplate to balance the count rate of each OPO on the SNSPD. The other port of the projecting PBS is used to lock the phase of the hybrid entangled state θ_{hybrid}. Typically, at a pump power of 1 mW for OPO II and 5 mW for OPO I (3 dB), we obtain a hybrid heralding rate of 100 kHz.

Phase control. If the relative phase between the two conditioning paths is not actively stabilized, the accumulated measured quadratures will correspond to hybrid states with different phases. This accumulation of phases yields a blurring of the coherence of the entangled state that can lead in the worst scenario to the creation of an entirely mixed state. It is thus important to actively control the phase of the hybrid state to make sure all the measured states correspond to the same phase θ_{hybrid}. The locking is performed digitally with a microcontroller using the interference fringe between the two seed beams of each OPO. We choose to lock to a relative phase $\theta_{hybrid} = \pi$. The phase noise is estimated at about 3%.

Two-mode state tomography. Similarly as for the single-mode schemes, we record the two homodyne traces corresponding to the DV and CV mode for each heralding event, apply the relevant temporal modes, and normalize to the variance of vacuum on each mode. The phases of the DV and CV local oscillators are obtained in the same manner as before. The same voltage ramp $V(t)$ is applied to the two PZT of the local oscillators. From this we recover the pre-processed data set $\{n, q^{(n)}_{f,DV}, q^{(n)}_{f,CV}, \theta^{(n)}_{LO,DV}, \theta^{(n)}_{LO,CV}\}$ with n the n-th heralding event of in total $N = 200\,000$ events. The total data acquisition takes about 20 minutes. The state reconstruction is done by performing two-mode quantum state tomography with Maximum-Likelihood, correcting for 15% detection losses on each mode. For the optimization we set the Hilbert dimension to 1+4 for the DV mode and 1+6 for the CV mode, which is well beyond the subspace we expect to be populated. The algorithm outputs a 77x77 two-mode density matrix that can be analyzed.

4.3 Results

4.4 Symmetric case

Several methods can be used to represent the two-mode density matrix. In our case we project the density matrix of the two-mode state $\hat{\rho}$ on the DV Fock basis $\langle i|\,\hat{\rho}\,|j\rangle_{DV}$, with $\{i, j\} \in \{0, 1\}$. We then represent the Wigner function of the four corresponding single-mode projections. The diagonal terms correspond to the projections on $|0\rangle\langle 0|$ and $|1\rangle\langle 1|$, which give the Wigner functions of the odd and even cat states respectively. The anti-

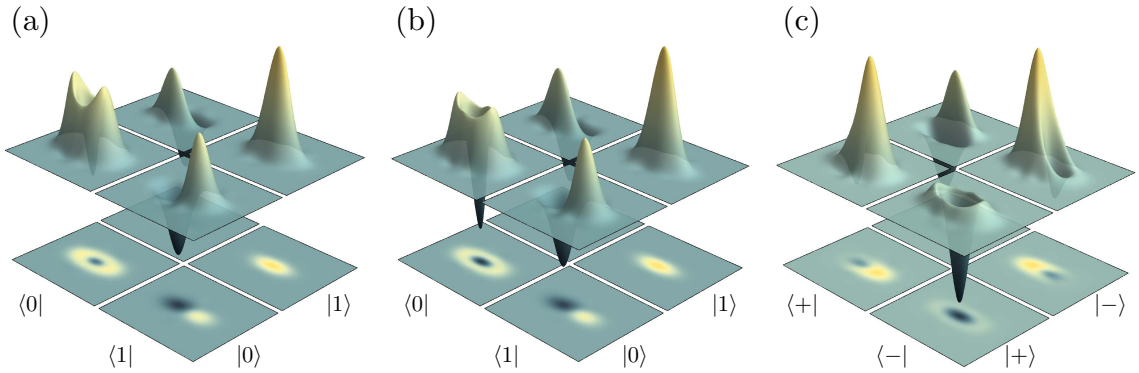

Figure 3.13: **Experimental results in the symmetric case.** (a) and (b) Wigner function of the reduced density matrices $\langle i|\,\hat{\rho}\,|j\rangle_{DV}$ with $\{i,j\} \in \{0,1\}$ with and without detection losses of 15% in each mode. The components with $i \neq j$ being not hermitian, the corresponding Wigner functions are not necessarily real, but conjugate. The plot gives therefore the real part in the back corner ($i < l$) and the imaginary part in the front corner ($i > j$). (c) Same results in the rotated DV basis $\{|+\rangle, |-\rangle\}$ with $|\pm\rangle = (|0\rangle \pm |1\rangle)/\sqrt{2}$. The negligible higher photon number terms (the amplitude of which being lower than 1% for each) are not represented.

diagonal terms are coherence terms characteristic of the entanglement. This representation is valid as long as the multi-photon components are negligible, which is true is our case since the total projections to higher number states correspond to less than 2% of the measured state.

The corresponding experimental states are represented in Figure 3.13 with and without correction for detection losses. The Wigner function of the odd cat state without correction, $\langle 0|\,\hat{\rho}\,|0\rangle$, is negative at the origin of phase space with $W(0,0) = -0.053$, which is a strong signature of non-classicality. The negativity of the Wigner function increases to $W(0,0) = -0.169$ as the detection losses are corrected.

The amount of entanglement of the entangled state is measured with the *negativity of entanglement*. As a reminder the negativity of entanglement is an entanglement measure defined as:

$$\mathcal{N} = \left(||\rho^{T_X}||_1 - 1\right)/2, \tag{3.27}$$

where ρ^{T_X} stands for the partial transpose of the two-mode density matrix ρ_{XY} and $||X||_1$ the trace norm:

$$||X||_1 = \mathrm{Tr}(\sqrt{X^\dagger X}). \tag{3.28}$$

In the ideal, lossless case, the negativity of entanglement is bounded to 0.5. We measure without correction an entanglement negativity of $\mathcal{N} = 0.27$ that increases to $\mathcal{N} = 0.385$ as we correct for detection losses, which is the maximum value attainable experimentally by taking into account the escape efficiency of the OPOs.

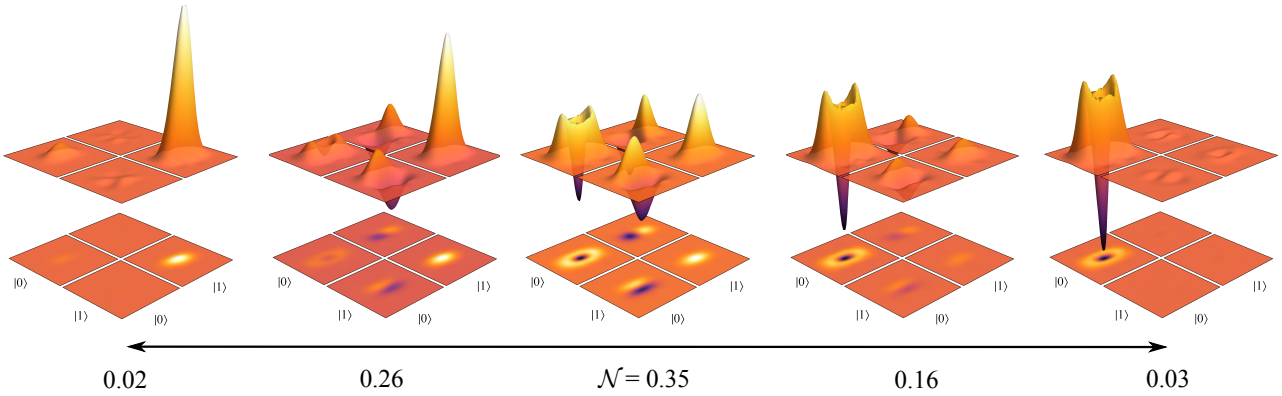

Figure 3.14: **Experimental results, from separable to maximally entangled hybrid state.** From [4]. Experimental hybrid state and negativity of entanglement with a relative phase set to zero. By rotating the half-waveplate, we can go from the one fully separable state $|1\rangle |cat+\rangle$ to the other $|0\rangle |cat-\rangle$ via a maximally entangled state $|1\rangle |cat+\rangle + |0\rangle |cat-\rangle$. The negativity of entanglement is indicated for each state.

We finaly represent the state projected in the DV basis $\{|+\rangle, |-\rangle\}$. We obtain a fidelity of 77% to the target state with $\theta_{hybrid} = \pi$ and $|\alpha|^2 = 0.9$. This experiment was the first published demonstration of hybrid entanglement of light [4], conjointly with [5] using a different generation strategy.

4.5 Assymmetric case and increased dimensionality

If the maximally entangled state is obtained by matching the heralding rates from each OPO, an asymmetric and non-maximally entangled state can be obtained by changing the angle of the projecting half waveplate. Such a state can be useful in some protocols such as remote state preparation [11] or quantum steering [12] where experimental biases need to be compensated. The asymmetric entangled state is then written:

$$|\Psi\rangle_{AB} = \sqrt{R}\,|0\rangle_A\,|cat-\rangle_B + \sqrt{1-R}e^{i\theta_{hybrid}}\,|1\rangle_A\,|cat+\rangle_B \tag{3.29}$$

where the probability of having the heralding click coming from OPO I is $R/(1-R)$ times as large as the probability of it coming from OPO II. As can be seen in Figure 3.14 it is thus possible to tune the hybrid state from fully separable to maximally-entangled state.

Several extensions of the engineering of the optical hybrid entangled state have been performed in our group and will not be detailed here. Two examples of them are the addition of a local subtraction on the CV mode to change the parity of the cats, in order to create the state:

$$|\Psi\rangle_{AB} = \frac{1}{\sqrt{2}}(|0\rangle_A\,|cat+\rangle_B + e^{i\theta_{hybrid}}\,|1\rangle_A\,|cat-\rangle_B) \tag{3.30}$$

and the addition of a second non-local clicks to create a hybrid entangled qutrit of the form:

$$|\Psi\rangle_{AB} \propto (|0\rangle_A \hat{a}^2 \hat{S} |0\rangle_B + |1\rangle_A \hat{a}\hat{S} |0\rangle_B + |2\rangle_A \hat{S} |0\rangle_B). \tag{3.31}$$

The experimental realization of these state has been performed in [158]. During this thesis we published a detailed theoretical analysis of the engineering of the optical hybrid entanglement, including its extension to qutrits [13].

5 Conclusion

This presentation of the quantum state engineering performed by combining the tools from the discrete- and continous-variable paradigms, concludes the introduction of the experimental resources that have been mastered in our group and that were present in the lab at the start of this thesis. We have presented, in addition, a novel benchmark for the characterization of the multi-photon interference capability of experimental single photons. Over the last years, our team has developed a strong expertise in the engineering of optical hybrid entangled states, that can now be employed as a resource in itself for quantum information processing protocols. In the rest of the manuscript we will study the two quantum teleportation protocols that were implemented during this work using hybrid entanglement of light, namely hybrid entanglement swapping and hybrid quantum teleportation. But before passing to the presentation of the schemes, we need to study theoretically a final requirement, which is the Bell-state measurement, essential for the success of the teleportation protocols.

Chapter 4

A hybrid Bell-state measurement for teleportation-based protocols

In this chapter we will introduce the hybrid Bell-state measurement (BSM) that has been implemented to perform teleportation protocols with hybrid entanglement of light. This Bell-state measurement, applied on discrete-variable (DV) modes, combines photon counting on a single-photon detector and quadrature conditioning with high efficiency homodyne detection. We will study theoretically the performances of this novel measurement both in the context of hybrid quantum teleportation and hybrid entanglement swapping, two protocols that will be experimentally implemented in the following chapters.

1 Finding the optimal Bell-state measurement

1.1 Our objectives

The goal of the thesis being to teleport DV qubits - or equivalently DV-DV entanglement - towards CV qubits via hybrid entanglement of light we need to choose a specific Bell-state measurement that is conveniently adapted to our system. Here we will present the strategy that has led us to devise a new hybrid Bell-state measurement that combines the tools from the DV and CV paradigms.

The scheme for hybrid teleportation is shown in Figure 4.1. A discrete-variable qubit in mode A is initially encoded in the Fock basis $\{|0\rangle, |1\rangle\}$ in the form:

$$|\psi_{in}\rangle_A = c_0 |0\rangle_A + c_1 e^{i\theta} |1\rangle_A . \tag{4.1}$$

For the teleportation we employ an optical hybrid entangled state. The DV mode, labeled B, is encoded in the Fock basis $\{|0\rangle, |1\rangle\}$ while the CV mode, labeled C, is encoded in the coherent state superposition basis $\{|cat+\rangle, |cat-\rangle\}$. This entangled state can be written as:

$$|\Psi\rangle_{BC} = \frac{1}{\sqrt{2}}(|0\rangle_B |cat-\rangle_C + |1\rangle_B |cat+\rangle_C). \tag{4.2}$$

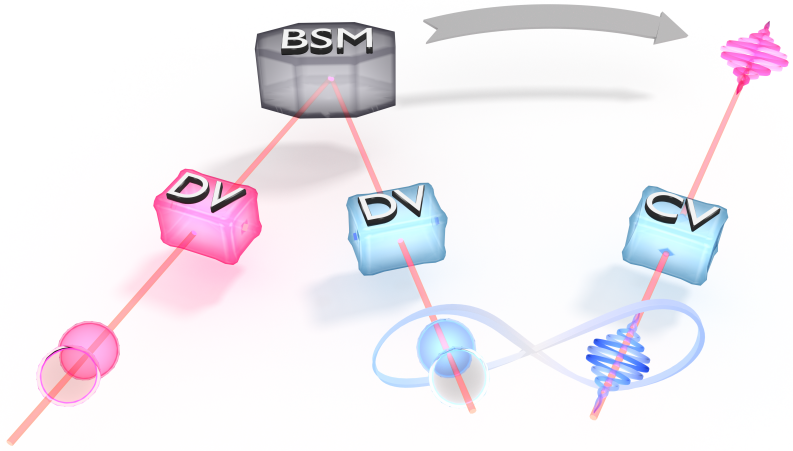

Figure 4.1: **Scheme for teleportation via hybrid entanglement of light.** A discrete-variable qubit is mixed with the DV mode of a hybrid entangled state. The state is teleported from DV to CV when the BSM is successful. The most efficient BSM needs to be implemented by combining the tools from the DV and the CV paradigms. The scheme can be extended naturally to entanglement swapping from DV-DV to DV-CV by replacing the DV qubit by one mode of a DV-DV entangled state.

As we have seen in **Chapter 1**, the three-mode state

$$|\Psi\rangle_{ABC} = \frac{1}{\sqrt{2}}(c_0\,|0\rangle_A + c_1 e^{i\theta}\,|1\rangle_A) \otimes (|0\rangle_B\,|cat-\rangle_C + |1\rangle_B\,|cat+\rangle_C), \tag{4.3}$$

can always be factorized in the form:

$$\begin{aligned} |\Psi\rangle_{ABC} = \frac{1}{2}\Big[&\left|\Psi^+\right\rangle_{AB} \otimes (c_0\,|cat+\rangle_C + c_1 e^{i\theta}\,|cat-\rangle_C\,) \\ &+ |\Psi^-\rangle_{AB} \otimes (c_0\,|cat+\rangle_C - c_1 e^{i\theta}\,|cat-\rangle_C\,) \\ &+ \left|\Phi^+\right\rangle_{AB} \otimes (c_1 e^{i\theta}\,|cat+\rangle_C + c_0\,|cat-\rangle_C\,) \\ &+ |\Phi^-\rangle_{AB} \otimes (-c_1 e^{i\theta}\,|cat+\rangle_C + c_0\,|cat-\rangle_C\,)\Big], \end{aligned} \tag{4.4}$$

where we recall the four Bell states defined as:

$$\begin{aligned} \left|\Psi^+\right\rangle_{AB} &= \frac{1}{\sqrt{2}}(\,|0\rangle_A\,|1\rangle_B + |1\rangle_A\,|0\rangle_B\,), \\ |\Psi^-\rangle_{AB} &= \frac{1}{\sqrt{2}}(\,|0\rangle_A\,|1\rangle_B - |1\rangle_A\,|0\rangle_B\,), \\ \left|\Phi^+\right\rangle_{AB} &= \frac{1}{\sqrt{2}}(\,|0\rangle_A\,|0\rangle_B + |1\rangle_A\,|1\rangle_B\,), \\ |\Phi^-\rangle_{AB} &= \frac{1}{\sqrt{2}}(\,|0\rangle_A\,|0\rangle_B - |1\rangle_A\,|1\rangle_B\,). \end{aligned} \tag{4.5}$$

We notice that this is the sum, except for the Pauli operators, of tensor products between the input state in the CV basis, $|\psi_{in}\rangle_C = c_0 |cat+\rangle_C + c_1 e^{i\theta} |cat-\rangle_C$, and each Bell state. It can indeed be rewritten as:

$$\begin{aligned} |\Psi\rangle_{ABC} = \frac{1}{2}\Big[&\left|\Psi^+\right\rangle_{AB} \otimes |\psi_{in}\rangle_C + \left|\Psi^-\right\rangle_{AB} \otimes \hat{\sigma}_Z |\psi_{in}\rangle_C \\ &+ \left|\Phi^+\right\rangle_{AB} \otimes \hat{\sigma}_X |\psi_{in}\rangle_C + \left|\Phi^-\right\rangle_{AB} \otimes e^{-i\pi/2}\hat{\sigma}_Y |\psi_{in}\rangle_C \Big]. \end{aligned} \tag{4.6}$$

Now if a measurement - called *Bell-state measurement* - between modes A and B enables the distinction of one of the four Bell states, it will project mode C into a unitary evolution of the input qubit, $\hat{U} |\psi_{in}\rangle_C$, where $\hat{U}$ is a Pauli operator depending on the result of the measurement. This result is transferred via a classical channel to the receiver who then applies the corresponding unitary transformation to convert this state into a replica of the original state $|\psi_{in}\rangle_C$.

1.2 Experimental techniques for the Bell-state measurement

Several techniques can be employed to perform the Bell-state measurement. A CV protocol enables the implementation of a complete BSM with feed-forward [132, 204]. As a reminder, in CV teleportation, double homodyne detection is used to perform the BSM by measuring simultaneously both the quadratures $\hat{x} = (\hat{x}_A - \hat{x}_B)/\sqrt{2}$ and $\hat{p} = (\hat{p}_A + \hat{p}_B)/\sqrt{2}$ after mixing modes A and B on a 50:50 beamsplitter. The corresponding results, i.e. the photocurrents x and p are then transferred classically to apply actively the unitary operation (corresponding, in general, to amplitude and phase modulation) in order to recover the original state. This CV BSM appears as the most efficient technique since it enables a complete distinction of the four Bell states, and represents an *active* protocol where the state is adapted depending on the BSM result. This CV teleportation scheme is in that sense typically called *unconditional* teleportation. However, and unfortunately in our specific case of hybrid entanglement, the CV mode on which the state is teleported is encoded in a coherent state basis $\{|cat+\rangle, |cat-\rangle\}$. For this encoding implementing the $\hat{\sigma}_X$ operator corresponding to phase shifting can be done efficiently, but the implementation of the $\hat{\sigma}_Z$ operator can be done efficiently with a displacement only for large values of α [205], which is not the case of our system. For that reason we cannot employ that type of CV BSM in an unconditional teleportation protocol.

We thus have to apply a DV BSM, which is actually more natural since the modes we are mixing are also DV. To differentiate the Bell states we first mix modes A and B on a balanced beamsplitter. Recalling the balanced beamsplitter operations:

$$\begin{aligned} \hat{a}^\dagger &\xrightarrow{50:50} \frac{1}{\sqrt{2}}(\hat{a}^\dagger + \hat{b}^\dagger), \\ \hat{b}^\dagger &\xrightarrow{50:50} \frac{1}{\sqrt{2}}(\hat{b}^\dagger - \hat{a}^\dagger), \end{aligned} \tag{4.7}$$

this transforms the four Bell states into:

$$\begin{aligned}
&\left|\Psi^+\right\rangle_{AB} \xrightarrow{50:50} |0\rangle_A |1\rangle_B ,\\
&\left|\Psi^-\right\rangle_{AB} \xrightarrow{50:50} |1\rangle_A |0\rangle_B ,\\
&\left|\Phi^+\right\rangle_{AB} \xrightarrow{50:50} \frac{1}{\sqrt{2}}(|0\rangle_A |0\rangle_B + \frac{1}{\sqrt{2}}(|0\rangle_A |2\rangle_B - |2\rangle_A |0\rangle_B)),\\
&\left|\Phi^-\right\rangle_{AB} \xrightarrow{50:50} \frac{1}{\sqrt{2}}(|0\rangle_A |0\rangle_B + \frac{1}{\sqrt{2}}(|2\rangle_A |0\rangle_B - |0\rangle_A |2\rangle_B)).
\end{aligned} \tag{4.8}$$

Using linear optics, we can distinguish the states $\left|\Psi^+\right\rangle_{AB}$ and $\left|\Psi^-\right\rangle_{AB}$ by applying the projector $|1\rangle\langle 1|$ on either the mode A or the mode B. However due to the symmetry of the states $\left|\Phi^+\right\rangle_{AB}$ and $\left|\Phi^-\right\rangle_{AB}$ it is not possible to discriminate them from all other Bell states. This is a fundamental limitation of DV BSM for which only two out of the four Bell-states can be distinguished using linear optics [206, 108, 207]. It thus yields a probabilistic teleportation protocol with a maximum efficiency - or probablity of success - of 1/2.

Several experimental techniques can be used to perform the single-photon projection. For simplicity and practical convenience we will only apply the measurement on mode B. This decreases the efficiency of the protocol from 1/2 to 1/4. As can be seen in Eq.(4.6), measuring $\left|\Psi^+\right\rangle_{AB}$ by applying $|1\rangle\langle 1|_B$ on mode B enables to recover the initial state $|\psi_{in}\rangle_C$ without the need to perform any unitary operation to retrieve the original qubit. Since no active operation is needed to recover the state we say that the protocol is *passive*. The Bell-state measurement in that case corresponds to the selection of the correct event that heralds the creation of the teleported state.

Measurement with single-photon detectors can be used to perform $|1\rangle\langle 1|_B$. Efficient and fast photon-number resolving detectors not being yet developed for our application [167] we will use superconducting nanowire single-photon detectors (SNSPDs) [155] for the single-photon projection. Yet, even if SNSPDs can currently achieve high quantum efficiencies and fast operational rates, they can only perform "On"/"Off" detection and are thus not able to distinguish between the single-photon and the multi-photon components. The multi-photon component can thus herald the detection of the Bell states $\left|\Phi^+\right\rangle_{AB}$ and $\left|\Phi^-\right\rangle_{AB}$ on top of the target $\left|\Psi^+\right\rangle_{AB}$. As we will see later, this multi-photon detection is equivalent to a pure channel loss that degrades the quality of the teleportation. We can thus conclude that a single SNSPD is insufficient for our purpose, and that the measurement needs to be improved in order to achieve a proper BSM.

Ideal photon-number resolving detection can be mimicked by using a series of multiplexed SNSPDs [160, 162]. The optical path can indeed be split in N branches that are connected to N SNSPDs. The single-photon projection is then done by considering the event corresponding to an "On" detection on a single SNSPD while detecting "Off" on the $N-1$ others. However this method is very inefficient [163, 164] because the measurement of an absence of photon is very likely to correspond to the loss of the photon, especially when the heralding losses due to spectral filtering are typically of 60-80%. We thus cannot implement a DV BSM based on a more-than-one-SNSPD scheme. We thus have to employ

another technique that introduces less transmission losses before the detection.

Nevertheless we have at our disposal an efficient CV experimental tool that enables the projection on a given Fock state to complete the click on the SNSPD with minimum detection losses. As we will see in the next section homodyne detection can be used as parity detector when conditioning on quadratures around $q = 0$ and efficient projection on vacuum $|0\rangle\langle 0|$ can be done when higher even-photon components are negligible. We can thus improve the detection on the SNSPD by combining it with homodyne conditioning in a hybrid technique.

2 A hybrid scheme combining photon counting and homodyne conditioning

In order to understand how homodyne conditioning can improve a BSM based on single-photon detection, let us here give a reminder on quadrature conditioning with homodyne detection. We will in addition detail the effect of experimental imperfections, such as transmission losses and finite conditioning window on the scheme.

2.1 Quadrature conditioning on homodyne detection

An optical homodyne detection measures the quadratures of an incident field along the phase of its local oscillator. This measurement can be described by the operator $\hat{q}_\theta = \hat{x}\cos\theta + \hat{p}\sin\theta$ where $\hat{x}$ and $\hat{p}$ denote the canonical position and momentum observables of the measured field and θ is the phase of the local oscillator. The quadrature result q_θ of the measurement operator $\hat{q}_\theta$ belongs to a given *marginal distribution* - i.e. the probability distribution for a fixed local oscillator phase θ - which depends on the quantum state measured. In the specific case of Fock states, their wavefunctions $\psi_n(q_\theta)$ can be expressed as the projections of the states $|n\rangle$ of the quadrature operator $\hat{q}_\theta$ [149]:

$$\psi_n(q_\theta) = \langle q_\theta|n\rangle = e^{in\theta}\frac{1}{(\sqrt{2\pi}\sigma_0 2^n n!\,)^{1/2}}\mathcal{H}_n(\frac{q}{\sigma_0\sqrt{2}})e^{-(q/\sigma_0\sqrt{2})^2/2}, \tag{4.9}$$

where σ_0^2 is the variance of vacuum and $\mathcal{H}_n$ is the n-th Hermite polynomial. The marginal distributions $P_n(q_\theta)$ are then given by:

$$P_n(q_\theta) = |\psi_n(q_\theta)|^2. \tag{4.10}$$

Quadrature conditioning can be understood by considering the marginal distributions of the quantum states measured on the homodyne detector. We show in Figure 4.2 the marginal distributions associated to the Fock states $|0\rangle$, $|1\rangle$ and $|2\rangle$. These states are indeed projected onto the quadrature operator $\hat{q}_\theta$ as:

$$\begin{gathered}\langle q_\theta|0\rangle = \frac{1}{(\sqrt{2\pi}\sigma_0)^{1/2}}e^{-q^2/(4\sigma_0^2)}, \qquad \langle q_\theta|1\rangle = \frac{(q/\sigma_0)e^{i\theta}}{(\sqrt{2\pi}\sigma_0)^{1/2}}e^{-q^2/(4\sigma_0^2)}, \\ \langle q_\theta|2\rangle = \frac{[(q/\sigma_0)^2-1]e^{2i\theta}}{(\sqrt{2\pi}\sigma_0 2)^{1/2}}e^{-q^2/(4\sigma_0^2)}.\end{gathered} \tag{4.11}$$

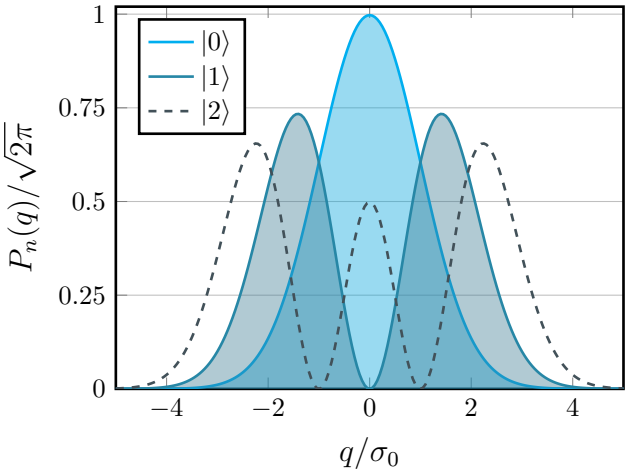

Figure 4.2: **Marginal distribution of Fock states.** Marginal distributions of the Fock states $|0\rangle$, $|1\rangle$ and $|2\rangle$ as a function of the homodyne quadrature results q. The marginal distributions are maximum around $q = 0$ for the even Fock states while being minimal for the odd Fock states. Large quadrature values are more likely to come from high number states. When considering only the subspace $\{|0\rangle, |1\rangle\}$, selecting quadrature values can perform efficient parity detection. Conditioning on quadratures around $q = 0$ is very likely to herald the state $|0\rangle$, while conditioning on large values of $q > \sigma_0$ is more likely to herald the state $|1\rangle$. The state $|0\rangle + |1\rangle$ can even be heralded when selecting quadrature values that have the same probability to originate from the two states, i.e. for $q = \sigma_0$, where σ_0^2 stands for the variance of vacuum.

As can be seen, the corresponding marginal distributions are maximal at $q = 0$ for the even Fock states while being minimal for the odd Fock states. Homodyne detection can thus be used as a parity detector, although it is imperfect as the amplitudes of the marginal distributions at zero are not the same for all the even Fock-states. If it is ensured that the quantum state one is interested in belongs to the Hilbert space $\{|0\rangle, |1\rangle\}$ - i.e if the two-photon component are in practice negligible - then conditioning on $q = 0$ amounts to a projection on $|0\rangle\langle 0|$. Conversely large values of q are then more likely to originate from the Fock state $|1\rangle$, so that conditioning on large enough values of q amounts to a projection on $|1\rangle\langle 1|$. One can even project the state on a superposition of vacuum and single photon when selecting quadrature values that have the same probability to come from the two states, i.e. for $q = \sigma_0$. Such a conditioning technique has already been employed in our group for the remote state preparation of CV qubits via hybrid entanglement [11].

2.2 Combining photon counting with homodyne conditioning

It is important to note that for teleportation the two-photon components cannot be neglected [130, 208, 209]. Indeed if one intends to teleport a single photon, there will be on average 1.5 photons on the DV mode after mixing. Thus a single SNSPD cannot be

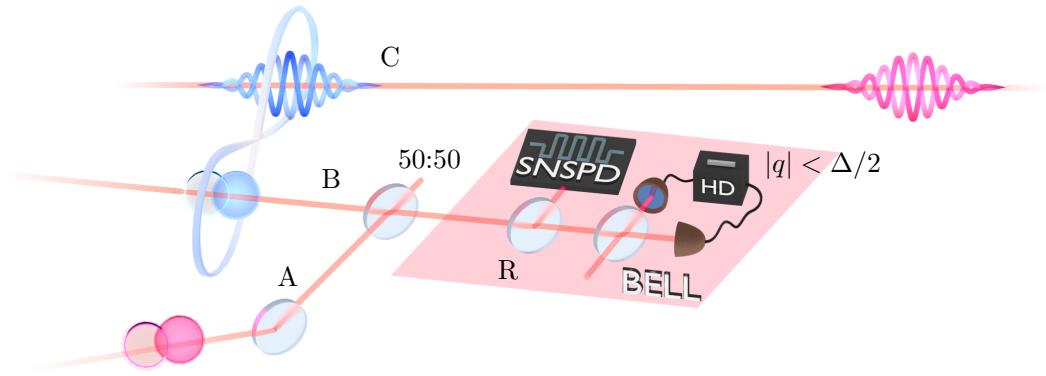

Figure 4.3: **The hybrid Bell-state measurement.** The two modes A and B are mixed on a 50:50 beamsplitter. First, a beamsplitter of reflectivity $R \ll 1$ taps the beam from one of the output ports of the beamsplitter to a SNSPD. The detection of a single-photon heralds the presence of either vacuum or single-photon states in the untapped mode. A homodyne detection setup is used to discriminate between vacuum and single-photon by applying quadrature selection. The Bell-state measurement is completed by conditioning on the measurement of quadratures $q = 0$ in a conditioning window Δ.

used since it does not distinguish between single and multi-photon components. Similarly, using only a single homodyne detector on which quadrature conditioning around large values of q is applied does not hold because the marginal distibution of the two-photon Fock-state is also important in that region. But combining a single-photon detector with a homodyne detection can lead to an improved Bell-state measurement [134, 158].

The scenario is shown in Figure 4.3 and proceeds as follow: first, a small fraction of the light is tapped on a beamsplitter of reflection R. This beam is sent to an SNSPD for heralding. It is important to choose the value of R as small as possible. Indeed the probability of tapping a single photon scale with R, while the probability of having two photons reflected scales with R^2, so that the smaller R the smaller the probability of detecting a two-photon event relative to a single-photon detection on the SNSPD. Yet this reflection should not be chosen too small otherwise the heralding rate of the BSM will not be functional. Once the click is detected, the state after the beamsplitter is projected onto the Hilbert space $\{|0\rangle, |1\rangle\}$. Then quadrature conditioning on the homodyne detection around $q = 0$ can be performed to complete the BSM by projecting the transmitted beam on $|0\rangle\langle 0|$, making sure that one and only one photon was present after mixing the two DV modes.

In the next section we will present the impact of experimental imperfections on the quality of the combined scheme, namely the requirement to select homodyne quadratures in a finite conditioning window, and the inherent losses of the homodyne detector.

2.3 Effect of losses and of a finite conditioning window

In practice, it is not possible to select on the homodyne detection only the events corresponding to the exact quadrature $q = 0$ since they have an infinitely small probability to occur. Instead we have to select the quadrature in a *conditioning window* Δ around the value of interest in the interval $[q - \Delta/2, q + \Delta/2]$. This finite conditioning window induces an overlap of the marginal distributions of vacuum and single photon that leads to an imperfect projection on vacuum which in turn degrades the fidelity of the BSM (typically the overlap amounts to 8% for a conditioning window equal to the variance of vacuum). As usual there is a trade-off between success rate and fidelity to adjust when setting the conditioning window. Homodyne conditioning corresponds to a filtering that was applied on the recorded quadrature results and thus corresponds to post-processing. It does not yet correspond to post-selection since the quadrature filtering can in principle be implemented in real time to act as a heralding method.

An experimentally implemented homodyne detector inevitably includes detection losses, which constitutes the second source of experimental imperfections. These losses take into account the propagation up to the detection, the interference visibility with the local oscillator, the efficiency of the photodiodes, the electronic noise, etc. These overall detection losses are equivalent to a loss of photon in the environment that impact the fidelity of the BSM. Indeed, when selecting quadrature values around $q = 0$, the state measured can actually correspond to a single photon that has been lost before being detected, and in that case the BSM detects a two-photon state. The higher the detection losses the lower the fidelity of the BSM. Importantly, we note that when using the HD for the BSM it is not possible to correct for the detection losses, so that they have to be minimized as much as possible. In the last section of this chapter we will detail the experimental implementation of this BSM and how the losses are minimized.

After describing intuitively our hybrid BSM, we will now study its performances theoretically with an analytical model taking into account all these experimental imperfections. We will focus on two figures of merit that are the *fidelity* of teleportation $\mathcal{F}$, i.e. the ability of the BSM to transfer qubit or entangled state without altering them, and the *efficiency* of the BSM, ε, i.e. the probability of success of the BSM. We will see that there is again a trade-off to take into account between fidelity and efficiency depending on the experimental parameters. Our hybrid BSM being passive (i.e. no active feed-forward is applied to recover the teleported state), its efficiency will always be limited to low values. What we are interested in here is to improve as much as possible the fidelity of the BSM - while still having a manageable operational efficiency - to ensure that the teleportation protocol occurs above the classical bound.

3 Hybrid Bell-state measurement for teleportation

We first study the Bell-state measurement in the context of hybrid quantum teleportation. We will consider the ideal case of a pure input qubit encoded in the Fock basis

$\{|0\rangle, |1\rangle\}$, $|\psi_{in}\rangle_A = c_0 |0\rangle_A + c_1 e^{i\theta} |1\rangle_A$ teleported to a CV qubit via a pure and maximally entangled hybrid state, $|\Psi\rangle_{BC} = \frac{1}{\sqrt{2}}(|0\rangle_B |cat-\rangle_C + |1\rangle_B |cat+\rangle_C)$. The model will include the transmission losses in the heralding path up to the SNSPD, η_{herald}, and the detection losses of the homodyne detector η_{HD}. The BSM will be parametrized by the beamsplitter tapping ratio R for the heralding and the quadrature conditioning window Δ. We will study, in particular, the behaviour of the teleportation process depending on the input qubit weight $|c_1|^2$ and phase θ.

The state after mixing the DV modes A and B on a 50:50 beamsplitter before the BSM can be rewritten from Eq. (4.4) as:

$$\begin{aligned} |\Psi\rangle_{ABC} \propto \sqrt{2} |0\rangle_A |0\rangle_B (c_0 |cat-\rangle_C) \\ + |1\rangle_A |0\rangle_B (c_0 |cat+\rangle_C - c_1 e^{i\theta} |cat-\rangle_C) \\ + |0\rangle_A |1\rangle_B (c_0 |cat+\rangle_C + c_1 e^{i\theta} |cat-\rangle_C) \\ + (|0\rangle_A |2\rangle_B - |2\rangle_A |0\rangle_B)(c_1 e^{i\theta} |cat+\rangle_C). \end{aligned} \tag{4.12}$$

We now apply the BSM. The first step consists in mixing mode C with a new mode D on a beam-splitter of reflectivity R. The single-photon detection will be performed in this new mode. Discarding the terms with no photon in D thereby not heralded gives

$$\begin{aligned} |\Psi\rangle_{ABCD} \propto \sqrt{R} |0\rangle_B |1\rangle_D |0\rangle_A (c_0 |cat+\rangle_C + c_1 e^{i\theta} |cat-\rangle_C) \\ + (R |0\rangle_B |2\rangle_D |0\rangle_A + \sqrt{2}\sqrt{1-R}\sqrt{R} |1\rangle_B |1\rangle_D |0\rangle_A)(c_1 e^{i\theta} |cat+\rangle_C), \end{aligned} \tag{4.13}$$

where we recall the beamsplitter transformations:

$$\begin{aligned} &|0\rangle_B |0\rangle_D \xrightarrow{\hat{\mathcal{B}}_R} |0\rangle_B |0\rangle_D , \\ &|1\rangle_B |0\rangle_D \xrightarrow{\hat{\mathcal{B}}_R} \sqrt{R} |0\rangle_B |1\rangle_D + \sqrt{1-R} |1\rangle_B |0\rangle_D , \\ &|2\rangle_B |0\rangle_D \xrightarrow{\hat{\mathcal{B}}_R} R |0\rangle_B |2\rangle_D + 2\sqrt{R}\sqrt{1-R} |1\rangle_B |1\rangle_D + (1-R) |2\rangle_B |0\rangle_D . \end{aligned} \tag{4.14}$$

We apply the SNSPD detection on mode D, which is described by the bucket operator $\hat{\prod}_D = \sum_{n=1}^{2} [1 - (1 - \eta_{herald})^n] |n\rangle \langle n|_D$. We recover the heralded state $\hat{\rho}_{click}$ after tracing out mode D: $\hat{\rho}_{click} = \mathrm{Tr}_D(\hat{\prod} |\Psi\rangle \langle\Psi|_{ABDC})$, that yields when tracing out mode A:

$$\begin{aligned} \hat{\rho}_{click} \propto |0\rangle \langle 0|_B (c_0^2 |cat+\rangle \langle cat+|_C + c_0 c_1 |cat+\rangle \langle cat-|_C \\ + c_1 c_0 |cat-\rangle \langle cat+|_C + c_1^2 |cat-\rangle \langle cat-|_C \\ + c_1^2 R(2 - \eta_{herald}) |cat+\rangle \langle cat+|_C) \\ + |0\rangle \langle 1|_B (c_0 c_1 \sqrt{2}\sqrt{1-R} |cat+\rangle \langle cat+|_C + c_1^2 \sqrt{2}\sqrt{1-R} |cat-\rangle \langle cat+|_C) \\ + |1\rangle \langle 0|_B (c_0 c_1 \sqrt{2}\sqrt{1-R} |cat+\rangle \langle cat+|_C + c_1^2 \sqrt{2}\sqrt{1-R} |cat+\rangle \langle cat-|_C) \\ + |1\rangle \langle 1|_B (c_1^2 2(1-R) |cat+\rangle \langle cat+|_C). \end{aligned} \tag{4.15}$$

From this expression we clearly see the need to improve the BSM by applying a measurement on mode B to distinguish between vacuum and single-photon. It is done by

applying homodyne conditioning within a conditioning window Δ centered around $q = 0$ that corresponds to the transformation:

$$\hat{\rho}_{click} \rightarrow \hat{\rho}_{tele} = \mathrm{Tr}_B(\int_{-\Delta/2}^{+\Delta/2} dq \, |q\rangle \langle q|_B \, \hat{\rho}_{click}), \tag{4.16}$$

with $|q\rangle$ the eigenvector of the quadrature operator $\hat{q}_\theta$, leading to the state:

$$\begin{aligned} \hat{\rho}_{tele} \propto A_{00}^{\Delta}(c_0^2 \, |cat+\rangle \langle cat+|_C + c_0 c_1 \, |cat+\rangle \langle cat-|_C \\ + c_1 c_0 \, |cat-\rangle \langle cat+|_C + c_1^2 \, |cat-\rangle \langle cat-|_C \\ + c_1^2 R(2-\eta_{herald}) \, |cat+\rangle \langle cat+|_C) \\ + A_{11}^{\Delta}(c_1^2 2(1-R) \, |cat+\rangle \langle cat+|_C). \end{aligned} \tag{4.17}$$

The terms $A_{ij}^{\Delta} = \int_{-\Delta/2}^{+\Delta/2} dx \, |x\rangle \langle x|_B \, |i\rangle \langle j|_B$ represent the overlap between the quadrature conditioning window and the marginal distribution of the states i and j. Noticing that $A_{01}^{\Delta} = A_{10}^{\Delta} = 0$ for all Δ, we finally obtain:

$$\begin{aligned} \hat{\rho}_{tele} \propto A_{00}^{\Delta} \, |\psi_{in}\rangle \langle \psi_{in}|_C \\ + c_1^2(2(1-R)A_{11}^{\Delta} + R(2-\eta_{herald})A_{00}^{\Delta}) \, |cat+\rangle \langle cat+|_C \, . \end{aligned} \tag{4.18}$$

In addition we can include in the model the detection losses on the homodyne detection η_{HD} by applying the transformations $A_{00}^{\Delta} \rightarrow A_{00}^{\Delta}$ and $A_{11}^{\Delta} \rightarrow \eta_{HD} A_{11}^{\Delta} + (1-\eta_{HD})A_{00}^{\Delta}$, and obtain the teleported state after complete BSM:

$$\begin{aligned} \hat{\rho}_{tele} \propto A_{00}^{\Delta} \, |\psi_{in}\rangle \langle \psi_{in}|_C \\ + c_1^2(2(1-R)(\eta_{HD}A_{11}^{\Delta} + (1-\eta_{HD})A_{00}^{\Delta}) + R(2-\eta_{herald})A_{00}^{\Delta}) \, |cat+\rangle \langle cat+|_C \end{aligned} \tag{4.19}$$

that can be renormalized to:

$$\begin{aligned} \hat{\rho}_{tele} \propto |\psi_{in}\rangle \langle \psi_{in}|_C \\ + c_1^2(2(1-R)(\eta_{HD}(A_{11}^{\Delta}/A_{00}^{\Delta}) + (1-\eta_{HD})) + R(2-\eta_{herald})) \, |cat+\rangle \langle cat+|_C \end{aligned} \tag{4.20}$$

We thus recover the initial qubit $|\psi_{in}\rangle_C$ with the addition of a squeezed-vacuum contribution that depends on c_1, R and the ratio $A_{11}^{\Delta}/A_{00}^{\Delta}$. This vacuum term is detrimental to the success of the teleportation and needs to be minimized. It increases as c_1 increases, showing directly the effect of the multi-photon component that directly translates to equivalent transmission losses. The vacuum term can be decreased by reducing the conditioning window Δ to reduce the ratio $A_{11}^{\Delta}/A_{00}^{\Delta}$. Typically a conditioning window of width σ_0 yields an overlap $A_{11}^{\Delta}/A_{00}^{\Delta}$ of 8%. The detection losses $(1-\eta_{HD})$ need also the be decreased a much as possible at fixed c_1 and BSM parameters R and Δ in order to improve the measurement. We note that the losses in the heralding path affect the teleported state only at the second order. We will see that conversely they impact drastically the BSM success rate.

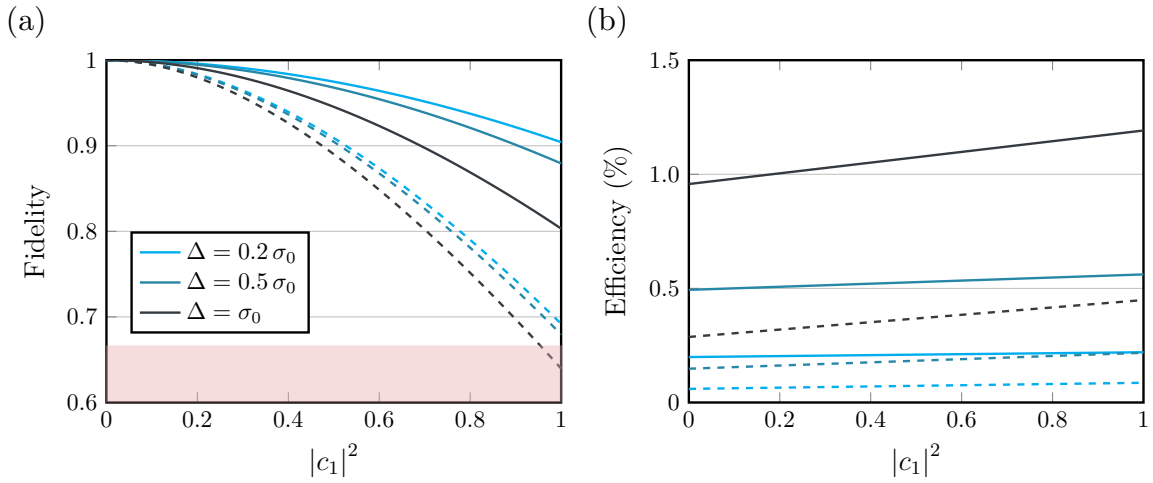

Figure 4.4: **Performance of the BSM for hybrid teleportation with a beamsplitter ratio R = 10%.** (a) Fidelity between the input and the teleported qubits and (b) efficiency of the BSM, as a function of $|c_1|^2$ for different conditioning windows Δ used for quadrature selection around $q = 0$. The classical bound for teleportation is represented by the pink region. Full lines represent a lossless heralding channel and homodyne detection, while the dashed lines take into account a transmission $\eta_{herald} = 30\%$ and $\eta_{HD} = 85\%$.

From this expression we can finally compute the fidelity with the target CV qubit, given by:

$$\mathcal{F} = \langle\phi|\,\hat{\rho}_B\,|\phi\rangle = \frac{A_{00}^{\Delta} + c_1^2(1-c_1^2)(2(1-R)(\eta_{HD}A_{11}^{\Delta} + (1-\eta_{HD})A_{00}^{\Delta}) + R(2-\eta_{herald})A_{00}^{\Delta})}{A_{00}^{\Delta} + c_1^2(2(1-R)(\eta_{HD}A_{11}^{\Delta} + (1-\eta_{HD})A_{00}^{\Delta}) + R(2-\eta_{herald})A_{00}^{\Delta})}. \tag{4.21}$$

The efficiency ε, or probability of success, of the Bell-state measurement is computed by tracing the state and re-injecting the omitted pre-factors. It can finally be written as:

$$\varepsilon = Tr(\hat{\rho}_B) = \frac{\eta_{herald}R}{4}(A_{00}^{\Delta} + c_1^2(2(1-R)(\eta_{HD}A_{11}^{\Delta} + (1-\eta_{HD})A_{00}^{\Delta}) + R(2-\eta_{herald})A_{00}^{\Delta}). \tag{4.22}$$

In this section we focus on the performances of the BSM for different qubits of weights $|c_1|^2$ (noting that the results do not depend on the phase of the input qubit θ), and the impact of the overall losses. We set for now the tapping ratio R to 10% which is the maximum value satisfying the relationship $R^2 \ll R$ - i.e. the probability of having a click coming from a single-photon on the SNSPD is preponderant relative to multi-photon events - while preserving a decent BSM efficiency. In the next section we will study the behaviour of R and Δ in details. We present in Figure 4.4 the expected fidelities and efficiency of teleportation both in the lossless case (full lines), and taking into account realistic experimental tranmission of $\eta_{herald} = 30\%$ and $\eta_{HD} = 85\%$ (dashed lines). As expected we observe a trade-off between fidelity and efficiency of the measurement. The

addition of the HD indeed improves the fidelity of teleportation, an effect increasing as the conditioning window is narrowed. The decrease of fidelity for higher value of $|c_1|^2$ results from the sensitivity of the BSM to the multi-photon components. The transmission losses before the HD strongly limits the maximum fidelity that can be reached, even with an infinitely narrow conditioning window. Still the overall fidelity does surpass the classical bound $\mathcal{F}_{classical} = 2/3$ over the whole Bloch sphere in realistic experimental conditions. The probalistic nature of our DV measurement leads to a rather low efficiency, strongly limited by the transmission losses in the heralding path of the BSM, and the small value of R that is required for the measurement. In any DV teleportation protocol, the BSM efficiency is theoretically limited to 50% since two of the four Bell-states cannot be distinguished using linear optics. On top of this, we only measure one port of the 50:50 beamsplitter mixing the DV modes which discards half of the events that can be measured. A simple scaling law would thus expect a BSM efficiency of $0.25 \times R \times \eta_{herald}$, which ultimately limits the success rate below the percent.

4 Hybrid Bell-state measurement for entanglement swapping

After studying the Bell-state measurement in the context of hybrid teleportation, we will study its performances for the swapping protocol of which the experimental implementation will be described in **Chapter 5**. The derivation is very similar to the one of teleportation, except that now we start from a pure single-photon maximally entangled state of the form: $|\Psi\rangle_{AB} = \frac{1}{\sqrt{2}}(|0\rangle_A |1\rangle_B + |1\rangle_A |0\rangle_B)$. We have to change the labels of the hybrid entangled state that is now between modes C and D: $|\Psi\rangle_{CD} = \frac{1}{\sqrt{2}}(|0\rangle_C |cat-\rangle_D + |1\rangle_C |cat+\rangle_D)$. In that case contrary to the teleportation where the BSM has to be studied for different qubits weights $|c_1|^2$, here the relative weights will be fixed at the start and we will study in more details the behavior depending on the parameters R and Δ and taking into account experimental losses $(1 - \eta_{herald})$ and $(1 - \eta_{HD})$.

We now consider the four-mode state:

$$|\Psi\rangle_{ABCD} = \frac{1}{2}(|0\rangle_A |1\rangle_B + |1\rangle_A |0\rangle_B) \otimes (|0\rangle_C |cat-\rangle_D + |1\rangle_C |cat+\rangle_D), \tag{4.23}$$

that gives after mixing the DV modes B and C on a 50:50 beamsplitter:

$$\begin{aligned} |\Psi\rangle_{ABCD} \propto & \sqrt{2} |0\rangle_B |0\rangle_C (|1\rangle_A |cat-\rangle_D) \\ & + |0\rangle_C |1\rangle_B (|0\rangle_A |cat-\rangle_D - |1\rangle_A |cat+\rangle_D) \\ & + |1\rangle_C |0\rangle_B (|0\rangle_A |cat-\rangle_D + |1\rangle_A |cat+\rangle_D) \\ & + (|2\rangle_C |0\rangle_B - |0\rangle_C |2\rangle_B)(|0\rangle_A |cat+\rangle_D). \end{aligned} \tag{4.24}$$

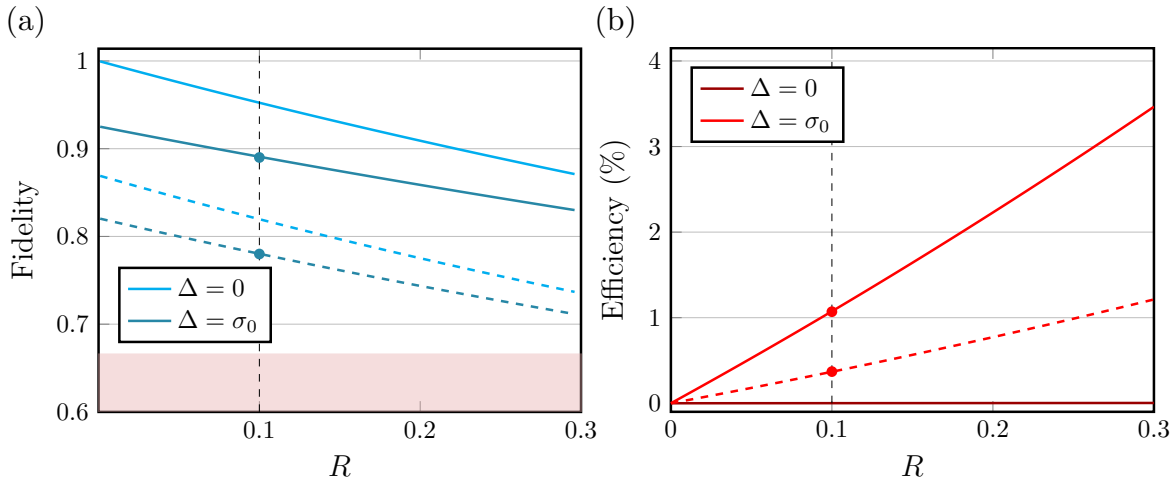

Figure 4.5: **Performance of the BSM as a function of the photon-subtracting beamsplitter reflectivity** R**.** (a) Fidelity between the swapped state and an ideal maximally entangled hybrid state, (b) Count-rate efficiency for a conditioning window $\Delta = 0$and $\Delta = \sigma_0$ with σ_0 the variance of vacuum. Dashed lines correspond to the model accounting for losses of 30% on the overall single-photon detection and 15% on the homodyne detection. $R = 10\%$ corresponds to the most practicable experimental value.

We finally apply the BSM on mode C, which gives similarly:

$$\hat{\rho}_{AD} \propto |\Psi_{in}\rangle \langle\Psi_{in}|_{AD} + \frac{1}{2}(2(1-R)(\eta_{HD}(A_{11}^{\Delta}/A_{00}^{\Delta}) + (1-\eta_{HD})) + R(2-\eta_{herald}))\, |cat+,0\rangle \langle cat+,0|_{AD}\,. \tag{4.25}$$

with $|\Psi_{in}\rangle_{AD} = \frac{1}{\sqrt{2}}(|0\rangle_A |cat-\rangle_D + |1\rangle_A |cat+\rangle_D)$.

We obtain the same results for the fidelity and efficiency as for the teleportation protocol taking into account a value of $c_1 = 1/\sqrt{2}$. This is indeed completely natural since swapping with a maximally entangled DV-DV input corresponds on average to the teleportation of a balanced DV qubit with the single photon equivalently distributed between the two modes of the DV-DV entangled state.

The corresponding fidelities and efficiencies are plotted in Figure 4.5 and Figure 4.6 as a function of R and Δ respectively. An ideal single-photon projection can be assymptotically reached when both R and Δ tend to zero. We compare the performances of an ideal BSM with vanishing R and Δ and a BSM taking realistic experimental parameters $R = 10\%$ and $\Delta = \sigma_0$ where σ_0^2 is the variance of vacuum. The ideal BSM gives an optimal fidelity of teleportation with a non-practical efficiency of zero. For realistic implementations we can see that the efficiency scales linearly with both R and Δ. The effect of loss on the heralding path and on the homodyne detection of 70% and 15% respectively are also taken into account, reducing both the fidelity and the efficiency. In any case the requirements

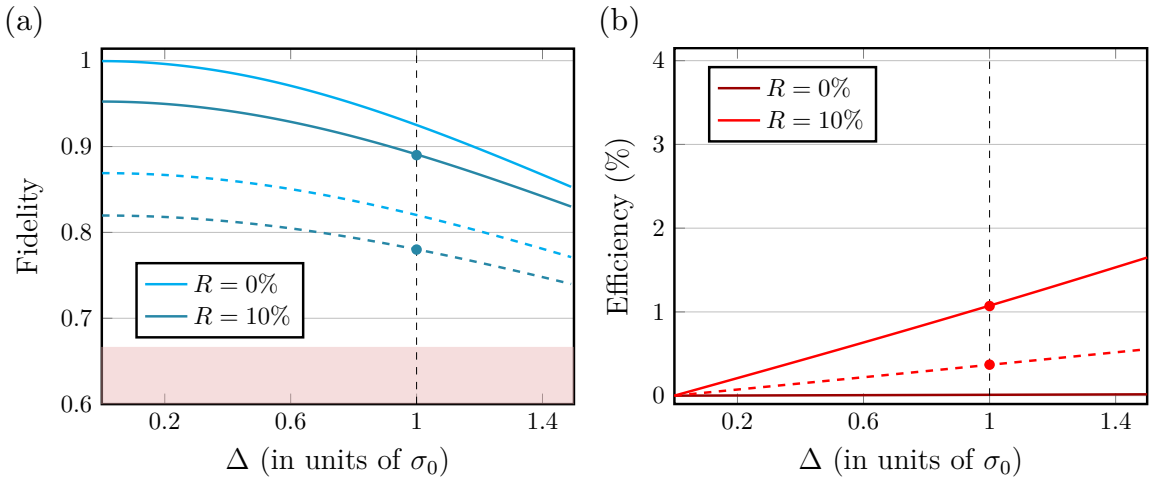

Figure 4.6: **Performance of the BSM as a function of the width of the conditioning window Δ.** (a) Fidelity between the swapped state and an ideal maximally entangled hybrid state, and (b) count-rate efficiency for a beamsplitter reflectivity $R = 0$ and $R = 10\%$. Dashed lines correspond to the model accounting for losses of 30% on the overall single-photon detection and 15% on the homodyne detection. $\Delta = \sigma_0$ corresponds to the most practicable experimental value.

of R and Δ can be strengthened or relaxed to trade between fidelity and success rate.

We can finally compute from Eq (5.5) the negativity of entanglement of the swapped state $\mathcal{N}(\rho_{AD})$, as a function of the parameters R and Δ. The evolutions are given in Figure 4.7 for different experimental parameters starting from two input maximally entangled states with a negativity of entanglement of 0.5. We note that the evolution of the negativity of entanglement naturally follows the fidelity of teleportation presented earlier. In addition here we take the opportunity to extend the range of parameters R and Δ as compared to before. We note that in the case of both R tending to 1 and Δ tending to infinity we measure a finite negativity of entanglement after swapping. This is due to the fact that even the worst scenario for BSM still heralds a statistical mixture of the input state with vacuum:

$$\hat{\rho}_{swap} \propto 0.5\,|\Psi_{in}\rangle\langle\Psi_{in}|_{AD} + 0.5\,|0, cat+\rangle\langle 0, cat+|_{AD} \tag{4.26}$$

that exhibits a negativity of entanglement of $\mathcal{N} \sim 0.1$. We will study this behaviour in a dedicated section in **Chapter 5**.

5 Experimental parameters and implementation

In this section we will present the experimental implementation of the hybrid BSM. We first study the behaviour of the BSM depending on the transmission losses of the heralding path and the homodyne detection. We then present how these losses are minimized exper-

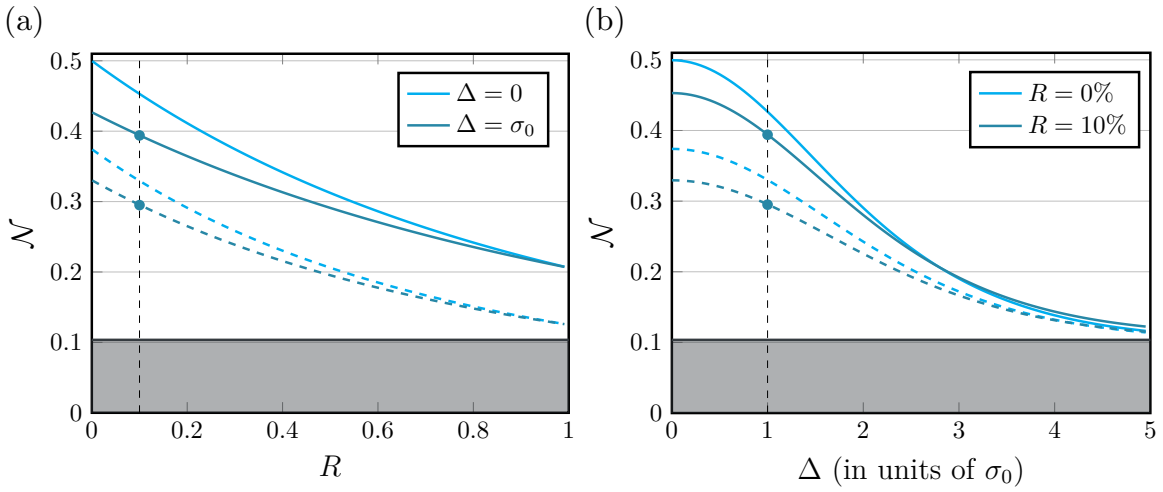

Figure 4.7: **Entanglement negativity of the swapped state depending on the BSM tapping ratio R and conditioning window Δ.** (a) Entanglement negativity as a function of the BSM tapping ratio R, for different conditioning window $\Delta = 0$ and $\Delta = \sigma_0$. (b) Entanglement negativity as a function of the BSM conditioning window Δ, for different tapping ratio $R = 0\%$ and $R = 10\%$. Full lines represent a lossless heralding channel and homodyne detection, while the dashed lines take into account a transmission $\eta_{herald} = 30\%$ and $\eta_{HD} = 85\%$. (Black line) For pure input maximally entangled states, the swapped state tends asymptotically to a evenly-weighted statistical mixture of the maximally entangled state and vacuum, for the worst BSM implementation, exhibiting a negativity $\mathcal{N} \sim 0.1$.

imentally to reach a functional BSM. Again, the hybrid Bell-state measurement presented here will be at the heart of the teleportation-based protocols implemented in **Chapter 5** and **Chapter 7**.

We present in Figure 4.8 the effect of the losses of the heralding path and of the homodyne detection on the BSM. It follows the behavior observed on the study of the BSM parameters R and Δ since these parameters can be treated as equivalent tunable losses. As can be seen, the heralding losses mostly affect the efficiency of the protocol. On the other hand the fidelity of teleportation is very sensitive to the efficiency of the homodyne detection. We note that, in particular, the classical limit of fidelity at $\mathcal{F}_{classical} = 2/3$ cannot be beaten for a BSM with $R = 10\%$ and $\Delta = \sigma_0$ for homodyne losses larger than 46%. This limit comes fundamentally from the incapability of the homodyne detection to distinguish between vacuum and single photon when the transmission decreases, and can be relaxed only very marginally by playing with the BSM parameters R and Δ. For large HD losses the BSM is defined only by the click on the SNSPD, that heralds an evenly-weighted statistical mixture between the target state and vacuum. We thus note that a great attention has to be put on the efficiency of the homodyne detection if one intends to improve the BSM by applying quadrature conditioning. Similarly the heralding losses

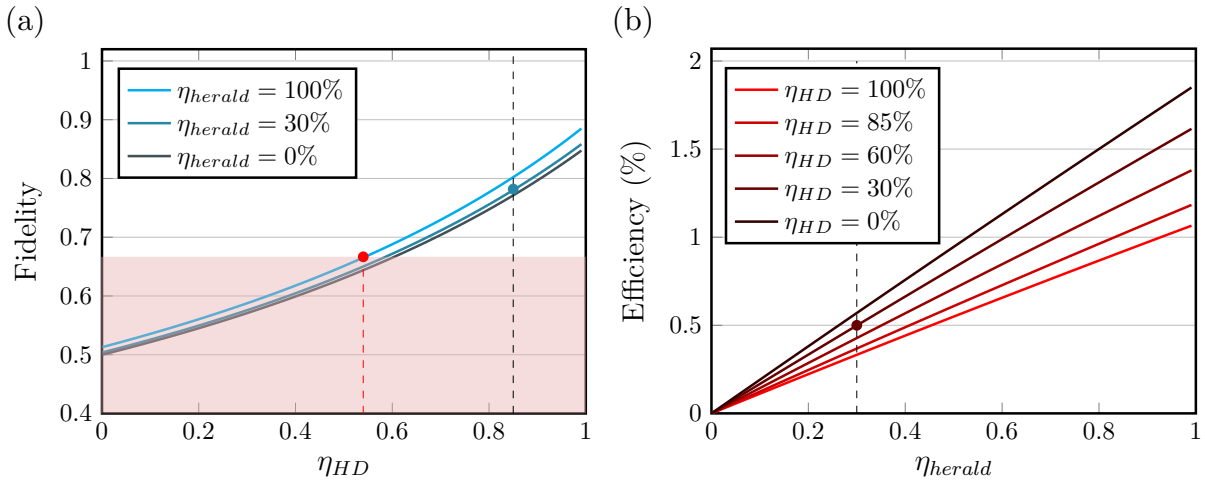

Figure 4.8: **Effect of heralding and homodyne losses on the BSM, for a tapping ratio $R = 10\%$ and a conditioning window $\Delta = \sigma_0$.** (a) Fidelity of teleportation as a function of the losses of the homodyne detection η_{HD}, for different values of heralding losses η_{herald}. The pink region represent the classical bound at $F = 2/3$. The blue point represents our experimental implementation with $\eta_{HD} = 0.85$. The fidelity depends only marginally on the heralding losses. The fidelity of teleportation decreases as the losses of the homodyne detection increase. (Dark red point) For $\eta_{HD} \leq 0.54$ the protocol does not beat the classical bound. For infinite homodyne detection losses the BSM heralds an evenly-weighted statistical mixture of the target state with vacuum. (b) Efficiency of teleportation as a function of the heralding losses η_{herald} for different values of homodyne losses η_{HD}. The red point represents our experimental implementation with $\eta_{herald} = 0.3$. The efficiency increases linearly with the heralding efficiency. Interestingly the efficiency increases - marginally - as the homodyne losses increase. This is due to the fact that the detection of vacuum on the homodyne detection is more likely to be happen as the losses of the homodyne detection increase (the variance of vacuum is smaller than the variance of a single-photon).

need to be as small as possible to reach a practicable probability of success. We will now detail how both these losses are minimized in our experimental implementation.

5.1 Mixing the DV modes

In order to perform the BSM, two DV modes have to be mixed on a balanced beamsplitter in a fully indistinguishable fashion. Any distinguishability will translate to transmission losses that will directly affect the teleported state. In particular a great attention is set on the interference visibility $\mathcal{V}$ between the two modes that leads to the corresponding losses $1-\mathcal{V}^2$. Two experimental techniques have been used to do the mixing of the spatial modes. The first one implemented in **Chapter 5** employed a plate 50:50 beamsplitter (**Altechna**

PRM-Spol-R50-1064). It allows to mix the modes with minimum extra losses induced by the absorption from the optics. The problem of this technique is that once the plate is set it is not possible to check the quality of the involved single photons since they require full transmission to the homodyne detection for efficient characterization. For that reason we decided to switch for the work of **Chapter 7** to a tunable beamsplitter employing a series of two polarizing beamsplitters (**Altechna 2-PCB-K-0125-[6R00-IBS]**) with a half-waveplate (**Altechna 2-CPW-ZO-L2-1064**) in between to adjust the transmission of the different beams depending on the task. This setting induces about $1-2\%$ extra losses due to the use of more optics components but is more convenient to check the sources from time to time.

In any case, since we work with continuous-wave single-mode beams with spatial modes properly defined by the OPO cavities, the visibility $\mathcal{V}$ can reach values above 99% yielding equivalent losses for the mixing of the DV modes of about $2-3\%$ overall.

5.2 Heralding path efficiency

As we have seen earlier, the losses on the heralding path only affect marginally the fidelity of teleportation. Yet they have a drastic impact on the probability of success that scales linearly with the transmission of the heralding mode. In that sense the heralding losses need to be minimized to reach an operational rate as high as possible. The photons of the heralding mode are subject to a filtering required to discard the non-degenerate down-converted photons generated by the OPOs. As detailed in **Chapter 2** this filtering is done by employing first an interferential filter (bandwidth 0.5 nm) followed by a home-made Fabry-Perot micro-cavity (FSR 330 GHz, bandwidth 320 MHz) that has a typical transmission of 50-60%. The filtered photons are then injected via a several-meter-long optical fiber to the SNSPD, with a coupling efficiency ranging from 90-99%. The SNSPD has itself a system detection efficiency of 85-93%. Taking into account the transmission through the optics in free space before the filtering with optical isolation, we can estimate the overall losses of the heralding mode to amount to about 70%.

5.3 Homodyne detection efficiency

The efficiency of the homodyne detection has a critical impact on the fidelity of teleportation. In particular, if the losses are too large homodyne conditioning will not be efficient enough to beat the classical bound. In our implementation the homodyne detection losses take into account the transmission in free-space up to the HD with optical isolation (**Qioptiq LINOS FR-1060-5SC**) (95%), the visibility of the signal with the local oscillator (above $(99\%)^2$), the efficiency of the photodiode (**Fermionics InGaAs FD500W-1064**) (above 97%), the electronic noise of the home-made transimpedance circuit (4% for 20 dB below vacuum noise), which corresponds overall to a homodyne detection efficiency of 85%, that is sufficient enough to see a significant improvement of the BSM. We note that this homodyne detection efficiency is really the most limiting factor of the BSM and that improving its value is crucial for reaching desirable fidelities with practicable BSM parameters.

6 Conclusion

In this chapter we have presented a hybrid discrete-variable Bell-state measurement that combines photon counting and homodyne conditioning. We have studied theoretically the performances of this BSM depending on its two parameters, namely the beamsplitter reflectivity R for the heralding, and the quadrature conditioning window Δ, both in the context of teleportation and entanglement swapping, and taking into account experimental imperfections. Finally we have estimated realistic experimental parameters for implementing this hybrid technique and quantified the limiting factors of the scheme. In the next chapters we will employ this novel BSM to perform entanglement swapping and teleportation with hybrid entanglement of light.

Chapter 5

Hybrid entanglement swapping

In this chapter we present the realization of an entanglement swapping scheme between single-photon (DV-DV) entanglement and optical hybrid (DV-CV) entanglement. By using consecutively the same optical parametric oscillators we first generate the single-photon entanglement and store one of its two modes in a free-space delay line. After an appropriate delay, this mode is brought to interfere with the DV mode a hybrid entangled state. Upon success of the hybrid Bell-state measurement, a new hybrid entangled state is created between two modes that have never interacted. This swapped state is fully characterized by two-mode quantum state tomography and the amount of entanglement in the bipartite state is numerically assessed. We theoretically study the performances of the swapping scheme as compared to direct propagation in lossy channels. In the context of quantum networks, entanglement swapping is a cornerstone capability of quantum repeaters, that opens up the prospect of connecting heterogeneous nodes, with the promise of increased integration and novel functionalities. This work was published in *Science Advances* [14].

1 Swapping for heterogeneous quantum networks

We first start by contextualizing our project in the framework of quantum networks. We will recall the most recent swapping experiments that have been performed in the optical domain for different types of encoding, and present our objectives for swapping with hybrid entanglement of light.

1.1 Previous studies: entanglement swapping with fixed encoding

Historically, entanglement swapping - the teleportation of entanglement - has been demonstrated for the first time by Pan *et al.* in 1998 [136] using DV polarization qubits with post-selection. The experimental setup, the principle of which has been explained in **Chapter 1**, is shown in Figure 5.1 (a). Two EPR sources were used to generate simultaneously each one a pair of entangled photons labeled 1-2 and 3-4 respectively. The Bell-state measurement consists in the simultaneous detection of photons 2 and 3

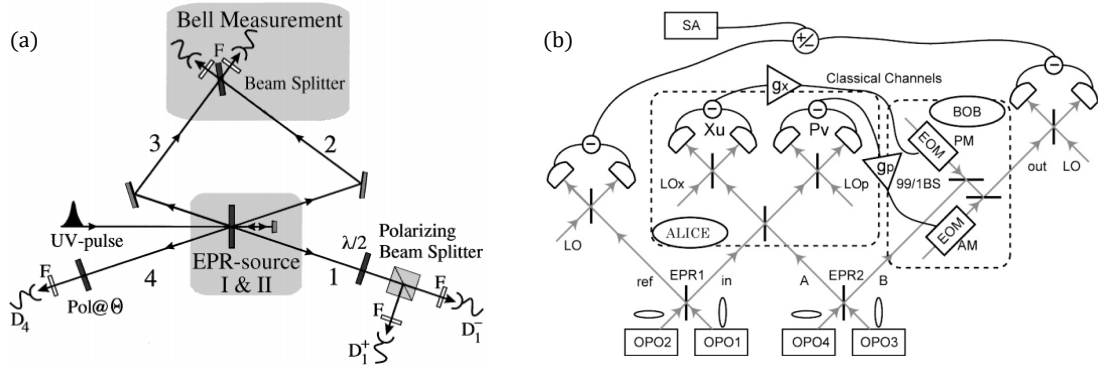

Figure 5.1: **Historical entanglement swapping setups**. (a) Experimental setup for DV qubit entanglement swapping demonstrated by Pan and collaborators [136]. The EPR sources creates two entangled photon pairs labeled 1-2 and 3-4 respectively. The BSM is performed between photon 2 and 3 and swapping is successfully performed upon detection of four-fold coincidences between photons 1-4. The correlations between photons 1 and 4 are checked by correlation measurements for different polarizer angles. (b) CV entanglement swapping as demonstrated by Takei and colleagues [204]. The EPR sources, labeled EPR1 with the modes ref and in and EPR2 with the modes A and B are two-mode squeezers. The BSM is performed between modes in and A with two homodyne detectors. The mode B is displaced according to the results of the BSM transmitted via classical channels of gains g_x and g_p. The quadrature correlations between modes ref and B are finally measured to asses the success of the swapping.

on two separate detectors labeled D_2 and D_3. In that case only the antisymmetric Bell state $|\Psi^-\rangle_{23} = \frac{1}{\sqrt{2}}(|H\rangle_2 |V\rangle_3 - |V\rangle_2 |H\rangle_3)$ out of the four Bell states, which has a two-photon fermionic statistics, can be distinguished, leading to a probabilistic scheme with a maximum efficiency of $1/4$. The swapped entanglement between photons 1 and 4 is checked by correlations measurements between D_1 and D_4 for different polarization angles. In the end four-fold coincidences are thus measured to verify that the polarizations of photons 1 and 4 are orthogonal in any polarization basis and confirm the success of entanglement swapping. One of the limitations of this scheme is that multi-photon effects, that lead to the measurement of the same coincidental events on D_2 and D_3, cannot be neglected. Therefore one must detect photons on detectors D_1 and D_4 to complete the swapping process, so that the swapped state cannot be exploited to perform any protocol afterward. This issue would be solved by the use of photon-resolving detectors [167] that can herald the creation of the swapped state only from coincidence detection between D_2 and D_3.

Unconditional, post-selection-free, entanglement swapping can be performed using CV systems. CV entanglement swapping has been demonstrated first by Jia and colleagues in 2004 [210] followed quickly by Takei and collaborators in 2005 [204] with unity gains of the classical channels. We show in Figure 5.1 (b) the experimental setup from Takei, *et al.* for clarity, but the two schemes are essentially the sames. The two independent EPR beams,

labeled EPR1 and EPR2, are generated from two two-mode squeezers. These states can be directly obtained either at the output of a type-II nondegenerate optical parametric amplifier, or by combining on a 50:50 beam splitter the single-mode squeezed vacuum states generated by two type-I OPOs. The joint Bell-state measurement is performed at a central station by mixing the intermediate CV modes in and A with a 50:50 beam splitter, and measuring simultaneously both the variances of the difference of the amplitude quadratures $\hat{x}_u = (\hat{x}_{in} - \hat{x}_A)/\sqrt{2}$ and the sum of phase quadratures $\hat{p}_v = (\hat{p}_{in} + \hat{p}_A)/\sqrt{2}$, with two optical homodyne detectors. The results, i.e the photocurrents, x_u and p_v of $\hat{x}_u$ and $\hat{p}_v$ are sent through two classical channels with respective gains g_x and g_p to Bob that recovers the entangled state by applying amplitude and phase modulations on mode B, which corresponds to a displacement of the state by $g_x x_u + i g_p p_v$. The swapping is finally assessed by measuring the quadrature correlations between modes ref and B with two homodyne detectors.

More recently, in 2015, a hybrid swapping technique combining the two optical paradigms to transfer DV-DV entanglement via CV-CV entanglement has been demonstrated by Takeda, *et al.* [211]. In their experiment the authors combined, in a "hybrid" setting, the loss robustness of DV-DV entanglement with a deterministic CV teleportation to transfer DV-DV entanglement efficiently and reliably. A maximally entangled state can then be obtained through post-selection even with a finite amount of squeezing. Even though this work demonstrated swapping using both DV and CV states, the hybrid DV-CV entanglement of light - at the heart of our work - was not involved there.

1.2 Our goal with hybrid entanglement swapping

Entanglement swapping has never been realized with a hybrid entangled state. Our goal is to implement for the first time a swapping protocol where hybrid entanglement of light is involved to link quantum nodes based on different encodings. Applying our hybrid BSM on the DV side yields then two possible scenarios. The first one, which will be described here, is the swapping between a hybrid DV-CV entangled state and DV-DV entanglement to remotely prepare hybrid entanglement, as can be seen in Figure 5.2. Swapping between two hybrid entangled states to create CV-CV entanglement is also feasible with our setup, but is less straightforward to implement for practical reasons. We will assess the quality of the implementation by measuring the negativity of entanglement for both the input states and the generated swapped state. Our input DV-DV entangled state will be based on single-photon entanglement.

In the context of heterogeneous quantum networks, the hybrid entanglement swapping protocol opens up the prospect of establishing remote hybrid quantum links to enable more versatile quantum interconnects [111]. In particular connecting disparate nodes via hybrid CV-DV entanglement of light even though one of the initial nodes were to be originating from a DV-only platform extends the range of accessible protocols, with the promise of increased integration and novel functionalities.

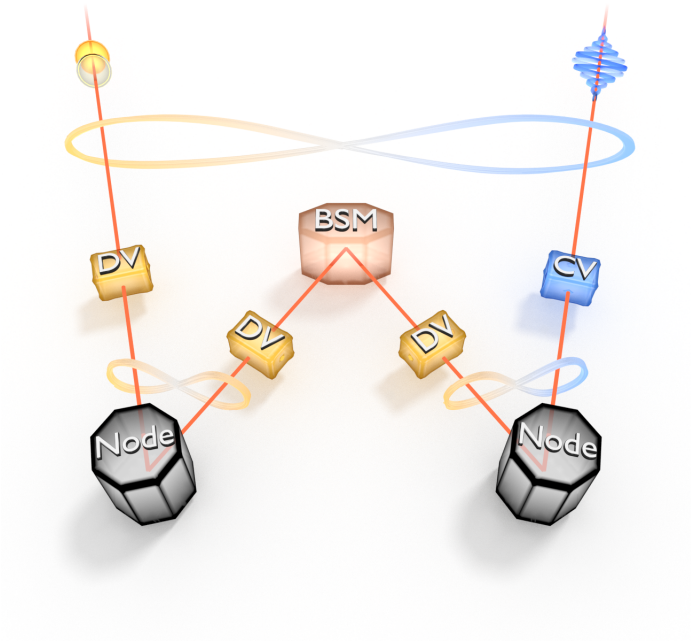

Figure 5.2: **Entanglement swapping with hybrid entanglement**. Starting from two independent entangled states, in our case single-photon DV-DV entanglement and optical hybrid DV-CV entanglement, we apply a BSM between the two DV modes to create remotely hybrid DV-CV entanglement between modes that never interacted, and thus connect quantum nodes based on different kinds of encoding.

2 Experimental setup

We present here the experimental setup we implemented to perform entanglement swapping with hybrid entanglement of light. Given the experimental resources available, i.e. only two OPOs and two SNSPDs, we propose a scheme where the consecutive use of the same resource is applied to perform the experiment in a time-multiplexed fashion. This time-multiplexing yields a rather complex setup that we will present step by step for clarity.

2.1 Consecutive use of the OPOs

The scheme presenting the consecutive use of the OPOs is shown in Figure 5.3. The creation of the initial entangled states proceeds as follow. First the type-II OPO (OPO II) is used to create a single-photon heralded by a click on SNSPD 1. Then, at a later time, the same OPO II is used jointly with a type-I OPO (OPO I) to create a hybrid entangled state with a heralding on SNSPD 2.

This consecutive creation of the inital state is made possible by the natural strong

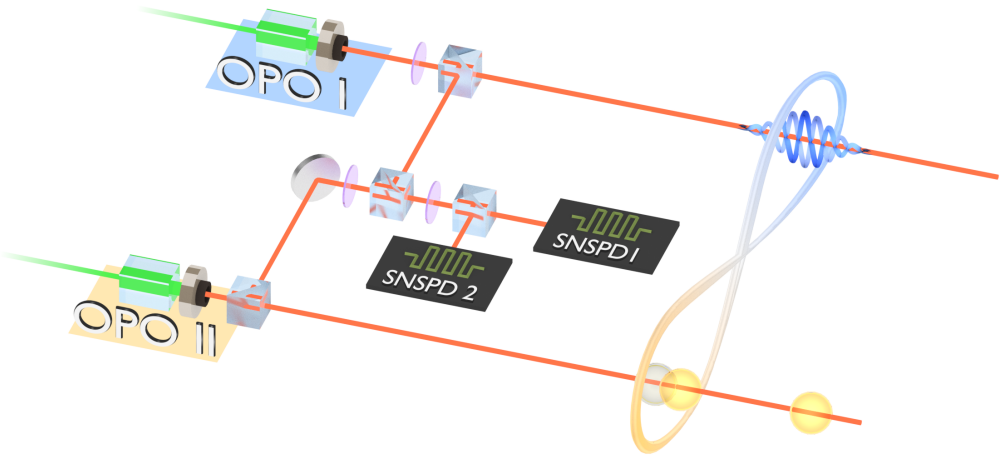

Figure 5.3: **Consecutive use of the OPOs.** A single-photon is heralded by a click on SNSPD 1 and hybrid entanglement is heralded by a click on SNSPD 2 at a later time. This consecutive creation of the states is made possible by the strong imbalance towards photons coming from OPO II on SNSPD 1 when the counts between OPO I and OPO II are balanced on SNSPD 2.

imbalance between the rates of OPO I and OPO II. Indeed, the hybrid entangled state is produced by mixing the tapped beam from OPO I with the idler beam of OPO II, and projecting them onto the same mode with two polarizing beamsplitters. The hybrid state is maximally entangled when the beamsplitters are rotated to have equal counts from each OPO on SNSPD 2. This balancing condition sets a constraint on the relative ratio of counts on the other port of the beamsplitter. With N_I and N_{II} the count rates from OPO I and OPO II respectively, a detector placed on the unbalanced port would see events at a rate $|N_I^2 - N_{II}^2|/(N_I^2 + N_{II}^2)$. Since the parametric down conversion rate of OPO II is much larger than the one of OPO I (the idler mode contains 50% of the emitted light while the tapped mode of OPO I only contains 3%) the imbalance in rates is naturally provided. At the typical pump powers used for this experiment of 6 mW for the OPO II and 15 mW for the OPO I, we have $N_I = 150$ kHz and $N_{II} = 800$ kHz, which corresponds to a fraction of about 95% of photons coming from OPO II that is used to herald a single photon on the signal mode with a click on SNSPD 1. By taking into account the purity of the initial single photon the scheme enables the creation of a single photon with a single-photon component above 80%, and the purity can be increased by tuning the relative pump powers between the OPOs. The setup in this configuration is then very close to two independent sources of single photon and hybrid entanglement at different times.

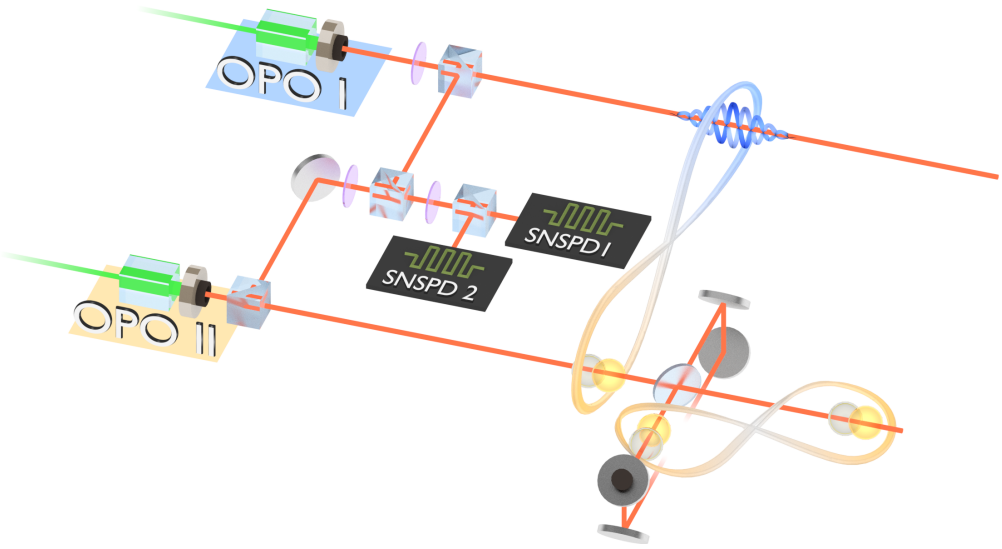

Figure 5.4: **Adding a delay line.** The single photon is sent on a 50:50 beamsplitter to create the DV-DV entanglement. One of its modes is sent to a loop-delay line. After an appropriate delay, a hybrid DV-CV entanglement is created. The DV modes interfere on the same 50:50 beamsplitter as the one that created the DV-DV entangled state.

The initial single-photon is then sent on a 50:50 beamsplitter to create a single-photon DV-DV entangled state of the form $|\Psi\rangle_{AB} = |0\rangle_A |1\rangle_B + |1\rangle_A |0\rangle_B$. Yet at that moment the DV-DV and hybrid DV-CV entangled states are still separated in time. In order to enable the mixing of the entangled states, one of the modes of the DV-DV entanglement is retarded by a free-space loop delay line.

2.2 Adding a delay line

The loop delay line is realized by a series of 15 mirrors (**Thorlabs NB1-K14**) distributed in free space so as to limit transmission losses, phase noise, and polarization instability. The delay line configuration is similar to a Sagnac interferometer [134]. The travel time inside the delay line should be long enough so as to enable the temporal discrimination of successive DV modes. The temporal mode of the states to be interfered being of the order of $\tau_{OPO} \approx 20$ ns, we choose to build a 14-m long delay line with a single-trip retardation time $\Delta t_{DL} = 47$ ns (i.e. $\Delta t_{DL} \geq 2\tau_{OPO}$). The transmission losses after one trip in the delay line are estimated to 10%. As can be seen on Figure 5.4, after creation of the DV-DV entanglement, one of the two modes propagates in the delay line. At $t = \Delta t_{DL}$ we wait for a click on SNSPD 2 to herald a hybrid DV-CV entangled state. The DV mode of the hybrid state interferes on the same 50:50 beamsplitter with the delayed mode of the single-photon entangled state. The phase of the mode propagating inside the delay line is actively controlled so as to ensure that the interfering modes arrive

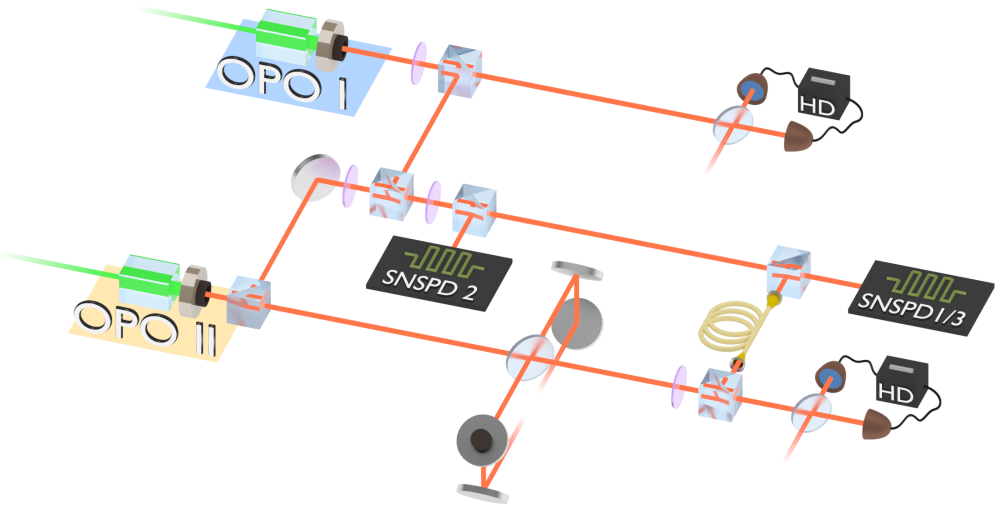

Figure 5.5: **Combining the heralding modes on the same SNSPD.** Due to our limited experimental capacity with two SNSPDs, we use the same detector (SNSPD 1/3) for heralding the DV-DV entanglement and the Bell-state measurement. We project the two heralding modes on the SNSPD mode, and delay the clicks for the BSM with a fibered delay line to ensure that the BSM occurs after the heralding of the initial entangled states.

in phase. To that end the free-space delay line is locked with a servo controller (**Newport LB1005**) on a Fano-like resonance shape obtained by slightly turning the polarization of the seed beam inside the loop before self-interference. The phase noise is estimated to be about 3%.

2.3 Delays and AOM switching of the heralding path

After mixing the two DV modes on the 50:50 beamsplitter, we apply the hybrid Bell state-measurement on one of the two DV modes. Since one of the modes is inside the delay line we cannot apply the Bell-state measurement there. Thus the BSM is performed on the beam propagating straight to the homodyne. For the Bell-state measurement we tap $R = 10\%$ of the light that is sent to an SNSPD for heralding on top of which homodyne conditioning is applied on the untapped mode. Since the cooling technique with the dipstick employed in this implementation only allowed the use of two independent SNSPDs, we decided to use the same SNSPD for heralding the DV-DV entanglement (SNSPD 1) and then herald the BSM (SNSPD 3). To that end we recombined the corresponding heralding paths with a polarizing beamsplitter to have the relevant modes co-propagate with orthogonal polarizations before the detector. The scheme is presented in Figure 5.5. The detector being polarization insensitive, we can use the same SNSPD to detect the two orthogonal photons. Nonetheless since the two events are detected on the same

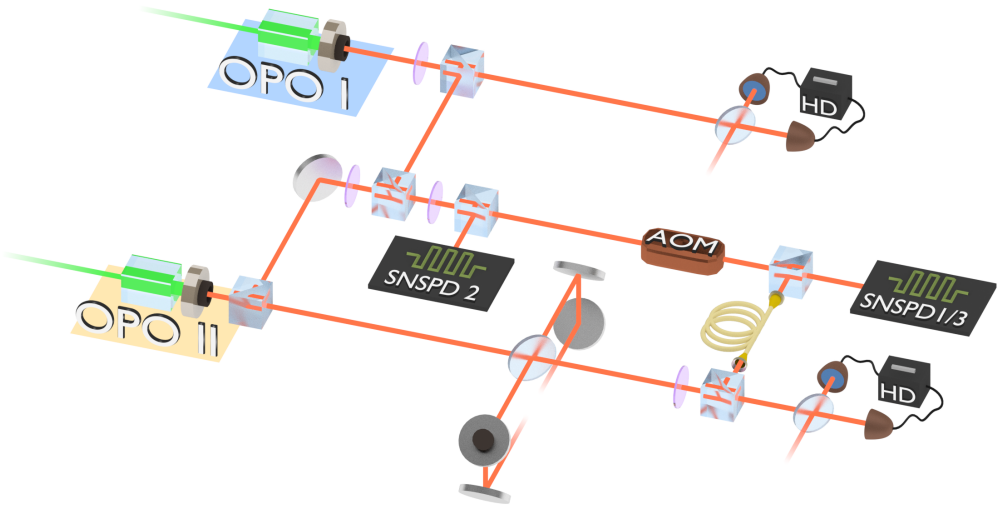

Figure 5.6: **Full setup for hybrid entanglement swapping.** A time-multiplexed detector (SNSPD 1/3) is used sequentially to herald the DV-DV entanglement and the BSM. Hybrid entanglement is heralded by SNSPD 2. An acousto-optic modulator is switched on by the first detection on SNSPD 1/3 to avoid subsequent events from the same heralding path. The delay line is experimentally realized by an optical loop in free space of delay Δt_{DL}. The heralding of the BSM is deferred by a fiber delay line until a time $t = t_{DL} + \Delta t_{fiber}$ to allow complete switching off the AOM.

SNSPD, one needs to delay one of the events to make sure that the BSM occurs after the heralding of the two input entangled states. To that end we use a fibered delay line which length must be larger than the dead time of the SNSPDs of about 100 ns. We can here use a fiber delay line since the transmission losses in the heralding mode only affect the overall count rate of the experiment and not the quality of the heralded states. After heralding on SNSPD 3 the BSM is completed by applying homodyne conditioning on the quadratures of the DV mode. We note that here, due to the looped configuration, the same homodyne detection is used to measure the DV mode of the swapped state and to perform the homodyne conditioning for the BSM.

Having the same detector heralding different states, we need to find a way to avoid measuring double events coming from the same path, as those events would be very detrimental to the success of the protocol. The rate of the Bell detection being much smaller than the one of the DV-DV entanglement creation, it can be efficiently done by switching off only the single-photon heralding path after the click is detected on SNSPD 1. To that end we use an acousto-optical modulator (**AA Opto-Electronic MT110 A1-IR**) in a single pass configuration that enables an 80% extinction of the zeroth order. This AOM is triggered directly by the electric signal originating from SNSPD 1 that is transformed in a

600 ns long pulse by a pulse delay generator (**SRS DG645**). This leads to an additional delay that is compensated by the 160-m fibered delay line (**Thorlabs SM980-5.8-125**) with a total delay of $\Delta t_{fiber} = 750$ ns that ensures both the temporal distinction of the two events on the same detector (dead time of 100 ns) and the efficient shutting of the beam by the AOM (600 ns). The complete experimental setup for swapping is given in Figure 5.6. Two high-efficiency homodyne detection setup are used to measure the swapped state that is reconstructed by two-mode quantum state tomography. Very interestingly, this time-multiplexed scheme allows the implementation of a complex experiment using minimal resources multiplexed in time. Here using only two OPOs and two SNSPDs, we can achieve a five-mode experiment conditioned on three-fold coincidences. Our scheme is completely equivalent to having two independent sources of entangled states that are then swapped by a remote BSM station. We can thus represent our setup in an expanded scheme (see Figure 5.7) with the panels representing the same resources used at different times. For clarity we will label A and B the modes of the DV-DV entangled state, and C and D the modes of the DV-CV hybrid state. With that simplified scheme in mind, let us recall the temporal list of events that needs to be achieved to complete the swapping.

2.4 Overal setup and detection sequence

First at $t = 0$ a detection event on SNSPD 1/3 heralds the DV-DV entangled state $|\Psi\rangle_{AB} \propto |0\rangle_A |1\rangle_B + |1\rangle_A |0\rangle_B$. This event triggers the shutting of the corresponding heralding path by the AOM. At $t = \Delta t_{DL}$, hybrid entanglement of the form $|\Psi\rangle_{CD} \propto |0\rangle_C |cat-\rangle_D + |1\rangle_C |cat+\rangle_D$ is heralded by a click on SNSPD 2. This ensures that the mode B, at the output of the delay line, and the mode C arrive simultaneously on the 50:50 beam splitter. The combined state after mixing is given by (c.f **Chapter 4**):

$$\begin{aligned} |\Psi\rangle_{ABCD} \propto & \sqrt{2} |0\rangle_B |0\rangle_C \otimes |1\rangle_A |cat-\rangle_D \\ & + |0\rangle_B |1\rangle_C \otimes (|0\rangle_A |cat-\rangle_D + |1\rangle_A |cat+\rangle_D) \\ & + |1\rangle_B |0\rangle_C \otimes (|0\rangle_A |cat-\rangle_D - |1\rangle_A |cat+\rangle_D) \\ & + (|0\rangle_B |2\rangle_C - |2\rangle_B |0\rangle_C) \otimes |0\rangle_A |cat+\rangle_D \end{aligned} \tag{5.1}$$

Finally at $t = \Delta t_{DL} + \Delta t_{fiber}$, the BSM is heralded by a click on SNSPD 1/3. The BSM mimics a projection on $|1\rangle\langle 1|_C$. We only consider detection events on mode C to ensure we always recover the same swapped state $|\Psi\rangle_{AD} \propto |0\rangle_A |cat-\rangle_D + |1\rangle_A |cat+\rangle_D$. The whole procedure inclusive of state preparation and filtering for successful swapping, i.e. three single-photon detections and one homodyne conditioning, occurs at a typical rate of three events per minute.

2.5 Characterization of the input states

In order to have a good estimate of the efficiency of the swapping process, we need to have a precise characterization of the initial entangled states. These states are measured independently using for each two separate homodyne detectors (HDs) and by performing two-mode quantum state tomography. To characterize the DV-DV input, we can directly

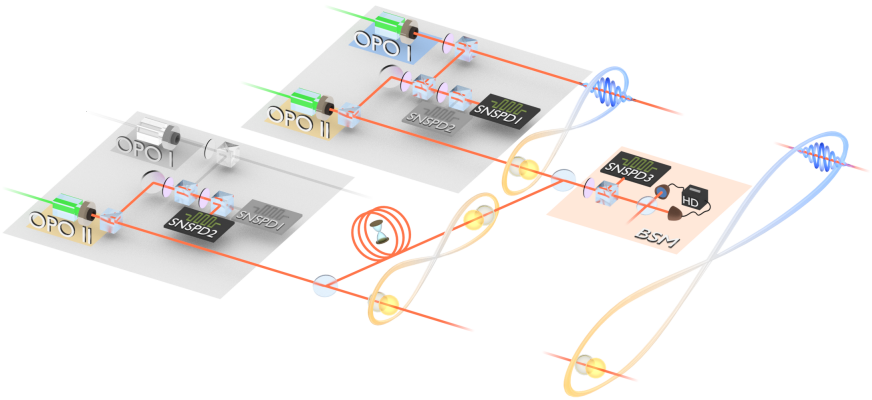

Figure 5.7: **Unwrapped experimental setup for swapping.** The sources are used at two different times to herald first the DV-DV entanglement with SNSPD 1 and then hybrid DV-CV entanglement with SNSPD 2. A delay lines holds off one of the modes on the DV-DV entangled state to enable the temporal matching with the DV mode of the hybrid entangled state. The two DV modes are mixed at the BSM station where a combination of a detection event on SNSPD 3 and quadrature measurement with homodyne detection is performed. Upon success, hybrid entanglement is heralded and high-efficiency homodyne detections are used for full two-mode quantum state tomography.

use the homodyne detection of the BSM for mode A, with an additional HD setup placed at the end of the delay line for the mode B. We show the state corrected only for detection losses corresponding to 18% on each mode. Similarly the hybrid state is reconstructed using two-mode quantum state tomography between modes C and D with this time 17% detection loss on the DV mode and 15% for the CV mode. The states are reconstructed from 600 000 and 200 000 quadratures respectively. Figure 5.8 shows the tomographic measurements of the initial entangled states. They are produced typically at a rate of 800 kHz and 300 kHz respectively. For each input state we compute the negativity of entanglement given by $\mathcal{N} = (\left\|\rho^{T_X}\right\|_1 - 1)/2$ where ρ^{T_X} is defined as the partial transpose of the two-mode density matrix ρ_{XY} with respect to mode X. For an ideal lossless state its maximal bound is 0.5. For the input states we measure 0.099 ± 0.002 for the DV-DV entanglement and 0.223 ± 0.003 for the hybrid entangled state. On top of the optical losses originating from the complex loop configuration with the delay line, these values are limited by the pump powers of the OPOs, that have been increased relative to previous works so as to obtain a decent operational rate. At this setting of the pump powers, the initial states have a slightly decreased purity relative to previous experiments in the group, reducing the measured values of negativity of entanglement.

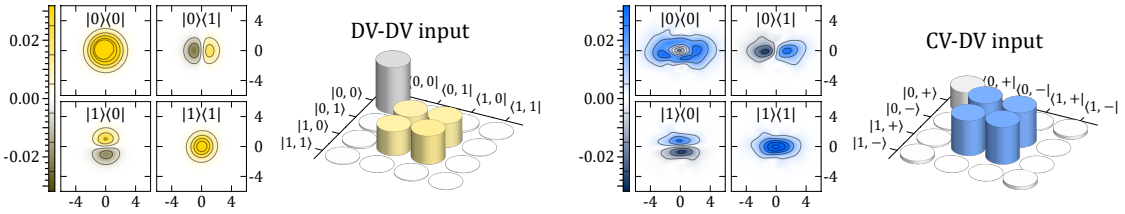

Figure 5.8: **Characterization of the initial entangled states.** All states are displayed using two representations, a hybrid density-Wigner plot and a density matrix giving the reconstructed state projected in the relevant basis, $\{|0\rangle, |1\rangle\}$ for DV and $\{|cat+\rangle, |cat-\rangle\}$ for CV. On the left (yellow) we show the input DV-DV entangled state reconstructed from 600 000 quadratures. On the right (blue) we show the input hybrid entangled state reconstructed from 200 000 quadratures. For clarity only the real part of the density matrices is shown, as the imaginary part consists of near-zero elements of magnitude smaller than 1%.

3 Swapping Results

In this section we will present the results of the hybrid swapping protocol. We will first show how the acquired data is filtered in order to recover the successful swapping events. We will then study the tomographic reconstruction of the down-sampled swapped state and estimate accurately the amount of entanglement in the system.

3.1 Identification of the events and homodyne conditioning

For the swapping experiment, the data acquisition is done by accumulating the different events and processing the data by selecting afterward the clicks that correspond to the correct events in time. This selection of the quadratures - that is only a consequence of an imperfect event filtering - does not correspond to post-selection since all the vacuum and multi-photon components of the states are taken into account. As we will see later this technique is interesting since it allows to tune the coincidence detection window manually once the experiment is performed. The drawback of this technique is that a lot of events that do not correspond to the coincidence of interest are recorded, thus yielding a much longer data acquisition and a massive weight of data.

More precisely the data acquisition is performed by accumulating three-fold coincidences in a temporal window of 900 ns. This is done by having the acquisition trigger coincide with the BSM at $t = 0$ (SNSPD 3) and recording prior event occurring up to 900 ns earlier on SNSPD 1 and SNSPD 2. We can then filter and select the triggers corresponding to the correct events in time in a given temporal window. The histograms of the events on SNSPD 1/3 and SNSPD 2 for a specific data run are shown in Figure 5.9. They are obtained from the accumulation of about 2 500 000 unfiltered events.

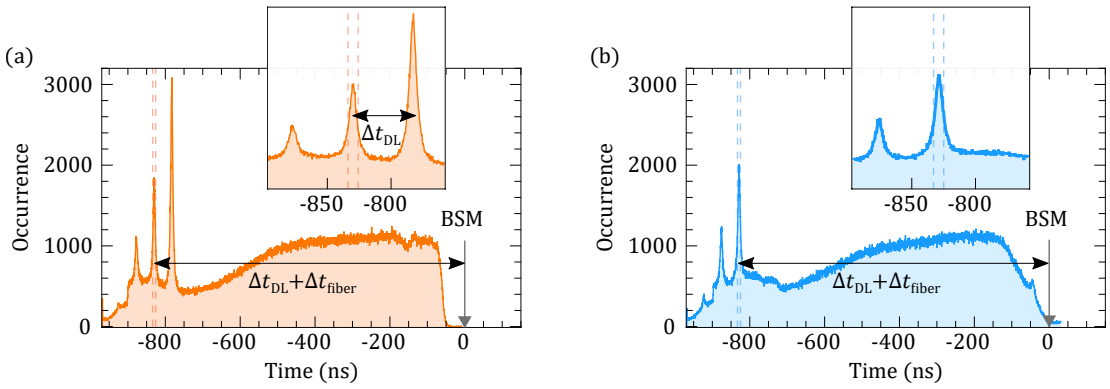

Figure 5.9: **Histograms of the detection events on the SNSPDs.** The BSM is set at $t = 0$ and prior events up to 900 ns are collected on SNSPD 1 for heralded DV-DV entanglement (a), and SNSPD 2 for the input hybrid entanglement (b). The trigger condition on SNSPD 3 defines the BSM that is temporally detected last. The noise floor level is reduced at about 600 ns where the switching by the AOM occurs. The dashed lines represent the selection window of 8 ns chosen for the time filtering.

As can be seen, several peaks can be identified on these histograms. For the SNSPD 1 (Figure 5.9 (a)), the first peak from the right at $t = -\Delta t_{fiber}$ originates from heralded single photons that arrived straight on the SNSPD without entering the free-space delay line. The second peak at $t = -\Delta t_{DL} - \Delta t_{fiber}$ corresponds to the photons that have done one turn in the delay line, which are the events of interest for our experiment. The final smaller peak at $t = -2\Delta t_{DL} - \Delta t_{fiber}$ corresponds to photons that have circulated twice though the delay. For SNSPD 2 (Figure 5.9 (b)) several peaks can be seen as well. This time, however, the events of interest are collected at $t = -\Delta t_{DL} - \Delta t_{fiber}$, that is when the DV mode of the hybrid input state comes to interfere with the delayed DV mode, forming thus the first peak of Figure 5.9 (b).

A finite noise floor level can be seen on the histograms. These events are resulting from the stochastic process of creation of the quantum states by parametric down conversion. These independent, stochastic, events carry no quantum correlations and induce a vacuum contribution that is added to our measured swapped state. The noise level is suppressed in correspondence to the peaks of interest thanks to the AOM that is used to shut the heralding path of the DV-DV entanglement at about 600 ns after the BSM. This increase of signal-to-noise ratio was key to the success of the protocol. Such problem would not perish should three independent SNSPDs be used.

Out of all these acquired events, we only select those occurring in a temporal window of 4 ns around $t = -\Delta t_{DL} - \Delta t_{fiber}$ (see dashed lines in 5.9). This preserves about 0.1% of the recorded events.

The effect of time selection can first be seen on the homodyne detection signals. On Figure 5.10 we show the variance of the homodyne signals during the 900 ns for a specific data run for the output CV and DV modes first for the unfiltered data set ((a) and (b),

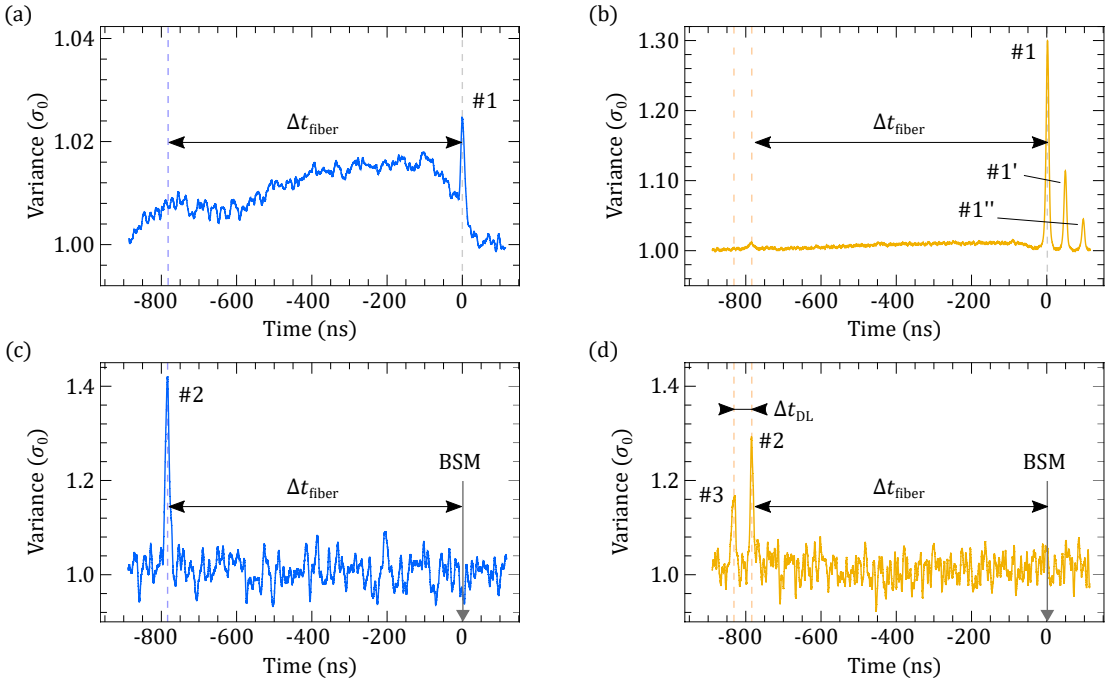

Figure 5.10: **Scanning the variance of the homodyne signals and filtering.** (a) and (b) Variance of the CV and DV homodyne signals respectively, as a function of time, before filtering. The plots are obtained from a set of 2 500 000 events. Peak #1 corresponds to the hyrid entanglement heralded at $t = 0$ when the BSM is unsuccessful. In (b) echoes of the DV mode in the delay line. (c) and (d) Variance of the CV and DV homodyne signals respectively, as a function of time, after time filtering with a temporal window of 8 ns. The plots are obtained from 3300 events. The complete disappearance of peak #1 and its echoes indicates an efficient filtering. The BSM is completed by conditioning on quadrature values around 0 in correspondence to peak #2, i.e. when the DV-DV and DV-CV entanglement are mixed. The CV and the DV quadratures of the swapped state are obtained by integrating the homodyne signals around peak #2 in (c) and peak #3 in (d).

about 2 500 000 events) and when the correct time filtering is applied to our events ((c) and (d), filtering window of 8 ns, about 900 events remaining). On these scans of the variance higher amplitudes are expected for photon-subtracted or single-photon states for the CV or DV modes respectively. For the unfiltered data, we see the emergence of a peak #1 at $t = 0$ corresponding to the input hybrid state measured on both the CV and DV homodynes when the trigger in incorrect, i.e does not correspond to the swapping. The peaks $\#1'$ and $\#1''$ at $t = \Delta t_{DL}$ and $t = 2\Delta t_{DL}$ respectively correspond to heralded single-photon echoing in the free-space delay line. The spread-out noise on the unfiltered scan of the variance for the CV mode corresponds to detected events that are not temporally aligned to the trigger.

A noticeable effect is observed on the variance scans when the correct time filtering is applied. The higher noise comes from smaller statistical sampling, which is reduced to 3300 after filtering. First we observe the disappearance of the peaks #1, #1′, and #1″ that indicate an efficient filtering since none of the input hybrid or single-photon states (that should not be expected anymore) are measured. Then, more significantly, we see the emergence of temporal-mode-shaped peaks (#2 and #3) at $t = -\Delta t_{fiber}$ and $t = -\Delta t_{DL} - \Delta t_{fiber}$. The peak #3 corresponds to the arrival of the DV mode on the HD after the trip in the free-space delay line. Peak #2 corresponds to the arrival, in coincidence, of the DV-DV and the hybrid entangled states on the 50:50 beamsplitter. The BSM homodyne conditioning is performed at time $t = -\Delta t_{fiber}$ on the DV mode. In the end the two-mode output state obtained after swapping is measured with respect to the appearance of peak #2 on the CV mode and peak #3 on the DV mode, by integration of the homodyne signals with the temporal modes centered around these peaks.

Once time filtering and homodyne conditioning are applied, the remaining quadratures of the swapped state are processed through quantum state tomography for each data run. The homodyne conditioning preserves about 30% of the filtered events. For each run we obtain about 1000 quadratures that enables us to estimated the relative phases of each data sets. By applying phase propagation to realign the different runs together, we were able to combine nine sets of data and reconstruct an entangled state from a total of 7800 filtered, conditioned, events. Each of the nine data sets required 5-7 hours of data acquisition, at an average rate of 0.05 Hz, with an active monitoring of the experiment.

3.2 Analysis of the swapped state

The swapped state is characterized by applying two-mode quantum state tomography on the filtered events, with the proper temporal modes. For the DV mode, the same homodyne is used for measuring the state and performing the Bell conditioning. In that configuration an additional 10% loss due to the low-reflectivity bleamsplitter used for the BSM photon subtraction is added. A total loss of 26% for the DV mode and 15% for the CV mode is corrected for the reconstruction. We show in Figure 5.11 the output state corresponding to the outcome when the BSM is successfully implemented (green, 7800 quadratures) and without performing the BSM in comparison (red, 200 000 quadratures). We clearly see that, given the swapping event, non-zero off-diagonal coherence terms appear - both in the hybrid density-Wigner plots and in the density matrix projected in the relevant basis - confirming the emergence of quantum correlations. Without performing the BSM the output modes are not correlated and no entanglement can be observed.

Since the conditioning for the BSM is performed after the data is acquired (yet it does not correspond to post-selection), we can study the effect of conditioning on the quality of the BSM. In the following we will refer to the Bell-state measurement carried out by only heralding the photon subtraction without conditioning on quadrature as "partial" BSM . We can note that is it not possible to do it the other way around (i.e. only performing conditioning without heralding) since the heralding is necessary to define the temporal mode of the output state. In Figure 5.12, we compare the output state when the BSM

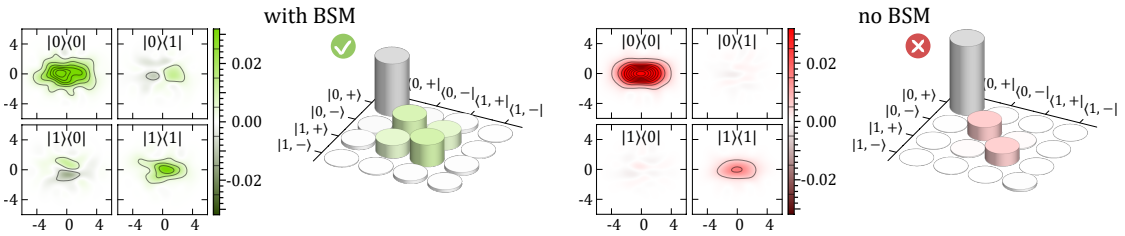

Figure 5.11: **Characterization of the swapped state.** All states are displayed using two representations, a hybrid density-Wigner plot and a density matrix giving the reconstructed state projected onto the relevant basis $\{|0\rangle, |1\rangle\}$ for DV and $\{|cat+\rangle, |cat-\rangle\}$ for CV. On the left (green) we show the output swapped state reconstructed from 7800 quadratures. For reference, on the right, (red) we show the output state when no BSM is implemented, reconstructed from 200.000 quadratures. For clarity only the real part of the density matrices is shown, as the imaginary part consists of near-zero elements of magnitude smaller than 1%.

is performed fully or partially based on the same data as the full result. The incomplete realization can directly be seen on the projected density matrix. Even though coherences can already be seen in the incomplete case, their relative amplitude is increased when the homodyne conditioning is applied, thus yielding a better entangled state. In addition the completion of the BSM depletes the vacuum component to strengthen the entanglement.

It is important to notice that without conditioning more points remain available for the tomographic reconstruction (about 26500 quadratures without conditioning, and 7800 after conditioning). This yields a smoother Wigner representation although much more quadratures should be needed to reach the quality of reconstruction of the inputs states. It

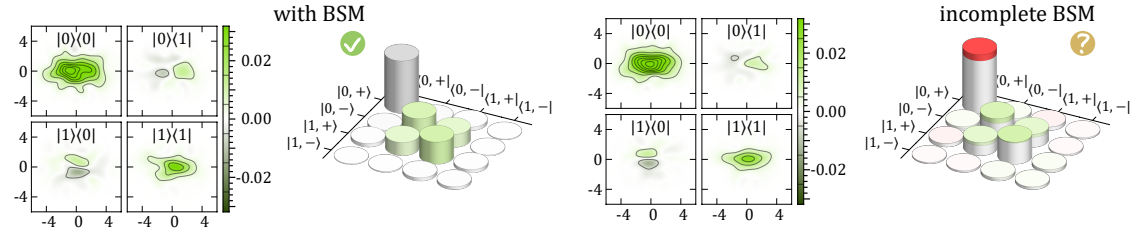

Figure 5.12: **Comparing full and partial BSM.** (Left) Output state following full BSM. (Right) Output state following a partial BSM, i.e. without homodyne quadrature conditioning. The colors on the density matrices represent the variations relative to the output state with full BSM. The number of tomographic samples for each state reconstruction is 7800 and 26500 respectively.

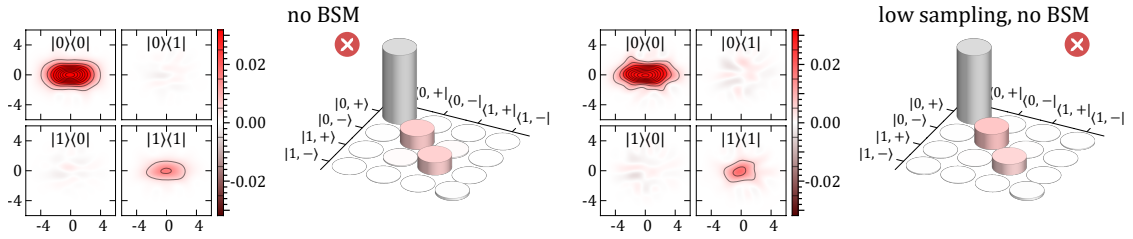

Figure 5.13: **Downsampling the reconstructed state.** (Left) Output state following no BSM. (Right) Output state following no BSM reconstructed from a downsampled data set matching that of the measured swapped state. The number of tomographic samples for each state reconstruction is 200 000 and 7800 respectively.

is then rather fair to wonder if the coherences measured are not simply artefacts resulting from a down-sampled reconstruction. To verify this hypothesis we can compare the state measured without performing the BSM to an artificially down-sampled state. The states are shown in Figure 5.13. On the left we show the state reconstructed without performing the BSM - that can in that case be reconstructed from 200 000 quadratures since we are here looking only at a two-fold coincidences events occurring at a rate of about 140 Hz. Taking a random subset of 7800 of these quadrature gives the state represented on the right. We can directly see the loss of smoothness in the Wigner representation but still no significant coherence terms can be observed neither on the Wigner representation nor on the projected density matrix. We can therefore conclude that the relative error in the reconstruction is sufficiently small and that the entanglement observed is not a product of artefacts due to limited sampling. Yet the effect of the limited sampling needs to be taken into account when quantifying precisely the amount of entanglement in the swapped state, as discussed in the following section.

3.3 Estimating the negativity of entanglement

The elements of the density matrix reconstructed by quantum state tomography are prone to higher uncertainties when a limited number of sample is available [212]. The resulting quantum state may be only partially affected as long as the absolute error is small relative to the value of the main contributing elements. Yet this becomes a fair issue when trying to estimate the entanglement of the state as high-occupancy elements (with near-zero values in the ideal case) may now acquire a finite value that statistically adds up to an overestimation of the entanglement negativity. From a measurement point of view the amount of entanglement estimated by the reconstruction then decreases as the events are accumulated and the reconstruction uncertainty decreases. It is thus very important to make sure that entanglement is still observed when the ideal tomographic precision is reached - that is of course not accessible in our case due to the limited operation rate of the experiment.

As explained empirically by Takashi, *et al.* [199], the logarithmic negativity, $E_{\mathcal{N}}$

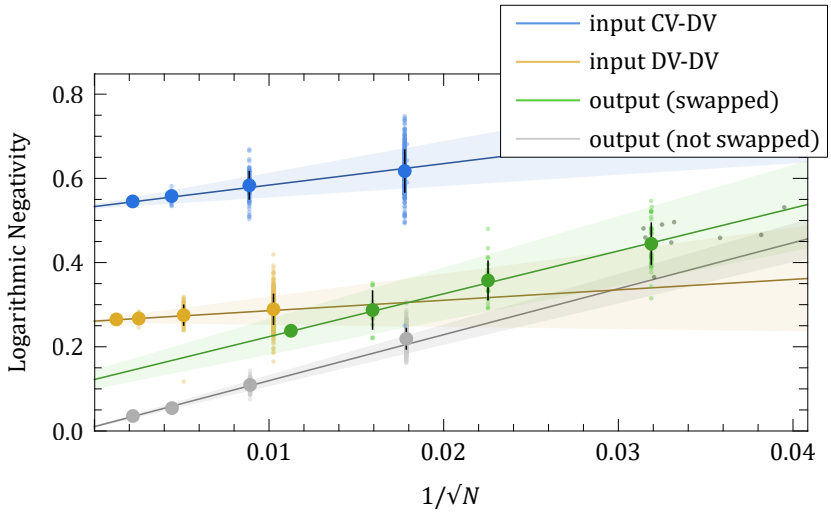

Figure 5.14: **Logarithmic negativity fits.** The logarithmic negativity of the reconstructed states is shown as a function of the inverse square root of the number of tomographic samples, $1/\sqrt{N}$, for the input states (yellow for DV-DV, blue for hybrid), the output swapped state with full BSM (green) and the state without performing the BSM (grey). The smaller dots correspond to the negativity of each individual partition. The larger dots represent the average over partitions of same size, with the leftmost point corresponding to the full data sets. In the case of the swapped output, the dark rightmost, small green dots represent the logarithmic negativities from each original experimental run, before pooling the data together.

connected to the negativity of entanglement $\mathcal{N}$ by $E_{\mathcal{N}} = log_2(2\mathcal{N}+1)$ scales in inverse proportion to the number of sample N used for reconstruction, in the form $E_{\mathcal{N}}(N) \approx E_\infty + C/\sqrt{N}$. The value E_∞ corresponds to the asymptotic value attainable from a sample of infinite size, i.e. with a maximally precise reconstruction. Thus by calculating the logarithmic negativity, for several data subsets of different sizes, we can extract the value of E_∞ and get a better evaluation of the actual negativity. The constant C represents the speed at which the reconstruction gets precise, and depends on the size of the Hilbert space used for the reconstruction of the state. A larger space is more sensitive to down-sampling errors, incrementing the rate at which a lower number of samples will be cause the negativity to be overestimated.

We show in Figure 5.14 the fits of the logarithmic negativity of entanglement for the input states (DV-DV in yellow, hybrid in blue), the swapped state (green), and the output state obtained without performing BSM (grey). Interestingly we observe that the state obtained without performing BSM shows a finite amount of entanglement measured for low-sampled states, even though these are completely uncorrelated states. For the fits we subdivide our data sets into consecutively smaller partitions. For a better sampling of statistical variations each partition is repeated six times, each time using a different randomly shuffled configuration. We then calculate the average logarithmic negativity for

partitions of the same size, and use these averaged values to fit the logarithmic negativities to obtain E_∞ for each state. We obtain 0.261 ± 0.004 for the input DV-DV entanglement and 0.533 ± 0.005 for the hybrid DV-CV input, 0.010 ± 0.002 for the output state without BSM and 0.122 ± 0.023 for the output state when the BSM is successful. Converting back these values to the negativity of entanglement we get for the input states the values given before and 0.044 ± 0.009 for the output state when the BSM is successful. We can thus conclude that we indeed create hybrid entanglement after swapping, demonstrating the ability to swap between disparate optical entangled states and to establish hybrid quantum links in heterogeneous quantum networks.

4 Propagating hybrid entanglement in networks by swapping

After demonstrating swapping, we study its performances for connecting disparate quantum nodes. Indeed swapping should allow the distribution of entanglement between nodes that would be too distant for direct propagation [92]. We develop a theoretical model to predict the propagation of entanglement as a function of the channel transmission losses, and compare different BSM implementations to direct propagation in the most resilient case of symmetric transmission losses in the two channels.

4.1 Theoretical model

Our model considers the effect of channel transmission losses applied on the DV modes of each entangled state before application of the BSM. Without losses, the input DV-DV and hybrid DV-CV entangled states can be written respectively:

$$\begin{aligned} |\Psi\rangle_{AB} &\propto |0\rangle_A |1\rangle_B + |1\rangle_A |0\rangle_B \,, \\ |\Psi\rangle_{CD} &\propto |0\rangle_C |cat-\rangle_D + |1\rangle_C |cat+\rangle_D \,. \end{aligned} \tag{5.2}$$

As shown in Figure 5.15, the channel loss η is modeled by adding a virtual beamsplitter of transmission η_B and η_C coupling modes B and C to environmental modes E and F respectively, with $\eta = \eta_B \eta_C$. After introducing losses and mixing modes B and C, the lossy state at the BSM station is given by (we keep only the terms with at list one photon in mode C since there are the ones that are heralded):

$$\begin{aligned} |\Psi\rangle_{BSM} \propto & \sqrt{\eta_B} |0\rangle_A |0\rangle_B |0\rangle_E |1\rangle_C |cat-\rangle_D |0\rangle_F \\ & + \sqrt{\eta_C} |1\rangle_A |0\rangle_B |0\rangle_E |1\rangle_C |cat+\rangle_D |0\rangle_F \\ & + \sqrt{\eta_B(1-\eta_C)} |0\rangle_A |0\rangle_B |0\rangle_E |1\rangle_C |cat+\rangle_D |1\rangle_F \\ & + \sqrt{\eta_C(1-\eta_B)} |0\rangle_A |0\rangle_B |1\rangle_E |1\rangle_C |cat+\rangle_D |0\rangle_F \\ & + \sqrt{\eta_B \eta_C} |0\rangle_A |0\rangle_B |0\rangle_E |2\rangle_C |cat+\rangle_D |0\rangle_F \,. \end{aligned} \tag{5.3}$$

We now apply the BSM to the state. This is done by first mixing mode C with a new mode G on a beamsplitter of reflectivity R and then project onto a bucket detection by

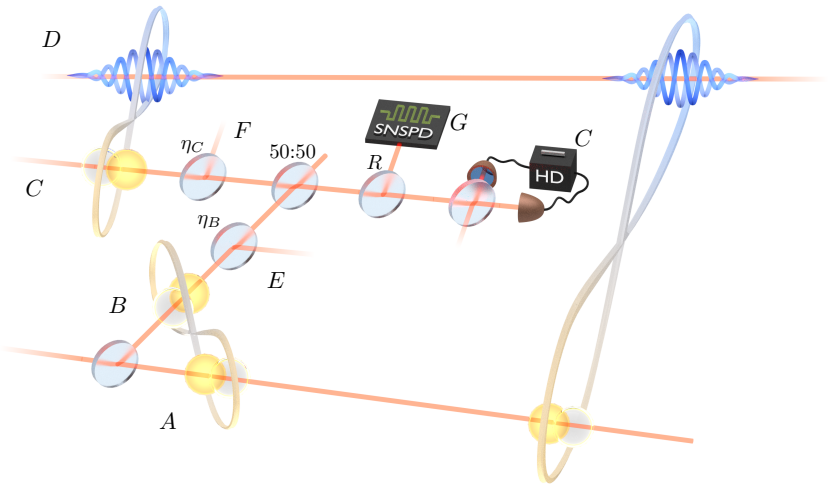

Figure 5.15: **Model for the propagation of hybrid entanglement in lossy channels via swapping.** The mode B of the DV-DV entanglement is mixed with an environmental mode E on a beamsplitter of reflectivity η_B, while the DV mode C of the hybrid entanglement is mixed with the mode F with a reflectivity η_C. The lossy modes are mixed on a 50:50 beampslitter and the Bell-state measurement is performed by sending a fraction R of the light in the mode G to apply the bucket detection $\sum_{n\geq 1} |n\rangle\langle n|_G$, while homodyne conditioning in applied on mode C.

applying the operator $\sum_{n\geq 1} |n\rangle\langle n|_G$, tracing out modes B, E, F and G gives:

$$\begin{aligned}
\hat{\rho}_{BSM}^{click} \propto |0\rangle\langle 0|_C \Big[& [\eta_B(1-\eta_C) + \eta_C(1-\eta_B) + \eta_B\eta_C R] \, |0\rangle\langle 0|_A \, |cat+\rangle\langle cat+|_D \\
& + \eta_B \, |0\rangle\langle 0|_A \, |cat-\rangle\langle cat-|_D \\
& + \eta_C \, |1\rangle\langle 1|_A \, |cat+\rangle\langle cat+|_D \\
& + \sqrt{\eta_B\eta_C} \, |0\rangle\langle 1|_A \, |cat-\rangle\langle cat+|_D \\
& + \sqrt{\eta_B\eta_C} \, |1\rangle\langle 0|_A \, |cat+\rangle\langle cat-|_D \Big] \\
+ |0\rangle\langle 1|_C \Big[& \eta_B\sqrt{2\eta_C(1-R)} \, |0\rangle\langle 0|_A \, |cat-\rangle\langle cat+|_D \\
& + \eta_C\sqrt{2\eta_B(1-R)} \, |1\rangle\langle 0|_A \, |cat+\rangle\langle cat+|_D \Big] \\
+ |1\rangle\langle 0|_C \Big[& \eta_B\sqrt{2\eta_C(1-R)} \, |0\rangle\langle 0|_A \, |cat+\rangle\langle cat-|_D \\
& + \eta_C\sqrt{2\eta_B(1-R)} \, |0\rangle\langle 1|_A \, |cat+\rangle\langle cat+|_D \Big] \\
+ |1\rangle\langle 1|_C \Big[& 2\eta_B\eta_C(1-R) \, |0\rangle\langle 0|_A \, |cat+\rangle\langle cat+|_D \Big].
\end{aligned} \tag{5.4}$$

We finally apply homodyne conditioning, corresponding to the transformation $\hat{\rho} \longrightarrow \hat{\rho}' \propto \mathrm{Tr_C}(\int_{-\Delta/2}^{+\Delta/2} dx \hat{\rho} \left|x\right\rangle \left\langle x\right|_{\mathrm{C}})$ to obtain the expression of the swapped state:

$$\begin{aligned}\hat{\rho}_{swap} \propto A_{00}^{\Delta}\Big[&[\eta_B(1-\eta_C)+\eta_C(1-\eta_B)+\eta_B\eta_C R]\left|0\right\rangle\left\langle 0\right|_A\left|cat+\right\rangle\left\langle cat+\right|_D \\ &+\eta_B\left|0\right\rangle\left\langle 0\right|_A\left|cat-\right\rangle\left\langle cat-\right|_D \\ &+\eta_C\left|1\right\rangle\left\langle 1\right|_A\left|cat+\right\rangle\left\langle cat+\right|_D \\ &+\sqrt{\eta_B\eta_C}\left|0\right\rangle\left\langle 1\right|_A\left|cat-\right\rangle\left\langle cat+\right|_D \\ &+\sqrt{\eta_B\eta_C}\left|1\right\rangle\left\langle 0\right|_A\left|cat+\right\rangle\left\langle cat-\right|_D\Big] \\ +A_{11}^{\Delta}\Big[&2\eta_B\eta_C(1-R)\left|0\right\rangle\left\langle 0\right|_A\left|cat+\right\rangle\left\langle cat+\right|_D\Big],\end{aligned} \tag{5.5}$$

defining $A_{ij}^{\Delta} = \mathrm{Tr_C}(\int_{-\Delta/2}^{\Delta/2} dx \left|x\right\rangle \left\langle x\right|_{\mathrm{C}} \left|i\right\rangle \left\langle j\right|_{\mathrm{C}})$, and noticing that $A_{ij}^{\Delta} = 0$ if $i-j = \pm 1$. The final result is obtained by applying the model losses $(1-\eta_{HD})$ to the HD of the BSM, which is equivalent to applying the transformation $A_{11}^{\Delta} \rightarrow \eta_{\mathrm{HD}} A_{11}^{\Delta} + (1-\eta_{\mathrm{HD}}) A_{00}^{\Delta}$.
The first and the last terms of Eq.(5.5) correspond to pure losses added to the maximally entangled state and should be minimized for optimal transmission. Fixing $\eta = \eta_B\eta_C$ one notices that the first term is minimum for $\eta_C = \sqrt{\eta}$, i.e for symmetric losses. We will thus show the theoretical predictions in the most resilient case of symmetric losses on the two channels ($\eta_B = \eta_C = \sqrt{\eta}$). In this symmetric case we have:

$$\begin{aligned}\hat{\rho}_{swap} \propto A_{00}^{\Delta}\Big[&[2(1-\sqrt{\eta})+\eta R]\left|0\right\rangle\left\langle 0\right|_A\left|cat+\right\rangle\left\langle cat+\right|_D \\ &+\left|0\right\rangle\left\langle 0\right|_A\left|cat-\right\rangle\left\langle cat-\right|_D \\ &+\left|1\right\rangle\left\langle 1\right|_A\left|cat+\right\rangle\left\langle cat+\right|_D \\ &+\left|0\right\rangle\left\langle 1\right|_A\left|cat-\right\rangle\left\langle cat+\right|_D \\ &+\left|1\right\rangle\left\langle 0\right|_A\left|cat+\right\rangle\left\langle cat-\right|_D\Big] \\ +\Big[&\eta_{HD}A_{11}^{\Delta}+(1-\eta_{HD})A_{00}^{\Delta}\Big]\Big[2\sqrt{\eta}(1-R)\left|0\right\rangle\left\langle 0\right|_A\left|cat+\right\rangle\left\langle cat+\right|_D\Big].\end{aligned} \tag{5.6}$$

We note that, as losses increase, the probability of observing a click due to the presence of two input photons before mixing on the 50:50 becomes dominant, leading in the case of an infinitely lossy channel to the expression:

$$\hat{\rho}_{swap} \propto 0.5\left|\Psi\right\rangle\left\langle\Psi\right|_{AD} + 0.5(\left|0\right\rangle\left\langle 0\right|_A\left|cat+\right\rangle\left\langle cat+\right|_D). \tag{5.7}$$

Starting from maximally entangled input states, this would lead to an entangled state with a negativity of entanglement $\mathcal{N}$ of about 0.1. We will now adapt our model to the case of non-maximally entangled input states in order to fit to our experiment.

4.2 Model with realistic input states

Realistic experimental input entangled states are obviously composed of a statistical mixture with fully mixed classical superpositions and with vacuum. Fitting our measured

experimental input states in this way, we can express them as:

$$\begin{aligned}\hat{\rho}_{AB} \propto |\Psi\rangle\langle\Psi|_{AB} &+ 0.025(|0,1\rangle\langle 0,1|_{AB} + |1,0\rangle\langle 1,0|_{AB}) \\ &+ 0.97 \times |0,0\rangle\langle 0,0|_{AB}\,, \\ \hat{\rho}_{CD} \propto |\Psi\rangle\langle\Psi|_{CD} &+ 0.0235(|0,cat-\rangle\langle 0,cat-|_{CD} + |1,cat+\rangle\langle 1,cat+|_{CD}) \\ &+ 0.438 \times |0,cat+\rangle\langle 0,cat+|_{CD}\,.\end{aligned} \tag{5.8}$$

Following the same reasoning as before, we can compute the experimental swapped state as:

$$\rho_{\text{swap}}^{\text{exp},0} = \text{Tr}_{\text{BCEFG}}\Big(\int_{-\Delta/2}^{+\Delta/2} dx\,|x\rangle\langle x|_{\text{C}} \sum_{n\geq 1} |n\rangle\langle n|_{\text{G}}\, B_{\text{CG}}^{1-R} B_{\text{BC}}^{\frac{1}{2}} B_{\text{BE}}^{\eta_{\text{B}}} B_{\text{CF}}^{\eta_{\text{C}}} (\rho_{AB}\otimes\rho_{CD})\Big), \tag{5.9}$$

where B_{XY}^{T} is the beamsplitter operator of transmission T mixing modes X and Y.

To that final expression we have to add as well the effect of false positive events and dark counts. False positive events appear naturally in the scenario with two SNSPDs since double events that do not correspond to swapping can be detected. The use of the AOM mitigates that effect, yet its effect does not become negligible since the AOM has an imperfect extinction of about 80%. The integration of the histograms of the events shown in Figure 5.9 over the 8 ns time-window selected for the filtering represents a large contribution of the false positive events, close to 40% as compared to the swapping events. Another effect to be taken into account is the dark count rate of the single-photon detectors. Although this might looks marginal relative to the generation rate of the states, it becomes dominant as losses increase and the overall rate decreases. At zero loss, we measure the ratio called η_{dc} to be about one over a hundred positive event. This leads to a refinement of the model to obtain the expression:

$$\rho_{\text{swap}}^{\text{exp}} = 0.6\rho_{\text{swap}}^{\text{exp},0} + 0.4\,|0,\text{cat}_+\rangle\langle 0,\text{cat}_+| + \frac{\eta_{dc}}{\eta_{\text{B}}\eta_{\text{C}}}\,|0,\text{cat}_+\rangle\langle 0,\text{cat}_+|\,. \tag{5.10}$$

4.3 Propagation results

Having our full model in mind, we can quantitatively study the distribution of hybrid entanglement using the swapping process. We study different BSM configurations (i.e. full BSM and partial BSM) and compare our values to what would be obtained by directly propagating entanglement in the channels (for symmetric losses in the two channels), both in the case of ideal maximally-entangled input states and with our experimental inputs. The results are shown in Figure 5.16. The white point indicates our measurement, in good agreement with the simulations. As can be seen, direct propagation of hybrid entanglement in lossy channels leads to an exponential decrease of the amount of entanglement with the distance. Moreover swapping would beat direct propagation after a given distance, which depends on the quality of the initial resources. Under our experimental conditions, swapping beats direct propagation for losses of about 9 dB (which corresponds

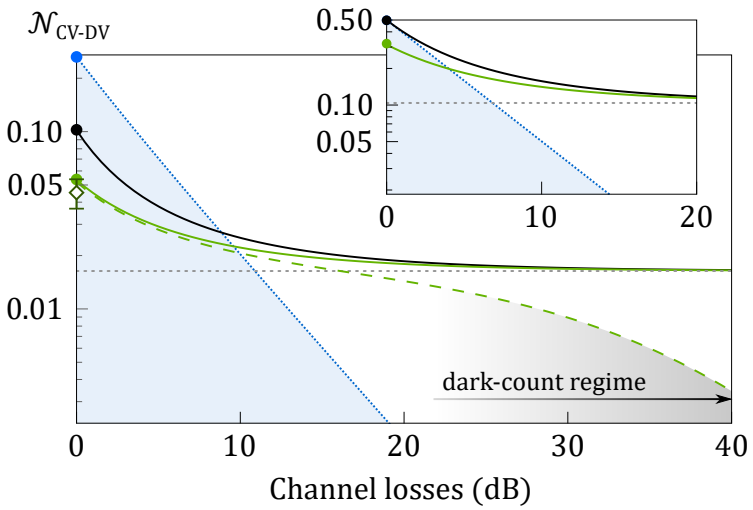

Figure 5.16: **Swapping for distributing hybrid entanglement at a distance.** We represent the expected entanglement negativity after swapping of the experimental input states as a function of channel losses considered symmetric for the two channels. The black solid line corresponds to an ideal BSM with vanishing reflectivity R and quadrature conditioning window Δ, while the green line corresponds to our implemented case. The grey dotted line corresponds to partial BSM without conditioning. The effect of dark counts (about 1% of the total events) is represented by the green dashed line. The white point gives our measured output negativity, in good agreement with the simulations. As a reference the blue line shows the evolution of the negativity for direct propagation. The inset provides the same plots but starting from ideal maximally entangled inputs states and without dark counts.

to about 45 km of fiber at telecom wavelength). For maximally entangled input states the effect is even more stringent since the improvement is reached after about 4 dB of losses, which corresponds to about 20 km of fibers at telecom wavelength. We note that in both cases homodyne conditioning leads to an improvement of entanglement distribution (as compared to partial BSM), an effect that is even more noticeable over shorter distances and with maximally entangled input states.

Of course, ultimately, any practical implementations will be limited to the heralding rate of the initial states and its ratio relative to the dark counts of the detectors. In our experiment, with a ratio of about 1/100, we expected a substantial decrease of the negativity from 20 dB of channel losses. The results confirm the performance of the swapping protocol and that its demonstration over longer distances could be achieved in future implementations. We can finally observe that the swapping protocols only ensures a slower decrease of the entanglement via propagation. If one wanted to recover entanglement some active protocols should be applied to the states. Such purification schemes for hybrid entanglement are currently under study [213], but they go unfortunately out of the scope of this thesis.

5 Limitations of the setup with two OPOs and two SNSPDs

After demonstrating swapping with hybrid entanglement, we will now study the limitations of the setup involving the consecutive use of the OPOs and of the SNSPDs. Indeed, even if, a priori, the time-multiplexed use of the same resources enables the implementation of complex schemes, it definitely leads to side effects which decrease the quality of the initial resources and of the protocol itself. We show how these effects shall be mitigated in order to achieve more scalable protocols.

5.1 Consecutive use of the OPOs: limited rates and transmission losses in the delay line

The most natural limitation that occurs when using consecutively the same OPO at different times is a reduction of the overall rate, typically by a factor 2 as compared to a scenario where several OPOs are used to create the states independently. It is particularly important for our experimental implementation in which the low generation rate of the initial resources limits the number of quadratures that can be measured to perform the two-mode quantum state tomography. In our case we obtain an overall operation rate of 0.05 Hz, that required about 45 hours of data acquisition to recover 7800 quadratures, that is at the limit of what can be used to have a trustworthy characterization of the two-mode swapped state where 200 000 quadratures are typically used [212]. In order to have a decent rate we also had to increase the pump power of the different OPOs which led to stronger multi-photon components in turn degrading the quality of the input states. Finally we were forced to use a quite large filtering temporal window for the coincidental detection, which in our case was chosen to be 8 ns, i.e. larger than the temporal mode FWHM of the photons of 5 ns. If the chosen selection window is too large, events corresponding to photons that have not interfered are detected, thus yielding the admixture of vacuum to the swapped state. In order to get a clean coincidental detection, the window should be of the order of about 1 ns, which was not accessible with the experiment in that configuration.

The second consequence of the consecutive use of the OPOs is the necessity to use a delay line to temporally rematch the modes. Even in free space the delay line induces some non-negligible transmission losses that limit the purity of the states and the quality of the process. In our specific scheme in which the losses amount to about 10%, it limits considerably the range of accessible states that can be created and teleported, especially when other sources of loss, such as the OPO intra-cavity losses or the homodyne detection losses, cannot be neglected. We note that other works have shown the same type of free-space delay lines - and even optical memories - having losses below the percent level [214, 215], making them as promising resources for quantum state engineering and quantum information processing.

Finally, when using a looped configuration, the photons are always propagating in the same spatial mode so that they need to be redirected if one wants to have them propagating freely. Overcoming this feature would include the use of a longer delay line and optical switches in order to deliver the desired propagating mode in time. Even though this goes

out of the scope of this thesis, we note that it is feasible, yet with non-zero losses, using existing technologies [216].

The experimental setup with the looped delay line was originally not implemented for swapping but for the teleportation of a DV qubit. Indeed once the DV-DV entangled state is created one can perform homodyne conditioning on the mode propagating straight to the HD to create a DV qubit inside the delay line. However defining properly the phase of the qubit requires to be able to lock the delay line relative to the local oscillator of the HD that acts as a phase reference. Since no assumption should be made on the unknown state to-be-teleported, the phase of the local oscillator of the homodyne detection must be randomized, so that the phase of the delay line should be adjusted in consequence in real time. This is not in theory impossible but it requires as very challenging lock to be implemented, especially since the delay line is 14 m long. On top of the challenging lock, it also introduces a conceptual problem since the setup has to be adapted to the input qubit, which should not happen in a standard teleportation protocol. In the end we saw that without performing this homodyne conditioning the DV-DV entanglement was directly available and could be used to perform the swapping with only having to lock the delay line on resonance.

Using independent OPOs would complety aleviate these issues. First it would lead to an increase of the overall operation rate that does not require to use input states with a lower purity and a filtering window injecting vacuum in the measured state. In addition using another OPO to create the DV qubit, or DV-DV entanglement, would enable a separate definition of the qubit phase, that could be easily actively adjusted by locking the relative phase of the two DV modes in an unlooped configuration.

5.2 Consecutive use of the SNSPDs: imperfect event detection

Having to use the same SNSPD for heralding the DV-DV entangled state and the BSM appears to be the experimental limitation degrading the most the quality of our implemented swapping scheme. As we have seen before it leads to the measurement of double-events coming from the same path that do not correspond to the swapping event. Even though this effect is drastically improved by the use of an AOM on the heralding path of the DV-DV entanglement to reduce the background stochastic noise, we see that it still corresponds to an admixture of vacuum of 40% which can be detrimental for the implementation of many protocols. A possible improvement of the scheme would be to add a second synchronized AOM on the path corresponding to the BSM, that would lead to a reduction by a factor five of false positive events, lowering their proportion from 40% to 8%. Still the AOM not having a perfect extinction, the effect would only be mitigated but not fully eliminated. One could also imagine using mechanical shutters to alleviate this problem, but their typical extinction time is longer by few orders of magnitude and would thus require a challenging extension of the delay line. We also note that its leads to a non-trivial distribution of the events in time that requires an accurate data analysis for the filtering and conditioning. In our case, the filtering can also be done only a posteriori, which extends drastically the data acquisition and processing durations since

only a ridiculous amount of the data acquired - in the end less than 0.04% - is finally useful. In the end the same use of the SNSPD also limits the maximum rate at which the experiment is performed since an event cannot be detected during the dead time of the SNSPD. This does not impact our work in which the operational rate is at the hertz level, but it can be detrimental when fast rates are desired [217, 218].

An evident solution of all of these issues would be to use three independent SNSPDs. In that case, since the heralding paths are completely separated no contamination from double-events can occur and a proper coincidental detection can be performed. In addition the use of three SNSPDs makes the detection of coincidences much easier since the delays can be calibrated and adjusted independently to make the desired events happen in a very specific time window. In this case the only limiting factor remaining is the dark count rate of the SNSPDs which corresponds to less of a percent of the initial states rates, and thus yields three-fold coincidence rates that have negligible likelihood to be detected.

6 Conclusion

In this chapter we have presented an entanglement swapping scheme based on the hybrid entanglement of light. We presented the experimental methods allowing to generate the necessary resource states in a time-multiplexed fashion. We completely characterized both the input and output states to confirm the success of the swapping protocol. The effects of down-sampling for the reconstruction of the swapped state have been studied extensively and the amount of entanglement in the systems were precisely assessed by fitting of the logarithmic negativity of entanglement. We have proposed a theoretical model that reveals the usefulness of the protocol for propagating hybrid entanglement in prospective heterogeneous quantum networks. Finally, we have presented the limitations of our experimental setup involving the consecutive use of the same resources.

Our work has thus introduced and demonstrated an entanglement swapping protocol that connects nodes with different optical encodings. This capability is central for the establishment of remote hybrid quantum links and the development of heterogeneous quantum networks, enabling more versatile quantum information interconnects. In the next chapter we will focus on the two main improvements that have been implemented on the setup, namely the building of a new OPO-based single-photon source and a cryogenic system that enables the use of four independent SNSPDs in parallel. This brings within reach even more ambitious quantum information processing protocols, such as the hybrid quantum teleportation that we will present in **Chapter 7**, and, in the future, the extension of hybrid entanglement to different encodings and devices.

Chapter 6

Reaching advanced quantum information protocols with an increased experimental capability

Following the analysis of the entanglement swapping protocol, we present in this chapter the two major assets that have been built to improve our experimental setup. We first designed a new type-II OPO-based heralded single-photon source that enables for the first time the use of several triply-resonant OPOs in parallel, a difficult task due to the limited number of parameters accessible experimentally for setting of the resonances. We present a technique allowing to create, from this OPO, any high-purity single-rail discrete-variable qubits encoded in the Fock basis $\{|0\rangle, |1\rangle\}$. In addition we introduce an improved heralding system composed of a cryogenic unit enabling the use of four independent SNSPDs. These additional tools bring within reach more advanced quantum information processing protocols that could not yet be performed efficiently due to a lack of resources, i.e. only two OPOs and two SNSPDs.

1 Adding a single-photon source based on a straight-cut linear cavity OPO

1.1 Motivations

Heralded single-photon sources are essential to the development of quantum information processing. Yet, increasing the number of photons involved in quantum optics experiment is a very challenging task because of an unoptimized scalability that increases linearly the number of required resources and the complexity of the overall experiments [219, 220]. Protocols have for now been limited to several modes, with record experiments going up to tens of photons at most [40, 221, 222, 223]. Several routes can be considered to mimic the behaviour of multiple independent photons. In particular the consecutive use of the same resources in time-multiplexed looped configurations [78, 79, 224, 225] can

efficiently simulate complex quantum networks. Yet, they do not always represent real-world protocols and they often lack of control over the optical modes involved which in turn translates into channel noise detrimental to many protocols.

In our particular case with the swapping experience presented in **Chapter 5**, the consecutive use of the OPO II and the required looped delay line led to at least 10% transmission losses on the state generated and required a very challenging phase control. Even though we managed to demonstrate swapping, we see that the quality of the involved states was really at the limit of what was required to prove that entanglement was present in the end. Having two completely independent type-II OPOs would not only eliminate these drawbacks, but would also offer a flexibility that permits the implementation of new protocols by mixing the non-Gaussian sources in creative ways. For that reason we decided to build a new type-II OPO to be used in parallel with the resources initially available on the experiment. Yet, as we will see in the next section, operating experimentally two type-II OPOs simultaneously is a challenging goal, as the semi-monolithic cavity configuration limits the number of experimental parameters which can accessed for the setting of two independent triple resonances.

1.2 Design considerations

Building a new type-II OPO, which combines in a unique device two single-mode squeezers, is not a trivial task. A particular attention has to be put on the design of this source since it has to be operated concurrently with the two OPOs already available on the experimental table. In addition the quantum states generated from the different OPOs need to be indistinguishable.

Let us first focus on the indistinguishably. The different quantum states to be interfered need to be indistinguishable in any degree of freedom. In particular the spectral properties of the states that are defined by the OPO cavity have to be properly matched. To match the bandwidth of the new OPO with the previous ones, we decide to build a cavity that has the same length as the previous OPOs, typically of 35-38 mm, and choose the same transmission of the output coupler for the IR of 10%. A mismatch of bandwidth will lead to a mismatch of the temporal modes that are emitted from the different non-linear sources, thus decreasing the temporal overlap and the indistinguishability. We note that the length of the cavity does not affect so much the temporal mode. Indeed the overlap between the different temporal modes is easily above 99% for a cavity length ranging from 30 to 40 mm [4]. The effect of the output coupler transmission however impacts a lot the bandwidth of the cavity, that scales linearly with the transmission.

We now consider the concurrent use of the OPOs, which is the most challenging consideration in our case. Since the double-resonance of the type-I OPO can be adjusted independently of the other OPOs - by tuning the temperature of the non-linear crystal only - we present our reasoning only for the case of the concurrent use of two type-II OPOs. A type-II OPO being triply resonant, three degrees of freedom are to be adjusted to operate the source. In the case of a single semi-monolithic OPO II, where the angle of the crystal cannot be changed, these three parameters are the length of the cavity, the

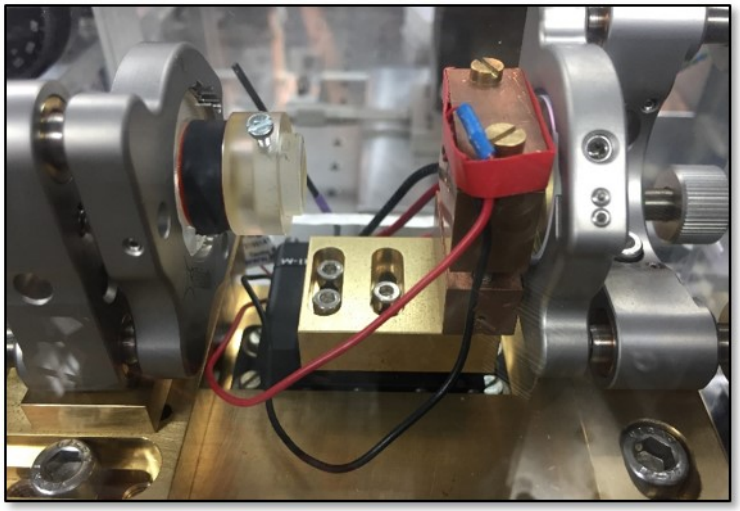

Figure 6.1: **Picture of the straight-cut type-II OPO.** The non-linear type-II KTP crystal is placed inside the oven in copper. The temperature is controlled using a Peltier element. The oven is screwed on a six-axis-precision alignment stage and the angle of the crystal is tilted around the z-axis in order to set the triple resonance (see the Allen key with the purple label on the back). The flat input mirror placed on a high stability mirror mount on the right is coated to be HR at 1064 nm and has a transmission of 5% for the pump at 532 nm. The concave output mirror is hihly-reflective (HR) for the pump and has a transmission of 10% for the IR. To adjust the length of the cavity, the output mirror is installed in a plastic mount glued on a piezo itself placed in a high stability mirror mount. The output mirror can be translated in order to fine tune the cavity bandwidth. A lens placed after the output mirror (not shown) is used to collimate the beam. The overall structure is fixed on a home-made bulk brass mount for an improved stability.

temperature of the non-linear crystal and the temperature of the laser crystal, that corresponds to a change of the pump laser wavelength. Now when these three parameters are fixed, adding a second type-II OPO requires to find three other independent parameters. Two degrees of freedom can easily be found: the length of the cavity and temperature of the non-linear crystal of the second OPO. But for the third degree of freedom we have now the laser wavelength fixed by the first OPO II, and a new parameter needs to be found. We decide for this third parameter to play with the angle of the crystal inside the cavity. We note that this parameter is very sensitive to the alignment, since a variation of the angle by one degree corresponds to a temperature mismatch of about 40 K [150]. For the precise setting of the crystal angle we use a six axis precision alignment stage (**Newport 9031-M**) on which the crystal oven is fixed. In addition, since the triple resonance implies to tilt the crystal inside the cavity, it is not possible to have the cavity input mirror coated directly onto the crystal surface, otherwise the coupling to the cavity would change depending on the triple resonance. We thus have to go from a semi-monolithic configuration

to a *straight-cut linear cavity* configuration [226] with two independent mirrors surrounding the crystal. A picture of the OPO is shown in Figure 6.1. As for the other OPOs the cavity is plano-concave and we choose the same radius of curvature for the output mirror of 38 mm in order to facilitate the matching of the spatial modes after the cavity. The non-linear crystal is placed as close as possible to the plane input mirror where the waist is located in order to optimize the conversion efficiency. The plane mirror has the same transmission properties as the other OPOs, i.e. HR for 1064 nm and a transmission of 5% at 532 nm. The output coupler is also HR-coated for 532 nm. The mirrors are coated from the company **Layertech GmbH**. Each mirror is attached by a high stability mirror mount (**Thorlabs Polaris K-1**) to the home-made brass stage. Same as for the other type-II OPO we use a High Gray Track Resistant (HGTR) type-II KTP crystal with a section of 3×3 mm^2 and a length of 10 mm. The crystal is double anti-reflection coated on each side for the two polarizations of the IR. The crystal is provided by the company **Raicol crystals**.

Fixing the transmission of the output coupler also defines the escape efficiency that can be expected with the OPO. For our OPOs with high escape efficiency, the value is dominated by the intra-cavity losses. These losses arise mostly from absorption of the photons, and scattering inside the non-linear crystal and at the level of the interfaces. Our design that includes an additional interface between the input mirror and the non-linear crystal should thus present more intra-cavity losses, and thus a lower escape efficiency than our previous designs. Yet, even in a very pessimistic case of 2% of intra-cavity losses, as we have seen in **Chapter 2**, the device should show an escape efficiency above 80%. We note yet that the precision on the coating of the output mirror in the IR of about 2% translates directly onto the same uncertainty on the escape efficiency of the OPO.

1.3 Results and discussion

The quality of the single photon generated by an OPO is hard to measure without performing direct measurements of the quantum state. Indeed as the purity is limited by losses that are typically below the percent level, indirect measurements such as the finesse of the cavity cannot be precise enough to estimate properly the quality of the state [227]. In addition, other effects independent of the OPO itself, such as the transmission losses up to the detectors, back-scattering and electronic noise, affect analogously the quality of the generation process that needs to be fully characterized in order to be make the source useful in some protocols. To that end we characterize the OPO with measurement of heralded single photons. The heralding beam is sent to an independent SNSPD using the same filtering procedure as for the other OPOs described in **Chapter 2**. The signal beam is sent to the homodyne detection already placed on the DV mode, which was used to measure photons at the output of the semi-monolithic type-II OPO. Having the same HD for characterizing the two type-II OPOs enables to fix the detection losses and thus precisely compare the two devices with each other. The OPO is locked on the pump resonance by the Pound Drever-Hall technique. A seed beam is locked in phase with the pump via digital locking. It is used for alignment reference and to determine the phase

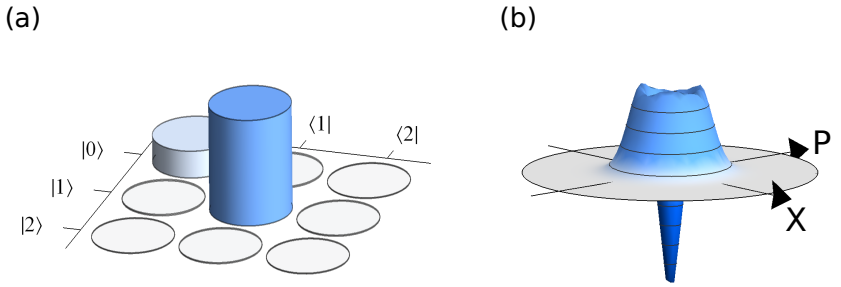

Figure 6.2: **Experimental heralded-single-photon from the straight-cut linear-cavity type-II OPO.** The state is reconstructed from 40 000 tomographic measurements and is corrected from 18% detection losses. (a) Density matrix of the heralded single-photon. The heralding efficiency is of 78.5%. The vacuum component amounts to 21%. (b) Wigner function of the heralded single-photon, showing a strong negativity at the origin.

of local oscillator of the HD. The measurement is performed in a sample-and-hold (S&H) fashion with 50 ms for measurement and 50 ms for readjusting the locks.

The results are shown in Figure 6.2. The OPO is pumped by 1 mW of green. At this pump power we measure a heralding rate of 100 kHz. The state is reconstructed from 40 000 quadratures by single-mode quantum state tomography and is corrected from 18% detection losses (visibility of 98.5%). We measure a heralding efficiency of 78.5%, with negligible multi-photon components below the percent. The heralding efficiency is slightly lower than our expected value. We attribute the extra vacuum component to losses originating either from heterogeneities in the non-linear crystal, or from defects at the level of the crystal/mirror coatings. Other crystal and mirrors are to be tested to verify this hypothesis. Yet the quality of the generated photon is already excellent enough to use the state in some protocols and we decided to keep it as it is.

1.4 Operating two triply-resonant OPOs in parallel

Now that our new OPO II gives useful photons, we need to verify that it can be used concurrently with the semi-monolithic type-II OPO. Indeed even if we have access to enough degrees of freedom to set the two triple resonances separately, they can be situated too far in the parameter space so that they cannot be set simultaneously. In particular if the crystal has to be tilted a lot (i.e by one degree angle) the corresponding the phase matching temperature can be out of the range accessible by the temperature controller. The non-linear KTP crystal can fortunately be engineered in order to work in a practicable parameter range. In particular it is cut along the crystallographic angles ($\theta_{KTP} = 90° \pm 10'$, $\phi_{KTP} = 25.5° \pm 10'$) so that the phase matching occurs close to normal incidence of the beam. The crystal is also set to have a phase matching temperature around $30°C$, i.e a bit above room temperature as to allow a convenient temperature control.

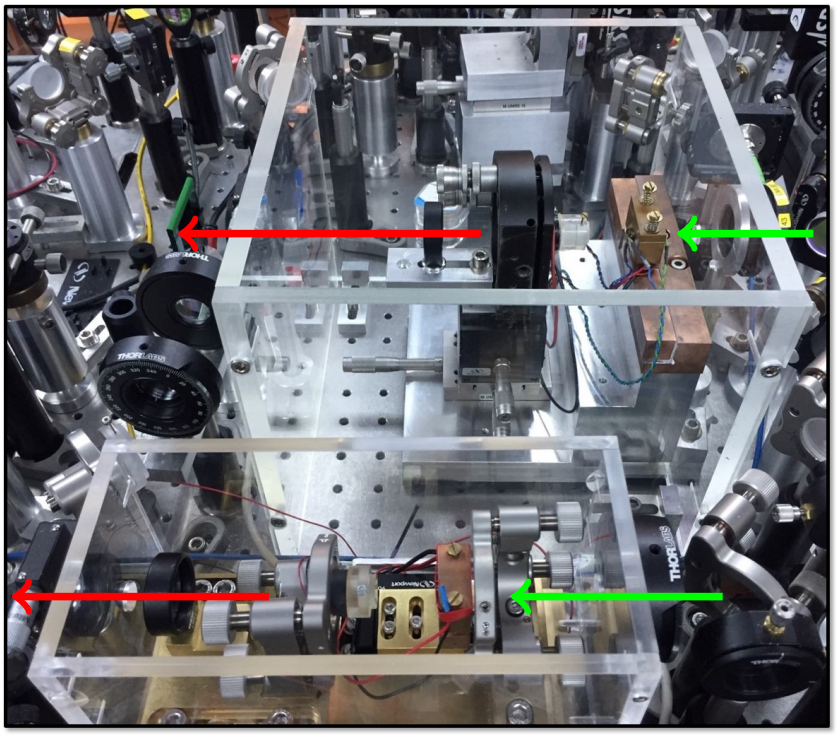

Figure 6.3: **Picture of the two type-II optical parametric oscillators side by side.** The two OPOs are oriented in the same direction, with the pump and the seed beams injected from the right (green arrow). We see on the top the initial, 20 years old, semi-monolithic type-II OPO. The input mirror is directly coated on the surface of the mirror placed in the copper oven. On the bottom is shown the straight-cut linear cavity OPO with the input plane mirror separated from the crystal. Each OPO is covered by a plexiglass box that reduces the effect of air fluctuations on the cavity. The new OPO design is much more compact that the previous one. Having the two OPOs located close to one another enables an easier mode matching of the heralded single-photon.

The procedure for setting the two triple resonances then proceeds as follow. As presented in **Chapter 3**, seed beams in the infrared are injected with the pump for the setting of the resonances. We first set the triple resonance of the semi-monolithic OPO by setting the laser wavelength and the temperature of the non-linear crystal while sweeping the cavity. Once the setting of the first triple resonance is done and the laser temperature is fixed, we set the triple-resonance of the second OPO by adjusting the angle of the crystal and its temperature while sweeping the cavity. Very luckily we manage to find a setting of the six independent parameters that allows the concurrent use of the two type-II OPOs. We can set the double-resonance of the type-I OPO independently and have three OPOs, amounting to five single-mode squeezers, working in parallel.

The stability of the triple resonance in time is also a very important point to take

into account since the protocols we want to implement require the operation of the OPOs for several hours in a row. Since the new OPO is less monolithic, alignment instabilities can be expected as compared to the semi-monolithic designs. We notice yet that the alignment stage is precise enough so as to allow a stability of the resonance over several weeks. Actually the instability are fully dominated by thermal effects coming from the temperature feedback.

To our knowledge it is the first time that two type-II OPOs triply-resonant are used in parallel in a quantum optics experiment. This is a strong achievement that opens a lot of prospects for increasing the number of involved heralded single-photons. Our scheme can trivially be extended to the use of any number of type-II OPOs in parallel since the three independent parameters depend only on the OPO to-be-added.

2 Single-rail discrete-variable qubit creation by displacement of the heralding mode

In **Chapter 3** we introduced the protocols employed for engineering of heralded single photons and optical Schrödinger cat states. In this section we present an additional state engineering where a type-II OPO can be used as a source of heralded discrete-variable qubits encoded in the Fock basis of the form $|\psi\rangle = c_0 |0\rangle + c_1 e^{i\theta} |1\rangle$. We will introduce the scheme that consists in displacing the heralding mode in a very efficient manner and display high-purity DV qubits that are created in this way. We compare theoretically our scheme to a standard remote state preparation protocol involving single-photon entanglement.

2.1 The scheme

Although statistically mixing a single photon to vacuum is a trivial task, adding *coherently* vacuum to a single photon requires a specific, well controlled procedure. We here adapt the scheme presented in [63] for the generation of high purity CV qubits to the case of DV qubits. We start by considering first a type-II OPO only. As can be seen in Figure 6.4, this type-II OPO emits pairs of photons orthogonally polarized. As introduced in **Chapter 3**, these two photons are separated by a polarizing beamsplitter defining a *signal* mode and a *idler* mode. The latter is used to herald the signal photon with a detection event on an SNSPD, with a given heralding rate labeled N_{photon}. This is the standard procedure for the creation of heralded single photons as reported in [6, 7]. By adapting this procedure we can create similarly heralded qubits. Indeed if some uncorrelated, but indistinguishable, photons are added on the heralding mode, they will create false events on the SNSPD that will be detected at a rate labeled N_{disp} - and which do not correspond to photons generated by the OPO. Since the photons in the idler mode are indistinguishable, this creates, when heralded, a *coherent* superposition of vacuum and a single-photon state, defined by the ratio of "false" events relative to the ones corresponding to the creation of a photon in the signal mode, i.e N_{disp}/N_{photon}. This addition of photon in the heralding path can be done by mixing the idler mode with an attenuated coherent state of amplitude β, which is equivalent to applying a displacement of the heralding mode. In the

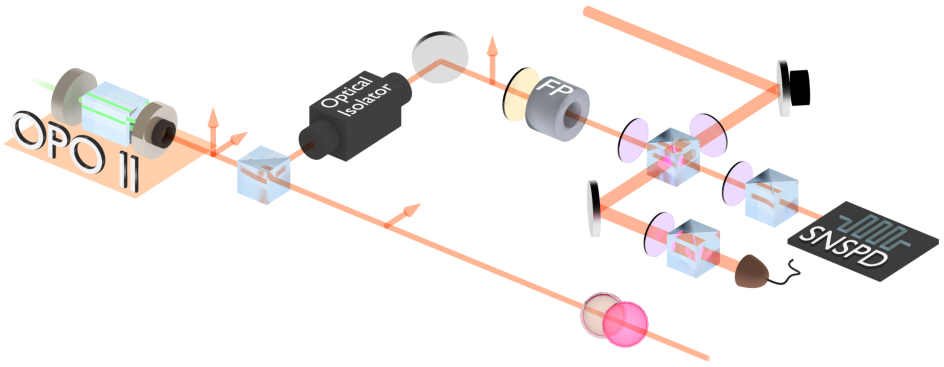

Figure 6.4: **Experimental scheme for the creation of the DV qubit with displacement of the heralding mode.** A type-II OPO emits pairs of polarization-entangled photons. One of them is sent to an SNSPD for heralding. On the way the photon is displaced by an attenuated coherent state. The two beams are mixed in an indistinguishable fashion by first having the photons co-propagate in the same spatial mode and sending them to a polarization independent SNSPD. One of the two beams is used to lock the relative phase θ between the two paths. Upon detection of a photon, a DV qubit of the form $c_0 |0\rangle + c_1 e^{i\theta} |1\rangle$ is heralded, where the ratio c_1/c_0 is defined by the ratio of clicks coming from the OPO and from the displacement beam N_{photon}/N_{disp}.

ideal case, if no displacement is applied ($N_{disp} = 0$), a pure single photon $|1\rangle$ is heralded. As the displacement increases vacuum is coherently added to the single photon, to give an evenly weighted qubit of the form $|0\rangle + e^{i\theta} |1\rangle$ for $N_{disp} = N_{photon}$, and tending to pure vacuum $|0\rangle$ for infinite displacement (which is equivalent to closing the heralding path of the OPO). The phase of the qubit θ is set by the relative phase between the idler photon and the one from the displacement beam, that can be locked to any desired value. We will now give a detailed analytical model of the scheme.

2.2 Theoretical model with losses

As we have seen in **Chapter 3**, the output of a type-II OPO can be described using a relatively simple model in the form:

$$|\psi\rangle_{AB} \propto |0\rangle_A |0\rangle_B + \lambda |1\rangle_A |1\rangle_B + \mathcal{O}(\lambda) \tag{6.1}$$

where λ is related to the squeezing factor s by $s = (1 - \lambda)/(1 + \lambda)$. For a pump power of 1 mW and an OPO threshold at 80 mW, we estimate $s = 0.22$ dB giving a value $\lambda \approx 2\%$.

Now let us apply a small displacement on the idler mode $\hat{D}_B(\beta) \approx \mathbb{1} + \beta\hat{b}^\dagger - \beta^*\hat{b}$, with $\hat{b}^\dagger$ and $\hat{b}$ the creation and annihilation operators in mode B, so that:

$$\begin{aligned}\hat{D}_B(\beta)\left|0\right\rangle_B &\approx (\mathbb{1} + \beta\hat{b}^\dagger - \beta^*\hat{b})\left|0\right\rangle_B = \left|0\right\rangle_B + \beta\left|1\right\rangle_B,\\ \hat{D}_B(\beta)\left|1\right\rangle_B &\approx (\mathbb{1} + \beta\hat{b}^\dagger - \beta^*\hat{b})\left|1\right\rangle_B = \left|1\right\rangle_B + \beta\left|2\right\rangle_B - \beta^*\left|0\right\rangle_B.\end{aligned} \tag{6.2}$$

Discarding the terms $\left|0\right\rangle_B$ that are not detected, we get:

$$\left|\psi\right\rangle_{AB} \propto (\beta\left|0\right\rangle_A + \lambda\left|1\right\rangle_A)\left|1\right\rangle_B + \lambda\beta\left|1\right\rangle_A\left|2\right\rangle_B. \tag{6.3}$$

In the ideal case on a projection on $\left|1\right\rangle\left\langle 1\right|_B$ and neglecting the second term since $(\lambda, \beta) \ll 1$, we herald the DV qubit:

$$\left|\psi\right\rangle_A \propto \beta\left|0\right\rangle_A + \lambda\left|1\right\rangle_A \tag{6.4}$$

The qubit is defined by the ratio β/λ. Again, if no displacement is applied ($\beta = 0$) the state prepared is $\left|1\right\rangle_A$, for a large displacement $\beta \ll \lambda$, the state prepared is $\left|0\right\rangle_A$ (indeed only false events will be detected on the SNSPD). One can also prepare an even-weighted qubit by setting $\beta = \lambda$. This ratio is directly related to the ratio in clicks detected on the SNSPD in a given time window:

$$\frac{\beta}{\lambda} = \sqrt{\frac{N_{disp}}{N_{phot}}}. \tag{6.5}$$

We can easily extend this model to a realistic bucket detection on mode B, with a detection efficiency η_{herald}, corresponding to the operator $\hat{\prod}_B = \sum_{n=1}^{2}[1-(1-\eta_{herald})^n]\left|n\right\rangle\left\langle n\right|_B$ and $\hat{\rho}_A = \mathrm{Tr}(\hat{\prod}_B\left|\psi\right\rangle\left\langle\psi\right|_{AB})$:

$$\hat{\rho}_A \propto (\beta\left|0\right\rangle_A + \lambda\left|1\right\rangle_A) \otimes (\beta^*\left\langle 0\right|_A + \lambda^*\left\langle 1\right|_A) + (2-\eta_{herald})\lambda^2\beta^2\left|1\right\rangle\left\langle 1\right|_A. \tag{6.6}$$

Taking into account the OPO losses, it gives:

$$\begin{aligned}\hat{\rho}_A \propto{}& \left|0\right\rangle\left\langle 0\right|_A(\beta^2 + \lambda^2(1-\eta_{OPO}) + \lambda^2\beta^2(2-\eta_{herald})(1-\eta_{OPO}))\\ &+ \left|0\right\rangle\left\langle 1\right|_A(\sqrt{\eta_{OPO}}\beta\lambda) + \left|1\right\rangle\left\langle 0\right|_A(\sqrt{\eta_{OPO}}\beta\lambda)\\ &+ \left|1\right\rangle\left\langle 1\right|_A(\lambda^2\eta_{OPO} + \lambda^2\beta^2\eta_{OPO}(2-\eta_{herald})).\end{aligned} \tag{6.7}$$

With that model in mind we can simulate the states created using this procedure taking into account experimental imperfections. The theoretical states are given in Figure 6.5. They are calculated for an OPO with a heralding efficiency $\eta_{OPO} = 0.9$ and a transmission of the heralding path of $\eta_{herald} = 0.3$. We plot in particular the fidelity of the generated state with its corresponding ideal qubit. Very interestingly, we see that by applying the displacement on the heralded mode only, we prevent the heralding transmission losses to affect the purity of the heralded state. Indeed, as for standard heralded single-photon, the transmission losses in the heralding channel will only affect the generation rate. The displacement being applied after all the filtering stages, it is not affected by the filtering transmission losses. Therefore, the qubit created is only limited by the escape efficiency

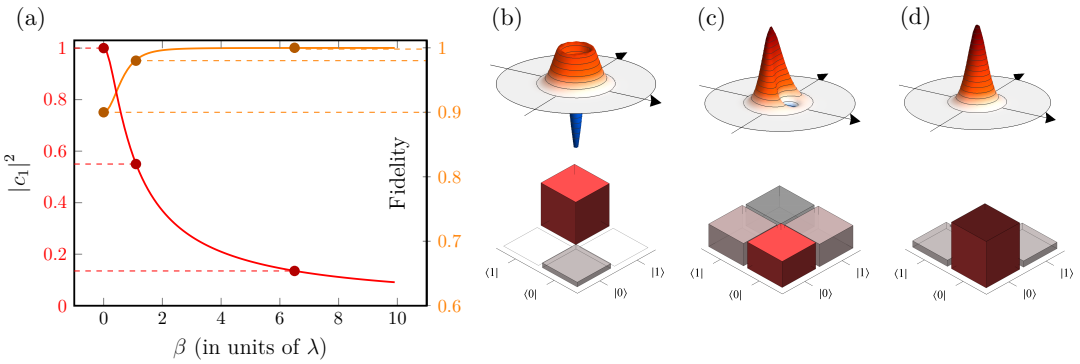

Figure 6.5: **Simulated qubit creation by displacement.** (a) Coefficients $|c_1|^2$ of the qubit maximizing the fidelity with the generated state (red), and its corresponding fidelity (orange), as a function of the amplitude of the displacement β applied on the heralding mode. The curves are extracted from Eq.(6.7) with the parameters $\eta_{OPO} = 0.9$, $\eta_{herald} = 0.3$. Any DV qubit can be created with a purity above 90%. The three values of β detailed on the right are represented by the dots (b) Wigner function and associated density matrix for a displacement $\beta = 0$. The fidelity is here only limited by the escape efficiency of the OPO. (c) Wigner function and associated density matrix for a displacement $\beta \approx \lambda$, giving an almost perfectly balanced qubit. (d) The Wigner function and density matrix tends to the one of the vacuum as β is increased.

of the initial OPO, leading to a wide range of accessible DV qubits, with a value of $|c_1|^2$ ranging from 0 and 1 with an average fidelity above 98%. In addition, as we will see later, the heralding rate of the qubit is even higher than the one of a heralded single photon (HSP) since photons are added on the heralding mode. The scheme is also rather easy to implement experimentally from the HSP setup, as it only involves a coherent state to be mixed with the idler mode. This can be achieved with visibilities above 95%, and the phase lock between the two beams can be performed digitally with a microcontroller.

2.3 Comparison with remote state preparation

Other strategies can be proposed to create a DV qubit encoded in the Fock basis $\{|0\rangle, |1\rangle\}$. In particular a DV qubit can be naturally created from a single-photon entangled state upon measurement on one of the modes in a remote state preparation (RSP) scheme. We compare here theoretically our strategy for creating a DV qubit by displacement of the heralding mode to a remote state preparation scheme. The scheme for RSP is shown in Figure 6.6. It proceeds as follows: a single photon heralded by a click on the SNSPD is sent to a 50:50 beamsplitter to create single-photon entanglement of the form $|\Psi\rangle_{AB} \propto |0\rangle_A |1\rangle_B + |1\rangle_A |0\rangle_B$. One of the two modes is sent to a homodyne detection setup which performs, as we have seen earlier, a quadrature measurement under the operator $\hat{q}_\theta = \hat{x}\cos\theta + \hat{p}\sin\theta$ where $\hat{x}$ and $\hat{p}$ denote the canonical position and momentum observables and θ is the phase of the local oscillator. The measurement of the quadrature

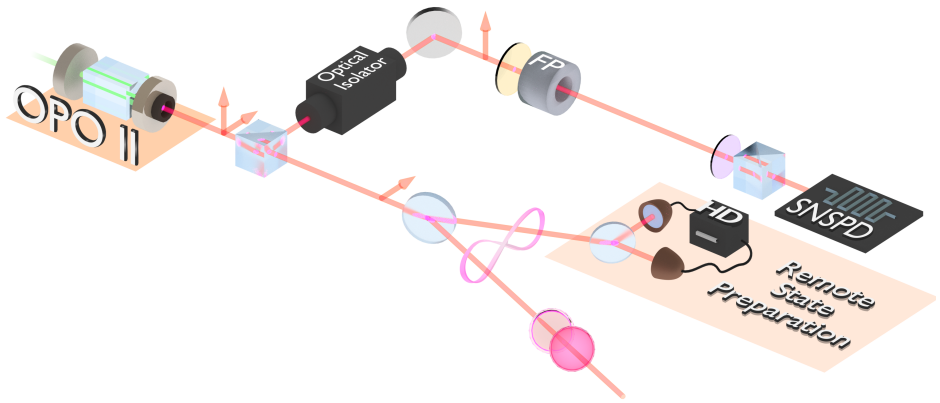

Figure 6.6: **DV qubit creation by remote state preparation.** A single-photon is heralded on the signal mode and sent to a 50:50 beamsplitter to create a single-photon entangled state of the form $|0\rangle_A |1\rangle_B + |1\rangle_A |0\rangle_B$. A homodyne detection setup is used to condition on specific quadrature value q on mode B. The selection of a given quadrature q, at a given local oscillator phase θ effectively creates a qubit of the form $qe^{i\theta} |0\rangle_A + |1\rangle_A$ in mode A .

q projects the entangled state $|\psi\rangle_{AB}$ onto a quadrature eigenstate $\langle q_\theta|$

$$|\psi\rangle_A \propto \langle q_\theta|\psi_{AB}\rangle = \langle q_\theta|1\rangle_B |0\rangle_A + \langle q_\theta|0\rangle_B |1\rangle_A , \tag{6.8}$$

with

$$\langle q_\theta|0\rangle_B = \frac{1}{(2\pi)^{1/4}} e^{-q^2/4}, \qquad \langle q_\theta|1\rangle_B = \frac{qe^{i\theta}}{(2\pi)^{1/4}} e^{-q^2/4}, \tag{6.9}$$

leading to the remotely prepared qubit

$$|\psi\rangle_A = \frac{1}{\sqrt{1+q^2}} (qe^{i\theta} |0\rangle_A + |1\rangle_A). \tag{6.10}$$

Thus by selecting specific quadrature values q at a given local oscillator phase θ, one can prepare remotely any coherent superposition of $|0\rangle$ and $|1\rangle$ [11]. However, this method is rather sensitive to the transmission losses before the heralding homodyne detection, which limits the purity of the DV qubits created in this way.

To understand this effect, we need to develop our model taking into account optical losses. First, the single photon heralded at the output of the OPO is not pure, it is better described as a statistical mixture of single-photon and vacuum under the form:

$$\hat{\rho}_A = \eta_{OPO} |1\rangle \langle 1|_A + (1 - \eta_{OPO}) |0\rangle \langle 0|_A . \tag{6.11}$$

This state is then mixed with a new mode B on a 50:50 BS, giving after mixing:

$$\begin{aligned} \hat{\rho}_{AB} = \frac{\eta_{OPO}}{2} (&|10\rangle \langle 10|_{AB} + |10\rangle \langle 01|_{AB} + |01\rangle \langle 10|_{AB} + |01\rangle \langle 01|_{AB}) \\ &+ (1 - \eta_{OPO}) |00\rangle \langle 00|_{AB} . \end{aligned} \tag{6.12}$$

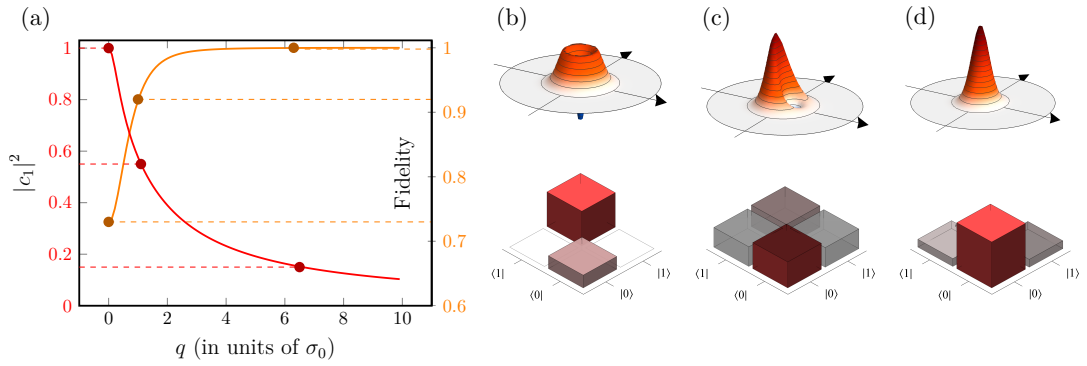

Figure 6.7: **Simulated qubit creation by RSP.** (a) Coefficients $|c_1|^2$ of the qubit maximizing the fidelity with the generated state (red), and its corresponding fidelity (orange), as a function of the quadrature value q selected on the heralding HD. The curves are extracted from Eq.(6.14) with the parameters $\eta_{OPO} = 0.9$, $\eta_{herald} = 0.85$. The three values of q detailed on the right are represented by the dark dots. (b) Wigner function and associated density matrix for a quadrature selection at $q = 0$. The fidelity is dropping to about 70% because of the additional transmission losses in the heralding path. (c) Wigner function and associated density matrix for a quadrature $q \approx 1$, giving the most balanced qubit. (d) The Wigner function and density matrix tends to the one of the vacuum as q is increased.

Mode B propagates up to the homodyne detection with transmission η_{herald}:

$$\hat{\rho}_{AB} = \frac{\eta_{OPO}}{2}(|10\rangle\langle 10|_{AB} + \sqrt{\eta_{herald}}\,|10\rangle\langle 01|_{AB} + \sqrt{\eta_{herald}}\,|01\rangle\langle 10|_{AB} + \eta_{herald}\,|01\rangle\langle 01|_{AB}) + ((1-\eta_{OPO}) + \frac{\eta_{OPO}}{2}(1-\eta_{herald}))\,|00\rangle\langle 00|_{AB}\,. \tag{6.13}$$

Finally, noting that $\langle q|1\rangle_B = qe^{i\theta}\langle q|0\rangle_B$, conditioning on homodyne detection gives:

$$\begin{aligned}\hat{\rho}_A \propto\ & |0\rangle\langle 0|_A\,(q^2\frac{\eta_{OPO}}{2}\eta_H + ((1-\eta_{OPO}) + \frac{\eta_{OPO}}{2}(1-\eta_H))) \\ & + (|0\rangle\langle 1|_A\,e^{-i\theta} + |1\rangle\langle 0|_A\,e^{i\theta})(q\frac{\eta_{OPO}}{2}\sqrt{\eta_H}) \\ & + |1\rangle\langle 1|_A\,(\frac{\eta_{OPO}}{2}).\end{aligned} \tag{6.14}$$

For simplicity we discard the effect of the size of the conditioning window chosen on the homodyne detection, which should decrease the purity of the generated qubits by a few percents. The expected results are given in Figure 6.7, considering the same escape efficiency as for the displacement scheme, and 15% losses in the homdyne detection heralding mode. One can see a drop in fidelity as compared to the displaced qubit, owing to the heralding losses that, in this scenario, directly affect the purity of the state. This is due to the fact that homodyne detection is unable to distinguish between vacuum and a lossy

single photon as the losses increase. In addition, since this procedure needs both heralding on the SNSPD and homodyne conditioning, the creation rate is limited to less than half the rate for a heralded single photon. This would give for the RSP protocol a qubit heralding rate at least five times smaller than what is achievable with the displacement scheme. Finally, in terms of implementation, it requires an additional homodyne setup that can be more demanding to set up experimentally with high efficiency.

2.4 Experimental implementation and results

We now experimentally implement the scheme given in Figure 6.4. A small fraction of the IR beam is used to create the attenuated coherent state. This beam has to be carefully attenuated since it has to be at the single-photon level on the SNSPD and at the same time we need enough macroscopic power on the photodiode to be able to lock the qubit phase. The coherent state is mixed on a imbalanced PBS with the heralding mode of the type-II OPO. For experimental convenience we use a combination of four half-waveplates (HWPs) and three PBSs which allows the independent tuning of the slipping ratio for the two different beams. For the idler beam from the OPO, 90% of the light is transmitted to the SNSPD while 10% of the light is reflected to the photodiode for the lock. For the coherent state we minimize first the reflection towards the SNSPD (0.5%) on the first PBS. After the two beams are mixed on the imbalanced PBS, they co-propagate in the same spatial modes but with different polarizations. These polarizations are projected using a HWP and a PBS both before the locking photodiode and before the SNSPD. To maximize the visibility on the photodiode the angle of the HWP is aligned at 45°. Since our SNSPD is polarization independent we can attenuate even more the coherent state by minimizing again the transmission of the coherent state on the second cube (0.5%). Once set the angles of the HWPs are not used to adjust the coherent state amplitude. We use for that purpose a variable neutral-density filter (**Thorlabs NDC-100C-4M**) to precisely tune the overall amplitude of the coherent state before the imbalance beamsplitter. The setting of the amplitude is done by adjusting the count rate directly on the SNSPD. The phase of the coherent state is adjusted with a piezo-electric transducer placed on the path of the coherent state before the mixing. The locking is controlled by a microcontroller (**Analog devices ADUC7020**).

The type-II OPO is pumped by 2 mW in order to generate single photons at a rate of 250 kHz. The states are corrected from 18% detection losses and reconstructed from 40 000 quadratures each in a Hilbert space of dimension 1+4. The corresponding state without displacement, i.e. $|1\rangle$, has a single-photon component of 72.5%. We then add a displacement to the heralding mode and tune its amplitude in order to balance the count from the two beams on the SNSPD. We lock the phase to the maximum of the fringe which is the locking point having the maximum precision (typical phase noise of 3%). This phase setting should thus create the qubit $|0\rangle + |1\rangle$. Since the setting of the HWPs for the mixing are not touched (this is possible because our SNSPD is polarization insensitive), displacing the heralding mode amounts to adding photons on the heralding mode, which increases the rate of production of the qubit. From a HSP at 250 kHz, we can create balanced DV

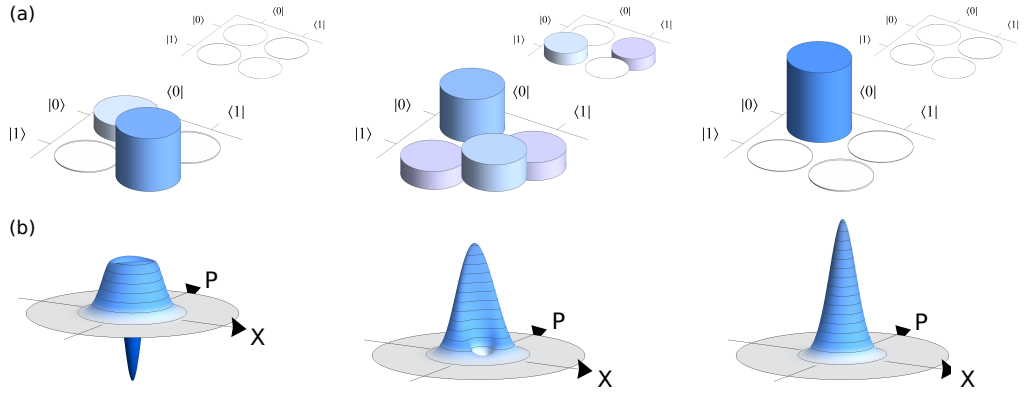

Figure 6.8: **Experimental DV qubits: control of the superposition weight and phase.** Each state is reconstruted from 40 000 quadratures in a Hilbert space of dimension 1+4. The states are corrected from 18% detection losses. (a) Density matrix of the states, the real part is in the center and imaginary part is in the top right corner. (b) Wigner function of the created DV qubits. Three DV qubits can be created by tuning the amplitude of the displacement following a rotation on the azimuthal angle of the Bloch sphere. (Left) Without any displacement the state $|1\rangle$ is created with a purity of 72%. (Center) When balancing the count from the displacement and heralding mode on the SNSPD, and locking the phase on maximum we create an evenly weighted qubit in the equator of the Bloch sphere. The phase of the qubit is offset relative to the locking point by about $\pi/4$. This phase offset originates from the difference of optical paths followed by the two orthogonal polarizations before detection on the SNSPD. (Right) When an infinite displacement is applied - i.e. when the OPO heralding path is closed - only false events are detected on the SNSPD, yielding the creation of $|0\rangle$ with a purity of 99%. The states are produced at a rate of 250 kHz, 500 kHz and 2 MHz respectively.

qubits at rate of 500 kHz. In the end we can increase the rate of the displacement to increase the vacuum component. To create the state $|0\rangle$ we can close the heralding path of the OPO and increase the amplitude of the coherent state up to a count rate of 2 MHz, after which saturation effects start to occur on the SNSPD.

We show in Figure 6.8 the results of the preparation of the different DV qubits. For the states at the north and south poles of the Block sphere, $|1\rangle$ and $|0\rangle$ respectively, the purity achieved is 72.5% and 99% respectively. The purity of the state is here limited only by the heralding efficiency of the type-II OPO. We notice on the balanced qubit a phase offset relative to the setting point of the lock. Indeed here, when locking the modes in phase we observe a qubit tilted by about $\pi/4$. This phase offset originates from the difference of propagation between the two different polarizations on the SNSPD path after the imbalanced PBS. By precisely tuning the angle of the HWP after the cube, we can adjust by hand this phase offset to the desired value. This is in practice very advantageous

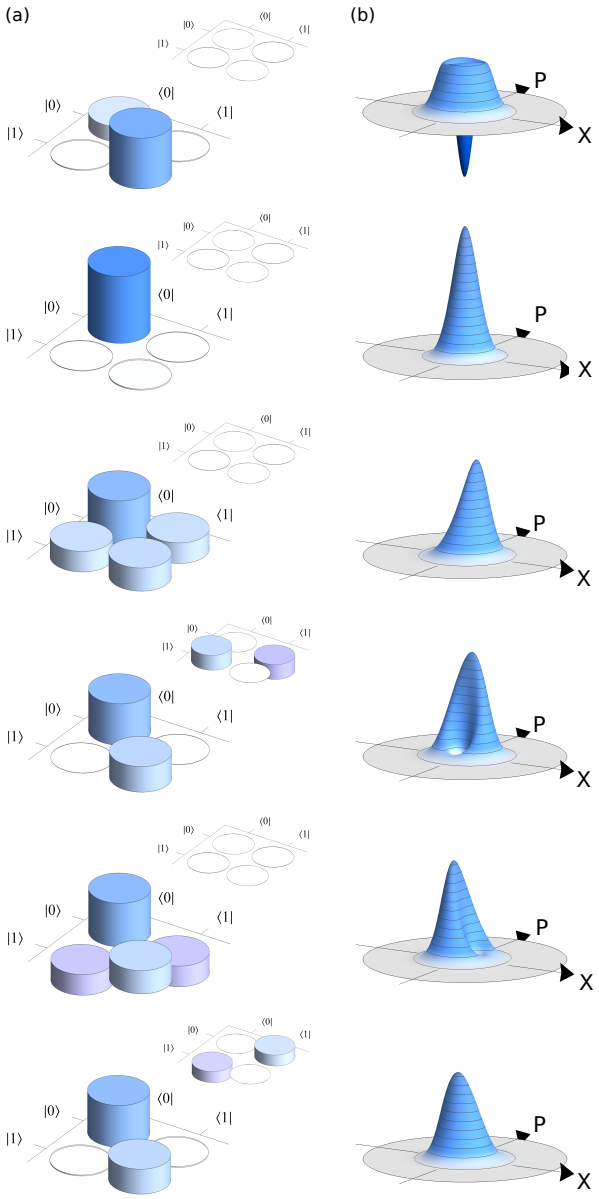

Figure 6.9: **Experimental DV qubits: control of the phase.** (a) Density matrix of the states, the real part is in the center and imaginary part is in the top right corner. (b) Wigner function of the created DV qubits. For comparison we repeat the states $|1\rangle$ and $|0\rangle$ from Figure 6.8. The phase offset of the qubit is adjusted by tuning the angle of the HWP before the projection cube on the SNSPD path. The offset can be adjusted to 0 or $\pi/2$ while locking the relative phase always on maximum. The phase of the qubit can be flipped by changing the sign of the qubit lock.

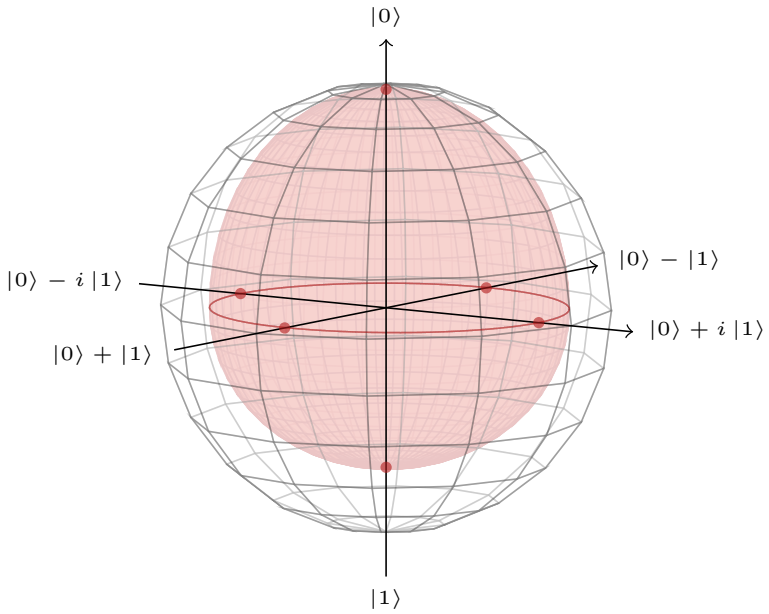

Figure 6.10: **Bloch sphere of the experimental discrete-variable qubits.** Bloch sphere spanned by the DV qubits encoded in the Fock basis $\{|0\rangle, |1\rangle\}$. The distance from the center of the sphere represents the purity of the states. As a reference, the outer transparent sphere represents the Bloch sphere spanned by pure states. The red dots represent our experimental states, from which the pink surface is numerically extracted. We obtain an average purity of 81% over the Bloch sphere with minimum purity of 72.5% on the south pole.

since the phase noise of the digital lock depends on the locking point on the fringe. At the extrema of the fringe the phase noise is minimum but in the middle of the fringe the noise is doubled, which is very inconvenient for preparing the qubit $|0\rangle + i\,|1\rangle$ or $|0\rangle - i\,|1\rangle$. Having the ability to adjust the offset by hand enables to stay locked always on a maximum (or a minimum for flipping the phase with the same precision) while making the offset correspond either to a phase of 0 or to a phase of $\pi/2$ directly.

2.5 Tuning the phase of the qubit

We now have at hand all the parameters that we need to create precisely any target qubit. For our study we will limit ourselves to the six poles of the sphere. The state $|1\rangle$ is created without applying any displacement. The state $|0\rangle$ is created by using the displacement beam only. The qubit weight $|c_1|^2$ is adjusted by playing with the ratio of counts on the SNSPD, which is equivalent to a rotation in the Bloch sphere around the azimuthal angle. To create a state on the equator of the sphere we adjust the amplitude of the coherent state to balance the counts on the SNSPD. The phase offset is adjusted

by fine-tuning the HWP between the two cubes on the SNSPD path, while always locking on the maxima on the fringe. This corresponds to a rotation along the polar angle of the Bloch sphere. We note that this small change of the HWP angle slightly changes the attenuation of the coherent state and thus the heralding rate of the qubit. Once the offset is calibrated, a phase flip can finally be applied if needed by locking on the minimum of the fringe. By using this procedure we are able to create the six poles of the Bloch sphere. The corresponding experimental density matrices and Wigner functions corrected from 18% detection losses are given in Figure 6.9. In addition we represent this experimental state in a DV Bloch sphere given in Figure 6.10. The qubits have an average purity around the Bloch sphere of 81%. The purity of the states is limited dominantly by the purity of the initial single-photon used to create the DV qubits. On top of that the phase noise on the qubit lock reduces the amplitude of the coherences. We estimate this phase noise to be about $5-10\%$ depending on the qubit created. This increased phase noise as compared to previous works originates from the reduced size of the locking fringe because of the attenuated beam. This could be improved by using an imbalanced PBS with better extinction of the coherent beam which could increase the power sent on the photodiode for the lock.

We have now fully presented our additional straight-cut type-II OPO-based single-photon source and showed how displacing the heralding mode of a heralded single photon can be used to generate experimentally high-purity discrete-variable qubits. We will now present the other main experimental implementations which was build during this thesis for producing efficient coincidental detections in advanced quantum information protocols.

3 An improved heralding system for efficient coincidence detection

In this section we will present the cryogenic system that was developed to enable the use of four independent SNSPDs. We will introduce the elements that have been designed for our particular application and compare the performances of the system with the original one, namely, the double-wall dipstick. At the end of the section we describe the efficient detection of coincidences from different events and suggest possible improvements of the cryogenic system.

3.1 Motivations

Many quantum information processing experiments involving single photons require the measurement of many-fold coincidences. As the complexity of the setup increases, single-photon detectors have to be added to detect the events of interest. As we have seen with the swapping experiment, a limited number of detectors can be used in a time-multiplexed fashion to mimic the detection of independent events. However this usage has many drawbacks, and in particular it does not enable an accurate discrimination of the events, which can be detrimental to many protocols. Since our setup with the dipstick only allows the use of two independent detectors, we decided to change our entire cooling

system to enable the use of more detectors. In addition, the dipstick system typically induces physical degradation of the valuable SNSPDs that we want to overcome. To that end we decided to transition to a cryocooler system. Our objective was to cool four independent SNSPDs below 1.5 K for more than 5 days in a row. Our system is a prototype that we developed conjointly with the company **MyCryoFirm**. It was custom-made for our experiment. It took overall more than two years to obtain an operational system, with many issues arising along the installation: leaks, breaking of the connection cables, breaking of the fibers, and failure of the compressor. The system has been fully operational for about two years now, and no issue requiring reparation of the system has arisen in the last year. The system is composed of two circuits. The first part is made of a two-stage Gifford-McMahon cooler cold head that enables to reach a temperature of 4 K. The second part cools down to the working temperature below 1.5 K through the adiabatic relaxation of He^4 in a pot in contact with the 4 K plate. We will now present the principle of the system and detail all the steps allowing the cooling down to 1.3 K.

3.2 The cryocooler: principle

The 4 K circuit is composed of a combination of a cold head (**Sumitomo RDK 101-D**) and a water-cooled helium compressor (**Sumitomo HC-4E2**). The cold head is composed of a compression and expansion space, a regenerator and a displacer. In general the regenerator and the displacer are combined in one element. The cold head is connected to the compressor by two helium lines at high pressure and low pressure. The cooling process is based on a two-stage Gifford-McMahon (GM) cooling cycle. A Gifford-McMahon is a closed cycle dynamic regenerative cryogenic refrigerator. As compared to a Stirling or Pulse tube the GM has valves at the level of the head that that can sequentially open to generate the desired pressure pulse from the two helium lines, typically at a low frequency of 1-5 Hz. The valves are synchronized with the displacer inside the cold head. The cooling cycle can be used in sequence to reach lower temperatures. In our case the first stage of the GM cools helium down from room temperature to 50 K while the second one cools down from 50 K to 4 K. In this two-stage process the two helium displacers are moved synchronously. Thermal screens enable the isolation of both the 50 K and the 4 K stages.

The GM cooling cycle proceeds in four steps. The scheme is shown in Figure 6.11. For simplicity the refrigerator is located inside the displacer. The displacer separates the cold volume V_{cold} to the warm volume V_{warm} that is connected to the compressor. We are only interested in looking at the evolution of the cold volume. Initially, the displacer is located at the bottom of the expander. The cold volume is minimum while the warm volume is maximum. The valve connected to the high pressure (HP) helium from the compressor is closed. First the high pressure valve is opened. The high pressure gas fills the constant volumes V_{cold} and V_{warm}. Then, the displacer is moved towards the top of the expander, displacing the gas from V_{warm} to V_{cold} through the regenerator that adsorbs the heat. The cold volume increases while the warm volume decreases. The valves are switched and the volumes are now connected to the low pressure that leads to an expansion of the gaz.

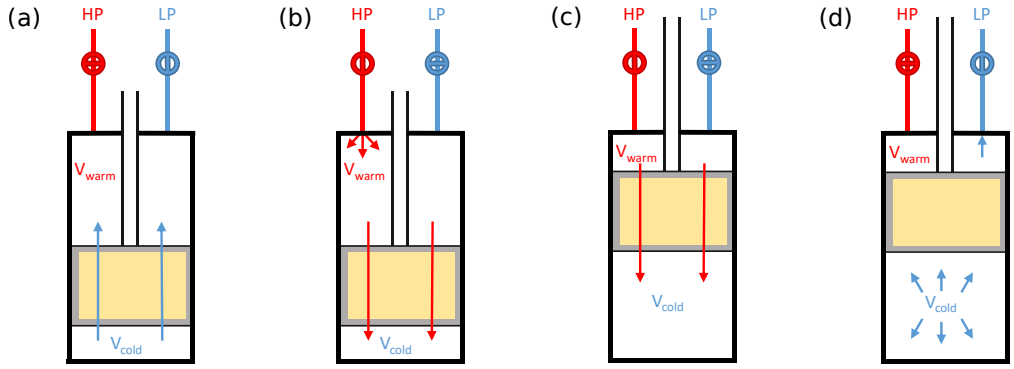

Figure 6.11: **Single-stage Gifford McMahon cooling cycle.** The cold head is connected to the compressor via two high pressure (HP) and a low pressure (LP) helium tubes. The connection is switched by two valves synchronized with the displacer. The displacer (grey) contains the regenerator (yellow) and separates the volume in a *cold* and a *warm* environments. (a) In the initial position the displacer is located at the bottom of the extender. The cold volume V_{cold} is minimum. The pressure inside the two volumes is low. (b) The valve of the HP is opened. The pressure of helium gas increases in both the *cold* and the *warms* volumes. (c) The displacer is moved towards the top of the chamber. V_{cold} is increased at constant pressure. The warm gas passes through the regenerator that stores the heat. (d) Finally the LP valve is opened and the cold gaz is expanded, leading to a decrease of the temperature at the bottom of the extender. To reset the cycle the displacer is moved at the bottom of the expander. The cold volume is decreased to its minimum value. The cold gas passes through the regenerator and recovers the stored heat. This cycle is repeated until the regenerator saturates. With a single-stage the cooling is possible from room temperature to 50 K. A second stage placed in series enables to cool down from 50 K to 4 K. The displacers of the two stages are then moved synchronously.

This is where the useful cooling power is produced. The displacer is finally moved back to the bottom of the expander. The cold gas passes through the regenerator while taking up heat from it, and the cycle is finished. The cycle continues to produce lower and lower temperature until the regenerator reaches saturation.

The two-stage GM thus enables to reach a temperature of 4 K, which is still not enough to operate our SNSPDs, as they require a temperature below 2 K. To that end a secondary He^4 circuit is used to cool down from 4 K to 1.3 K. The secondary circuit is independent of the two-stage GM. Yet it requires the first circuit to reach 4 K to operate. The helium is initially stored in a tank close to the cold head at a pressure of 800-1000 mbar. It is circulated in capillaries through the GM using a dry scroll pump (**Edwards nXDS 15i**). The capillary circulates first around the 50 K stage for thermalization and then passes through the 4 K stage. When the helium passes next to the 4 K stage, at a pressure of about 1000 mbar, it passes below the vapor pressure and thus condenses in a 1 K pot. This 1 K pot is thermally connected to the sample region where the detectors are located. A schematic of the cold head is shown in Figure 6.12.

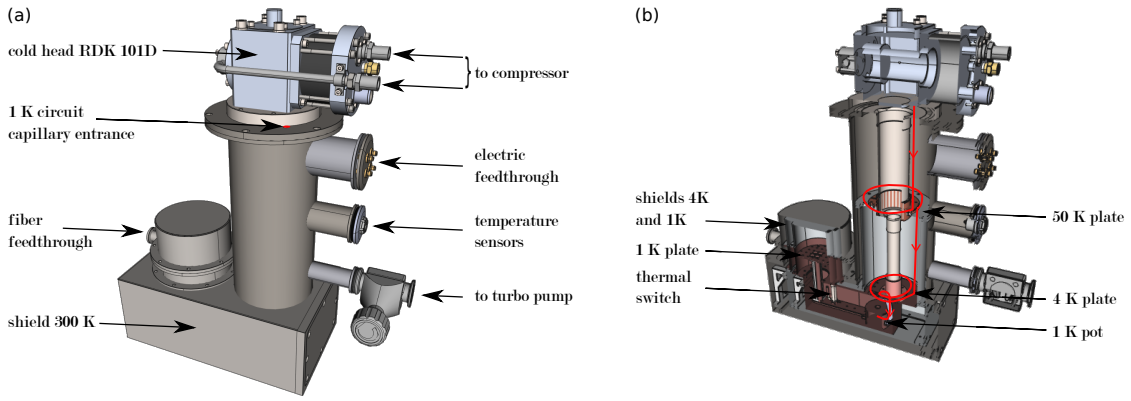

Figure 6.12: **Schematic of the cold head.** (a) The two-stage Gifford-McMahon is embedded in an aluminum enclosure. The enclosure ensures the isolation of the system with the 300 K environment. The cold head is connected to the helium compressor by two high pressure and low pressure helium pipes. A rotary valve ensures the switching of the lines at the desired frequency. Electric and fiber feedthroughs enable the connection to the SNSPDs inside the cryocooler. Temperature sensors enable the monitoring of the temperature on the 4 K and 1 K stages. For simplicity we only show in red the point corresponding to the entrance of the capillary of the secondary circuit. (b) Cut view of the cold head. The two stages of the GM are visible with a 50 K plate and a 4 K plate. Below is found the 1 K pot where the helium of the secondary circuit condensates. This pot is thermally connected via a switch to a 1 K plate where the SNSPDs are settled. Shields at 4 K and 50 K enable the thermal isolation of the different parts. We indicate in red the path followed by the helium of the secondary circuit. It goes from the outside of the chamber to the 50 K plate, the 4 K plate before condensing in the 1 K pot. The capillary is thermallized in each step around the plates. The helium is retrieved at the back of the chamber (not shown) so that the circuit is closed. The helium is circulated by a dry scroll pump.

3.3 Assembling the cryocooler

Once the efficient cooling of the SNSPD is ensured, we need to make sure that we can access them optically and electrically from the room-temperature environment. We developed in that sense a dedicated electrical and fiber feedthrough system. The SNSPD are located on a 1 K copper plate spatially separated from the GM that we will call the *sample* region. It provides a smooth access to the SNSPDs. The SNSPD mounts are directly screwed on the plate for mechanical stability. The electric and fiber feedthroughs are made directly on the sample region. As shown in Figure 6.13, the electric feedthrough is made using vacuum-compatible SMA connectors. A 50 cm SMA-to-SMP coaxial cable connects the SMA connector at 300 K to the SNSPD at 1 K. It is looped each time around the 50 K and 4 K shields for thermalization.

A home-made system was designed for the fiber feedthrough. The fiber we use are from

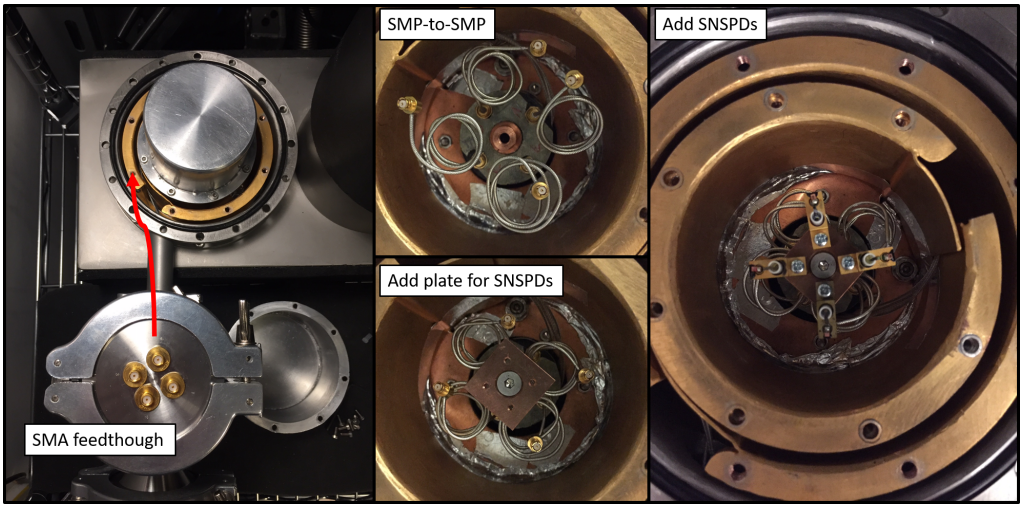

Figure 6.13: **Electric feedthrough and SNSPD fixation.** (Left) The feedthrough is enabled by four vacuum compatible SMA connectors fixed on a QF50 flange. It is fixed through a reducing nipple to the structure. The 50 cm SMA-to-SMP coaxial cables are passed throught the 4 K and 1 K shields, with a least one turn each time for thermalization. (Middle) The SMP ends are fixed on a plastic plate at the bottom of the sampling region. Small SMP-to-SMP cables enable the connection to the top of the sampling region. (Right) The copper 1 K plate is added and the SNSPDs mounts are fixed on it. The SMP ends are plugged to the SNSPDs.

the company **Oz Optics** (**SMJ-32.5F-1064/125-0.25-1.1-AR2**). They are composed of a FC/PC connector for outside the cryo and a fiber ferrule end face that is AR coated and plugged directly to the SNSPD. The feedthrough technique consists in passing the four optical fibers through vacuum epoxy (**Variant Torr Seal**). If this technique enables a much cheaper feedthrough than commercial solutions, it is much harder to implement in practice. First the vacuum epoxy has to be installed properly in order to maintain reasonable vacuum inside the cold head chamber. Then, and more importantly, the fiber ends glued with the epoxy are very fragile mechanically, and can break very easily upon manipulation. In particular the fibers cannot hang directly out of the chamber and need to be attached and protected. To that end we developed a dedicated structure shown in Figure 6.14. First the fibers are passed through a home-made QF16 centering ring. Compared to commercial rings, our ring is made in bulk and only four 5 mm diameter holes are drilled to pass the fibers. Vacuum epoxy is then applied on the four holes to glue each fiber separately. Once the epoxy has dried the fiber ends hanging out of the chamber are passed through a QF16 to QF50 reducing nipple that protects the sensitive parts at the level of the glue. In the end the fiber ends are fixed on a QF50 flange on which four FC/PC to FC/PC mating sleeves (**Thorlabs ADAFC2**) are screwed. Once the fiber ends are fixed and protected outside the chamber, the fibers are passed through the QF16 hole of the QF to CF adapter surrounding the sampling region. We note that the

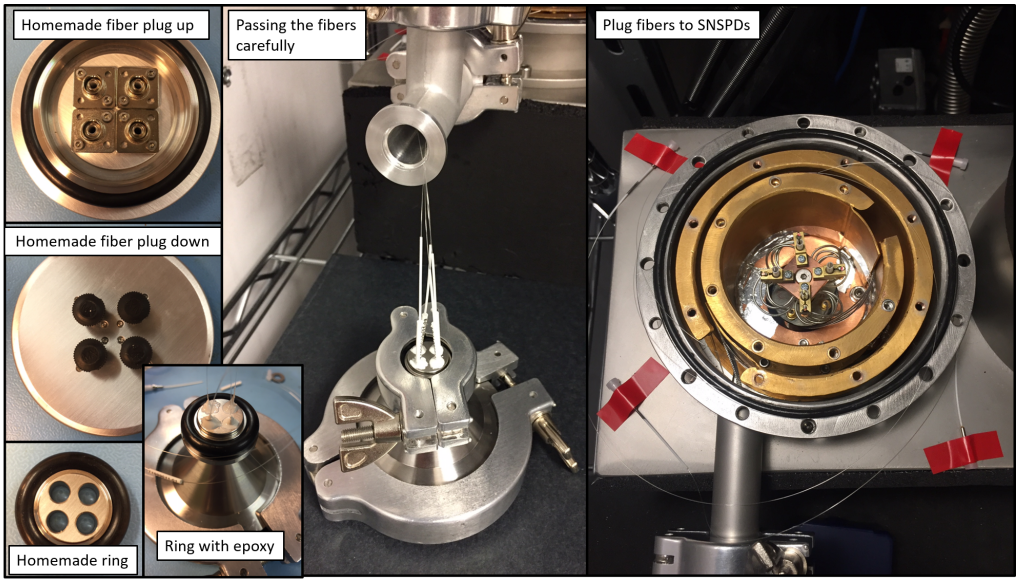

Figure 6.14: **Fiber feedthrough design and installation.** (Left) On a QF50 flange are installed four FC/PC to FC/PC mating sleeves. They enable the connection of optical fibers outside of the cryocooler to the optical fibers used for the feedthrough. A home-made QF16 bulk centering ring is used to pass the four fibers. Each fiber is glued using vacuum epoxy. Once glued the fiber ends are protected by a reducing nipple and the end of the fiber is attached to the mating sleeve. (Middle) Once the sensitive parts are protected the fibers are passed through the chamber. (Right) The fibers are connected directly to the SNSPDs after being thermalized on the 50 K and 4 K shields.

vacuum is ensures solely at the level of the home-made QF16 ring. Inside the chamber the optical fibers are passed around the 50 K and 4 K shields for thermalization and are finally plugged directly on the SNSPDs. The quality of the feedthrough is ensured by measuring the pressure while pumping with a turbo pump (**Edwards T-station 75**). The pressure inside the chamber when the cryocooler is cold is typically of 1-3 $\times$ 10^{-7} mbar. A picture of the assembled cryocooler with the electrical and fiber feedthroughs is given in Figure 6.15.

3.4 Performances

With the four SNSPDs installed in the cold head and the feedthrough completed we can turn on the system and operate the detectors at low temperature. The cooling cycle is shown in Figure6.16. The cooling from room temperature to below 1.5 K takes about 10 hours. We reach a temperature of 1.31 K at the level on the SNSPD, lower than the 1.7 K achievable with the dipstick. This decrease in temperature enables to push further the polarization current of the SNSPD and so to work higher in the system detection efficiency plateau introduced in **Chapter 2**, i.e. where the voltage pulses from the detectors are best

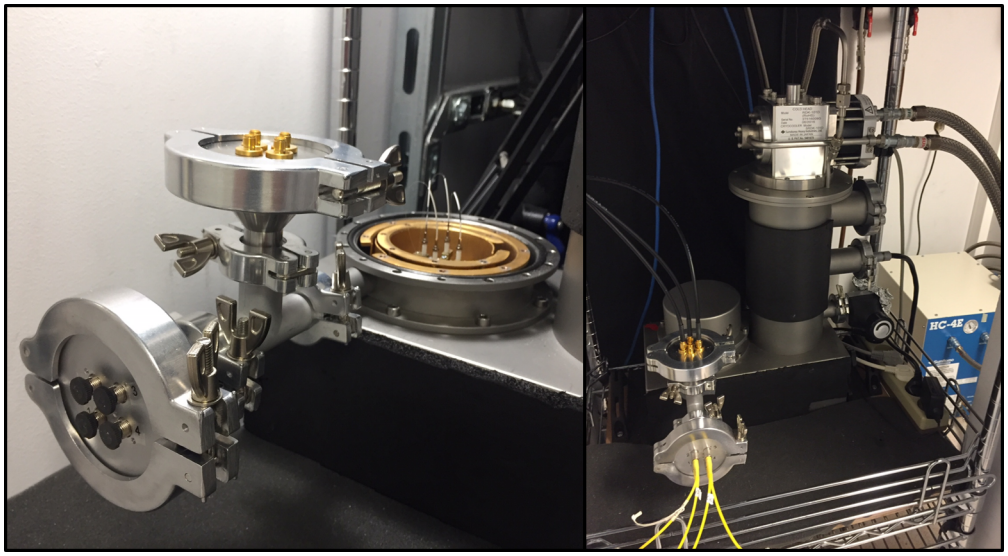

Figure 6.15: **Pictures of the cold head.** (Left) Four SNSPDs are installed in the cold head. The electric and fiber feedthrough is complete. The fibers from the experiment can be connected directly on the FC/PC mating sleeves and the electric signal from the SNSPDs can be recovered from the SMA connectors. (Right) Picture of the cold head while operating the cryo.

defined and have the most consistent rising edge. In addition we measure a dead time of the SNSPDs reduced by almost a factor two. The temperature is actively stabilized thanks to the phase transition of helium, with a precision of about 1.5 mK. The cryocooler offers a much better mechanical stability as compared to the dipstick, which can be assessed by considering the number of SNSPDs that have broken while being operated. We note that inside the cryocooler no SNSPD has broken for more than two years. The cryocooler can remain cold for more than 5 days in a row. After that it requires the warm up to room temperature to reset the cycle of the secondary circuit. Since it can be remotely started we synchronize the cooling and warming sessions in order to have the SNSPDs operational for 5 working days a week. In addition, since our helium circuits are closed we do not need to replace the helium (in practice refills are performed every year to ensure a constant helium pressure) in contrast to the disptick system which required one working day per week for helium renewal. It also drastically reduces the cost of the cooling operation as helium is recycled.

In terms of maintenance, the system typically suffers from clogging that may occur inside the capillaries of the secondary circuit. They originate from impurities - such as O_2 molecules, N_2 molecules, etc - which enter the circuit because of imperfect sealing. To solve this issue the secondary circuit need to be repumped once every month to a typical pressure of 10^{-5} mbar at room temperature.

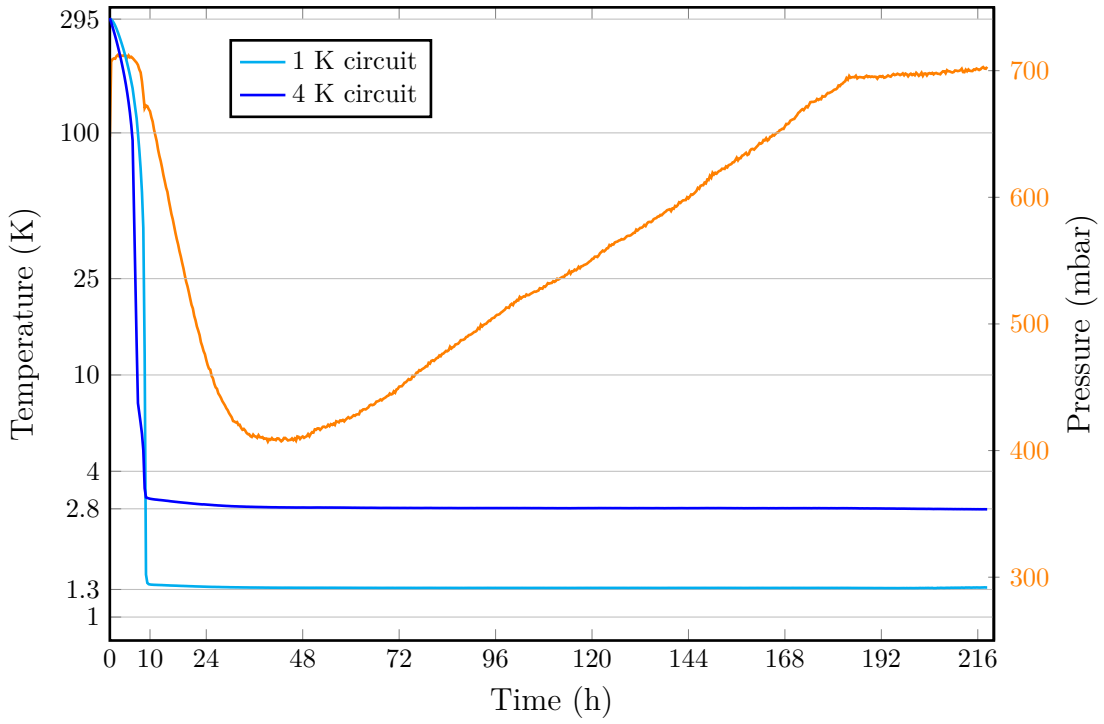

Figure 6.16: **Endurance test of the cryocooler.** (Blue) Temperature of the sensor in the 4 K circuit and in the 1 K sampling region as a function of time. (Orange) Pressure of the helium in the secondary circuit as a function of time. The cooling from room temperature down to 1.31 K takes about 10 hours. The helium condensates in the 1 K pot when the temperature of the 4 K circuit reaches its working temperature. It is characterized by a decrease of the pressure of helium from about 700 mbar to 400 mbar. The temperature is actively maintained at 1.31 K ± 1.5 mK for about 7 days until all the liquid helium has evaporated. Once the helium has fully evaporated the 1 K region is passively maintained at its working temperature thanks to efficient thermal isolation. The temperature slowly rises and remains below 2 K for several days. Yet we do not operate the detectors during that passive stage since the fluctuations of temperature are not controlled.

3.5 Compatibility with the experiment

Not only do we need to have the SNSPDs working at low temperature for a long time, but we also need to be able to detect the clicks from the SNSPDs without excessive noise. Indeed the cryocooler system involves a lot of electronics that can induce noise captured by the SNSPD amplifiers. Among them are the power supplies of the cold head, the compressor and the corresponding water exchanger, the turbo station and scroll pump, the temperature sensors, and the remote control of the system. Bad contacts on the electronic feedthrough are also be detrimental to the measurement of clicks. In addition,

for practical reasons the cryogenic system is located in a separate room to reduce the acoustic noise in the lab. It is optically connected to the optical table by 15 m long fibers (**Thorlabs 1060XP**). The electric signal for the SNSPDs are amplified at room temperature using the home-made NIST circuits presented in **Chapter 2** and in [7], and sent through 15 m long BNC cables to the lab. The BNC cables catch ambient noise at few tens of MHz that are filtered using low-pass filters (**Crystek Corp. CLPFL-0021-BNC**).

Thus with proper signal amplification and filtering we manage to recover the clicks from the four SNSPDs. The system detection efficiency is estimated to be above 85% for the four detectors, with a dark count rate below 10 Hz. The typical dead time of the SNSPDs are 50-70 ns.

3.6 Discussions - Improvements

Several enhancements can be introduced to our cryogenic system. First we note that the existing amplification of the SNSPD signal is done at room temperature. It induces latching of the detectors (i.e the polarization current needs to be reset when the SNSPD saturates), additional thermal noise on the SNSPD clicks that has to be filtered and limits the maximal operational rate of the system that can be a limiting factor for some security protocols. Pre-amplification at low temperatures could be added to the system, yet the small volume available in the sampling region where the SNSPDs are located prevents the installation of electronics inside the cooling device. We note that other systems (**ID Quantique ID 238**) present that type of pre-amplification at low temperature in a latching-free system, yet they do not reach the record quantum efficiency that we measure with our SNSPDs at our working wavelength.

A natural extension of the device would be the addition of more SNSPDs in the cryogenic system, either to perform very complex schemes or to operate several experiments in parallel. Again we are limited in our case to the volume available in the sampling region but we note that an extension up to 8 detectors could be done with the appropriate design of the 1 K plate and of the feedthrough system.

3.7 Coincidence detections

With a system operating four independent SNSPDs, the detection of coincidence becomes less trivial. Previously with two SNSPDs the detection of a two-fold coincidence could be done directly at the level of the ultrafast acquisition oscilloscope (**Lecroy Teledyne WaveRunner 6 Zi**) which can perform programmable coincidental triggering. However when the number of SNSPD used increases the number of channels necessary for the triggering increases as well, so that we are quickly limited by the number of input ports available on the scope. To overcome that limit we decided to use a dedicated *coincidence detection* system. Our goal is to be able to measure up to four-fold coincidences and to create a pulse upon detection of the desired combination of events that will trigger the recording of the quadratures. Since the heralded non-Gaussian states to be interfered have a temporal mode width of about 5 ns we need a system to be able to detect coincidences in a temporal window down to 500 ps, with a time resolution of 100

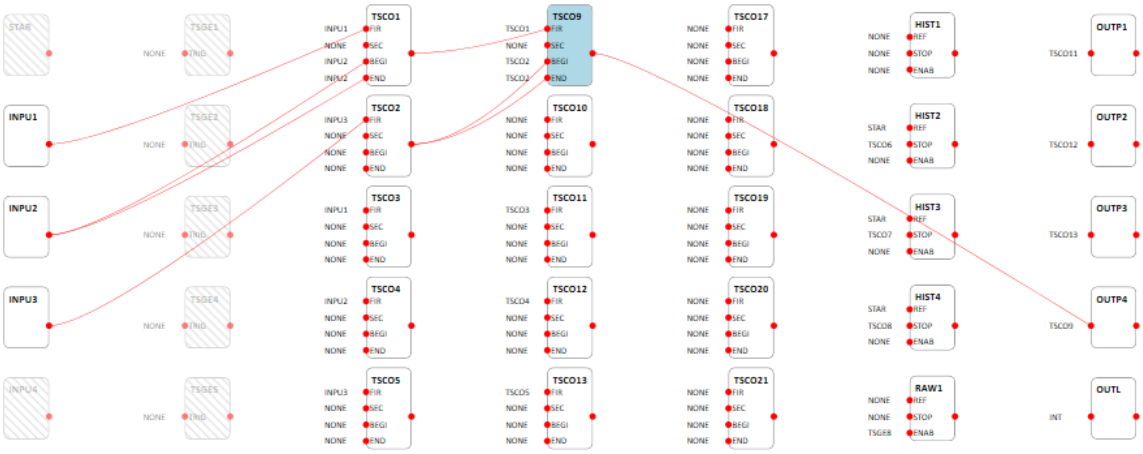

Figure 6.17: **ID900 Configuration Editor.** Schematic of the configuration editor presenting the different block layers. The time controller is set for triple coincidence detection realized by a series of two two-fold coincidences. The signals from the SNSPDs are connected to the INPU# blocks. The logical operations are performed by the TSCO elements. The results of the combiners can be either transfered to an additional operation layer, or directly to the OUTP# physical blocks from which the TTL pulses are emitted.

ps. This kind of performance requires ultra-fast electronics since typical FPGA modules have a clock frequency up to 40 MHz which renders very challenging the temporal resolution below the nanosecond. Other, faster solutions, are available, but they typically represent a cost that grows exponentially with the operational speed. We thus decided on a commercial solution that was offered by the company **ID Quantique** with their **ID900 Time Controller** which was one of the only devices available on the market that enables programmable conditional output generation. The device handles up to four inputs and can deliver up to four conditional outputs. In high speed mode it can have a maximum processing rate of 100 MHz with a resolution of 100 ps. It has an input-output latency of 400 ns that needs to be balanced by additional delays on the experiments which can easily be adjusted either with coaxial cables or optical fibers of few tens of meters.

As pictured in Figure 6.17, the device is provided with a configuration editor that allows to program it to the task at hand with a clear and simple interface. The editor is composed of different layers that represent the logical blocks that are created in hardware within the FPGA. These blocks can graphically be connected one with the other for programming. It corresponds to entering the desired SCPI command. The timestamps are processed from left to right. In particular for our application we use the four input blocks (INPU#) that receives the signal from its corresponding physical inputs. The signal can be directly transmitted to the next layer or shaped as a short pulse of 5 ns. The value of the trigger chosen to create the input pulse can be set independently for the four inputs in a range from 0 to 5 V. The combiner blocks (TSCO) are used to create the different logical operations between the input timestamps. Each TSCO consists in

four inports. The FIRst and SECond are the two main ports from which the TSCO gives the result of the chosen logical operation (AND, OR, ONLYFIR, ONLYSEC and MUTE). Two additional ports BEGin and END define the time window where the logical operation can be performed. Both these ports can be artificially delayed. Different TSCOs can be used in series to perform complex logical circuits. In the end the signal are connected to the output block (OUTPut#) that transmits the signal received to the corresponding physical output port. This block can also be delayed and reshaped. In our case we select for the output triggering pulses TTL signals with a duration of 100 ns.

A coincidence detection can thus be programmed very efficiently using this architecture. The signals from the SNSPDs are directly plugged on the input ports. The signals are processed by the TSCOs and the desired triggers are created at the output ports. For a two-fold coincidence detection the signal from one click is used to define the temporal window when the TSCO operates (BEGin port). The signal from the other SNSPD is connected to the FIRst port. By selecting the ONLYFIR logical operation we can create a temporal filter that lets the signal pass only when another click has been detected in the correct temporal window. The coincidental window can be adjusted with a internal delay between the BEGin and END ports. The output of the TSCO is directly connected to the output port to create the TTL signal. To implement three- or four-fold coincidences detection several logical layers are performed by using several TSCOs in series. We can implement in that way a coincidence detector that can process the clicks from up to four independent SNSPDs, with a coincidence window ranging from 100 ps to several ns.

4 Conclusion

In conclusion we have here presented the two major experimental improvements that have been performed on the experiment during the thesis. We have first created a new heralded single-photon source from a brand-new type-II OPO design that enables the parallel operation of in principle any large number of independent sources. We presented high-purity discrete-variable qubits that have been experimentally generated from this new device using an efficient scheme based on the displacement of the heralding mode. In the end we improved the cryogenic system that can now handle up to four SNSPDs and detect properly coincidental events. These innovative improvements increase substantially the capability of the experiment and bring within reach even more ambitious quantum information processing protocols to be implemented. In the next chapter we will employ these new resources in a quantum teleportation protocol which, contrary to the swapping protocol presented in the previous chapter, would have been impossible to implement otherwise.

Chapter 7

Quantum teleportation with hybrid entanglement

In this last chapter, we will present the experimental demonstration of a long-standing goal of our team, namely, quantum teleportation with hybrid entanglement of light. We will study the teleportation of a discrete-variable qubit to a continuous-variable quantum state heralded by our hybrid Bell-state measurement in a completely post-selection-free scheme. Such an experiment can be seen as the quantum equivalent of a digital-to-analog converter. We will first introduce the benefits of the scheme in the context of heterogeneous quantum networks, before presenting its implementation and the experimental results. In the end we will study the limitations of the scheme and its extension to other quantum encodings.

1 Converting quantum information via teleportation

1.1 Previous works and limitations

1.1.1 Quantum teleportation with fixed encodings

Quantum teleportation has historically been performed earlier than entanglement swapping for both the DV and the CV paradigms. Quantum teleportation indeed requires less experimental resources than entanglement swappping. The first experiment of DV qubit teleportation was performed by Bouwmeester and colleagues in 1997 [130] using polarization qubits with post-selection. The experimental setup is shown in Figure 7.1 (a). The initial DV polarization qubit $|\psi\rangle_1 = c_0 |H\rangle + c_1 |V\rangle$ is conditionally prepared from an EPR source labeled 1-4 at a detector p following a historical scheme proposed by Kwiat *et al.* [228]. One EPR source is used to generate a pair of polarization entangled photons labeled 2-3. The Bell-state measurement consists in the simultaneous detection of photons 1 and 2 on two separate detectors labeled $f1$ and $f2$. Again the scheme depends on post-selection and 3/4 of the events are discarded, yielding a success probability of 1/4. The teleported state is finally polarization-analysed using a polarization beamsplitter and two

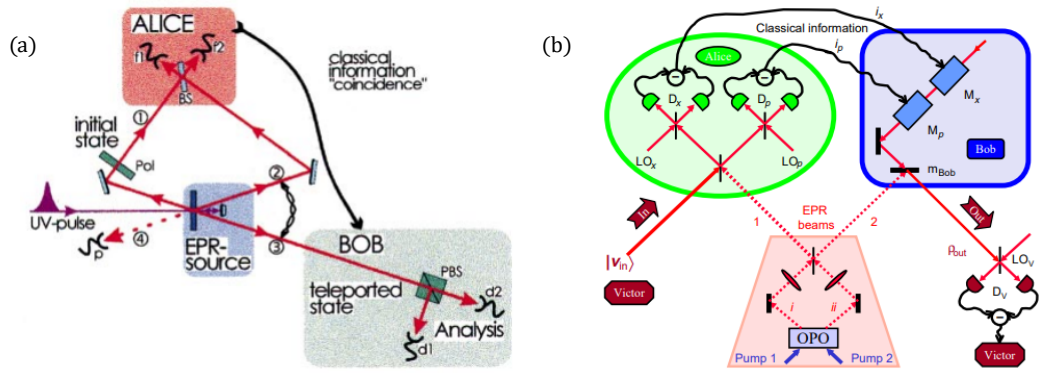

Figure 7.1: **Historical quantum teleportation setups**. (a) Experimental setup for DV qubit teleportation demonstrated by Bouwmeester and collaborators [130]. The EPR sources creates two entangled photon pairs labeled 1-4 and 2-3 respectively. The DV polarization qubit is heralded by a click on detector p. The BSM is performed between photon 1 and 2 and teleportation is successfully performed upon detection of four-fold coincidences on detector p, $f1$, $f2$ and $d1$ ($d2$). (b) CV quantum teleportation as demonstrated by Furusawa and colleagues [132]. The EPR source between modes A and B is a two-mode squeezed vacuum. The BSM is performed between modes in and A with two homodyne detectors. The mode B is displaced according to the results of the BSM transmitted via classical channels of gain g. The success of the teleportation is assessed by looking at the spectrum of the teleported state on a homodyne dectection.

detectors $d1$ and $d2$. The success of the teleportation was assessed by four-fold coincidences detection of photons at detectors p (qubit heralding), $f1$, $f2$ (Bell-state measurement) and $d1$ (or $d2$, proper output). The observation of a dip for the four-fold coincidence at zero delay for the corresponding polarization signifies the success of the teleportation.

Again the necessity to detect a photon at the output for the success of the teleportation makes the teleported qubits unavailable for any subsquent operation. This problem was pointed out by Braunstein and Kimble which referred to the scheme as *a posteriori teleportation* and led to a famous historical debate [208].

Unconditional CV quantum teleportation, performed by Furusawa and colleagues in 1998 [132] has thus been a reply to this post-selected work. The corresponding experimental scheme is shown in Figure 7.1 (b). The state of the electromagnetic field to-be-teleported $(\hat{x}_{in}, \hat{p}_{in})$ belongs to a prepared set of coherent states. The CV EPR beams between modes A and B is prepared by mixing two single-mode squeezed vacua on a 50:50 beamsplitter. The beam to-be-teleported is combined with the EPR beam A $(\hat{x}_A, \hat{p}_A)$ on a 50:50 beamsplitter. The Bell-state measurement is performed by measuring the two mixed quadratures $\hat{x}_u = (\hat{x}_{in} - \hat{x}_A)/\sqrt{2}$ and $\hat{p}_v = (\hat{p}_{in} + \hat{p}_A)/\sqrt{2}$ using two homodyne detectors to obtain the classical results x_u and p_v. The measurement results x_u and p_v are finally transmitted to modulate a coherent beam in both amplitude and phase with an overall gain g. This modulated beam is then combined coherently using a highly reflective mirror

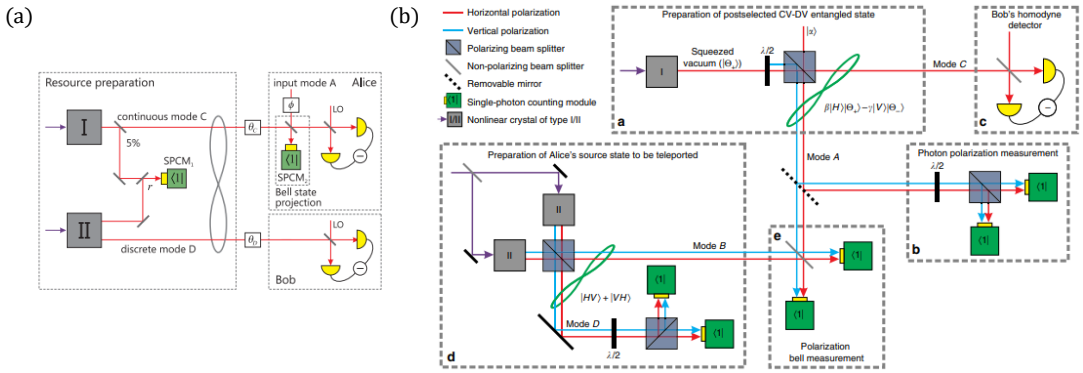

Figure 7.2: **Post-selected hybrid quantum teleportation setups**. (a) Experimental setup for hybrid teleportation from coherent-state superposition CV qubits to DV Fock state qubits demonstrated by Ulanov and collaborators [133]. The input CV qubit is approximated by an attenuated coherent state. The hybrid entanglement is generated using a methode similar to ours. Post-selected teleportation is heralded by a double-event on two single-photon detectors, and the teleported state is characteried by single-mode quantum state tomography with 54% correction for detection losses. (b) Experimental setup for hybrid teleportation from DV polarization qubit to CV coherent-state superposition basis demonstrated by Sychev and colleagues [209]. The polarization qubit is conditionally prepared from the mixing of two two-mode squeezers. The hybrid entangled state is generated by tapping a portion of a squeezed vacuum and mixing the tapped mode with an attenuated coherent state. The teleportation is post-selected upon triple coincidence on one single-photon detector for the qubit heralding and two detectors for the Bell-state measurement. The teleported state is characterized by single-mode quantum state tomography with 55% detection losses and 1500 quadratures for each state.

m_{bob} to interfere with the mode B of the entangled EPR beam $(\hat{x}_B, \hat{p}_B)$ thereby creating the teleported output state $(\hat{x}_{tel}, \hat{p}_{tel})$ by phase displacement following $\hat{x}_{tel} = \hat{x}_B + \sqrt{2}g\hat{x}_u$ and $\hat{p}_{tel} = \hat{p}_B + \sqrt{2}g\hat{p}_v$. In this way the four Bell states can be distinguished, and with the application of a feed-forward, the protocol becomes fully unconditional.

From these two experiments in the optical domain with fixed encoding in DV and CV, quantum teleportation has been extended to other physical platforms [229], ranging from atomic cloud [230], spin systems [231], and even optomechanical systems [232]. Quantum teleportation has also been performed in a hybrid setup to teleport deterministicly DV time-bin qubits via CV entanglement [197], to perform the teleportation of non-Gaussian wavepackets of light [233], and the high-fidelity teleportation of CV states with delocalized single photons [234]. Yet the hybrid entanglement of light between DV and CV states was not involved in these experiments.

1.1.2 Post-selected hybrid quantum teleportation

Contrary to hybrid entanglement swapping which had never been attempted before, several teleportation experiments involving hybrid entanglement of light have been performed. Yet, the reported work so far only relied on post-selected schemes. We will here detail two post-selected teleportation experiments, the first one from CV qubits encoded in coherent-state superposition basis $\{|cat+\rangle, |cat-\rangle\}$ to DV qubits encoded in the Fock basis $\{|0\rangle, |1\rangle\}$ [133], and the second one from DV polarization qubits to coherent-state superposition CV qubits [209]. The corresponding experimental setups are given in Figure 7.2.
In the first experiment:

- The input CV state is approximated by a low amplitude coherent state, which has many limitations. First the input state is always classical, i.e. its Wigner function is always positive and it cannot be used to create any entangled state, while the CV basis chosen should by definition present negativites of their Wigner function. Second, the input state is never heralded, and its creation is post-selected upon the success of the Bell-state measurement, so that the experiment cannot represent any practical protocol. Third, only the qubit phase can be tuned (i.e. the qubit weight remains fixed in all the study), meaning that only one direction of the Bloch sphere is probed. Finally the definition of the input qubit encoding is not clear, since an attenuated coherent state can be seen at the same time as a DV qubit or a CV qubit:

$$|in\rangle_A = \left|\alpha e^{i\phi}\right\rangle \approx |0\rangle_A + \alpha e^{i\phi} |1\rangle_A \approx \frac{1}{2}\left[\frac{|cat+\rangle_A}{N_+} + e^{i\phi}\frac{|cat-\rangle_A}{N_-}\right], \tag{7.1}$$

  which renders obsolete the need to convert quantum information between encodings.

- The hybrid entanglement is generated using a method similar to ours with a CV state encoded in the basis $\{\hat{S}|0\rangle, \hat{a}\hat{S}|0\rangle\}$, albeit a lower squeezing of 1.5 dB. This encoding is closest to the basis $\{|cat+\rangle^{\alpha_+}, |cat-\rangle^{\alpha_-}\}$ with $|\alpha_+| = 0.42$ and $|\alpha_-| = 0.72$. At these amplitude levels the populations of squeezed-vacuum and photon-subtracted squeezed vacuum are essentially zero. The experiment is thus naturally biased to the teleportation of vacuum that increases artificially the teleportation fidelity.

- The Bell-measurement is implemented using only one single-photon detector instead of a parity sensitive detector. As we have seen in **Chapter 4** the teleportation is successful only for state close to vacuum, and cannot be extended to pure cat states.

- The experiment is not actively stabilized and the phase of the qubit is post-processed directly given the result of the Bell-state measurement.

- The experimental data is corrected from 54% detection inefficiency, which is very prone to overestimate the quality of the experimental state, especially when the mean photon number is close to zero.

In the second experiment:

- The input DV polarization qubit is created following the proposal from Shapiro and collegues [235] to create ultra bright entangled photon pairs. The input qubit is prepared by conditioning on the desired polarization. Only one of the two detectors of the DV qubit heralded shown in the experimental scheme is used.

- The hybrid entangled state between DV polarization qubit and CV coherent-state superposition qubit is prepared by tapping a portion of a squeezed vacuum state on a variable polarizing beamsplitter and mixing the tapped mode with an attenuated coherent state. This creates the target hybrid entangled state with a large vacuum contribution that can be discarded only via post-selection.

- The Bell-state measurement is performed following the DV experiment presented in the previous section. In that case only one of the four Bell states is distinguished, and the Bell-state measurement is contaminated by the double events that have the same photon statistics. These double effects can be lowered by decreasing the pump power of the non-linear crystals, but in this implementation their probability is at the same order of magnitude than the "good" Bell detection events.

- The teleportation occurs post-selectively upon triple coincidence (one click for the DV qubit heralding, and two clicks for the Bell-state measurement) at a rate of 0.015 Hz, which limits the number of tomographic samples to 1500 quadratures for each teleportation measurement. Given that the characterization is done with more than 50% detection losses, it is very prone to statistical errors on the measurement of the fidelity of teleportation.

- The classical bound for teleportation at $\mathcal{F} = 2/3$ is only beaten on average over the Block sphere but not for all the sampled states.

- An extrapolation to entanglement swapping is performed via post-selection as an interpretation, but it does not constitute a proper entanglement swapping experiment since the swapped state is destroyed as soon as it is heralded.

The two experiments thus offer first insights of quantum teleportation with hybrid entanglement of light despite being strongly limited to post-selection. The first scheme is limited by the size of the CV state that can be successfully teleported and cannot be scaled to large values of $|\alpha|$. The second scheme is limited by the large vacuum component in the hybrid state and an intrinsic small success rate which restricts the number of tomographic samples available.

1.2 Our goal with hybrid teleportation

Our goal is to perform a post-selection-free teleportation experiment where an input DV qubit encoded in the Fock basis $\{|0\rangle, |1\rangle\}$ is converted into a CV qubit encoded into

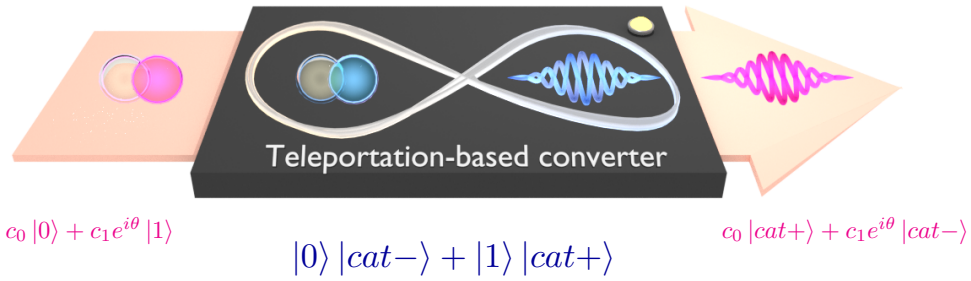

Figure 7.3: **Quantum information converter via teleportation.** An input DV qubit encoded in the Fock basis, in the form $c_0\,|0\rangle + c_1 e^{i\theta}\,|1\rangle$ is converted to a CV qubit encoded in the coherent-state superposition basis $\{|cat+\rangle, |cat-\rangle\}$ by a teleportation protocol relying on hybrid entanglement of light.

the coherent-state superposition basis $\{|cat+\rangle, |cat-\rangle\}$. The principle of the protocol is presented in Figure 7.3. In our scheme, all the involved quantum states are heralded, and both the vacuum and the multi-photon contributions will be experimentally taken into account in the process. This makes the experiment much more challenging than the other works presented earlier where these detrimental effects are discarded by post-selection. It represents a completely realistic protocol that would be performed in future heterogeneous quantum networks.

In the context of quantum networks, hybrid teleportation can be seen as a mean to convert quantum information between different encodings, and thus link different physical platforms that can couple preferentially to a DV or a CV system. In the classical domain the emergence of digital-to-analog (DAC) and analog-to-digital (ADC) converters has enabled the full transport, storage, and processing of classical information in the most efficient manner. It is thus legitimate to believe that such teleportation-based quantum converters will be essential blocks of future heterogeneous quantum networks.

For the experiment, high-purity DV qubits will first be characterized by single-mode quantum state tomography. The teleportation protocol will then be performed by mixing the heralded DV qubit with the DV mode of a heralded hybrid entangled state on a 50:50 beamsplitter. Finally the teleportation will occur upon the realization of the hybrid Bell-state measurement that is composed of a heralding on a single-photon detector and of quadrature conditioning on homodyne detection. The teleported state will finally be fully characterized by single-mode quantum state tomography and the success of the teleportation will be assessed by the measurement of the teleportation fidelity between the input and teleported states projected in the relevant encoding basis.

2 Experimental setup

The experimental setup for hybrid teleportation is shown in Figure 7.4. First the DV qubit is heralded by a click on SNSPD 1. This creates a coherent superposition of vacuum and single photon in the form:

$$|\psi\rangle_{in} = c_0 |0\rangle + c_1 e^{i\theta} |1\rangle . \tag{7.2}$$

Then hybrid entanglement is heralded by a click on SNSPD 2, creating the state:

$$|\Psi\rangle_{hybrid} = |0\rangle_{DV} |cat-\rangle_{CV} + |1\rangle_{DV} |cat+\rangle_{CV} , \tag{7.3}$$

where DV and CV label respectively the DV and CV modes.

The input DV qubit is mixed with the DV mode of the hybrid entangled state, and upon the success of the Bell-state measurement, it creates in an ideal scenario:

$$|\psi\rangle_{out} = c_0 |cat+\rangle + c_1 e^{i\theta} |cat-\rangle , \tag{7.4}$$

thus transfering the information of the qubits (c_0, c_1, θ) from a DV qubit to a CV qubit.

We will now detail each step of the procedure with our experimental setup including three OPOs and three SNSPDs.

2.1 DV qubit preparation

The method for the preparation of the DV qubit is the same as the one presented in **Chapter 6**. The heralding mode of the straight-cut (i.e. not the semi-monolithic) triply resonant OPO (OPO IIa) is mixed with an attenuated coherent state following the scheme proposed by Nielsen and colleagues [63]. This OPO is pumped by 2 mW of light at 532 nm, which creates (without displacement) a single-photon at a heralding rate of 250 kHz with a heralding efficiency of 71.2% ±1.5%. Then, several single-rail qubits of the form $c_0 |0\rangle + c_1 e^{i\theta} |1\rangle$ can be prepared depending on the amplitude and phase of the displacement beam applied. The qubit weight is defined by the ratio of clicks between the heralding of the OPO and the displacement, with an evenly-weighted qubit prepared when the rates are equal on SNSPD 1. The phase of the qubit θ is defined by the locking of the relative phase between the two paths with a phase noise of about 10%. We can generate, in particular, the six poles of the Block sphere, labeled $\{|0\rangle , |1\rangle , |0-1\rangle , |0+1\rangle , |0-i1\rangle , |0+i1\rangle\}$ with an average fidelity of 81%. The qubits at the equator of the Bloch sphere are prepared at a rate of 500 kHz, while the qubit $|0\rangle$ (prepared by closing the heralding path of the OPO and only injecting the displacement) is generated at a rate of 2 MHz. More details on the DV qubit preparation have been given in **Chapter 6**.

2.2 Hybrid entanglement generation

The hybrid entanglement is prepared similarly to the previous experiments by mixing the heralding mode of the semi-monolithic type-II OPO (OPO IIb) with the tapped mode

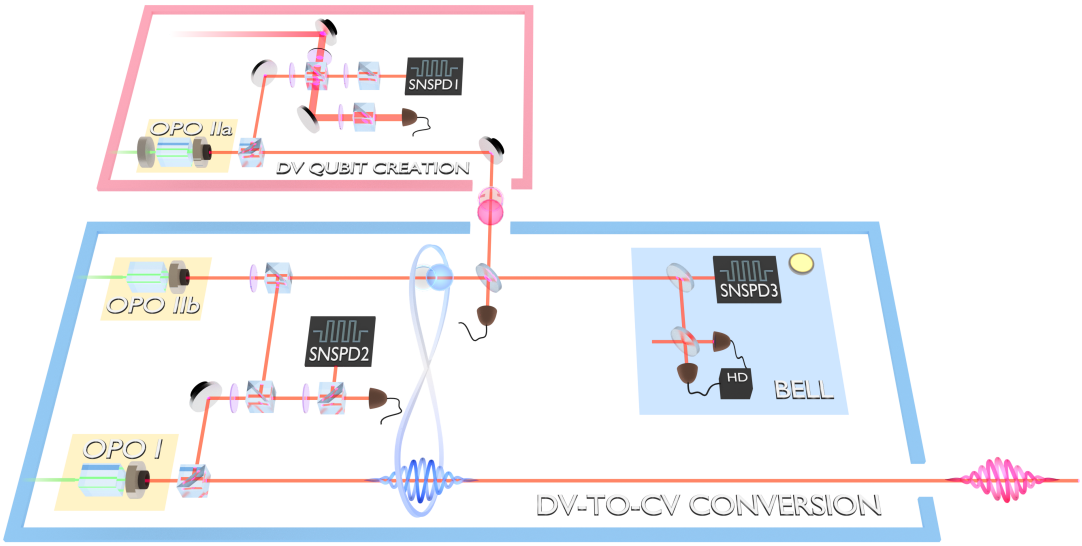

Figure 7.4: **Experimental setup for hybrid teleportation.** One single-mode squeezer (OPO I) is used to produce the continuous-variable states while two independent two-mode squeezers (OPO IIa and OPO IIb) are used to generate discrete-variable states. (Pink box) The discrete-variable input qubit is prepared by applying a displacement on the heralding mode of OPO IIa. The DV qubit is heralded by a click on SNSPD 1, while its phase is defined by the lock on P_1. (Blue box) Hybrid entanglement is prepared by projecting the conditioning paths of the OPO I and OPO IIb with a heralding on SNSPD 2. The input qubit is mixed with the DV mode of the hybrid entanglement and the Bell-state measurement (BSM, blue panel) is heralded by a clicks on SNSPD 3 followed by quadrature conditioning on homodyne detection (HD). Upon coincidental detection on the three SNSPDs, the qubit is teleported from DV to CV and the output qubit is characterized via single-mode quantum state tomography with a high-efficiency homodyne detection.

of the type-I OPO (OPO I), with a heralding on SNSPD 2. The type-II OPO is pumped by 3.5 mW of light at 532 nm while the type-I OPO is pumped by 15 mW, yielding about 4 dB of squeezing. For achieving a larger hybrid entanglement heralding rate, the tapping ratio of OPO I is increased from 3% to 7%, which gives a heralding rate of about 400 kHz for both the type-II and the type-I, and so for the hybrid entanglement. The relative phase between the two heralding paths is locked on maximum on the interference fringe using a microcontroller (3% phase noise). All the three OPOs are locked co-resonant for the pump and the down-converted fields, which corresponds to 8 experimental parameters (laser wavelength, temperature of the crystal (×3), OPO cavity length (×3), and angle of the crystal in the straight-cut OPO). This amounts overall to the use of five independent single-mode squeezers.

2.3 Bell-state measurement

To prepare for the Bell-state measurement, the input DV qubit is mixed on a 50:50 beamsplitter with the DV mode of the hybrid entangled state. One output of the beamsplitter is used to digitally lock the relative phase between the two DV paths either in phase, or out of phase (phase noise 3%). This enables to flip the phase of the qubit-to-teleport without the need to change the setting the of displacement beam which is more prone to uncertainty. The other port of the beamsplitter is send to the BSM station. First, a fraction $R = 10\%$ of the beam is tapped and send to SNSPD 3 for heralding, while the transmitted mode is send to homodyne detection for quadrature conditioning around $q = 0$ in a given conditioning window Δ that can be adjusted once the data is acquired.

2.4 Phase control

Since the information encoded in the phase of the input qubit has to be transfered without modification to the teleported state, an active control of the phase has to be perfomed all over the experiment. Overall, 14 locks are performed in parallel during the experiment that could last up to 16 hours for a single qubit. Apart from the typical locks that are required to operate the resources (i.e. two for the laser, two for each OPO, and one for each filtering micro-cavity before each SNSPD) three locks (indicated by the photodiode in Figure 7.4) are essential for the preservation of the phase through the process. First, the phase of the initial qubit θ has to be properly defined. This is done following the procedure given in **Chapter 6** to prepare the initial qubit phase either in phase or in quadrature (only these two settings are sufficient). Then, the phase of the hybrid entanglement needs to be actively controlled (in phase) otherwise the CV state phase would blur during the data acquisition. Finally the relative phase between the DV qubit and the DV mode of the hybrid entanglement needs to be fixed. Changing this phase corresponds to a rotation of the prepared qubit before the teleportation. In practice we can flip this phase to rotate the qubit to be teleported by π. So that starting from the two intial qubit phases (in phase, $\theta = 0$, and in quadrature, $\theta = \pi/2$) we can obtain the four qubits at the equator of the Bloch sphere ($\theta = 0$, $\theta = -\pi$, $\theta = \pi/2$, $\theta = -\pi/2$).

2.5 SNSPD operation

For the experiment three independent SNSPDs were operated in the cryocooler at a temperature of 1.3 K. In these conditions, the system detection efficiencies range between 85% and 90%, with a dark count rate at the few hertz level. The effect of dark count is completely negligible since they occur at a rate 10^{-3} smaller than the coincidence detected, yielding a triple-coincidence rate with at least one dark count below 1/1000 second. The SNSPDs being separated by 15 m to the optical table, the homodyne detection traces need to be delayed accordingly by about 100 ns.

2.6 Delay calibration

In order to have the photons interfering properly, we need to make sure that the delays before the three independent SNSPDs are correctly set, otherwise a coincidence between two SNSPDs can result in the optical table in two photons too separate in time, and that would thus not see each other. This delay calibration is performed by looking at the scan of the variance on the homodyne detection of the Bell-state measurement. Indeed, as we have seen in **Chapter 3**, such a scan presents the delay between the photon detected on the SNSPD and the photon detected on the homodyne detection. Our strategy is thus to make sure that for each independent heralding the increase in the variance appears at the same time on the homodyne detection. The delays are adjusted by increasing or reducing the length of the BNC cables before the coincidence detector. A precise delay can be ajusted using a coaxial delay box (**SRS DB64**). Using this procedure we can adjust the delay between the different SNSPDs with a precision of 200 ps. In addition about 80 m of BNC cables overall was used to delay the homodyne traces so that they match the arrival time at the SNSPD station.

2.7 Coincidence detection

Once the delay calibration is set, the coincidence detection can be performed efficiently. To that end we use the time controller presented in **Chapter 6** (**IDQuantique ID900**), which can perform this coincidence detection with a sub-nanosecond resolution.

Before presenting the parameters for the coincidence detection, we quantify the effect of the temporal coincidence window on the interference of two heralded single photons. It was not relevant to perform this study earlier since the coincidence detection was not performed as well in the swapping protocol. To that end, let us go back to the temporal modes of the heralded states. As we have seen in **Chapter 3**, the probability of measuring a signal photon at t when detection the idler at $t = 0$ is given by:

$$p'(t) = \pi\gamma_{OPO} e^{-2\pi\gamma_{OPO}|t|}. \tag{7.5}$$

Now, we want to calculate the temporal mode overlap $\chi(\tau)$ between two independent signal photons detected with a delay τ. Since the events are independent, we can directly consider the probabilities $p'(t)$, so that:

$$\begin{aligned} \chi(\tau) &= 2\int_{\frac{\tau}{2}}^{+\infty} \pi\gamma_{OPO} e^{-2\pi\gamma_{OPO}t} dt \\ &= e^{-\pi\gamma_{OPO}\tau}. \end{aligned} \tag{7.6}$$

In the case of a coincidence detection, we fix a given temporal window Δ_t between the two events. This corresponds, while accumulating the experimental data, to an averaging of all the possible overlaps $e^{-\pi\gamma_{OPO}\tau}$ in the chosen window:

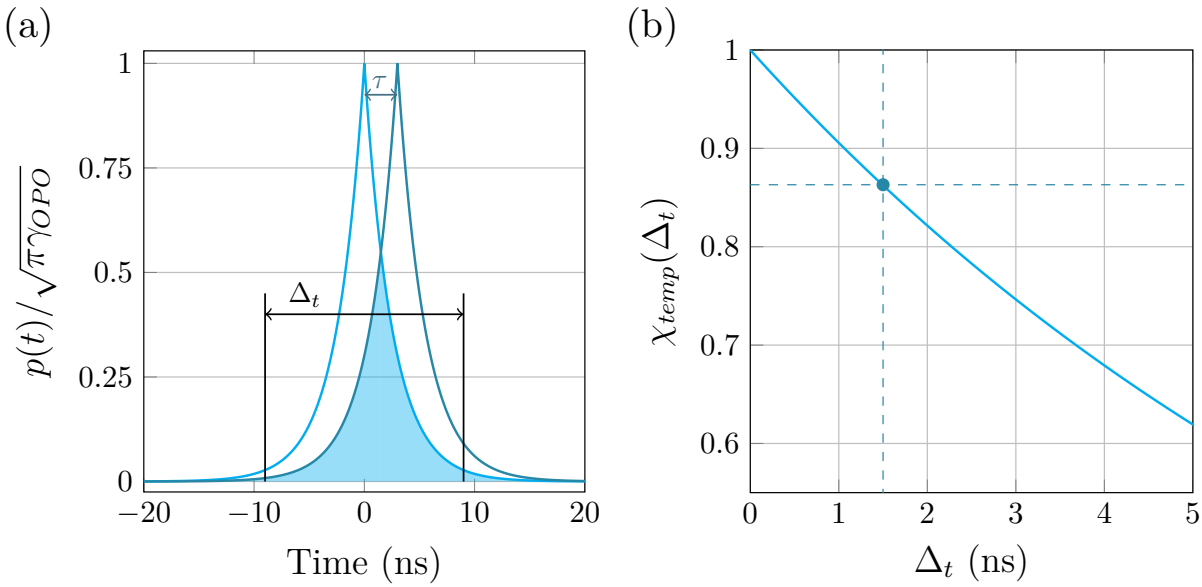

Figure 7.5: **Temporal overlap** (a) Two heralded single photons with a temporal width at half maximum of 10 ns are separated by a delay τ. The overlap between the two probabilities of presence is represented by the blue area. All these overlaps are integrated over the coincidence window Δ_t selected. (b) Temporal overlap χ_{temp} as a function of the coincidence window Δ_t. Our experimental implementation is represented by the blue dot. For a triple-coincidence window of 1.5 ns, the corresponding temporal overlap amounts to 86%.

$$\begin{aligned}\overline{\chi}(\Delta_t) &= \frac{2}{\Delta_t}\int_0^{\frac{\Delta_t}{2}} e^{-\pi\gamma_{OPO}\tau}d\tau \\ &= \frac{2}{\pi\gamma_{OPO}\Delta_t}\left[1-e^{-\pi\gamma_{OPO}\Delta_t/2}\right].\end{aligned} \tag{7.7}$$

In the case of the Bell-state measurement where two two-fold coincidences are detected in sequence, this temporal overlap has to be squared: $\chi_{temp}(\Delta_t) = (\overline{\chi}(\Delta_t))^2$. We give in Figure 7.5 the evolution of the overlap as a function of the temporal coincidence window Δ_t. As we can see, the shorter the coincidence window the larger the temporal mode overlap.

In terms of rates, it is important to note that the two-fold coincidence rate between two independent events is linearly related to the coincidence window. Indeed, if we label $\mathcal{R}_I$ the rate of the first event and $\mathcal{R}_{II}$ the rate of the second event, the rate of detection of the event II in the coincidence window Δ_t coincidentally to the event I is:

$$\mathcal{R}_{II,I} = \mathcal{R}_I \times \Delta_t \times \mathcal{R}_{II}, \tag{7.8}$$

since $\Delta_t \times \mathcal{R}_{II}$ corresponds to the probability of detection the event II in the window Δ_t. Therefore, starting from two events with rate $\mathcal{R}_I = \mathcal{R}_{II} = 100$ kHz and a coincidence window $\Delta_t = 1$ ns, the two-fold rate drops to $\mathcal{R}_{II,I} = 10$ Hz.

A small conditioning window has thus a drastic impact on the coincidence rate, but still the window cannot be chosen too large otherwise the temporal overlap between the two photons will be reduced. In our case, the window is limited by the temporal mode of the photon, which width at half maximum is of 10 ns. We decide for the experiment to fix the temporal window at 1.5 ns, which gives a temporal overlap of 86%. A larger coincidence window, leading to a better overlap and an increased rate could be achieved shall the OPO bandwidth should be reduced, which however typically comes with a decrease of the escape efficiency.

The three-fold coincidence detection is programmed on the time controller as a series of two two-fold coincidences. First a two-fold coincidence is detected between the click on SNSPD 1 and the clicks on SNSPD 2 - coincidental preparation of the two initial states - in a window of 1.5 ns, which occurs at a rate of 150 Hz. Next, a coincidence between the result of the first two-fold coincidence and the click on SNSPD 3 is detected in a window of 1.5 ns, decreasing the rate to 1 Hz (note that here we only look at the rate of the three fold coincidence and neglect the acquisition time on the computer). The coincidence detector finally emits a TTL pulse of duration 100 ns - with a delay of 400 ns as compared to the arrival of the clicks that is compensated by BNC cables on the homodyne detection - that is used to trigger the high definition oscilloscope. Note that, in addition, in practice, the events need also to be delayed by $\Delta_t/2$ for the centering of the temporal mode to maximize the overlap.

2.8 Data acquisition

Apart from the coincidental detection (which was before performed directly on the oscilloscope but which cannot be done with three independent SNSPDs), the data acquisition is very similar to the one of the swapping. The traces of the homodyne detections for both the BSM and the teleported state are recorded for each three-fold coincidence detection. Taking into account the data transfer to the computer, each event is recorded at a rate of 0.2 Hz. It is important to note that this rate corresponds to the phase stability of the experiment (i.e. the phase is preserved between two events separated by maximum 10 s) and cannot be reduced more in the current version of the setup. The phase of the each corresponding local oscillator are determined with the same technique presented before. For each qubit, we accumulate 10 000 three-fold unconditioned events, leading to a data acquisition ranging between 10 and 16 hours. The quadrature conditioning is performed on the pre-processed data in a conditioning window of $\Delta = 0.5\sigma_0$ (i.e. half the one of the swapping). This reduces the number of quadratures by a factor 3. The conditioned quadratures are then used to perform single-mode quantum state tomography in a Hilbert space of dimensions 1+9 with 15% detection losses with about 2500 quadratures for each qubit.

2.9 Comparaison to swapping

Before presenting the results of the teleportation, let us compare the performances of the swapping and teleportation setups in order to estimate the impact of the new resources presented in **Chapter 6**.

First, the use of three independent OPOs and three independent SNSPDs increases the success rate of the experiment. This enables us to increase much less the pump power of the OPOs required to reach a reasonable operational rate, thus increasing the purity of the states involved in the protocol. As compared to the swapping, **the purity of the input teleported state has been increased by a factor 2**. It also allows us to decrease the temporal coincidence window from 8 ns to 1.5 ns, increasing the temporal mode overlap between the states from 47% to 86%, and increasing the quality of the protocol by the same amount. In the end, more quadratures available enable us to reduce even more the quadrature coincidence window Δ to increase the teleportation fidelity. At equivalent pump powers and coincidence window size, we estimate that **we increased the rate of the experiment by a factor 20**.

Second, it is important to note that in the teleportation experiment, the filtering of the correct events is performed before the data is acquired, and not on the pre-processed quadratures. This enables to decrease a lot the amount of data that needs to be recorded and thus the duration of the experiment. For the same number of final filtered quadratures, **the weight of experimental data recorded has been decreased by a factor 1000**.

In this section we have presented the experimental setup for the hybrid quantum teleportation of discrete-variable qubits encoded in the Fock basis $\{|0\rangle, |1\rangle\}$ to a CV qubits encoded in the coherent-state superposition basis $\{|cat+\rangle, |cat-\rangle\}$. This setup makes use of the additional experimental resources that we have presented in **Chapter 6**. They improve substantially the quality of the protocol as compared to the scheme presented in **Chapter 5**. In the following we will present the experimental results of the teleportation protocol implemented in this way.

3 Teleportation results

The quality of the teleportation experiment is evaluated by comparing the experimental discrete-variable input states to the teleported states projected in the relevant continuous-variable basis. To that end both the input and output states are characterized independently by single-mode quantum state tomography. The success of the hybrid teleportation protocol is assessed by measuring a fidelity of teleportation above the classical bound over the full Bloch sphere. In the end we discuss the impact of the Bell-state measurement, the projection on the CV basis, and the impurities of the input states on the teleportation procedure.

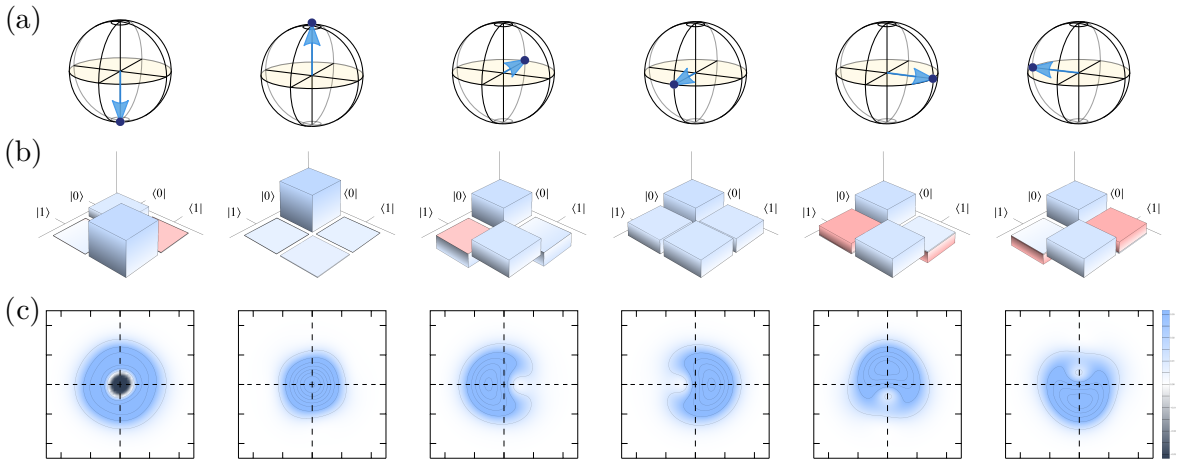

Figure 7.6: **Characterization of the input DV qubits** (a) Schematic representation of the position of the target qubit on the DV Bloch sphere. (b) Density matrices of the six input DV qubits in the Fock basis $\{|0\rangle, |1\rangle\}$, corrected from 18% detection losses. The real part are represented in blue while the imaginary part are represented in red. The gray vertical line indicates a unity height. (c) Experimental Wigner function of the six input DV qubits, corrected from 18% detection losses. The dashed lines represent the two quadrature axis. Each state is reconstructed from 40 000 quadratures in a Hilbert space of dimensions 1+4.

3.1 Characterization of the input states

Similarly to entanglement swapping, the input states need to be characterized in order to assess the quality of the teleportation protocol. The six input qubits at the poles of the Bloch sphere are prepared by applying the corresponding displacement beam. For the input DV qubit characterization, the states are analyzed with single-mode quantum state tomography, using the same homodyne detection as the Bell-state measurement in full transmission. The states are reconstructed from 40 000 quadratures in a 1+4 dimensional Hilbert space, correcting for 18% detection losses. The density matrices and Wigner functions of the measured input states are shown in Figure 7.6. We obtain for the input state a minimum purity of 71.2% for the state $|1\rangle$, 98.5% for the state $|0\rangle$ and on average 80% for the qubits at the equator of the Bloch sphere. The purity of the input qubits is limited first by the escape efficiency of the straight-cut type-II OPO, second by the qubit phase noise estimated to be of 10%, and finally by the pump power that has to be increased to achieve a practical operational rate.

3.2 Choice of the CV cat basis: loss of information

The teleported state has to be projected in a fixed CV basis $\{|cat+\rangle, |cat-\rangle\}$ in order to calculate the fidelity with the input DV qubit. However, as we have seen in **Chapter 3**, the state generated by the OPO I belongs to the basis $\{\hat{S}|0\rangle_{ideal}, \hat{a}\hat{S}|0\rangle_{ideal}\}$, which has a given

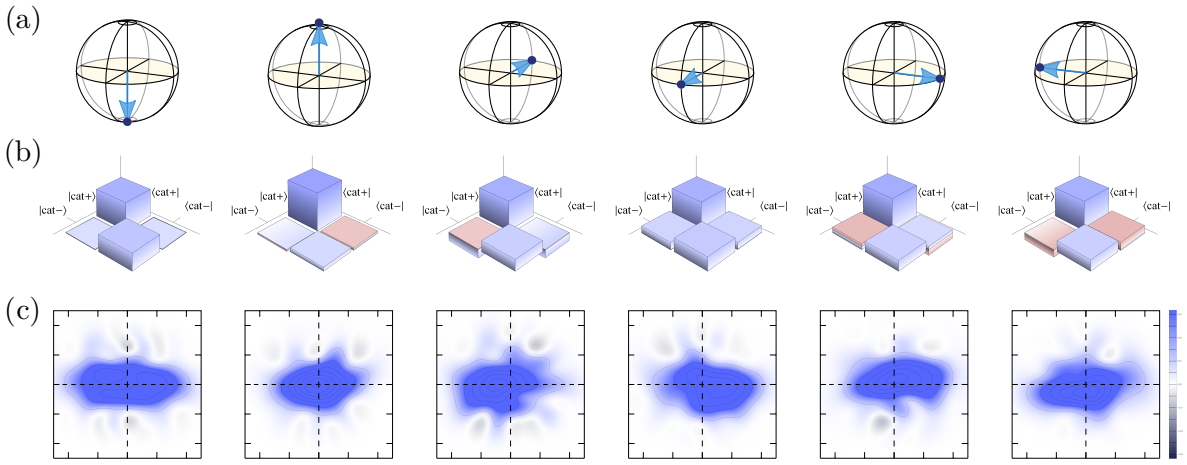

Figure 7.7: **Characterization of the teleported CV qubits** (a) Schematic representation of the position of the target qubit on the CV Bloch sphere. (b) Density matrices of the six teleported CV qubits in the cat basis $\{|cat+\rangle, |cat-\rangle\}$, with $|\alpha| = 0.9$, corrected from 15% detection losses. The real part are represented in blue while the imaginary part are represented in red. The gray vertical line indicates a unity height. (c) Experimental Wigner function of the six teleported CV qubits, corrected from 15% detection losses. The dashed lines represent the two quadrature axis. The states are reconstructed from 2185, 3691, 2802, 2657, 3641 and 2839 quadratures respectively, in a Hilbert space of dimensions 1+9.

fidelity with the target cat basis. In addition, because of the intra-cavity losses, the photon-subtracted squeezed vacuum experimentally generated contains a mixture of squeezed vacuum so that the experimentally generated states $\{\hat{S}\,|0\rangle_{exp}, \hat{a}\hat{S}\,|0\rangle_{exp}\}$ also have a given fidelity with the ideal photon-subtracted squeezed vacuum state $\{\hat{S}|0\rangle_{ideal}, \hat{a}\hat{S}\,|0\rangle_{ideal}\}$. Overall, in our operating regime, i.e. at about 4 dB of squeezing, the fidelity of the experimental computational basis elements $\{\hat{S}\,|0\rangle_{exp}, \hat{a}\hat{S}\,|0\rangle_{exp}\}$ with a target cat basis $\{|cat+\rangle, |cat-\rangle\}$ with $|\alpha| = 0.9$ are about 85%.

The means that, in principle, even with a perfect teleportation, the maximum achievable teleportation fidelity will be limited to about 85%. This limitation is intrinsic to the CV source we use based on type-I OPO. It is important to note that in our post-selection-free scheme, it is not possible to correct from this loss of information - by for instance renormalizing the state afterwards -, so that the experimental parameters have to be strengthened even more in order to beat the classical bound.

3.3 Measured teleported states

The teleported states are reconstructed by single-mode quantum state tomography, in a Hilbert space of dimension 1+9 and with 15% detection losses. The states are represented in Figure 7.7. First, and very interestingly, the physiognomy of the input qubits

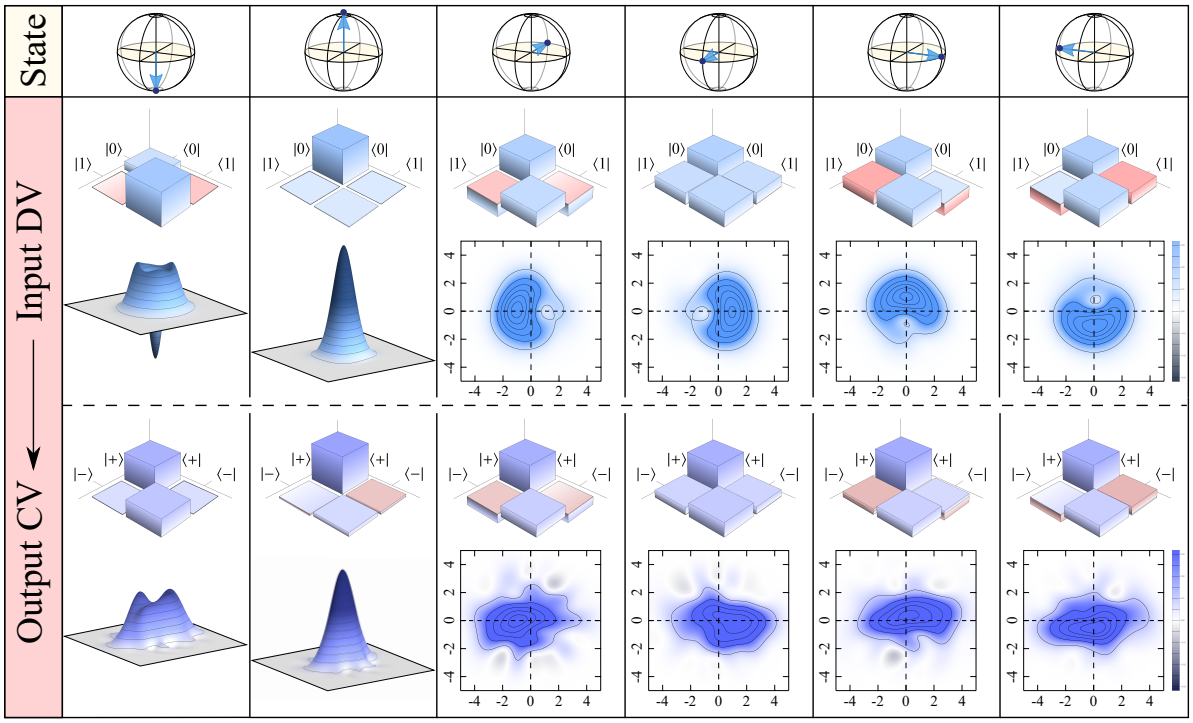

Figure 7.8: **Conversion table from DV to CV qubits** The six high-purity DV qubits at the poles of the Bloch sphere are converted into the corresponding CV qubits in the coherent-state superposition basis $\{|cat+\rangle, |cat-\rangle\}$.

are preserved in phase space, with in addition the application of a squeezing operation characteristic of the basis change. In particular the phase of the four qubits at the equator of the Bloch sphere is preserved through the process, as the direction of the dip in the Wigner function is the same for the input and the output states. For the teleportation of the DV single photon $|1\rangle$ to the CV odd cat state $|cat-\rangle$ we can recover a dip at the origin of phase space after teleportation. The Wigner function being a very sensitive state representation, this first qualitative observation is a strong signature of the quality of the teleportation process. Nevertheless the teleported odd cat state does not show negativity of the Wigner function. This is due to the the transmission losses of the homodyne detection for the Bell-state measurement, estimated to 17%, and the requirement of a finite coincidence window, which yields overall a vacuum admixture to the teleported state of about 30%. In order to achieve a transfer of negativity with our current setup, we estimate that, starting from an input single photon with a purity of 90%, BSM homodyne losses below 10% and a three-fold coincidence window of below 1 ns would be required to observe a negativity of the Wigner function, which is for the moment not achievable with current technologies.

The effect of the teleportation can also be seen in the density matrices of the states projected in the target $\{|cat+\rangle, |cat-\rangle\}$ basis with $|\alpha| = 0.9$. The transmission losses

in the Bell-state measurement and the limited purity of the hybrid entangled state lead to a squeezed-vacuum admixture to the teleported state, which increases the height of the projection on $|cat+\rangle\langle cat+|$ relative to the input DV state projection on $|0\rangle\langle 0|$. The real and imaginary parts of the coherences, i.e. the anti-diagonal terms of the matrices, conserve their sign after teleportation, which indicates a conservation of the phase through the process. Yet the amplitude of the coherences decrease because of phase noise. This effect is reduced by applying an active control on all the phases involved.

We can finally represent the experimental DV input and CV output qubits in the conversion table given in Figure 7.8.

3.4 Teleportation fidelity

A qualitative description of the teleported states is not enough to assess the success of the teleportation. A quantitative approach can be performed by measuring the teleportation fidelity between the input and outut states projected in the relevant DV or CV basis. It is defined as:

$$\mathcal{F} = \left[\mathrm{Tr}\Big(\sqrt{\sqrt{\hat{\rho}_{in,DV}}\hat{\rho}_{out,CV}\sqrt{\hat{\rho}_{in,DV}}}\Big)\right]^2, \tag{7.9}$$

where $\hat{\rho}_{in,DV}$ and $\hat{\rho}_{out,CV}$ are the density matrices of the input and output states projected in the DV and CV basis respectively. In the case of pure input and output qubits, the fidelity bound to ensure that quantum teleportation has occurred, is $\mathcal{F}_{pure} = 2/3$.

We give in Figure 7.9 the teleportation fidelity between the six input DV qubits characterized earlier, projected in the Fock basis $\{|0\rangle, |1\rangle\}$ and the six output qubits projected in the cat basis $\{|cat+\rangle, |cat-\rangle\}$ with $|\alpha| = 0.9$. We can see that the classical bound is beaten for all the qubits, with an average teleportation fidelity of 80% over the full Bloch sphere. We see, in particular, that the teleportation fidelity increases as the single-photon component of the input state decreases. For the logical qubit $|\mathbf{0}\rangle$, the fidelity is maximum at 83% while being minimum for the logical qubit $|\mathbf{1}\rangle$ with 76.4%, with a value around 80% for the evenly-weighted qubits at the equator of the Bloch sphere. This effect is to be expected since the higher the single-photon component in the input qubit, the higher the probability to detect a multi-photon event at the Bell-state measurement, which degrades the quality of the process. This coincides with the theoretical expectations given in **Chapter 4**.

3.5 Effect of homodyne conditioning

Similarly to entanglement swapping, we can study the effect of homodyne conditioning on the BSM and compare our results to what would be obtained with a "partial" Bell-state measurement, i.e. performing only the photon subtraction for the Bell-state measurement. The corresponding teleportation fidelities are also shown in Figure 7.9. As we can see it drastically increases the teleportation fidelity of the logical qubit $|\mathbf{1}\rangle$, for which the impact of multi-photon events, and thus the need to improve the BSM by conditioning, is the

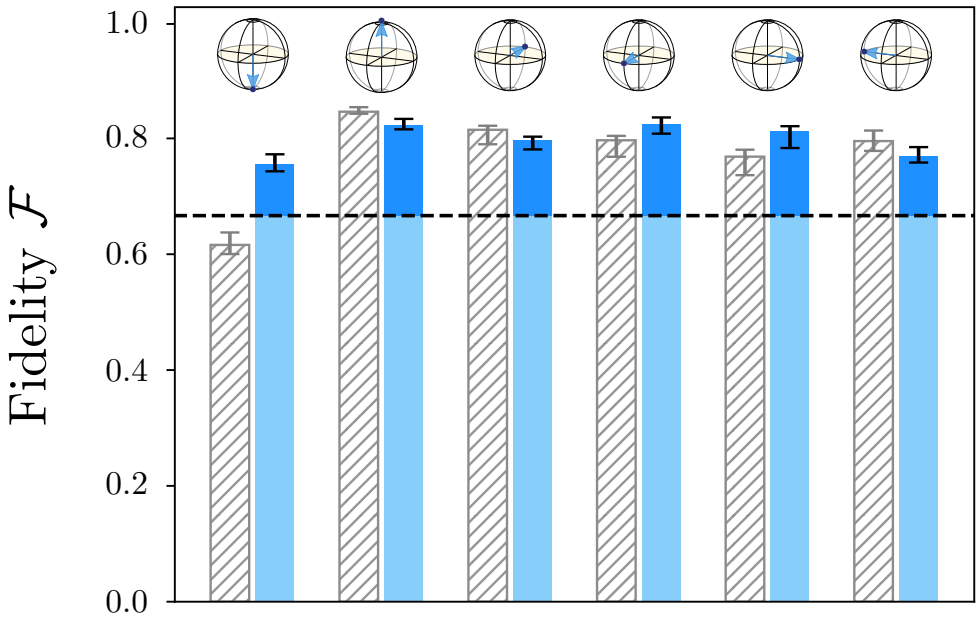

Figure 7.9: **Experimental teleportation fidelity** Teleportation fidelity $\mathcal{F}$ between the input qubits projected in the DV Fock basis $\{|0\rangle, |1\rangle\}$ and the teleported CV qubit projected in the basis $\{|cat+\rangle, |cat-\rangle\}$ with $|\alpha| = 0.9$, for the six poles of the Boch sphere. The grey dashed bars correspond to the result of teleportation without performing homodyne conditioning for the Bell-state measurement. The dashed line indicates the classical fidelity bound at $\mathcal{F}_{pure} = 2/3$.

most requisite. In particular, and very importantly, the quantum teleportation above the classical bound cannot be achieved for this state if homodyne conditioning is discarded, showing the efficiency of the hybrid Bell-state measurement combining photon counting and homodyne conditioning. The effect on the other qubits is marginal, as they contain a large vacuum component of at least 60% that is not affected by conditioning. We note that the drop in fidelity observed for two qubits by conditioning is just an effect of the projection on the cat basis, as the size of the measured state can slightly change when the conditioning is performed.

3.6 Error bar estimation

The estimation of the fidelity is subject to uncertainties that originate from the precision of the quantum state tomography and the stability of the experiment that is reproduced for several days during more than 10 hours. Indeed, how do we ensure that the qubit that has been teleported corresponds to the qubit that has been characterized prior the protocol ? In order to take into account both the uncertainty of the reconstruction of

the input state and the variations of the experiment, our strategy consisted in measuring a set of 30 input states over several days, and calculated the fidelity of the teleported states with that ensemble of states. This gives us the error on the fidelity measurement. As we will see the instabilities of the experiment represent the major contribution in this error, so that given the uncertainty estimation for the reconstruction given in other works [209, 197], we can neglect the uncertainty of the reconstruction of the output state. This uncertainty is indeed harder to estimate with high accuracy since we only have at our disposal one experimental point for each teleported state.

By applying this uncertainty estimation, we obtain the error bar plotted on the fidelity histograms given in Figure 7.9, which corresponds to the maximum and minimum teleportation fidelities $\mathcal{F}_{max}$ and $\mathcal{F}_{min}$ estimated in Table 7.1:

	$\|0\rangle$	$\|1\rangle$	$\frac{1}{\sqrt{2}}(\|0\rangle - \|1\rangle)$	$\frac{1}{\sqrt{2}}(\|0\rangle + \|1\rangle)$	$\frac{1}{\sqrt{2}}(\|0\rangle + i\|1\rangle)$	$\frac{1}{\sqrt{2}}(\|0\rangle - i\|1\rangle)$
$\mathcal{F}_{max}$	83.4%	77.3%	80.3%	83.6%	82.1%	78.5%
$\mathcal{F}_{min}$	81.6%	74.3%	78.1%	80.8%	78.3%	75.8%
$\Delta_{\mathcal{F}}$	1.8%	3%	2.2%	2.8%	3.8%	2.7%

Table 7.1: Error estimation of the teleportation fidelity

It is important to note that the teleportation fidelity $\mathcal{F}_{min}$ can only correspond to an overestimation of the quality of the input state, and so an underestimation of the quality of the teleportation. Since the classical fidelity bound is beaten for all the values of $\mathcal{F}_{min}$ - which is the fidelity obtained with the best input states measured - then teleportation is successfully assessed even by taking into account the experimental variations and reconstruction uncertainties.

3.7 Extending the scheme to pure input qubits

The experimentally generated input DV qubits are naturally composed of a statistical mixture of the target qubits with vacuum and multi-photon components. If the teleportation is well assessed by considering the teleportation fidelity for pure states above the classical bound $\mathcal{F}_{pure} = 2/3$, it is legitimate to study how the vacuum and multi-photon contributions affect our post-selection-free teleportation protocol. Indeed these elements can lead to an overestimation of the fidelity of teleportation as the purity of the input state decreases. For example, an admixture of vacuum in the input qubit always above 2/3, will always induce a teleportation fidelity above 2/3 even if the teleportation does not occur and pure squeezed-vacuum is created. It is thus important to note that the fidelity bound for quantum teleportation $\mathcal{F}_{pure} = 2/3$ is valid starting only from pure input DV qubits.

This discussion has been presented in the work from Takeda and collaborators [197] in the context of the unconditional teleportation of DV qubits encoded in time-bins. Starting from an input qubit with a qubit fraction η orthogonal to the vacuum admixture, the

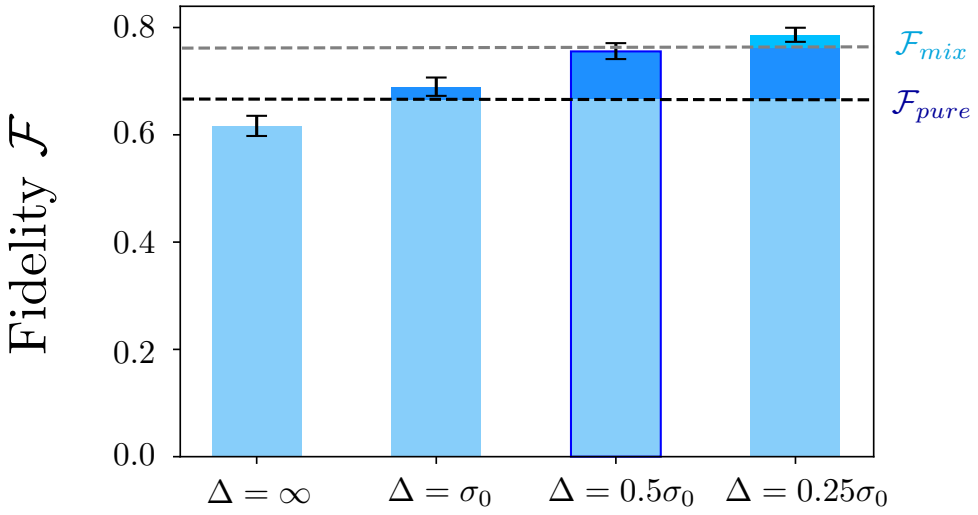

Figure 7.10: **Towards a pure input single photon** Fidelity of teleportation between the experimental single photon $|1\rangle$ and the odd cat state $|cat-\rangle$ projected in the corresponding basis, as a function of the Bell-state measurement conditioning window Δ. The dashed lines represent the classical bound for pure and mixed input states. The fidelity of teleportation increases as the conditioning window is narrowed, until the fidelity bound for mixed states $\mathcal{F}_{mix}$ is beaten.

fidelity bound for teleportation therefore becomes $\mathcal{F}_{mix} = 1 - \eta/3$, that reaches the value $\mathcal{F}_{mix} = \mathcal{F}_{pure} = 2/3$ in the case of pure input qubits.

This method can be adpated to our work. However, when working in the DV Fock basis $\{|0\rangle, |1\rangle\}$, the admixture of vacuum is orthogonal to the qubit subspace only from the logical qubit $|\mathbf{1}\rangle$, so that the adaptation of the fidelity bound for our qubit teleportation cannot be performed over the Full Bloch sphere. Yet we can restrain ourselves to the study of the teleportation of the state $|1\rangle$ only, which is the state the most sensitive to multi-photon effects and thus the most difficult to teleport above the classical bound, as we have seen in **Chapter 4**. If the teleportation succeeds for that state it will ultimately succeed over the full Bloch sphere in the same experimental conditions.

Considering only the input qubit $|1\rangle$, we can now consider the adapted fidelity bound $\mathcal{F}_{mix} = 1 - \eta_{OPO}/3$ with η_{OPO} being the heralding efficiency of the single-photon created by the OPO IIa, i.e. the straight-cut type-II OPO. It is important to note that beating experimentally the classical bound $\mathcal{F}_{mix}$ with a single photon of heralding efficiency η_{OPO} is equivalent to beating experimentally the classcial bound $\mathcal{F}_{pure}$ with a pure single-photon ($\eta_{OPO} = 1$), assuming that such state could be generated experimentally. The heralding efficiency is measured independently and we obtain the value $\eta_{OPO} = 71.2\% \pm 1.5\%$, which yields a fidelity bound $\mathcal{F}_{mix} = 76.3\%$, which is significantly higher than the previous bound at $\mathcal{F}_{pure} = 2/3$.

Using our experimental data, we can observe the evolution of the teleportation fidelity

for different conditioning windows Δ and focus on the two bounds $\mathcal{F}_{mix}$ and $\mathcal{F}_{pure}$ in the specific case of the teleportation of the single-photon $|1\rangle$ to the odd cat state $|cat-\rangle$. The corresponding results are represented in the histogram shown in Figure 7.10. As can be seen first, the teleportation fidelity does not beat neither $\mathcal{F}_{pure}$ nor $\mathcal{F}_{mix}$ if the homodyne conditioning is not applied ($\Delta = \infty$), which is exactly what we observed in the previous section.

We can however observe the success of the hybrid BSM combining photon counting with homodyne conditioning since the fidelity of teleportation increases as the homodyne conditioning is applied and the conditioning window is narrowed. Indeed, for a conditioning window $\Delta = \sigma_0$ and $\Delta = 0.5\sigma_0$, where σ_0^2 is the variance of vacuum, the fidelity beats the classical bound for mixed state $\mathcal{F}_{pure} = 2/3$. However this is not enough to reach the classcial bound for mixed states. The fidelity of the BSM can be strengthened by reducing even more the conditioning window. We see that, in particular, for a conditioning window of $\Delta = 0.25\sigma_0$, the fidelity bound for the mixed state is beaten, proving that the experiment can be employed using the same experimental settings for the teleportation of a pure single-photon, and a fortiori for the teleportation of any pure DV qubit encoded in the Fock basis $\{|0\rangle, |1\rangle\}$.

3.8 An artefact of the projection ?

It is fair to argue that the fidelity of teleportation measured depends also on the choice of the CV basis selected for the projection of the output state. Indeed, one unscrupulous experimentalist could choose on purpose a CV basis that would artificially give higher values of fidelities. To check this possibility we show in Figure 7.10 the fidelities of teleportation of the teleported single photon (which is the state with the lowest performance) with both a photon-substracted squeezed vacuum and an odd cat state, for different values of squeezing and cat sizes respectively, for two Bell-state measurement conditioning windows $\Delta = 0.5\sigma_0$ and $\Delta = 0.25\sigma_0$. We can see that the fidelity bound for pure states $\mathcal{F}_{pure}$ is beaten no matter the value of squeezing chosen for the projection and for a cat size ranging from $\alpha = 0.2$ to $\alpha = 1.3$, which is entirely within the range of states that can be obtained experimentally with our type-I OPO. When considering the fidelity bound for mixed states $\mathcal{F}_{mix}$, it is clearly beaten in the $\{\hat{S}|0\rangle, \hat{a}\hat{S}|0\rangle\}$ basis in a squeezing range of a few dB around our measured squeezing of 4 dB. For the basis $\{|cat+\rangle, |cat-\rangle\}$ the fidelity is reduced by a few percent and the conditioning window has to be narrowed in order to beat the classical bound. We can thus conclude that the observed teleportation fidelity is not an artefact from the projection on the CV basis, and that teleportation is successfully achieved.

3.9 Bloch sphere representation

We can finally study the teleportation process by looking at the transfer of purity. To that end we show in Figure 7.12 the Bloch spheres spanned by the initial and teleported states in the DV and CV basis respectively. For the CV basis, the Bloch sphere does not represent the purity of the CV state but the fidelity with the corresponding input state.

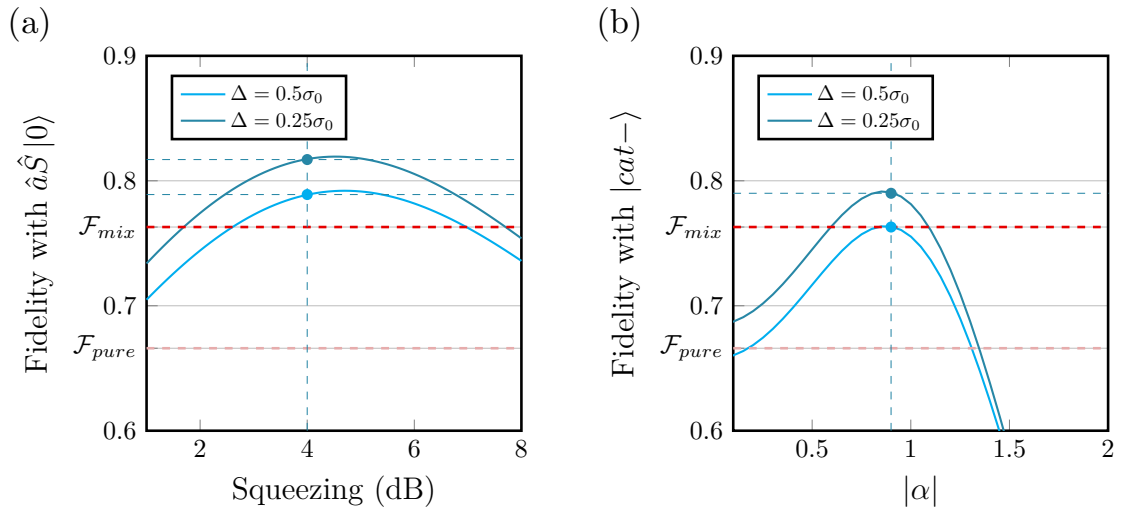

Figure 7.11: **Experimental fidelity of the teleported single photon with different basis element choices** (a) Fidelity of the teleported single photon to the photon-subtracted squeezed vacuum $\hat{a}\hat{S}\,|0\rangle$, as a function of the squeezing in dB, for two Bell-state measurement conditioning windows. In the two cases, both the fidelity bounds for pure and mixed states are beaten for a large range of squeezing value. (b) Fidelity of the teleported single photon to an odd cat state $|cat-\rangle$, as a function of the cat size $|\alpha|$, for two Bell-state measurement conditioning windows. As compared to the projection in the $\{\hat{S}\,|0\rangle\,, \hat{a}\hat{S}\,|0\rangle\}$ basis, the fidelity is reduced by about 3%, owing to the fidelity of the experimental state to the target cat. The fidelity bound for mixed states is beaten only for a reduced conditioning window $\Delta = 0.25\sigma_0$. The blue dots represent the chosen projection basis which gives the results presented earlier, i.e. a squeezing of 4 dB and a cat size $|\alpha| = 0.9$.

In a post-selection-free scheme with the DV qubit encoded in the Fock basis, the states are very sensitive to the loss of photon that correspond to a logical bit flip. As we have studied before, the states at the south of the equator are more prone to photon loss as the proportion of multi-photon effects is increased in that region. This effect is reflected by the asymmetry of the sphere along the azimuthal angle. The spheres are however very symmetric along a rotation along the polar angle, showing a proper phase definition of the input qubits and conservation of the phase via teleportation.

4 Discussion

Given these first promising results for the conversion of quantum information from DV to CV qubits, several improvements can be suggested to make the protocol operational at larger scales and represent a real application for prospective heterogeneous quantum networks. First, the rates are for now too limited and need to be drastically, i.e. exponen-

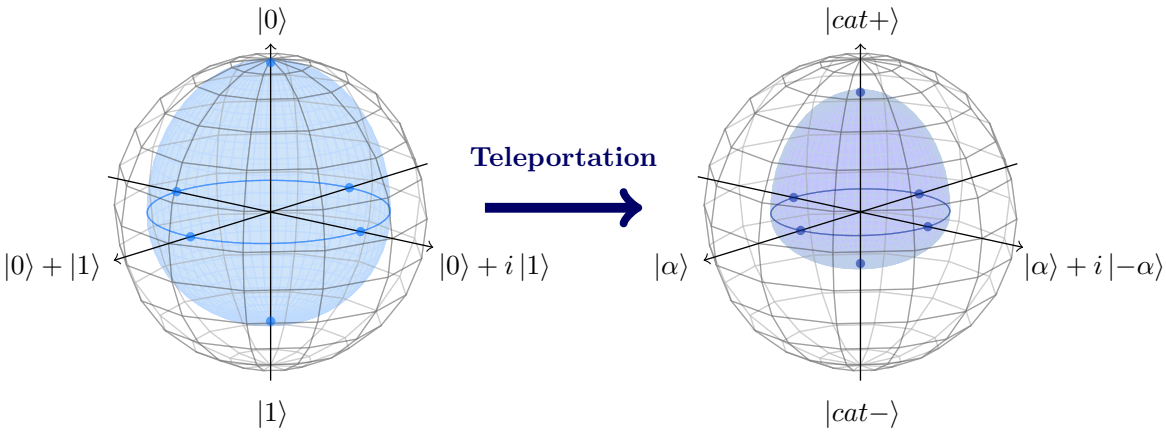

Figure 7.12: **Bloch sphere representations** (Left) Bloch sphere of the input DV qubits in the Fock basis $\{|0\rangle, |1\rangle\}$. The distance from the center is the purity of the state. (Right) Bloch sphere of the teleported CV qubits in the coherent-state superposition basis $\{|cat+\rangle, |cat-\rangle\}$. The distance from the center is the fidelity of teleportation with the corresponding DV qubit. As a reference the outer transparent sphere gives the Bloch sphere spanned by pure states .The blue and darker blue spots represent the experimental input and output states respectively, from which the surfaces are extracted.

tially, improved. Second, the DV encoding in the Fock basis leads to a large bit flip error rate that limits the possible extension of the protocol. Finally the reverse conversion, from CV to DV qubits has to be investigated and performed post-selectively-free.

4.1 Increasing the rates

Even though in our implementation the rate of the experiment has been increased by more than an order of magnitude, the overall operational rate, typically at a few events per minute, is far too low to make our protocol applicable. A trivial extension of the experiment would be to add a second Bell-state measurement at the second output port of the 50:50 beamsplitter mixing the two DV modes. This would increase the rate by a factor two, which is far from the exponential increase that is required.

When looking closely at the limiting factor of the overall success rate, we observe that it is mostly the two-fold coincidence rate between the two initial resources that restricts the probability of success. Indeed, the two resources are based on the stochastic creation of two independent states, so that the probability of the two occurring at the same time is naturally poor. This is a recurrent and topical problem in quantum information processing [221, 139]. As we have seen earlier, considering two independent stochastic events at a rate of 100 kHz, the probability of detecting a two-fold event in a one nanosecond window decreases by a factor 10^4, yielding a rate of 10 Hz. A strategy to bring an exponential increase of the success rate would be to synchronize these two stochastic events by the use of a quantum memory [117, 236]. By using this technique, the memory can store

the first state emitted while waiting for the second one to occur. The two-fold rate is in that case equal to the rate of the slowest source, which would be 100 kHz taking our previous example. Taking into account realistic heralded single-photon sources, a quantum memory with an efficiency of 90% and a memory time of 100 $\text{kHz}^{-1} = 10$ μs at our working wavelength could be employed. Quantum memories can now be achieved with performances close to these requirements, either all-optically [237, 224], or by employing matter systems [101, 238, 239].

Another strategy to get rid of the limited two-fold rate is to employ on demand, i.e. non-probabilistic sources [140, 240, 241]. Such a type of sources promise much larger generation rates and are even now employed in quantum teleportation protocols [242, 243]. Yet these on-demand sources suffer for the moment from smaller collection efficiencies, and can hardly compete with our heralded single-photon sources with up to 90% heralding efficiency. The reduced collection efficiency directly translates in a decrease of the success rate of the experiment, so that on-demand sources so far reach, for teleportation protocols, the same success rates as our probabilistic sources. Second, and more importantly, on-demand sources are for now very difficult to be build in an reproducible fashion [244], so that quantum states created from different sources cannot be indistinguishable. The protocols based on these sources are thus limited to a time-multiplexed usage of the source [225], which brings the limitations we have introduced in the framework of the swapping experiment, and cannot represent a practical protocol where two remote quantum nodes aim at sharing their quantum states. Finally, on-demand sources are up to date limited to the generation of discrete-variable states only, and should be extended to continuous-variable states should some hybrid protocols be targeted [245].

In parallel, progress to overcome the probabilistic generation of single-photon has been performed by employing time-multiplexed generation techniques [246, 247]. An increase of the heralding probability has been recently demonstrated by the use of mode analysis and adaptative optical switching on multimode heralded single-photon sources [248].

4.2 Extension of the DV basis

The second main disadvantage of our protocol is the choice of the DV encoding. Indeed with the single-rail encoding in the Fock basis $\{|0\rangle, |1\rangle\}$, the loss of a photon in the environment leads to the transformation $|1\rangle \rightarrow |0\rangle$ which is purely equivalent to a bit flip error. Thus, the only way to decrease this error rate is to minimize the transmission losses, which can become very struggling in the lab, and cannot be be extended asymptotically as optical elements, such as optical fibers, will intrinsically lead to losses by absorption or scattering. Other encodings can thus be suggested to improve the resilience of the scheme to channel losses. The extension of hybrid entanglement to time-bin or polarization encoding for the DV mode have been theoretically proposed [249, 250] to extend its applications over long distances. Such dual-rail approaches appear very interesting in that prospect and are definitely natural extensions and routes we are pursuing in our lab.

Nonetheless, the implementation of a dual-rail encoding with heralded sources requires to double the experimental tools necessary for the production of the DV mode, and was

up to now out of reach. The installation of a second type-II OPO in this thesis enables the creation of the required DV states, and so the extension in our lab of hybrid entanglement to polarization encoding. Our team is, in parallel, collaborating with the group of Virginia D'Auria who aims at producing hybrid entanglement using the time-bin DV encoding.

Such an extension should be implemented, many adaptions of the setup will be required. First hybrid entanglement with a polarization DV mode needs to be created, which can require just for itself the use of three independent OPOs and up to four SNSPDs. The creation of a DV polarization qubit to-be-teleported will then require additional resources to be built. Finally the hybrid Bell-state measurement combining photon counting and homodyne conditioning will need to be adapted to the choice of encoding.

4.3 A quantum analog-to-digital converter

A final curiousness that can be addressed is the ability to perform the protocol opposite to the one we presented, namely, the teleportation from a CV qubit to a DV qubit. This protocol can be implemented following a scheme very similar to ours, without in theory any supplementary limitation. The experimental scheme will, of course, need to be adapted to the states involved. First, the CV cat qubit can be prepared, not from a type-II OPO, but from a type-I OPO, as it has been reported in the work from [63]. The creation of hybrid entanglement can be performed in the exact same way as we did so far. The first difference comes with the mixing of the two CV modes, for which the two squeezing axis need to be aligned accordingly. Second, and more importantly, the Bell-state measurement will need to be modified as our implementation of the single-photon projection might not be relevant anymore.

5 Conclusion

We have demonstrated the post-selection-free teleportation of discrete-variable optical qubits encoded in the Fock basis $\{|0\rangle, |1\rangle\}$ to continuous-variable qubits encoded in the coherent-state superposition basis $\{|cat+\rangle, |cat-\rangle\}$ with $|\alpha| = 0.9$. We have presented the experimental scheme improved relative to the swapping experiment thanks to the use of three independent optical parametric oscillators and three independent single-photon detectors. We have assessed precisely the success of the teleportation in different continuous-variable basis using the fidelity of teleportation as a measure and studied the impact of the hybrid Bell-state measurement parameters on the success of the protocol. We demonstrated that our scheme could be extended, without any modification, to the teleportation of any pure discrete-variable qubit encoded in the Fock basis. Finally we have presented the limitations of the protocol in terms of success rate and choice of encoding, and given some possible improvements that can be included in the future, to make our hybrid teleportation-based protocols applicable in future heterogeneous quantum networks.

Conclusion

Summary

In this thesis we have experimentally demonstrated entanglement swapping and quantum teleportation with hybrid entanglement of light. To that end, we have first motivated our objectives in the framework of heterogeneous quantum networks and introduced the conceptual, theoretical, and experimental tools at the basis of our work. In particular we have presented the engineering of optical hybrid entanglement between discrete- and continuous variable qubits, central to the implementation of hybrid teleportation protocols. We have developed a novel hybrid technique for the implementation of a discrete-variable Bell-state measurement which combines for the first time discrete- and continuous-variable tools: photon counting on a single-photon detector and quadrature conditioning on homodyne detection.

By assembling these resources, we first performed an entanglement swapping protocol which made use of the same two optical parametric oscillators and superconducting nanowire single-photon detectors in a time-multiplexed fashion. We investigated the limitations of the protocol with minimum resources and developed new systems to circumvent them. These major improvements were composed first of an additional triply-resonant type-II optical parametric oscillator that enables the creation of discrete-variable qubits encoded in the Fock basis with an average purity of 80%, and second a cryocooler in which up to four superconducting nanowire single-photon detectors can be operated for more than 5 consecutive days. We finally employed these tools to demonstrate hybrid quantum teleportation between a discrete-variable qubits encoded in the Fock basis and a continuous-variable qubit encoded in the coherent-state superposition basis.

In the framework of heterogeneous quantum networks, this work opens up the possibility of connecting disparate quantum nodes based on different physical platforms and converting quantum information between encodings. It promises an increase in integration of systems of diverse natures and the development of novel functionalities for the most-efficient processing of quantum information in prospective modular architectures.

Perspectives

Following these fruitful results, several extensions of the work can be proposed. They include memory assistance for the increase of the operational rates, the extension of hybrid entanglement to other quantum encodings, and the development of active protocols based on hybrid entanglement, such as hybrid entanglement purification.

Increasing the rates

First, increasing operational rates is a requirement for the implementation of a next generation of protocols. This limitation arises from the stochastic generation process at the level of our optical parametric oscillators. Several challenging strategies can be employed to enable an exponential increase in success rates. The first one relies on the assistance by quantum memories to synchronize the stochastic sources. They are now implemented both all-optically or by using matter systems, but these platforms are not to date compatible with our experiment. On the one hand all-optical memories do not offer lifetimes which enable a sufficiently long storage of the quantum states. In our operating regime, with generations rates at the order of the megahertz, it requires several microseconds memory lifetime which are far from the several tens of nanoseconds observed in all-optical memories [224, 237]. In addition, these type of memories are not entirely on-demand as the storage time is always a multiple of a given unit memory time, and so the memory time resolution decreases as the memory lifetime increases. On the other hand, matter systems can yield much longer lifetimes, up to several milliseconds with modest memory efficiency [125], or about ten microseconds with record memory efficiencies of 90% [101]. Yet these platforms are not compatible with our working wavelength, and the development of matter memories, or frequency conversion systems that could be effective for our experiment is a very challenging, but rewarding, goal. Other techniques based on the multiplexing of heralded sources have recently been proposed to obtain increase of rates [248] and could be adapted to improve the rates of our protocols.

Hybrid entanglement with polarization-encoded discrete-variable qubits

The increase in experimental capability brings within reach the implementation of hybrid entanglement in more resilient quantum encodings. The transition of the discrete-variable basis from the Fock basis $\{|0\rangle, |1\rangle\}$ to the polarization basis $\{|H\rangle, |V\rangle\}$ could be straightforwardly implemented with our three optical parametric oscillators and four single-photon detectors [235, 250], though requiring a reorganization of the optical paths and being limited in generation rates. Such a change of encoding basis would enable the protection of the discrete-variable mode to logical bit flips that are a consequence of the inherent channel losses.

Towards purification of hybrid entanglement

Following all the protocols we developed with hybrid entanglement, that were up to now passive, it would be of great interest to pursue experimental efforts to the development of active protocols such as unconditional teleportation or entanglement purification. In particular, entanglement purification is a natural extension of the entanglement swapping protocol we implemented in this work. As we have seen, entanglement swapping certainly extends the distance to which entanglement can be propagated, but ultimately decreases the amount of entanglement that was present before propagation. Such hybrid entanglement purification protocols [213], central to the development of quantum repeaters, still need to be theoretically and experimentally investigated.

Appendix A

Properties of the density matrix

In Chapter 1, we defined the density matrix of a mixed state as the sum of the density matrices of the pure states $|\psi_k\rangle \langle\psi_k|$ weighted by their probability p_k:

$$\hat{\rho} = \sum_k p_k |\psi_k\rangle \langle\psi_k| . \tag{A.1}$$

Since it is linear, any density matrix $\hat{\rho}$ can be decomposed in the Fock basis $\{|n\rangle\}_n$:

$$\hat{\rho} = \sum_{n,m} c_{n,m} |n\rangle \langle m| . \tag{A.2}$$

We will now recall some mathematical properties of the density matrix.

- The probability completeness implies that the density matrix has unit trace:

$$\mathrm{Tr}(\hat{\rho}) = 1. \tag{A.3}$$

- The density matrix is Hermitian:

$$\hat{\rho}^\dagger = \hat{\rho}, \tag{A.4}$$

  so that it is diagonalizable with only positive eigenvalues.

- The expectation value of an observable $\hat{A}$ is given by:

$$\langle \hat{A} \rangle = \mathrm{Tr}(\hat{A}\hat{\rho}). \tag{A.5}$$

- The state purity $\mathcal{P}$ is given by:

$$\mathcal{P} = \mathrm{Tr}(\hat{\rho}^2) \leq 1. \tag{A.6}$$

- The fidelity $\mathcal{F}$ between two mixed states $\hat{\rho}_1$ and $\hat{\rho}_2$ is given by:

$$\mathcal{F}(\hat{\rho}_1, \hat{\rho}_2) = \mathcal{F}(\hat{\rho}_2, \hat{\rho}_1) = \left[\mathrm{Tr}\left(\sqrt{\sqrt{\hat{\rho}_1}\hat{\rho}_2\sqrt{\hat{\rho}_1}} \right) \right]^2 \leq 1. \tag{A.7}$$

Appendix B

Properties of the Wigner function

In Chapter 1, we defined the Wigner function as a root function from which any marginal distribution could be extracted:

$$P(q_\theta) = \int W(q_\theta, p_\theta) dp_\theta, \tag{B.1}$$

with p_θ the conjugate quadrature defined as $\hat{p}_\theta = -\hat{x}\sin\theta + \hat{p}\cos\theta$.

The Wigner function can be calculated from any density matrix $\hat{\rho}$ following:

$$W_{\hat{\rho}}(x,p) = \frac{1}{2\pi\sigma_0^2} \int e^{ipy/\sigma_0^2} \langle x-y| \hat{\rho} |x+y\rangle \, dy. \tag{B.2}$$

In practice as the Wigner function is linear in $\hat{\rho}$, it can be reconstructed from its Fock state decomposition:

$$W_{\hat{\rho}}(x,p) = \sum_{n,m} c_{n,m} W_{|n\rangle\langle m|}(x,p), \tag{B.3}$$

with

$$W_{|k\rangle\langle l|}(x,p) = \frac{(-1)^l}{2\pi\sigma_0^2} \sqrt{\frac{l!}{k!}} \left(\frac{x-ip}{\sigma_0}\right)^{k-l} e^{-\frac{x^2+p^2}{2\sigma_0^2}} L_l^{k-l}\left(\frac{x^2+p^2}{\sigma_0^2}\right), \text{if } k \geq l \tag{B.4}$$

and considering for $k \leq l$ that

$$W_{|k\rangle\langle l|}(x,p) = W_{|l\rangle\langle k|}(x,-p), \tag{B.5}$$

and L_l^{k-l} a Laguerre polynomial.

We will now recall some mathematical properties of the Wigner function.

- The Wigner function of a hermitian operator is real over the whole phase space.
- The Wigner function is normalized following:

$$\iint_{\mathbb{R}^2} W(x,p)\,dx\,dp = 1. \tag{B.6}$$

- The expectation value of an operator $\hat{A}$ is given by:

$$\langle \hat{A} \rangle = 4\pi\sigma_0^2 \iint_{\mathbb{R}^2} W_{\hat{A}}(x,p) W_{\hat{\rho}}(x,p)\,dx\,dp. \tag{B.7}$$

- The purity $\mathcal{P}$ is given by:

$$\mathcal{P} = \mathrm{Tr}(\hat{\rho}^2) = 4\pi\sigma_0^2 \iint_{\mathbb{R}^2} W_{\hat{\rho}}^2(x,p)\,dx\,dp \leq 1. \tag{B.8}$$

- The fidelity between two pure state $\hat{\rho}_1$ and $\hat{\rho}_2$ is given by:

$$\mathcal{F}(\hat{\rho}_1, \hat{\rho}_2) = \mathrm{Tr}(\hat{\rho}_1 \hat{\rho}_2^\dagger) = 4\pi\sigma_0^2 \iint_{\mathbb{R}^2} W_{\hat{\rho}_1}(x,p) W_{\hat{\rho}_2}(x,p)\,dx\,dp \leq 1. \tag{B.9}$$

- The value of the Wigner function at the origin in phase space $W(0,0)$ depends only on the diagonal elements of the density matrix:

$$2\pi\sigma_0^2 W_{\hat{\rho}}(0,0) = \sum_n (-1)^n \hat{\rho}_{nn}. \tag{B.10}$$

- The Wigner function is lower and upper bounded by:

$$|W(x,p)| \leq \frac{1}{2\pi\sigma_0^2}. \tag{B.11}$$

Appendix C

Micro-cavity design and characterization

A Fabry-Pérot cavity composed of two mirrors of low transmissions T_1 and T_2 (with $T_1+T_2 \ll 1$) and a round-trip cavity length l_{cav} is decribed by two independent quantities:

- The finesse F:
$$F = \frac{2\pi}{T_1 + T_2}. \tag{C.1}$$
- The free spectral range FSR:
$$\mathrm{FSR} = \frac{c}{l_{cav}}. \tag{C.2}$$
- The ratio of the two giving the bandwidth γ:
$$\gamma = \frac{\mathrm{FSR}}{F} = \frac{c(T_1 + T_2)}{2\pi l_{cav}}. \tag{C.3}$$

Thus any cavity of given bandwidth and FSR can be engineered by chosing the correct transmission of mirror and cavity length.

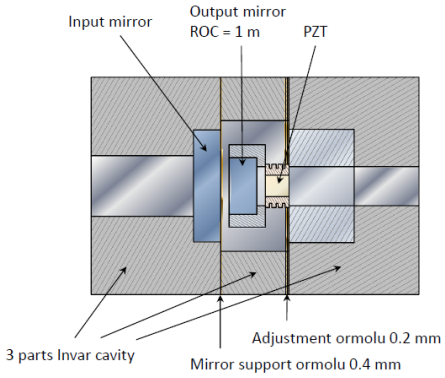

Figure C.1: **Micro-cavity design**.

As we have seen in Chapter 2, we target for the spectral filtering an FSR of 330 GHz, imposing a cavity length of about 400 μm, and a bandwidth of 320 MHz, which, given the length of the cavity, yields $T_1 = T_2 = 0.3\%$. To that end we use a micro-cavity design given in Figure C.1. For an improved mechanical stability the cavity is composed of three invar modules that are screwed one to the other in a bulk configuration. Such a design is quite challenging as, once the cavity is closed, it is not possible to adjust the angles of the mirrors for the alignment. It is thus important to ensure that all the layers assembled parallel to each other so that the optical axis is reachable from outside the cavity. The length of the cavity is adusted by inserting 200 μm and 300 μm thick ormolu plate. The cavity is plano-concave. The curved mirror has a radius of curvature ROC of one meter.

Once the cavity is assembled, it is important to verify that the bandwidth and FSR of the cavity correspond to the ones that are targeted. These quantities can be measured by looking at the transmission spectrum of the slightly misaligned cavity while sweeping its length with a piezo-electric module. Two successive FSRs, labeled I and II are observed on the same sweep of the cavity. As the cavity is slightly misaligned, several peaks, corresponding to the modes TEM_{00}, TEM_{01}, etc., will appear. We will call c_{0i}^{j} the position of the center of the peak of the mode $(0, i)$ in the FSR j (with $j \in (I, II)$), and ω_{0i}^{j} its width.

From this we can measure the length of the cavity l_{cav} following:

$$l_{cav} = \mathrm{ROC} \times (1 - \cos^2(\pi \times \mathrm{rap})), \tag{C.4}$$

where ROC is the radius of curvature of the curved mirror, and rap is defined by:

$$\mathrm{rap} = \frac{c_{01}^{I} - c_{00}^{I}}{c_{00}^{II} - c_{00}^{I}} = \frac{\nu_{01}^{0} - \nu_{00}^{0}}{\nu_{00}^{1} - \nu_{00}^{0}}, \tag{C.5}$$

where we recall ν_{nm}^{q} the frequency of the mode (n, m) in the FSR q:

$$\nu_{nm}^{q} = \frac{c}{2l_{cav}}\Big[q + \Big(\frac{1+m+n}{\pi}\Big)\cos^{-1}(\sqrt{g_1 g_2})\Big] \text{ with } g_i = 1 - l_{cav}/\mathrm{ROC}_i. \tag{C.6}$$

The finesse of the cavity is determined similarly following:

$$\mathrm{F} = \frac{1}{2}\left(\frac{c_{00}^{I}}{\omega_{00}^{I}} + \frac{c_{00}^{II}}{\omega_{00}^{II}}\right). \tag{C.7}$$

From these two quantities we can finally estimate the bandwidth of the cavity γ.

If the FSR does not correspond to the one targeted, then it is necessary to reopen the cavity, adjust the thickness of the ormolu plate and repeat the alignment procedure.

Three of these micro-cavities are now in place on the experiment (one for each SNSPD). The third micro-cavity has been built during this work.

Bibliography

[1] P. Kok, W. J. Munro, K. Nemoto, T. C. Ralph, J. P. Dowling & G. J. Milburn; "Linear optical quantum computing with photonic qubits"; Rev. Mod. Phys. **79**, pp. 135–174 (2007). https://link.aps.org/doi/10.1103/RevModPhys.79.135.

[2] S. L. Braunstein & P. van Loock; "Quantum information with continuous variables"; Rev. Mod. Phys. **77**, pp. 513–577 (2005). https://link.aps.org/doi/10.1103/RevModPhys.77.513.

[3] U. L. Andersen, J. S. Neergaard-Nielsen, P. van Loock & A. Furusawa; "Hybrid discrete- and continuous-variable quantum information"; Nature Physics **11**, pp. 713–719 (2015). ISSN 1745-2481. https://doi.org/10.1038/nphys3410.

[4] O. Morin, K. Huang, J. Liu, H. Le Jeannic, C. Fabre & J. Laurat; "Remote creation of hybrid entanglement between particle-like and wave-like optical qubits"; Nature Photonics **8**, pp. 570–574 (2014). ISSN 1749-4893. https://doi.org/10.1038/nphoton.2014.137.

[5] H. Jeong, A. Zavatta, M. Kang, S.-W. Lee, L. S. Costanzo, S. Grandi, T. C. Ralph & M. Bellini; "Generation of hybrid entanglement of light"; Nature Photonics **8**, pp. 564–569 (2014). ISSN 1749-4893. https://doi.org/10.1038/nphoton.2014.136.

[6] O. Morin, J. Liu, K. Huang, F. Barbosa, C. Fabre & J. Laurat; "Quantum State Engineering of Light with Continuous-wave Optical Parametric Oscillators"; Journal of Visualized Experiments **87**, p. e51224 (2014). https://www.jove.com/t/51224/quantum-state-engineering-light-with-continuous-wave-optical.

[7] H. L. Jeannic, V. B. Verma, A. Cavaillès, F. Marsili, M. D. Shaw, K. Huang, O. Morin, S. W. Nam & J. Laurat; "High-efficiency WSi superconducting nanowire single-photon detectors for quantum state engineering in the near infrared"; Opt. Lett. **41**, pp. 5341–5344 (2016). http://ol.osa.org/abstract.cfm?URI=ol-41-22-5341.

[8] K. Huang, H. Le Jeannic, J. Ruaudel, V. B. Verma, M. D. Shaw, F. Marsili, S. W. Nam, E. Wu, H. Zeng, Y.-C. Jeong, R. Filip, O. Morin &

J. Laurat; "Optical Synthesis of Large-Amplitude Squeezed Coherent-State Superpositions with Minimal Resources"; Phys. Rev. Lett. **115**, p. 023602 (2015). https://link.aps.org/doi/10.1103/PhysRevLett.115.023602.

[9] H. Le Jeannic, A. Cavaillès, K. Huang, R. Filip & J. Laurat; "Slowing Quantum Decoherence by Squeezing in Phase Space"; Phys. Rev. Lett. **120**, p. 073603 (2018). https://link.aps.org/doi/10.1103/PhysRevLett.120.073603.

[10] K. Huang, H. Le Jeannic, J. Ruaudel, O. Morin & J. Laurat; "Microcontroller-based locking in optics experiments"; Review of Scientific Instruments **85**, p. 123112 (2014). https://doi.org/10.1063/1.4903869.

[11] H. L. Jeannic, A. Cavaillès, J. Raskop, K. Huang & J. Laurat; "Remote preparation of continuous-variable qubits using loss-tolerant hybrid entanglement of light"; Optica **5**, pp. 1012–1015 (2018). http://www.osapublishing.org/optica/abstract.cfm?URI=optica-5-8-1012.

[12] A. Cavaillès, H. Le Jeannic, J. Raskop, G. Guccione, D. Markham, E. Diamanti, M. D. Shaw, V. B. Verma, S. W. Nam & J. Laurat; "Demonstration of Einstein-Podolsky-Rosen Steering Using Hybrid Continuous- and Discrete-Variable Entanglement of Light"; Phys. Rev. Lett. **121**, p. 170403 (2018). https://link.aps.org/doi/10.1103/PhysRevLett.121.170403.

[13] K. Huang, H. L. Jeannic, O. Morin, T. Darras, G. Guccione, A. Cavaillès & J. Laurat; "Engineering optical hybrid entanglement between discrete- and continuous-variable states"; New Journal of Physics **21**, p. 083033 (2019). https://doi.org/10.1088/1367-2630/ab34e7.

[14] G. Guccione, T. Darras, H. Le Jeannic, V. B. Verma, S. W. Nam, A. Cavaillès & J. Laurat; "Connecting heterogeneous quantum networks by hybrid entanglement swapping"; Science Advances **6** (2020). https://advances.sciencemag.org/content/6/22/eaba4508; https://advances.sciencemag.org/content/6/22/eaba4508.full.pdf.

[15] P. Zapletal, T. Darras, H. L. Jeannic, A. Cavaillès, G. Guccione, J. Laurat & R. Filip; "Experimental Fock-state bunching capability of non-ideal single-photon states"; Optica **8**, pp. 743–748 (2021). http://www.osapublishing.org/optica/abstract.cfm?URI=optica-8-5-743.

[16] A. Furusawa & van Loock Peter; *Introduction to Quantum Information Processing*; chapter 1, pp. 1–77 (John Wiley and Sons, Ltd) (2011); ISBN 9783527635283. https://onlinelibrary.wiley.com/doi/abs/10.1002/9783527635283.ch1; https://onlinelibrary.wiley.com/doi/pdf/10.1002/9783527635283.ch1.

[17] G. E. Moore; "Cramming more components onto integrated circuits, Reprinted from Electronics, volume 38, number 8, April 19, 1965, pp.114 ff." IEEE Solid-State Circuits Society Newsletter **11**, pp. 33–35 (2006).

[18] R. P. Feynman *et al.*; "There's plenty of room at the bottom"; California Institute of Technology, Engineering and Science magazine (1960).

[19] M. A. Nielsen & I. L. Chuang; *Quantum Computation and Quantum Information: 10th Anniversary Edition* (Cambridge University Press) (2010).

[20] E. Bernstein & U. Vazirani; "Quantum Complexity Theory"; SIAM Journal on Computing **26**, pp. 1411–1473 (1997). https://doi.org/10.1137/S0097539796300921.

[21] P. W. Shor; "Polynomial-Time Algorithms for Prime Factorization and Discrete Logarithms on a Quantum Computer"; SIAM Journal on Computing **26**, pp. 1484–1509 (1997). https://doi.org/10.1137/S0097539795293172.

[22] J. I. Cirac & P. Zoller; "Goals and opportunities in quantum simulation"; Nature Physics **8**, pp. 264–266 (2012). ISSN 1745-2481. https://doi.org/10.1038/nphys2275.

[23] R. P. Feynman; "Simulating physics with computers"; International Journal of Theoretical Physics **21**, pp. 467–488 (1982). ISSN 1572-9575. https://doi.org/10.1007/BF02650179.

[24] J. P. Dowling & G. J. Milburn; "Quantum technology: the second quantum revolution"; Philosophical Transactions of the Royal Society of London. Series A: Mathematical, Physical and Engineering Sciences **361**, pp. 1655–1674 (2003). https://doi.org/10.1098/rsta.2003.1227.

[25] A. Acín, I. Bloch, H. Buhrman, T. Calarco, C. Eichler, J. Eisert, D. Esteve, N. Gisin, S. J. Glaser, F. Jelezko, S. Kuhr, M. Lewenstein, M. F. Riedel, P. O. Schmidt, R. Thew, A. Wallraff, I. Walmsley & F. K. Wilhelm; "The quantum technologies roadmap: a European community view"; New Journal of Physics **20**, p. 080201 (2018). https://doi.org/10.1088/1367-2630/aad1ea.

[26] N. Gisin & R. Thew; "Quantum communication"; Nature Photonics **1**, pp. 165–171 (2007). ISSN 1749-4893. https://doi.org/10.1038/nphoton.2007.22.

[27] C. H. Bennett & G. Brassard; "Quantum cryptography: Public key distribution and coin tossing"; Theoretical Computer Science **560**, pp. 7–11 (2014). ISSN 0304-3975. https://www.sciencedirect.com/science/article/pii/S0304397514004241; theoretical Aspects of Quantum Cryptography – celebrating 30 years of BB84.

[28] J. Yin, Y.-H. Li, S.-K. Liao, M. Yang, Y. Cao, L. Zhang, J.-G. Ren, W.-Q. Cai, W.-Y. Liu, S.-L. Li, R. Shu, Y.-M. Huang, L. Deng, L. Li, Q. Zhang, N.-L. Liu, Y.-A. Chen, C.-Y. Lu, X.-B. Wang, F. Xu, J.-Y. Wang, C.-Z. Peng, A. K. Ekert & J.-W. Pan; "Entanglement-based secure quantum cryptography over 1,120 kilometres"; Nature **582**, pp. 501–505 (2020). ISSN 1476-4687. https://doi.org/10.1038/s41586-020-2401-y.

[29] J. Laurat, K. S. Choi, H. Deng, C. W. Chou & H. J. Kimble; "Heralded Entanglement between Atomic Ensembles: Preparation, Decoherence, and Scaling"; Phys. Rev. Lett. **99**, p. 180504 (2007). https://link.aps.org/doi/10.1103/PhysRevLett.99.180504.

[30] P. Magnard, S. Storz, P. Kurpiers, J. Schär, F. Marxer, J. Lütolf, T. Walter, J.-C. Besse, M. Gabureac, K. Reuer, A. Akin, B. Royer, A. Blais & A. Wallraff; "Microwave Quantum Link between Superconducting Circuits Housed in Spatially Separated Cryogenic Systems"; Phys. Rev. Lett. **125**, p. 260502 (2020). https://link.aps.org/doi/10.1103/PhysRevLett.125.260502.

[31] S. Daiss, S. Langenfeld, S. Welte, E. Distante, P. Thomas, L. Hartung, O. Morin & G. Rempe; "A quantum-logic gate between distant quantum-network modules"; Science **371**, pp. 614–617 (2021). ISSN 0036-8075. https://science.sciencemag.org/content/371/6529/614; https://science.sciencemag.org/content/371/6529/614.full.pdf.

[32] O. Bechler, A. Borne, S. Rosenblum, G. Guendelman, O. E. Mor, M. Netser, T. Ohana, Z. Aqua, N. Drucker, R. Finkelstein, Y. Lovsky, R. Bruch, D. Gurovich, E. Shafir & B. Dayan; "A passive photon–atom qubit swap operation"; Nature Physics **14**, pp. 996–1000 (2018). ISSN 1745-2481. https://doi.org/10.1038/s41567-018-0241-6.

[33] Y. Okazaki, I. Mahboob, K. Onomitsu, S. Sasaki, S. Nakamura, N.-H. Kaneko & H. Yamaguchi; "Dynamical coupling between a nuclear spin ensemble and electromechanical phonons"; Nature Communications **9**, p. 2993 (2018). ISSN 2041-1723. https://doi.org/10.1038/s41467-018-05463-3.

[34] B. Hacker, S. Welte, S. Daiss, A. Shaukat, S. Ritter, L. Li & G. Rempe; "Deterministic creation of entangled atom–light Schrödinger-cat states"; Nature Photonics **13**, pp. 110–115 (2019). ISSN 1749-4893. https://doi.org/10.1038/s41566-018-0339-5.

[35] A. Tchebotareva, S. L. N. Hermans, P. C. Humphreys, D. Voigt, P. J. Harmsma, L. K. Cheng, A. L. Verlaan, N. Dijkhuizen, W. de Jong, A. Dréau & R. Hanson; "Entanglement between a Diamond Spin Qubit and a Photonic Time-Bin Qubit at Telecom Wavelength"; Phys. Rev. Lett. **123**, p. 063601 (2019). https://link.aps.org/doi/10.1103/PhysRevLett.123.063601.

[36] B. Korzh, C. C. W. Lim, R. Houlmann, N. Gisin, M. J. Li, D. Nolan, B. Sanguinetti, R. Thew & H. Zbinden; "Provably secure and practical quantum key distribution over 307 km of optical fibre"; Nature Photonics **9**, pp. 163–168 (2015). https://doi.org/10.1038/nphoton.2014.327.

[37] J. Benhelm, G. Kirchmair, C. F. Roos & R. Blatt; "Towards fault-tolerant quantum computing with trapped ions"; Nature Physics **4**, pp. 463–466 (2008). ISSN 1745-2481. https://doi.org/10.1038/nphys961.

[38] A. Kandala, A. Mezzacapo, K. Temme, M. Takita, M. Brink, J. M. Chow & J. M. Gambetta; "Hardware-efficient variational quantum eigensolver for small molecules and quantum magnets"; Nature **549**, pp. 242–246 (2017). ISSN 1476-4687. https://doi.org/10.1038/nature23879.

[39] F. Arute, K. Arya, R. Babbush, D. Bacon, J. C. Bardin, R. Barends, R. Biswas, S. Boixo, F. G. S. L. Brandao, D. A. Buell, B. Burkett, Y. Chen, Z. Chen, B. Chiaro, R. Collins, W. Courtney, A. Dunsworth, E. Farhi, B. Foxen, A. Fowler, C. Gidney, M. Giustina, R. Graff, K. Guerin, S. Habegger, M. P. Harrigan, M. J. Hartmann, A. Ho, M. Hoffmann, T. Huang, T. S. Humble, S. V. Isakov, E. Jeffrey, Z. Jiang, D. Kafri, K. Kechedzhi, J. Kelly, P. V. Klimov, S. Knysh, A. Korotkov, F. Kostritsa, D. Landhuis, M. Lindmark, E. Lucero, D. Lyakh, S. Mandrà, J. R. McClean, M. McEwen, A. Megrant, X. Mi, K. Michielsen, M. Mohseni, J. Mutus, O. Naaman, M. Neeley, C. Neill, M. Y. Niu, E. Ostby, A. Petukhov, J. C. Platt, C. Quintana, E. G. Rieffel, P. Roushan, N. C. Rubin, D. Sank, K. J. Satzinger, V. Smelyanskiy, K. J. Sung, M. D. Trevithick, A. Vainsencher, B. Villalonga, T. White, Z. J. Yao, P. Yeh, A. Zalcman, H. Neven & J. M. Martinis; "Quantum supremacy using a programmable superconducting processor"; Nature **574**, pp. 505–510 (2019). ISSN 1476-4687. https://doi.org/10.1038/s41586-019-1666-5.

[40] J. M. Arrazola, V. Bergholm, K. Brádler, T. R. Bromley, M. J. Collins, I. Dhand, A. Fumagalli, T. Gerrits, A. Goussev, L. G. Helt, J. Hundal, T. Isacsson, R. B. Israel, J. Izaac, S. Jahangiri, R. Janik, N. Killoran, S. P. Kumar, J. Lavoie, A. E. Lita, D. H. Mahler, M. Menotti, B. Morrison, S. W. Nam, L. Neuhaus, H. Y. Qi, N. Quesada, A. Repingon, K. K. Sabapathy, M. Schuld, D. Su, J. Swinarton, A. Száva, K. Tan, P. Tan, V. D. Vaidya, Z. Vernon, Z. Zabaneh & Y. Zhang; "Quantum circuits with many photons on a programmable nanophotonic chip"; Nature **591**, pp. 54–60 (2021). ISSN 1476-4687. https://doi.org/10.1038/s41586-021-03202-1.

[41] D. P. DiVincenzo; "The physical implementation of quantum computation"; Fortschritte der Physik: Progress of Physics **48**, pp. 771–783 (2000).

[42] L. Henriet, L. Beguin, A. Signoles, T. Lahaye, A. Browaeys, G.-O. Reymond & C. Jurczak; "Quantum computing with neutral atoms"; Quantum **4**, p. 327 (2020). ISSN 2521-327X. https://doi.org/10.22331/q-2020-09-21-327.

[43] M. Korobko, Y. Ma, Y. Chen & R. Schnabel; "Quantum expander for gravitational-wave observatories"; Light: Science & Applications **8**, p. 118 (2019). ISSN 2047-7538. https://doi.org/10.1038/s41377-019-0230-2.

[44] K.-N. Schymik, V. Lienhard, D. Barredo, P. Scholl, H. Williams, A. Browaeys & T. Lahaye; "Enhanced atom-by-atom assembly of arbitrary tweezer arrays"; Phys. Rev. A **102**, p. 063107 (2020). https://link.aps.org/doi/10.1103/PhysRevA.102.063107.

[45] I. Bloch, J. Dalibard & S. Nascimbène; "Quantum simulations with ultracold quantum gases"; Nature Physics **8**, pp. 267–276 (2012). ISSN 1745-2481. https://doi.org/10.1038/nphys2259.

[46] R. Blatt & C. F. Roos; "Quantum simulations with trapped ions"; Nature Physics **8**, pp. 277–284 (2012). ISSN 1745-2481. https://doi.org/10.1038/nphys2252.

[47] A. Aspuru-Guzik & P. Walther; "Photonic quantum simulators"; Nature Physics **8**, pp. 285–291 (2012). ISSN 1745-2481. https://doi.org/10.1038/nphys2253.

[48] V. Giovannetti, S. Lloyd & L. Maccone; "Advances in quantum metrology"; Nature Photonics **5**, pp. 222–229 (2011). ISSN 1749-4893. https://doi.org/10.1038/nphoton.2011.35.

[49] S. Pirandola, B. R. Bardhan, T. Gehring, C. Weedbrook & S. Lloyd; "Advances in photonic quantum sensing"; Nature Photonics **12**, pp. 724–733 (2018). ISSN 1749-4893. https://doi.org/10.1038/s41566-018-0301-6.

[50] R. Schnabel, N. Mavalvala, D. E. McClelland & P. K. Lam; "Quantum metrology for gravitational wave astronomy"; Nature Communications **1**, p. 121 (2010). ISSN 2041-1723. https://doi.org/10.1038/ncomms1122.

[51] A. D. Ludlow, M. M. Boyd, J. Ye, E. Peik & P. O. Schmidt; "Optical atomic clocks"; Rev. Mod. Phys. **87**, pp. 637–701 (2015). https://link.aps.org/doi/10.1103/RevModPhys.87.637.

[52] V. Menoret, P. Vermeulen, N. Le Moigne, S. Bonvalot, P. Bouyer, A. Landragin & B. Desruelle; "Gravity measurements below ten to minus nine g with a transportable absolute quantum gravimeter"; Scientific Reports **8**, p. 12300 (2018). ISSN 2045-2322. https://doi.org/10.1038/s41598-018-30608-1.

[53] J.-P. Tetienne, T. Hingant, J.-V. Kim, L. H. Diez, J.-P. Adam, K. Garcia, J.-F. Roch, S. Rohart, A. Thiaville, D. Ravelosona & V. Jacques; "Nanoscale

imaging and control of domain-wall hopping with a nitrogen-vacancy center microscope"; Science **344**, pp. 1366–1369 (2014). ISSN 0036-8075. https://science.sciencemag.org/content/344/6190/1366; https://science.sciencemag.org/content/344/6190/1366.full.pdf.

[54] G. Balasubramanian, I. Y. Chan, R. Kolesov, M. Al-Hmoud, J. Tisler, C. Shin, C. Kim, A. Wojcik, P. R. Hemmer, A. Krueger, T. Hanke, A. Leitenstorfer, R. Bratschitsch, F. Jelezko & J. Wrachtrup; "Nanoscale imaging magnetometry with diamond spins under ambient conditions"; Nature **455**, pp. 648–651 (2008). ISSN 1476-4687. https://doi.org/10.1038/nature07278.

[55] J. L. Webb, L. Troise, N. W. Hansen, C. Olsson, A. M. Wojciechowski, J. Achard, O. Brinza, R. Staacke, M. Kieschnick, J. Meijer, A. Thielscher, J.-F. Perrier, K. Berg-Sørensen, A. Huck & U. L. Andersen; "Detection of biological signals from a live mammalian muscle using an early stage diamond quantum sensor"; Scientific Reports **11**, p. 2412 (2021). ISSN 2045-2322. https://doi.org/10.1038/s41598-021-81828-x.

[56] M. Aspelmeyer, T. J. Kippenberg & F. Marquardt; "Cavity optomechanics"; Rev. Mod. Phys. **86**, pp. 1391–1452 (2014). https://link.aps.org/doi/10.1103/RevModPhys.86.1391.

[57] R. Bach, D. Pope, S.-H. Liou & H. Batelaan; "Controlled double-slit electron diffraction"; New Journal of Physics **15**, p. 033018 (2013). https://doi.org/10.1088/1367-2630/15/3/033018.

[58] R. P. Feynman, R. B. Leighton & M. Sands; *The Feynman Lectures on Physics, Volume 3*; 1st edition (Addison-Wesley) (1965); ISBN 978-0201021189. https://www.feynmanlectures.caltech.edu/III_toc.html.

[59] R. P. Crease; "The most beautiful experiment"; Physics World **15**, pp. 19–20 (2002). https://doi.org/10.1088/2058-7058/15/9/22.

[60] A. Zeilinger; "Experiment and the foundations of quantum physics"; Rev. Mod. Phys. **71**, pp. S288–S297 (1999). https://link.aps.org/doi/10.1103/RevModPhys.71.S288.

[61] D. Bouwmeester, A. Ekert & A. Zeilinger; *The Physics of Quantum Information*; 1st edition (Springer) (2000); ISBN 3-540-66778-4. https://link.springer.com/book/10.1007%2F978-3-662-04209-0.

[62] E. Schrödinger; "Die gegenwärtige Situation in der Quantenmechanik"; Naturwissenschaften **23**, pp. 807–812 (1935). ISSN 1432-1904. https://doi.org/10.1007/BF01491891.

[63] J. S. Neergaard-Nielsen, M. Takeuchi, K. Wakui, H. Takahashi, K. Hayasaka, M. Takeoka & M. Sasaki; "Optical Continuous-Variable Qubit";

Phys. Rev. Lett. **105**, p. 053602 (2010). https://link.aps.org/doi/10.1103/PhysRevLett.105.053602.

[64] R. Lescanne, M. Villiers, T. Peronnin, A. Sarlette, M. Delbecq, B. Huard, T. Kontos, M. Mirrahimi & Z. Leghtas; "Exponential suppression of bit-flips in a qubit encoded in an oscillator"; Nature Physics **16**, pp. 509–513 (2020). ISSN 1745-2481. https://doi.org/10.1038/s41567-020-0824-x.

[65] A. P. Lund, T. C. Ralph & H. L. Haselgrove; "Fault-Tolerant Linear Optical Quantum Computing with Small-Amplitude Coherent States"; Phys. Rev. Lett. **100**, p. 030503 (2008). https://link.aps.org/doi/10.1103/PhysRevLett.100.030503.

[66] A. Facon, E.-K. Dietsche, D. Grosso, S. Haroche, J.-M. Raimond, M. Brune & S. Gleyzes; "A sensitive electrometer based on a Rydberg atom in a Schrödinger-cat state"; Nature **535**, pp. 262–265 (2016). ISSN 1476-4687. https://doi.org/10.1038/nature18327.

[67] C. Cohen-Tannoudji, B. Diu & F. Laloë; *Mécanique Quantique-Tome 1* (EDP Sciences) (2021).

[68] W. Schleich; *Wigner Function* (John Wiley and Sons Ltd) (2001); ISBN 9783527602971. https://onlinelibrary.wiley.com/doi/abs/10.1002/3527602976.ch3; https://onlinelibrary.wiley.com/doi/pdf/10.1002/3527602976.ch3.

[69] M. Walschaers; "Non-Gaussian Quantum States and Where to Find Them"; (2021); 2104.12596.

[70] A. Einstein, B. Podolsky & N. Rosen; "Can Quantum-Mechanical Description of Physical Reality Be Considered Complete?" Phys. Rev. **47**, pp. 777–780 (1935). https://link.aps.org/doi/10.1103/PhysRev.47.777.

[71] J. S. Bell; "On the Einstein Podolsky Rosen paradox"; Physics Physique Fizika **1**, pp. 195–200 (1964). https://link.aps.org/doi/10.1103/PhysicsPhysiqueFizika.1.195.

[72] S. J. Freedman & J. F. Clauser; "Experimental Test of Local Hidden-Variable Theories"; Phys. Rev. Lett. **28**, pp. 938–941 (1972). https://link.aps.org/doi/10.1103/PhysRevLett.28.938.

[73] A. Aspect, J. Dalibard & G. Roger; "Experimental Test of Bell's Inequalities Using Time-Varying Analyzers"; Phys. Rev. Lett. **49**, pp. 1804–1807 (1982). https://link.aps.org/doi/10.1103/PhysRevLett.49.1804.

[74] L. K. Shalm, E. Meyer-Scott, B. G. Christensen, P. Bierhorst, M. A. Wayne, M. J. Stevens, T. Gerrits, S. Glancy, D. R. Hamel, M. S. Allman,

K. J. Coakley, S. D. Dyer, C. Hodge, A. E. Lita, V. B. Verma, C. Lambrocco, E. Tortorici, A. L. Migdall, Y. Zhang, D. R. Kumor, W. H. Farr, F. Marsili, M. D. Shaw, J. A. Stern, C. Abellán, W. Amaya, V. Pruneri, T. Jennewein, M. W. Mitchell, P. G. Kwiat, J. C. Bienfang, R. P. Mirin, E. Knill & S. W. Nam; "Strong Loophole-Free Test of Local Realism"; Phys. Rev. Lett. **115**, p. 250402 (2015). https://link.aps.org/doi/10.1103/PhysRevLett.115.250402.

[75] B. Hensen, H. Bernien, A. E. Dréau, A. Reiserer, N. Kalb, M. S. Blok, J. Ruitenberg, R. F. L. Vermeulen, R. N. Schouten, C. Abellán, W. Amaya, V. Pruneri, M. W. Mitchell, M. Markham, D. J. Twitchen, D. Elkouss, S. Wehner, T. H. Taminiau & R. Hanson; "Loophole-free Bell inequality violation using electron spins separated by 1.3 kilometres"; Nature **526**, pp. 682–686 (2015). ISSN 1476-4687. https://doi.org/10.1038/nature15759.

[76] M. Giustina, M. A. M. Versteegh, S. Wengerowsky, J. Handsteiner, A. Hochrainer, K. Phelan, F. Steinlechner, J. Kofler, J.-A. Larsson, C. Abellán, W. Amaya, V. Pruneri, M. W. Mitchell, J. Beyer, T. Gerrits, A. E. Lita, L. K. Shalm, S. W. Nam, T. Scheidl, R. Ursin, B. Wittmann & A. Zeilinger; "Significant-Loophole-Free Test of Bell's Theorem with Entangled Photons"; Phys. Rev. Lett. **115**, p. 250401 (2015). https://link.aps.org/doi/10.1103/PhysRevLett.115.250401.

[77] M. Chen, N. C. Menicucci & O. Pfister; "Experimental Realization of Multipartite Entanglement of 60 Modes of a Quantum Optical Frequency Comb"; Phys. Rev. Lett. **112**, p. 120505 (2014). https://link.aps.org/doi/10.1103/PhysRevLett.112.120505.

[78] M. V. Larsen, X. Guo, C. R. Breum, J. S. Neergaard-Nielsen & U. L. Andersen; "Deterministic generation of a two-dimensional cluster state"; Science **366**, pp. 369–372 (2019). ISSN 0036-8075. https://science.sciencemag.org/content/366/6463/369; https://science.sciencemag.org/content/366/6463/369.full.pdf.

[79] W. Asavanant, Y. Shiozawa, S. Yokoyama, B. Charoensombutamon, H. Emura, R. N. Alexander, S. Takeda, J.-i. Yoshikawa, N. C. Menicucci, H. Yonezawa & A. Furusawa; "Generation of time-domain-multiplexed two-dimensional cluster state"; Science **366**, pp. 373–376 (2019). ISSN 0036-8075. https://science.sciencemag.org/content/366/6463/373; https://science.sciencemag.org/content/366/6463/373.full.pdf.

[80] Y.-S. Ra, A. Dufour, M. Walschaers, C. Jacquard, T. Michel, C. Fabre & N. Treps; "Non-Gaussian quantum states of a multimode light field"; Nature Physics **16**, pp. 144–147 (2020). ISSN 1745-2481. https://doi.org/10.1038/s41567-019-0726-y.

[81] M. B. Plenio & S. Virmani; "An Introduction to Entanglement Measures"; Quantum Info. Comput. **7**, p. 1–51 (2007)ISSN 1533-7146.

[82] R. Horodecki, P. Horodecki, M. Horodecki & K. Horodecki; "Quantum entanglement"; Rev. Mod. Phys. **81**, pp. 865–942 (2009). https://link.aps.org/doi/10.1103/RevModPhys.81.865.

[83] G. Vidal & R. F. Werner; "Computable measure of entanglement"; Phys. Rev. A **65**, p. 032314 (2002). https://link.aps.org/doi/10.1103/PhysRevA.65.032314.

[84] L. Pezzé & A. Smerzi; "Entanglement, Nonlinear Dynamics, and the Heisenberg Limit"; Phys. Rev. Lett. **102**, p. 100401 (2009). https://link.aps.org/doi/10.1103/PhysRevLett.102.100401.

[85] R. Raussendorf & H. J. Briegel; "A One-Way Quantum Computer"; Phys. Rev. Lett. **86**, pp. 5188–5191 (2001). https://link.aps.org/doi/10.1103/PhysRevLett.86.5188.

[86] P. Walther, K. J. Resch, T. Rudolph, E. Schenck, H. Weinfurter, V. Vedral, M. Aspelmeyer & A. Zeilinger; "Experimental one-way quantum computing"; Nature **434**, pp. 169–176 (2005). ISSN 1476-4687. https://doi.org/10.1038/nature03347.

[87] R. N. Alexander, P. Wang, N. Sridhar, M. Chen, O. Pfister & N. C. Menicucci; "One-way quantum computing with arbitrarily large time-frequency continuous-variable cluster states from a single optical parametric oscillator"; Phys. Rev. A **94**, p. 032327 (2016). https://link.aps.org/doi/10.1103/PhysRevA.94.032327.

[88] A. K. Ekert; "Quantum cryptography based on Bell's theorem"; Phys. Rev. Lett. **67**, pp. 661–663 (1991). https://link.aps.org/doi/10.1103/PhysRevLett.67.661.

[89] C. H. Bennett, G. Brassard & N. D. Mermin; "Quantum cryptography without Bell's theorem"; Phys. Rev. Lett. **68**, pp. 557–559 (1992). https://link.aps.org/doi/10.1103/PhysRevLett.68.557.

[90] H. M. Wiseman, S. J. Jones & A. C. Doherty; "Steering, Entanglement, Nonlocality, and the Einstein-Podolsky-Rosen Paradox"; Phys. Rev. Lett. **98**, p. 140402 (2007). https://link.aps.org/doi/10.1103/PhysRevLett.98.140402.

[91] H. J. Kimble; "The quantum internet"; Nature **453**, pp. 1023–1030 (2008). ISSN 1476-4687. https://doi.org/10.1038/nature07127.

[92] S. Wehner, D. Elkouss & R. Hanson; "Quantum internet: A vision for the road ahead"; Science **362** (2018). ISSN 0036-8075. https://science.sciencemag.org/

content/362/6412/eaam9288; https://science.sciencemag.org/content/362/6412/eaam9288.full.pdf.

[93] Y.-A. Chen, Q. Zhang, T.-Y. Chen, W.-Q. Cai, S.-K. Liao, J. Zhang, K. Chen, J. Yin, J.-G. Ren, Z. Chen, S.-L. Han, Q. Yu, K. Liang, F. Zhou, X. Yuan, M.-S. Zhao, T.-Y. Wang, X. Jiang, L. Zhang, W.-Y. Liu, Y. Li, Q. Shen, Y. Cao, C.-Y. Lu, R. Shu, J.-Y. Wang, L. Li, N.-L. Liu, F. Xu, X.-B. Wang, C.-Z. Peng & J.-W. Pan; "An integrated space-to-ground quantum communication network over 4,600 kilometres"; Nature **589**, pp. 214–219 (2021). ISSN 1476-4687. https://doi.org/10.1038/s41586-020-03093-8.

[94] S. Barz, E. Kashefi, A. Broadbent, J. F. Fitzsimons, A. Zeilinger & P. Walther; "Demonstration of Blind Quantum Computing"; Science **335**, pp. 303–308 (2012). ISSN 0036-8075. https://science.sciencemag.org/content/335/6066/303; https://science.sciencemag.org/content/335/6066/303.full.pdf.

[95] P. Kómár, E. M. Kessler, M. Bishof, L. Jiang, A. S. Sørensen, J. Ye & M. D. Lukin; "A quantum network of clocks"; Nature Physics **10**, pp. 582–587 (2014). ISSN 1745-2481. https://doi.org/10.1038/nphys3000.

[96] X. Guo, C. R. Breum, J. Borregaard, S. Izumi, M. V. Larsen, T. Gehring, M. Christandl, J. S. Neergaard-Nielsen & U. L. Andersen; "Distributed quantum sensing in a continuous-variable entangled network"; Nature Physics **16**, pp. 281–284 (2020). ISSN 1745-2481. https://doi.org/10.1038/s41567-019-0743-x.

[97] C.-W. Chou, J. Laurat, H. Deng, K. S. Choi, H. de Riedmatten, D. Felinto & H. J. Kimble; "Functional Quantum Nodes for Entanglement Distribution over Scalable Quantum Networks"; Science **316**, pp. 1316–1320 (2007). ISSN 0036-8075. https://science.sciencemag.org/content/316/5829/1316; https://science.sciencemag.org/content/316/5829/1316.full.pdf.

[98] K. Hammerer, A. S. Sørensen & E. S. Polzik; "Quantum interface between light and atomic ensembles"; Rev. Mod. Phys. **82**, pp. 1041–1093 (2010). https://link.aps.org/doi/10.1103/RevModPhys.82.1041.

[99] A. Stute, B. Casabone, B. Brandstätter, K. Friebe, T. E. Northup & R. Blatt; "Quantum-state transfer from an ion to a photon"; Nature Photonics **7**, pp. 219–222 (2013). ISSN 1749-4893. https://doi.org/10.1038/nphoton.2012.358.

[100] A. Delteil, Z. Sun, W.-b. Gao, E. Togan, S. Faelt & A. Imamoğlu; "Generation of heralded entanglement between distant hole spins"; Nature Physics **12**, pp. 218–223 (2016). ISSN 1745-2481. https://doi.org/10.1038/nphys3605.

[101] M. Cao, F. Hoffet, S. Qiu, A. S. Sheremet & J. Laurat; "Efficient reversible entanglement transfer between light and quantum memories"; Optica **7**, pp. 1440–1444 (2020). http://www.osapublishing.org/optica/abstract.cfm?URI=optica-7-10-1440.

[102] N. V. Corzo, J. Raskop, A. Chandra, A. S. Sheremet, B. Gouraud & J. Laurat; "Waveguide-coupled single collective excitation of atomic arrays"; Nature **566**, pp. 359–362 (2019). ISSN 1476-4687. https://doi.org/10.1038/s41586-019-0902-3.

[103] A. Goban, C.-L. Hung, J. D. Hood, S.-P. Yu, J. A. Muniz, O. Painter & H. J. Kimble; "Superradiance for Atoms Trapped along a Photonic Crystal Waveguide"; Phys. Rev. Lett. **115**, p. 063601 (2015). https://link.aps.org/doi/10.1103/PhysRevLett.115.063601.

[104] A. Boaron, G. Boso, D. Rusca, C. Vulliez, C. Autebert, M. Caloz, M. Perrenoud, G. Gras, F. Bussières, M.-J. Li, D. Nolan, A. Martin & H. Zbinden; "Secure Quantum Key Distribution over 421 km of Optical Fiber"; Phys. Rev. Lett. **121**, p. 190502 (2018). https://link.aps.org/doi/10.1103/PhysRevLett.121.190502.

[105] H. A. Bachor & T. C. Ralph; *Basic Optical Components*; chapter 5, pp. 139–198 (John Wiley and Sons Ltd) (2019); ISBN 9783527695805. https://onlinelibrary.wiley.com/doi/abs/10.1002/9783527695805.ch5; https://onlinelibrary.wiley.com/doi/pdf/10.1002/9783527695805.ch5.

[106] X.-T. Fang, P. Zeng, H. Liu, M. Zou, W. Wu, Y.-L. Tang, Y.-J. Sheng, Y. Xiang, W. Zhang, H. Li, Z. Wang, L. You, M.-J. Li, H. Chen, Y.-A. Chen, Q. Zhang, C.-Z. Peng, X. Ma, T.-Y. Chen & J.-W. Pan; "Implementation of quantum key distribution surpassing the linear rate-transmittance bound"; Nature Photonics **14**, pp. 422–425 (2020). ISSN 1749-4893. https://doi.org/10.1038/s41566-020-0599-8.

[107] S. Shi, L. Tian, Y. Wang, Y. Zheng, C. Xie & K. Peng; "Demonstration of Channel Multiplexing Quantum Communication Exploiting Entangled Sideband Modes"; Phys. Rev. Lett. **125**, p. 070502 (2020). https://link.aps.org/doi/10.1103/PhysRevLett.125.070502.

[108] J. Calsamiglia & N. Lütkenhaus; "Maximum efficiency of a linear-optical Bell-state analyzer"; Applied Physics B **72**, pp. 67–71 (2001). ISSN 1432-0649. https://doi.org/10.1007/s003400000484.

[109] A. Gilchrist, K. Nemoto, W. J. Munro, T. C. Ralph, S. Glancy, S. L. Braunstein & G. J. Milburn; "Schrödinger cats and their power for quantum information processing"; Journal of Optics B: Quantum and Semiclassical Optics **6**, pp. S828–S833 (2004). https://doi.org/10.1088/1464-4266/6/8/032.

[110] C. J. Myatt, B. E. King, Q. A. Turchette, C. A. Sackett, D. Kielpinski, W. M. Itano, C. Monroe & D. J. Wineland; "Decoherence of quantum superpositions through coupling to engineered reservoirs"; Nature **403**, pp. 269–273 (2000). ISSN 1476-4687. https://doi.org/10.1038/35002001.

[111] C. R. Monroe, R. J. Schoelkopf & M. D. Lukin; "Quantum Connections"; Scientific American **314**, p. 50—57 (2016). ISSN 0036-8733. https://doi.org/10.1038/scientificamerican0516-50.

[112] H.-J. Briegel, W. Dür, J. I. Cirac & P. Zoller; "Quantum Repeaters: The Role of Imperfect Local Operations in Quantum Communication"; Phys. Rev. Lett. **81**, pp. 5932–5935 (1998). https://link.aps.org/doi/10.1103/PhysRevLett.81.5932.

[113] L.-M. Duan, M. D. Lukin, J. I. Cirac & P. Zoller; "Long-distance quantum communication with atomic ensembles and linear optics"; Nature **414**, pp. 413–418 (2001). ISSN 1476-4687. https://doi.org/10.1038/35106500.

[114] N. Sangouard, C. Simon, H. de Riedmatten & N. Gisin; "Quantum repeaters based on atomic ensembles and linear optics"; Rev. Mod. Phys. **83**, pp. 33–80 (2011). https://link.aps.org/doi/10.1103/RevModPhys.83.33.

[115] W. K. Wootters & W. H. Zurek; "A single quantum cannot be cloned"; Nature **299**, pp. 802–803 (1982). ISSN 1476-4687. https://doi.org/10.1038/299802a0.

[116] "Quantum Flagship: Discover Quantum Technologies - The Quantum Repeaters"; https://qt.eu/discover-quantum/underlying-principles/quantum-repeaters/.

[117] A. I. Lvovsky, B. C. Sanders & W. Tittel; "Optical quantum memory"; Nature Photonics **3**, pp. 706–714 (2009). ISSN 1749-4893. https://doi.org/10.1038/nphoton.2009.231.

[118] A. M. Childs; "Secure assisted quantum computation"; Quantum Information and Computation **5** (2005). ISSN 1533-7146. http://dx.doi.org/10.26421/QIC5.6.

[119] M. Bozzio, A. Orieux, L. Trigo Vidarte, I. Zaquine, I. Kerenidis & E. Diamanti; "Experimental investigation of practical unforgeable quantum money"; npj Quantum Information **4**, p. 5 (2018). ISSN 2056-6387. https://doi.org/10.1038/s41534-018-0058-2.

[120] J.-W. Pan, C. Simon, Č. Brukner & A. Zeilinger; "Entanglement purification for quantum communication"; Nature **410**, pp. 1067–1070 (2001). ISSN 1476-4687. https://doi.org/10.1038/35074041.

[121] C. H. Bennett, G. Brassard, S. Popescu, B. Schumacher, J. A. Smolin & W. K. Wootters; "Purification of Noisy Entanglement and Faithful Teleportation

via Noisy Channels"; Phys. Rev. Lett. **76**, pp. 722–725 (1996). https://link.aps.org/doi/10.1103/PhysRevLett.76.722.

[122] A. Franzen, B. Hage, J. DiGuglielmo, J. Fiurášˇek & R. Schnabel; "Experimental Demonstration of Continuous Variable Purification of Squeezed States"; Phys. Rev. Lett. **97**, p. 150505 (2006). https://link.aps.org/doi/10.1103/PhysRevLett.97.150505.

[123] N. Kalb, A. A. Reiserer, P. C. Humphreys, J. J. W. Bakermans, S. J. Kamerling, N. H. Nickerson, S. C. Benjamin, D. J. Twitchen, M. Markham & R. Hanson; "Entanglement distillation between solid-state quantum network nodes"; Science **356**, pp. 928–932 (2017). ISSN 0036-8075. https://science.sciencemag.org/content/356/6341/928; https://science.sciencemag.org/content/356/6341/928.full.pdf.

[124] Z.-D. Li, R. Zhang, X.-F. Yin, L.-Z. Liu, Y. Hu, Y.-Q. Fang, Y.-Y. Fei, X. Jiang, J. Zhang, L. Li, N.-L. Liu, F. Xu, Y.-A. Chen & J.-W. Pan; "Experimental quantum repeater without quantum memory"; Nature Photonics **13**, pp. 644–648 (2019). ISSN 1749-4893. https://doi.org/10.1038/s41566-019-0468-5.

[125] Y.-F. Pu, S. Zhang, Y.-K. Wu, N. Jiang, W. Chang, C. Li & L.-M. Duan; "Experimental demonstration of memory-enhanced scaling for entanglement connection of quantum repeater segments"; Nature Photonics **15**, pp. 374–378 (2021). ISSN 1749-4893. https://doi.org/10.1038/s41566-021-00764-4.

[126] D. Lago-Rivera, S. Grandi, J. V. Rakonjac, A. Seri & H. de Riedmatten; "Telecom-heralded entanglement between remote multimode solid-state quantum memories"; (2021); 2101.05097.

[127] M. Pompili, S. L. N. Hermans, S. Baier, H. K. C. Beukers, P. C. Humphreys, R. N. Schouten, R. F. L. Vermeulen, M. J. Tiggelman, L. dos Santos Martins, B. Dirkse, S. Wehner & R. Hanson; "Realization of a multinode quantum network of remote solid-state qubits"; Science **372**, pp. 259–264 (2021). ISSN 0036-8075. https://science.sciencemag.org/content/372/6539/259; https://science.sciencemag.org/content/372/6539/259.full.pdf.

[128] D. Gottesman & I. L. Chuang; "Demonstrating the viability of universal quantum computation using teleportation and single-qubit operations"; Nature **402**, pp. 390–393 (1999). ISSN 1476-4687. https://doi.org/10.1038/46503.

[129] M. V. Larsen, C. Chamberland, K. Noh, J. S. Neergaard-Nielsen & U. L. Andersen; "A fault-tolerant continuous-variable measurement-based quantum computation architecture"; (2021); 2101.03014.

[130] D. Bouwmeester, J.-W. Pan, K. Mattle, M. Eibl, H. Weinfurter & A. Zeilinger; "Experimental quantum teleportation"; Nature **390**, pp. 575–579 (1997). ISSN 1476-4687. https://doi.org/10.1038/37539.

[131] C. H. Bennett, G. Brassard, C. Crépeau, R. Jozsa, A. Peres & W. K. Wootters; "Teleporting an unknown quantum state via dual classical and Einstein-Podolsky-Rosen channels"; Phys. Rev. Lett. **70**, pp. 1895–1899 (1993). https://link.aps.org/doi/10.1103/PhysRevLett.70.1895.

[132] A. Furusawa, J. L. Sørensen, S. L. Braunstein, C. A. Fuchs, H. J. Kimble & E. S. Polzik; "Unconditional Quantum Teleportation"; Science **282**, pp. 706–709 (1998). ISSN 0036-8075. https://science.sciencemag.org/content/282/5389/706; https://science.sciencemag.org/content/282/5389/706.full.pdf.

[133] A. E. Ulanov, D. Sychev, A. A. Pushkina, I. A. Fedorov & A. I. Lvovsky; "Quantum Teleportation Between Discrete and Continuous Encodings of an Optical Qubit"; Phys. Rev. Lett. **118**, p. 160501 (2017). https://link.aps.org/doi/10.1103/PhysRevLett.118.160501.

[134] A. Cavaillès; *Non-locality tests and quantum communication protocols using hybrid entanglement of light*; Theses; Sorbonne Université (2019). https://tel.archives-ouvertes.fr/tel-02968173.

[135] S. Massar & S. Popescu; "Optimal Extraction of Information from Finite Quantum Ensembles"; Phys. Rev. Lett. **74**, pp. 1259–1263 (1995). https://link.aps.org/doi/10.1103/PhysRevLett.74.1259.

[136] J.-W. Pan, D. Bouwmeester, H. Weinfurter & A. Zeilinger; "Experimental Entanglement Swapping: Entangling Photons That Never Interacted"; Phys. Rev. Lett. **80**, pp. 3891–3894 (1998). https://link.aps.org/doi/10.1103/PhysRevLett.80.3891.

[137] M. Żukowski, A. Zeilinger, M. A. Horne & A. K. Ekert; ""Event-ready-detectors" Bell experiment via entanglement swapping"; Phys. Rev. Lett. **71**, pp. 4287–4290 (1993). https://link.aps.org/doi/10.1103/PhysRevLett.71.4287.

[138] S. J. van Enk, N. Lütkenhaus & H. J. Kimble; "Experimental procedures for entanglement verification"; Phys. Rev. A **75**, p. 052318 (2007). https://link.aps.org/doi/10.1103/PhysRevA.75.052318.

[139] E. Meyer-Scott, N. Prasannan, I. Dhand, C. Eigner, V. Quiring, S. Barkhofen, B. Brecht, M. B. Plenio & C. Silberhorn; "Exponential enhancement of multi-photon entanglement rate via quantum interference buffering"; (2019); 1908.05722.

[140] M. Müller, S. Bounouar, K. D. Jöns, M. Glässl & P. Michler; "On-demand generation of indistinguishable polarization-entangled photon pairs"; Nature Photonics **8**, pp. 224–228 (2014). ISSN 1749-4893. https://doi.org/10.1038/nphoton.2013.377.

[141] P. C. Humphreys, N. Kalb, J. P. J. Morits, R. N. Schouten, R. F. L. Vermeulen, D. J. Twitchen, M. Markham & R. Hanson; "Deterministic delivery of remote entanglement on a quantum network"; Nature **558**, pp. 268–273 (2018). ISSN 1476-4687. https://doi.org/10.1038/s41586-018-0200-5.

[142] U. L. Andersen, T. Gehring, C. Marquardt & G. Leuchs; "30 years of squeezed light generation"; Physica Scripta **91**, p. 053001 (2016).

[143] R. W. Boyd; "Chapter 2 - Wave-Equation Description of Nonlinear Optical Interactions"; in "Nonlinear Optics (Third Edition)," , edited by R. W. Boyd; third edition edition; pp. 69–133 (Academic Press, Burlington) (2008); ISBN 978-0-12-369470-6. https://www.sciencedirect.com/science/article/pii/B9780123694706000022.

[144] A. I. Lvovsky; "Squeezed light"; (2016); 1401.4118.

[145] R. E. Slusher, P. Grangier, A. LaPorta, B. Yurke & M. J. Potasek; "Pulsed Squeezed Light"; Phys. Rev. Lett. **59**, pp. 2566–2569 (1987). https://link.aps.org/doi/10.1103/PhysRevLett.59.2566.

[146] T. Hirano, K. Kotani, T. Ishibashi, S. Okude & T. Kuwamoto; "3 dB squeezing by single-pass parametric amplification in a periodically poled KTiOPO4 crystal"; Opt. Lett. **30**, pp. 1722–1724 (2005). http://ol.osa.org/abstract.cfm?URI=ol-30-13-1722.

[147] W. Wasilewski, A. I. Lvovsky, K. Banaszek & C. Radzewicz; "Pulsed squeezed light: Simultaneous squeezing of multiple modes"; Phys. Rev. A **73**, p. 063819 (2006). https://link.aps.org/doi/10.1103/PhysRevA.73.063819.

[148] L. L. Volpe, S. De, T. Kouadou, D. Horoshko, M. I. Kolobov, C. Fabre, V. Parigi & N. Treps; "Multimode single-pass spatio-temporal squeezing"; Opt. Express **28**, pp. 12385–12394 (2020). http://www.opticsexpress.org/abstract.cfm?URI=oe-28-8-12385.

[149] O. Morin; *Non-Gaussian states and measurements for quantum information*; Theses; Université Pierre et Marie Curie - Paris VI (2013). https://tel.archives-ouvertes.fr/tel-01066655.

[150] J. Laurat; *Génération d'états non-classiques et intrication en variables continues à l'aide d'un oscillateur paramétrique optique*; Theses; Université Pierre et Marie Curie - Paris VI (2004). https://tel.archives-ouvertes.fr/tel-00007442.

[151] A. Mari & J. Eisert; "Positive Wigner Functions Render Classical Simulation of Quantum Computation Efficient"; Phys. Rev. Lett. **109**, p. 230503 (2012). https://link.aps.org/doi/10.1103/PhysRevLett.109.230503.

[152] A. I. Lvovsky, P. Grangier, A. Ourjoumtsev, V. Parigi, M. Sasaki & R. Tualle-Brouri; "Production and applications of non-Gaussian quantum states of light"; (2020); 2006.16985.

[153] R. H. Hadfield; "Single-photon detectors for optical quantum information applications"; Nature photonics **3**, pp. 696–705 (2009).

[154] F. Marsili, F. Najafi, E. Dauler, F. Bellei, X. Hu, M. Csete, R. J. Molnar & K. K. Berggren; "Single-Photon Detectors Based on Ultranarrow Superconducting Nanowires"; Nano Letters **11**, pp. 2048–2053 (2011). https://doi.org/10.1021/nl2005143; pMID: 21456546; https://doi.org/10.1021/nl2005143.

[155] F. Marsili, V. B. Verma, J. A. Stern, S. Harrington, A. E. Lita, T. Gerrits, I. Vayshenker, B. Baek, M. D. Shaw, R. P. Mirin *et al.*; "Detecting single infrared photons with 93% system efficiency"; Nature Photonics **7**, pp. 210–214 (2013).

[156] Y. Lixing; "Superconducting nanowire single-photon detectors for quantum information"; Nanophotonics **9**, pp. 2673–2692 (2020). https://doi.org/10.1515/nanoph-2020-0186.

[157] C. M. Natarajan, M. G. Tanner & R. H. Hadfield; "Superconducting nanowire single-photon detectors: physics and applications"; Superconductor science and technology **25**, p. 063001 (2012).

[158] H. Le Jeannic; *Optical Hybrid Quantum Information processing*; Theses; Université Pierre et Marie Curie - Paris VI (2016). https://tel.archives-ouvertes.fr/tel-01665496.

[159] L. A. Jiang, E. A. Dauler & J. T. Chang; "Photon-number-resolving detector with 10 bits of resolution"; Phys. Rev. A **75**, p. 062325 (2007). https://link.aps.org/doi/10.1103/PhysRevA.75.062325.

[160] F. Marsili, D. Bitauld, A. Gaggero, S. Jahanmirinejad, R. Leoni, F. Mattioli & A. Fiore; "Physics and application of photon number resolving detectors based on superconducting parallel nanowires"; New Journal of Physics **11**, p. 045022 (2009). https://doi.org/10.1088/1367-2630/11/4/045022.

[161] V. B. Verma, R. Horansky, F. Marsili, J. Stern, M. Shaw, A. E. Lita, R. P. Mirin & S. W. Nam; "A four-pixel single-photon pulse-position array fabricated from WSi superconducting nanowire single-photon detectors"; Applied Physics Letters **104**, p. 051115 (2014).

[162] M. Jönsson, M. Swillo, S. Gyger, V. Zwiller & G. Björk; "Temporal array with superconducting nanowire single-photon detectors for photon-number resolution"; Phys. Rev. A **102**, p. 052616 (2020). https://link.aps.org/doi/10.1103/PhysRevA.102.052616.

[163] R. Kruse, J. Tiedau, T. J. Bartley, S. Barkhofen & C. Silberhorn; "Limits of the time-multiplexed photon-counting method"; Phys. Rev. A **95**, p. 023815 (2017). https://link.aps.org/doi/10.1103/PhysRevA.95.023815.

[164] J. Provazník, L. Lachman, R. Filip & P. Marek; "Benchmarking photon number resolving detectors"; Opt. Express **28**, pp. 14839–14849 (2020). http://www.opticsexpress.org/abstract.cfm?URI=oe-28-10-14839.

[165] N. Sridhar, R. Shahrokhshahi, A. J. Miller, B. Calkins, T. Gerrits, A. Lita, S. W. Nam & O. Pfister; "Direct measurement of the Wigner function by photon-number-resolving detection"; J. Opt. Soc. Am. B **31**, pp. B34–B40 (2014). http://josab.osa.org/abstract.cfm?URI=josab-31-10-B34.

[166] M. Endo, T. Sonoyama, M. Matsuyama, F. Okamoto, S. Miki, M. Yabuno, F. China, H. Terai & A. Furusawa; "Quantum detector tomography of a superconducting nanostrip photon-number-resolving detector"; Opt. Express **29**, pp. 11728–11738 (2021). http://www.opticsexpress.org/abstract.cfm?URI=oe-29-8-11728.

[167] A. E. Lita, A. J. Miller & S. W. Nam; "Counting near-infrared single-photons with 95% efficiency"; Opt. Express **16**, pp. 3032–3040 (2008). http://www.opticsexpress.org/abstract.cfm?URI=oe-16-5-3032.

[168] K. Irwin; "An application of electrothermal feedback for high resolution cryogenic particle detection"; Applied Physics Letters **66**, pp. 1998–2000 (1995).

[169] M. E. Huber, A. M. Corey, K. L. Lumpkins, F. N. Nafe, J. O. Rantschler, G. Hilton, J. M. Martinis & A. H. Steinbach; "DC SQUID series arrays with intracoil damping to reduce resonance distortions11Contribution of the U.S. Government; not subject to copyright in the United States." Applied Superconductivity **5**, pp. 425–429 (1997). ISSN 0964-1807. https://www.sciencedirect.com/science/article/pii/S0964180798000659.

[170] C. Cahall, K. L. Nicolich, N. T. Islam, G. P. Lafyatis, A. J. Miller, D. J. Gauthier & J. Kim; "Multi-photon detection using a conventional superconducting nanowire single-photon detector"; Optica **4**, pp. 1534–1535 (2017). http://www.osapublishing.org/optica/abstract.cfm?URI=optica-4-12-1534.

[171] B. E. A. Saleh & M. C. Teich; *Fundamentals of Photonics, Volume 2*; 3rd edition (Wiley) (2019); ISBN 978-1-119-50687-4. https://www.wiley.com/en-us/Fundamentals+of+Photonics%2C+2+Volume+Set%2C+3rd+Edition-p-9781119506874.

[172] O. Morin, C. Fabre & J. Laurat; "Experimentally Accessing the Optimal Temporal Mode of Traveling Quantum Light States"; Phys. Rev. Lett. **111**, p. 213602 (2013). https://link.aps.org/doi/10.1103/PhysRevLett.111.213602.

[173] H. Ogawa, H. Ohdan, K. Miyata, M. Taguchi, K. Makino, H. Yonezawa, J.-i. Yoshikawa & A. Furusawa; "Real-Time Quadrature Measurement of a Single-Photon Wave Packet with Continuous Temporal-Mode Matching"; Phys. Rev. Lett. **116**, p. 233602 (2016). https://link.aps.org/doi/10.1103/PhysRevLett.116.233602.

[174] D. A. Shaddock, M. B. Gray & D. E. McClelland; "Frequency locking a laser to an optical cavity by use of spatial mode interference"; Opt. Lett. **24**, pp. 1499–1501 (1999). http://ol.osa.org/abstract.cfm?URI=ol-24-21-1499.

[175] R. Kumar, E. Barrios, A. MacRae, E. Cairns, E. Huntington & A. Lvovsky; "Versatile wideband balanced detector for quantum optical homodyne tomography"; Optics Communications **285**, pp. 5259–5267 (2012). ISSN 0030-4018. https://www.sciencedirect.com/science/article/pii/S0030401812008255.

[176] A. I. Lvovsky & M. G. Raymer; "Continuous-variable optical quantum-state tomography"; Rev. Mod. Phys. **81**, pp. 299–332 (2009). https://link.aps.org/doi/10.1103/RevModPhys.81.299.

[177] L. Aolita, C. Gogolin, M. Kliesch & J. Eisert; "Reliable quantum certification of photonic state preparations"; Nature Communications **6**, p. 8498 (2015). ISSN 2041-1723. https://doi.org/10.1038/ncomms9498.

[178] T. Giordani, F. Flamini, M. Pompili, N. Viggianiello, N. Spagnolo, A. Crespi, R. Osellame, N. Wiebe, M. Walschaers, A. Buchleitner & F. Sciarrino; "Experimental statistical signature of many-body quantum interference"; Nature Photonics **12**, pp. 173–178 (2018). ISSN 1749-4893. https://doi.org/10.1038/s41566-018-0097-4.

[179] H. Ollivier, S. E. Thomas, S. C. Wein, I. M. de Buy Wenniger, N. Coste, J. C. Loredo, N. Somaschi, A. Harouri, A. Lemaitre, I. Sagnes, L. Lanco, C. Simon, C. Anton, O. Krebs & P. Senellart; "Hong-Ou-Mandel Interference with Imperfect Single Photon Sources"; Phys. Rev. Lett. **126**, p. 063602 (2021). https://link.aps.org/doi/10.1103/PhysRevLett.126.063602.

[180] P. Zapletal & R. Filip; "Multi-copy quantifiers for single-photon states"; Scientific Reports **7**, p. 1484 (2017). ISSN 2045-2322. https://doi.org/10.1038/s41598-017-01333-y.

[181] J. C. Matthews, X.-Q. Zhou, H. Cable, P. J. Shadbolt, D. J. Saunders, G. A. Durkin, G. J. Pryde & J. L. O'Brien; "Towards practical quantum metrology with photon counting"; npj Quantum Information **2**, p. 16023 (2016). ISSN 2056-6387. https://doi.org/10.1038/npjqi.2016.23.

[182] A. E. Ulanov, I. A. Fedorov, D. Sychev, P. Grangier & A. I. Lvovsky; "Loss-tolerant state engineering for quantum-enhanced metrology via the reverse Hong–

Ou–Mandel effect"; Nature Communications **7**, p. 11925 (2016). ISSN 2041-1723. https://doi.org/10.1038/ncomms11925.

[183] S. Slussarenko, M. M. Weston, H. M. Chrzanowski, L. K. Shalm, V. B. Verma, S. W. Nam & G. J. Pryde; "Unconditional violation of the shot-noise limit in photonic quantum metrology"; Nature Photonics **11**, pp. 700–703 (2017). ISSN 1749-4893. https://doi.org/10.1038/s41566-017-0011-5.

[184] M. H. Michael, M. Silveri, R. T. Brierley, V. V. Albert, J. Salmilehto, L. Jiang & S. M. Girvin; "New Class of Quantum Error-Correcting Codes for a Bosonic Mode"; Phys. Rev. X **6**, p. 031006 (2016). https://link.aps.org/doi/10.1103/PhysRevX.6.031006.

[185] M. Bergmann & P. van Loock; "Quantum error correction against photon loss using NOON states"; Phys. Rev. A **94**, p. 012311 (2016). https://link.aps.org/doi/10.1103/PhysRevA.94.012311.

[186] L. Hu, Y. Ma, W. Cai, X. Mu, Y. Xu, W. Wang, Y. Wu, H. Wang, Y. P. Song, C.-L. Zou, S. M. Girvin, L.-M. Duan & L. Sun; "Quantum error correction and universal gate set operation on a binomial bosonic logical qubit"; Nature Physics **15**, pp. 503–508 (2019). ISSN 1745-2481. https://doi.org/10.1038/s41567-018-0414-3.

[187] M. Klaas, E. Schlottmann, H. Flayac, F. P. Laussy, F. Gericke, M. Schmidt, M. v. Helversen, J. Beyer, S. Brodbeck, H. Suchomel, S. Höfling, S. Reitzenstein & C. Schneider; "Photon-Number-Resolved Measurement of an Exciton-Polariton Condensate"; Phys. Rev. Lett. **121**, p. 047401 (2018). https://link.aps.org/doi/10.1103/PhysRevLett.121.047401.

[188] J. Tiedau, T. J. Bartley, G. Harder, A. E. Lita, S. W. Nam, T. Gerrits & C. Silberhorn; "Scalability of parametric down-conversion for generating higher-order Fock states"; Phys. Rev. A **100**, p. 041802 (2019). https://link.aps.org/doi/10.1103/PhysRevA.100.041802.

[189] W. Pfaff, C. J. Axline, L. D. Burkhart, U. Vool, P. Reinhold, L. Frunzio, L. Jiang, M. H. Devoret & R. J. Schoelkopf; "Controlled release of multiphoton quantum states from a microwave cavity memory"; Nature Physics **13**, pp. 882–887 (2017). ISSN 1745-2481. https://doi.org/10.1038/nphys4143.

[190] D. Kienzler, H.-Y. Lo, V. Negnevitsky, C. Flühmann, M. Marinelli & J. P. Home; "Quantum Harmonic Oscillator State Control in a Squeezed Fock Basis"; Phys. Rev. Lett. **119**, p. 033602 (2017). https://link.aps.org/doi/10.1103/PhysRevLett.119.033602.

[191] S. Hong, R. Riedinger, I. Marinković, A. Wallucks, S. G. Hofer, R. A. Norte, M. Aspelmeyer & S. Gröblacher; "Hanbury Brown and Twiss

interferometry of single phonons from an optomechanical resonator"; Science **358**, pp. 203–206 (2017). ISSN 0036-8075. https://science.sciencemag.org/content/358/6360/203; https://science.sciencemag.org/content/358/6360/203.full.pdf.

[192] D. V. Sychev, A. E. Ulanov, A. A. Pushkina, M. W. Richards, I. A. Fedorov & A. I. Lvovsky; "Enlargement of optical Schrödinger's cat states"; Nature Photonics **11**, pp. 379–382 (2017). ISSN 1749-4893. https://doi.org/10.1038/nphoton.2017.57.

[193] A. Ourjoumtsev, R. Tualle-Brouri, J. Laurat & P. Grangier; "Generating Optical Schrödinger Kittens for Quantum Information Processing"; Science **312**, pp. 83–86 (2006). ISSN 0036-8075. https://science.sciencemag.org/content/312/5770/83; https://science.sciencemag.org/content/312/5770/83.full.pdf.

[194] J. S. Neergaard-Nielsen, B. M. Nielsen, C. Hettich, K. Mølmer & E. S. Polzik; "Generation of a Superposition of Odd Photon Number States for Quantum Information Networks"; Phys. Rev. Lett. **97**, p. 083604 (2006). https://link.aps.org/doi/10.1103/PhysRevLett.97.083604.

[195] M. Dakna, T. Anhut, T. Opatrný, L. Knöll & D.-G. Welsch; "Generating Schrödinger-cat-like states by means of conditional measurements on a beam splitter"; Phys. Rev. A **55**, pp. 3184–3194 (1997). https://link.aps.org/doi/10.1103/PhysRevA.55.3184.

[196] O. Morin, J.-D. Bancal, M. Ho, P. Sekatski, V. D'Auria, N. Gisin, J. Laurat & N. Sangouard; "Witnessing Trustworthy Single-Photon Entanglement with Local Homodyne Measurements"; Phys. Rev. Lett. **110**, p. 130401 (2013). https://link.aps.org/doi/10.1103/PhysRevLett.110.130401.

[197] S. Takeda, T. Mizuta, M. Fuwa, P. van Loock & A. Furusawa; "Deterministic quantum teleportation of photonic quantum bits by a hybrid technique"; Nature **500**, pp. 315–318 (2013). ISSN 1476-4687. https://doi.org/10.1038/nature12366.

[198] A. Ourjoumtsev, A. Dantan, R. Tualle-Brouri & P. Grangier; "Increasing Entanglement between Gaussian States by Coherent Photon Subtraction"; Phys. Rev. Lett. **98**, p. 030502 (2007). https://link.aps.org/doi/10.1103/PhysRevLett.98.030502.

[199] H. Takahashi, J. S. Neergaard-Nielsen, M. Takeuchi, M. Takeoka, K. Hayasaka, A. Furusawa & M. Sasaki; "Entanglement distillation from Gaussian input states"; Nature Photonics **4**, pp. 178–181 (2010). ISSN 1749-4893. https://doi.org/10.1038/nphoton.2010.1.

[200] A. E. Ulanov, I. A. Fedorov, A. A. Pushkina, Y. V. Kurochkin, T. C. Ralph & A. I. Lvovsky; "Undoing the effect of loss on quantum entanglement"; Nature

Photonics **9**, pp. 764–768 (2015). ISSN 1749-4893. https://doi.org/10.1038/nphoton.2015.195.

[201] J. B. Brask, I. Rigas, E. S. Polzik, U. L. Andersen & A. S. Sørensen; "Hybrid Long-Distance Entanglement Distribution Protocol"; Phys. Rev. Lett. **105**, p. 160501 (2010). https://link.aps.org/doi/10.1103/PhysRevLett.105.160501.

[202] H. Kwon & H. Jeong; "Violation of the Bell–Clauser-Horne-Shimony-Holt inequality using imperfect photodetectors with optical hybrid states"; Phys. Rev. A **88**, p. 052127 (2013). https://link.aps.org/doi/10.1103/PhysRevA.88.052127.

[203] Y. Lim, J. Joo, T. P. Spiller & H. Jeong; "Loss-resilient photonic entanglement swapping using optical hybrid states"; Phys. Rev. A **94**, p. 062337 (2016). https://link.aps.org/doi/10.1103/PhysRevA.94.062337.

[204] N. Takei, H. Yonezawa, T. Aoki & A. Furusawa; "High-Fidelity Teleportation beyond the No-Cloning Limit and Entanglement Swapping for Continuous Variables"; Phys. Rev. Lett. **94**, p. 220502 (2005). https://link.aps.org/doi/10.1103/PhysRevLett.94.220502.

[205] K. Park, S.-W. Lee & H. Jeong; "Quantum teleportation between particlelike and fieldlike qubits using hybrid entanglement under decoherence effects"; Phys. Rev. A **86**, p. 062301 (2012). https://link.aps.org/doi/10.1103/PhysRevA.86.062301.

[206] N. Lütkenhaus, J. Calsamiglia & K.-A. Suominen; "Bell measurements for teleportation"; Phys. Rev. A **59**, pp. 3295–3300 (1999). https://link.aps.org/doi/10.1103/PhysRevA.59.3295.

[207] S.-W. Lee & H. Jeong; "Bell-state measurement and quantum teleportation using linear optics: two-photon pairs, entangled coherent states, and hybrid entanglement"; (2013); 1304.1214.

[208] S. L. Braunstein & H. J. Kimble; "A posteriori teleportation"; Nature **394**, pp. 840–841 (1998). ISSN 1476-4687. https://doi.org/10.1038/29674.

[209] D. V. Sychev, A. E. Ulanov, E. S. Tiunov, A. A. Pushkina, A. Kuzhamuratov, V. Novikov & A. I. Lvovsky; "Entanglement and teleportation between polarization and wave-like encodings of an optical qubit"; Nature Communications **9**, p. 3672 (2018). ISSN 2041-1723. https://doi.org/10.1038/s41467-018-06055-x.

[210] X. Jia, X. Su, Q. Pan, J. Gao, C. Xie & K. Peng; "Experimental Demonstration of Unconditional Entanglement Swapping for Continuous Variables"; Phys. Rev. Lett. **93**, p. 250503 (2004). https://link.aps.org/doi/10.1103/PhysRevLett.93.250503.

[211] S. Takeda, M. Fuwa, P. van Loock & A. Furusawa; "Entanglement Swapping between Discrete and Continuous Variables"; Phys. Rev. Lett. **114**, p. 100501 (2015). https://link.aps.org/doi/10.1103/PhysRevLett.114.100501.

[212] E. S. Tiunov, V. V. T. (Vyborova), A. E. Ulanov, A. I. Lvovsky & A. K. Fedorov; "Experimental quantum homodyne tomography via machine learning"; Optica **7**, pp. 448–454 (2020). http://www.osapublishing.org/optica/abstract.cfm?URI=optica-7-5-448.

[213] Y.-B. Sheng, L. Zhou & G.-L. Long; "Hybrid entanglement purification for quantum repeaters"; Phys. Rev. A **88**, p. 022302 (2013). https://link.aps.org/doi/10.1103/PhysRevA.88.022302.

[214] M. Bouillard; *Développement de cavités synchrones et d'une mémoire quantique : des outils pour l'ingénierie quantique hybride.*; Theses; Université Paris Saclay (COmUE) (2017). https://pastel.archives-ouvertes.fr/tel-01709020.

[215] J.-i. Yoshikawa, K. Makino, S. Kurata, P. van Loock & A. Furusawa; "Creation, Storage, and On-Demand Release of Optical Quantum States with a Negative Wigner Function"; Phys. Rev. X **3**, p. 041028 (2013). https://link.aps.org/doi/10.1103/PhysRevX.3.041028.

[216] S. Takeda, K. Takase & A. Furusawa; "On-demand photonic entanglement synthesizer"; Science Advances **5** (2019). https://advances.sciencemag.org/content/5/5/eaaw4530; https://advances.sciencemag.org/content/5/5/eaaw4530.full.pdf.

[217] C. Lv, W. Zhang, L. You, P. Hu, H. Wang, H. Li, C. Zhang, J. Huang, Y. Wang, X. Yang, Z. Wang & X. Xie; "Improving maximum count rate of superconducting nanowire single-photon detector with small active area using series attenuator"; AIP Advances **8**, p. 105018 (2018). https://doi.org/10.1063/1.5049549.

[218] W. Zhang, J. Huang, C. Zhang, L. You, C. Lv, L. Zhang, H. Li, Z. Wang & X. Xie; "A 16-Pixel Interleaved Superconducting Nanowire Single-Photon Detector Array With A Maximum Count Rate Exceeding 1.5 GHz"; IEEE Transactions on Applied Superconductivity **29**, pp. 1–4 (2019).

[219] L. Li, Z. Liu, X. Ren, S. Wang, V.-C. Su, M.-K. Chen, C. H. Chu, H. Y. Kuo, B. Liu, W. Zang, G. Guo, L. Zhang, Z. Wang, S. Zhu & D. P. Tsai; "Metalens-array–based high-dimensional and multiphoton quantum source"; Science **368**, pp. 1487–1490 (2020). ISSN 0036-8075. https://science.sciencemag.org/content/368/6498/1487; https://science.sciencemag.org/content/368/6498/1487.full.pdf.

[220] R. Uppu, F. T. Pedersen, Y. Wang, C. T. Olesen, C. Papon, X. Zhou, L. Midolo, S. Scholz, A. D. Wieck, A. Ludwig & P. Lodahl; "Scalable integrated single-photon source"; Science Advances **6** (2020). https://advances.

sciencemag.org/content/6/50/eabc8268; https://advances.sciencemag.org/content/6/50/eabc8268.full.pdf.

[221] H.-S. Zhong, Y. Li, W. Li, L.-C. Peng, Z.-E. Su, Y. Hu, Y.-M. He, X. Ding, W. Zhang, H. Li, L. Zhang, Z. Wang, L. You, X.-L. Wang, X. Jiang, L. Li, Y.-A. Chen, N.-L. Liu, C.-Y. Lu & J.-W. Pan; "12-Photon Entanglement and Scalable Scattershot Boson Sampling with Optimal Entangled-Photon Pairs from Parametric Down-Conversion"; Phys. Rev. Lett. **121**, p. 250505 (2018). https://link.aps.org/doi/10.1103/PhysRevLett.121.250505.

[222] H. Wang, J. Qin, X. Ding, M.-C. Chen, S. Chen, X. You, Y.-M. He, X. Jiang, L. You, Z. Wang, C. Schneider, J. J. Renema, S. Höfling, C.-Y. Lu & J.-W. Pan; "Boson Sampling with 20 Input Photons and a 60-Mode Interferometer in a 10^{14}-Dimensional Hilbert Space"; Phys. Rev. Lett. **123**, p. 250503 (2019). https://link.aps.org/doi/10.1103/PhysRevLett.123.250503.

[223] H.-S. Zhong, H. Wang, Y.-H. Deng, M.-C. Chen, L.-C. Peng, Y.-H. Luo, J. Qin, D. Wu, X. Ding, Y. Hu, P. Hu, X.-Y. Yang, W.-J. Zhang, H. Li, Y. Li, X. Jiang, L. Gan, G. Yang, L. You, Z. Wang, L. Li, N.-L. Liu, C.-Y. Lu & J.-W. Pan; "Quantum computational advantage using photons"; Science **370**, pp. 1460–1463 (2020). ISSN 0036-8075. https://science.sciencemag.org/content/370/6523/1460; https://science.sciencemag.org/content/370/6523/1460.full.pdf.

[224] M. Bouillard, G. Boucher, J. Ferrer Ortas, B. Pointard & R. Tualle-Brouri; "Quantum Storage of Single-Photon and Two-Photon Fock States with an All-Optical Quantum Memory"; Phys. Rev. Lett. **122**, p. 210501 (2019). https://link.aps.org/doi/10.1103/PhysRevLett.122.210501.

[225] D. Istrati, Y. Pilnyak, J. C. Loredo, C. Antón, N. Somaschi, P. Hilaire, H. Ollivier, M. Esmann, L. Cohen, L. Vidro, C. Millet, A. Lemaître, I. Sagnes, A. Harouri, L. Lanco, P. Senellart & H. S. Eisenberg; "Sequential generation of linear cluster states from a single photon emitter"; Nature Communications **11**, p. 5501 (2020). ISSN 2041-1723. https://doi.org/10.1038/s41467-020-19341-4.

[226] P. K. Lam; *Applications of Quantum Electro-Optics Control of Squeezed Light*; Theses; Australian National University (1998).

[227] M. S. Stefsky; *Generation and Detection of Low-Frequency Squeezing for Gravitational-Wave Detection*; Theses; Australian National University (2012).

[228] P. G. Kwiat, K. Mattle, H. Weinfurter, A. Zeilinger, A. V. Sergienko & Y. Shih; "New High-Intensity Source of Polarization-Entangled Photon Pairs"; Phys. Rev. Lett. **75**, pp. 4337–4341 (1995). https://link.aps.org/doi/10.1103/PhysRevLett.75.4337.

[229] S. Pirandola, J. Eisert, C. Weedbrook, A. Furusawa & S. L. Braunstein; "Advances in quantum teleportation"; Nature Photonics **9**, pp. 641–652 (2015). ISSN 1749-4893. https://doi.org/10.1038/nphoton.2015.154.

[230] H. Krauter, D. Salart, C. A. Muschik, J. M. Petersen, H. Shen, T. Fernholz & E. S. Polzik; "Deterministic quantum teleportation between distant atomic objects"; Nature Physics **9**, pp. 400–404 (2013). ISSN 1745-2481. https://doi.org/10.1038/nphys2631.

[231] W. Pfaff, B. J. Hensen, H. Bernien, S. B. van Dam, M. S. Blok, T. H. Taminiau, M. J. Tiggelman, R. N. Schouten, M. Markham, D. J. Twitchen & R. Hanson; "Unconditional quantum teleportation between distant solid-state quantum bits"; Science **345**, pp. 532–535 (2014). ISSN 0036-8075. https://science.sciencemag.org/content/345/6196/532; https://science.sciencemag.org/content/345/6196/532.full.pdf.

[232] N. Fiaschi, B. Hensen, A. Wallucks, R. Benevides, J. Li, T. P. M. Alegre & S. Gröblacher; "Optomechanical quantum teleportation"; (2021); 2104.02080.

[233] N. Lee, H. Benichi, Y. Takeno, S. Takeda, J. Webb, E. Huntington & A. Furusawa; "Teleportation of Nonclassical Wave Packets of Light"; Science **332**, pp. 330–333 (2011). ISSN 0036-8075. https://science.sciencemag.org/content/332/6027/330; https://science.sciencemag.org/content/332/6027/330.full.pdf.

[234] U. L. Andersen & T. C. Ralph; "High-Fidelity Teleportation of Continuous-Variable Quantum States Using Delocalized Single Photons"; Phys. Rev. Lett. **111**, p. 050504 (2013). https://link.aps.org/doi/10.1103/PhysRevLett.111.050504.

[235] J. H. Shapiro & N. C. Wong; "An ultrabright narrowband source of polarization-entangled photon pairs"; Journal of Optics B: Quantum and Semiclassical Optics **2**, pp. L1–L4 (1999). https://doi.org/10.1088/1464-4266/2/1/101.

[236] J. Nunn, N. K. Langford, W. S. Kolthammer, T. F. M. Champion, M. R. Sprague, P. S. Michelberger, X.-M. Jin, D. G. England & I. A. Walmsley; "Enhancing Multiphoton Rates with Quantum Memories"; Phys. Rev. Lett. **110**, p. 133601 (2013). https://link.aps.org/doi/10.1103/PhysRevLett.110.133601.

[237] Y. Hashimoto, T. Toyama, J.-i. Yoshikawa, K. Makino, F. Okamoto, R. Sakakibara, S. Takeda, P. van Loock & A. Furusawa; "All-Optical Storage of Phase-Sensitive Quantum States of Light"; Phys. Rev. Lett. **123**, p. 113603 (2019). https://link.aps.org/doi/10.1103/PhysRevLett.123.113603.

[238] A. Seri, D. Lago-Rivera, A. Lenhard, G. Corrielli, R. Osellame, M. Mazzera & H. de Riedmatten; "Quantum Storage of Frequency-Multiplexed

Heralded Single Photons"; Phys. Rev. Lett. **123**, p. 080502 (2019). https://link.aps.org/doi/10.1103/PhysRevLett.123.080502.

[239] Y.-Y. Lai, G.-D. Lin, J. Twamley & H.-S. Goan; "Single-nitrogen-vacancy-center quantum memory for a superconducting flux qubit mediated by a ferromagnet"; Phys. Rev. A **97**, p. 052303 (2018). https://link.aps.org/doi/10.1103/PhysRevA.97.052303.

[240] P. Senellart, G. Solomon & A. White; "High-performance semiconductor quantum-dot single-photon sources"; Nature Nanotechnology **12**, pp. 1026–1039 (2017). ISSN 1748-3395. https://doi.org/10.1038/nnano.2017.218.

[241] D. Huber, M. Reindl, S. F. Covre da Silva, C. Schimpf, J. Martín-Sánchez, H. Huang, G. Piredda, J. Edlinger, A. Rastelli & R. Trotta; "Strain-Tunable GaAs Quantum Dot: A Nearly Dephasing-Free Source of Entangled Photon Pairs on Demand"; Phys. Rev. Lett. **121**, p. 033902 (2018). https://link.aps.org/doi/10.1103/PhysRevLett.121.033902.

[242] F. Basso Basset, M. B. Rota, C. Schimpf, D. Tedeschi, K. D. Zeuner, S. F. Covre da Silva, M. Reindl, V. Zwiller, K. D. Jöns, A. Rastelli & R. Trotta; "Entanglement Swapping with Photons Generated on Demand by a Quantum Dot"; Phys. Rev. Lett. **123**, p. 160501 (2019). https://link.aps.org/doi/10.1103/PhysRevLett.123.160501.

[243] F. Basso Basset, F. Salusti, L. Schweickert, M. B. Rota, D. Tedeschi, S. F. Covre da Silva, E. Roccia, V. Zwiller, K. D. Jöns, A. Rastelli & R. Trotta; "Quantum teleportation with imperfect quantum dots"; npj Quantum Information **7**, p. 7 (2021). ISSN 2056-6387. https://doi.org/10.1038/s41534-020-00356-0.

[244] H. Ollivier, I. Maillette de Buy Wenniger, S. Thomas, S. C. Wein, A. Harouri, G. Coppola, P. Hilaire, C. Millet, A. Lemaître, I. Sagnes, O. Krebs, L. Lanco, J. C. Loredo, C. Antón, N. Somaschi & P. Senellart; "Reproducibility of High-Performance Quantum Dot Single-Photon Sources"; ACS Photonics **7**, pp. 1050–1059 (2020). https://doi.org/10.1021/acsphotonics.9b01805.

[245] J. C. Loredo, C. Antón, B. Reznychenko, P. Hilaire, A. Harouri, C. Millet, H. Ollivier, N. Somaschi, L. De Santis, A. Lemaître, I. Sagnes, L. Lanco, A. Auffèves, O. Krebs & P. Senellart; "Generation of non-classical light in a photon-number superposition"; Nature Photonics **13**, pp. 803–808 (2019). ISSN 1749-4893. https://doi.org/10.1038/s41566-019-0506-3.

[246] T. B. Pittman, B. C. Jacobs & J. D. Franson; "Single photons on pseudodemand from stored parametric down-conversion"; Phys. Rev. A **66**, p. 042303 (2002). https://link.aps.org/doi/10.1103/PhysRevA.66.042303.

[247] A. L. Migdall, D. Branning & S. Castelletto; "Tailoring single-photon and multiphoton probabilities of a single-photon on-demand source"; Phys. Rev. A **66**, p. 053805 (2002). https://link.aps.org/doi/10.1103/PhysRevA.66.053805.

[248] F. Kaneda & P. G. Kwiat; "High-efficiency single-photon generation via large-scale active time multiplexing"; Science Advances **5** (2019). https://advances.sciencemag.org/content/5/10/eaaw8586; https://advances.sciencemag.org/content/5/10/eaaw8586.full.pdf.

[249] E. Gouzien, F. Brunel, S. Tanzilli & V. D'Auria; "Scheme for the generation of hybrid entanglement between time-bin and wavelike encodings"; Phys. Rev. A **102**, p. 012603 (2020). https://link.aps.org/doi/10.1103/PhysRevA.102.012603.

[250] H. Kwon & H. Jeong; "Generation of hybrid entanglement between a single-photon polarization qubit and a coherent state"; Phys. Rev. A **91**, p. 012340 (2015). https://link.aps.org/doi/10.1103/PhysRevA.91.012340.

Tom Darras **30 Juin 2021**

Sujet : Protocoles de téléportation quantique reposant sur l'intrication hybride de la lumière

Résumé : Cette thèse porte sur l'implémentation de protocoles de téléportation quantique impliquant conjointement les approches en variables discrètes et en variables continues de l'information quantique optique. Nous commençons par présenter l'intérêt de ces protocoles dans le cadre des réseaux quantiques hétérogènes, puis nous introduisons les techniques expérimentales pour la production d'états non-Gaussiens tels que des photons uniques, des chats de Schrödinger optiques, jusqu'à l'intrication hybride de la lumière entre des états quantiques en variables discrètes et continues. Nous développons un nouvel outil expérimental pour la mise en place d'une mesure de Bell qui intègre des techniques de comptage de photon et de sélection de quadratures du champ. Nous combinons ces méthodes en réalisant un protocole de transfert d'intrication entre deux états intriqués de natures différentes: une intrication à un photon et une intrication hybride de la lumière. Nous décrivons ensuite la mise en place d'une source de photons uniques annoncés supplémentaire et d'un système de cryogénie pour le fonctionnement de détecteurs de photon supraconducteurs. Enfin nous employons ces nouvelles ressources dans un protocole de téléportation quantique hybride permettant la conversion d'information quantique de variables discrètes à variables continues. Ces travaux ouvrent la voie à l'interconnexion de plateformes de natures différentes dans les réseaux quantiques hétérogènes.

Mots clés : optique quantique, information quantique hybride, photon unique, chat de Schrödinger, intrication, téléportation quantique, transfert d'intrication, mesure de Bell

Subject : Quantum teleportation-based protocols with hybrid entanglement of light

Abstract: This thesis focuses on the implementation of quantum teleportation-based protocols involving conjointly the discrete- and continuous-variable approaches of optical quantum information processing. We first present the interest of these protocols in the framework of heterogeneous quantum networks, and we introduce the experimental techniques for the generation of non-Gaussian quantum states such as single photons, optical Schrödinger cat states, up to hybrid entanglement between discrete- and continuous-variable quantum states. We develop a novel experimental tool for the implementation of a Bell-state measurement composed of photon counting and quadrature selection. By combining these methods, we demonstrate an entanglement swapping protocol between two entangled states of different natures: single-photon entanglement and hybrid entanglement of light. We describe the installation of an additional heralded single-photon source and a cryogenic system for the operation of superconducting single-photon detectors. We finally employ these new resources in a hybrid quantum teleportation protocol which enables the conversion of quantum information from discrete- to continuous-variables. This work paves the way towards the interconnection of platforms of different natures in heterogeneous quantum networks.

Keywords : quantum optics, hybrid quantum information processing, single photon, Schrödinger's cat, entanglement, quantum teleportation, entanglement swapping, Bell-state measurement